Photodisintegration cross section of ^{4}He in the giant dipole resonance energy region

Motoki Murata

A dissertation submitted in partial fulfillment of the requirements
for the degree of Doctor of Philosophy in Science, Kyoto University

January 2024

Truth is found neither in the thesis nor the antithesis, but in an emergent synthesis which reconciles the two.

Georg Wilhelm Friedrich Hegel[a]

[a]It was pointed out that this aphorism was not written by Hegel himself. See, for example, a refenrence: G. E. Mueller, J. Hist. Ideas **19**, 411 (1958).

Abstract

Isovector Giant Dipole Resonance (IVGDR) is the most well examined collective excitation mode of atomic nuclei and is attributed to linear anti-phase oscillations of protons and neutrons. The IVGDR in various nuclei heave long been studied systematically via photonuclear reactions by means of various experimental probes and reactions including photodisintegration. Consequently, several properties of the IVGDR in heavy nuclear system are well explained from macroscopic models, but those in light nuclei are rather complicated due to the relative importance of individual nucleon degrees of freedom. Recently, ab initio calculations, which is a general framework based on realistic nuclear forces, can give qualitative predictions on the nuclear reaction relevant to the IVGDR in light nuclei.

As for ^{4}He photodisintegration in IVGDR energy region, recent theoretical calculations concluded the IVGDR resonance peak should locate approximately at the E_γ =26 MeV in the excitation function. On the other hand, the recent experimental results show a serious discrepancy in peak energies. According to one of two doctrines, the IVGDR peak would be at E_γ >30 MeV, which even disagrees with the theoretical predictions. This striking result by Shima *et al.* was constructed upon the robust experimental procedures and therefore may force knowledge regarding nuclear structure and nuclear astrophysics based on the current understanding on the nuclear force to be modified.

In the present work, we performed the simultaneous measurement of ^{4}He(γ, n)^{3}He and ^{4}He(γ, p)^{3}H reactions in the energy range around the IVGDR. Aiming to give a criteria to judge the origin of the experimental discrepancy, our measurement was conducted inheriting the experimental scheme adopted by Shima *et al.* The quasi-mono-energetic photon beams at E_γ = 23.0, 24.0, 25.0, 27.0, 28.0, and 30.0 MeV, were produced at BL01 in the NewSUBARU synchrotron facility via the laser Compton scattering technique. The beam was irradiated on the MAIKo active target time projection chamber filled with helium gas. The trajectories of charged decay particles emitted from ^{4}He were recorded and analyzed event by event. The fine-pitched readout and optimization of the operating condition of the detector system improved the quality of the acquired data compared to the previous study.

The differential cross sections of the ^{4}He(γ, n)^{3}He and ^{4}He(γ, p)^{3}H re-

actions were computed from the experimental yields, the deduced detection efficiency, and the integrated beam flux. The angular dependence of the cross section was well explained from the assumption that the photodisintegration in this energy region was induced via pure $E1$ transition. The total cross section was evaluated assuming the $E1$ transition. Our data suggested ^{4}He(γ, n)^{3}He and ^{4}He(γ, p)^{3}H cross sections showed peak structures around E_γ = 26 MeV. This result contradicted the previous experimental study reported by Shima *et al.*, but was consistent with several theoretical calculations and another experimental studies. We could conclude that the unconventional result was less likely, and there were no need to revise the conventional view on the nuclear physics.

This thesis is based on the original article published in the Physical Review C journal: M. Murata *et al.*, Phys. Rev. C 107, 064317 (2023) [1].

Contents

List of Figures **ix**

List of Tables **xiii**

1 Introduction **1**

1.1 Photodisintegration and the IVGDR 1

1.1.1 Electromagnetic Probes for the Nuclear Physics 1

1.1.2 Energy Dependence of Photonuclear Reactions 2

1.1.3 Photoabsorption in Low Energy Region 4

1.1.4 Isovector Giant Dipole Resonance (IVGDR) 6

1.2 ^{4}He Photodisintegration 12

1.2.1 Profile of ^{4}He Nuclei 12

1.2.2 Topics Regarding Nucleon Few-Body Calculations 13

1.2.3 Astrophysical Interests 22

1.3 Theoretical Works 31

1.4 Experimental Review 33

1.4.1 Overview 33

1.4.2 Prehistory until 1980s 37

1.4.3 Experimental Attempts before 2000s 39

1.4.4 Recent Measurements 42

1.5 Aim of Present Work 48

2 Experimental Setup **51**

2.1 BL01 NewSUBARU 51
2.1.1 NewSUBARU Synchrotron Radiation Facility 51
2.1.2 BL01 53
2.1.3 Beam Conditions 56
2.2 MAIKo Active Target 57
2.2.1 Overview 57
2.2.2 Detector Structure and Readout 59
2.2.3 Operating Condition 65
2.3 Data Acquisition 69
2.3.1 Overview 69
2.3.2 Trigger 70

3 Data Analysis **71**
3.1 Overview 71
3.2 Analysis of Beam Particles 72
3.2.1 Timing Structure and Energy Spectra 72
3.2.2 Response Functions 74
3.2.3 Template Fitting 77
3.2.4 Uncertainties 82
3.2.5 Energy Profile Estimation 85
3.3 Analysis of Decay Particles 87
3.3.1 Preprocessing and Tracking Analysis 87
3.3.2 Selection Analysis 105
3.3.3 Efficiency Estimation 107
3.4 Cross Sections 113
3.4.1 Overview 113
3.4.2 Differential Cross Section 113
3.4.3 Total Cross Section 114

4 Results & Discussions **117**

4.1 Differential Cross Section 117
4.2 Total Cross sections 120
4.3 Comparison with the Previous Studies 122

5 Summary **123**

Acknowledgement **125**

Bibliography **127**

A Derivation of Low-Energy Photoabsorption Cross Sections **155**

B Data Tables of Cross Sections **159**

List of Figures

1.1 Photon energy dependence of $\sigma_{\rm tot}/A$ 4
1.2 Total photoabsorption cross section of ^{197}Au 7
1.3 Energy integrated cross sections of the GDR 8
1.4 Resonance energy of the GDR 9
1.5 Known levels of ^{4}He 14
1.6 Nucleon-Nucleon (NN) potential 16
1.7 Mass fraction distribution of elements in supernovae 25
1.8 Reaction flow-path in the ν-process of the light elements 26
1.9 Abundance of ^{7}Li and ^{9}Be in stars 27
1.10 Primordial abundance of light elements predicted by the standard BBN . 29
1.11 Constraints on the non-standard BBN model 30
1.12 Theoretical (γ, n) and (γ, p) cross sections by Horiuchi *et al.* 34
1.13 Experimental (γ, n) and (γ, p) cross sections by Calarco *et al.* 40
1.14 Experimental (γ, n) and (γ, p) cross sections by Shima *et al.* 44
1.15 Experimental (γ, n) cross sections by Nilsson *et al.* 45
1.16 Experimental photoabsorption cross sections by Nakayama *et al.* 47
1.17 Experimental (γ, p) cross sections by Raut *et al.* 48
1.18 Experimental (γ, n) cross sections by Tornow *et al.* 49

2.1 NewSUBARU synchrotron radiation facility 52
2.2 BL01 beam line 54
2.3 Laser Compton scattering (LCS) 54

2.4 MAIKo active target 58
2.5 Circuit diagram of the MAIKo active target. 61
2.6 Gas electron multiplier (GEM) 63
2.7 Micro pixel chamber (μ-PIC) 63
2.8 Block diagram of the data processing in the Iwaki board 64
2.9 Gas handling system 66
2.10 Ranges of the decay particles 68

3.1 Timing structures of the beam 73
3.2 Beam energy spectra 75
3.3 One-photon response function 78
3.4 Beam flux estimation 81
3.5 Beam energy spectrum 86
3.6 $^{4}\mathrm{He}(\gamma, n)^{3}\mathrm{He}$ event 89
3.7 $^{4}\mathrm{He}(\gamma, p)^{3}\mathrm{H}$ event 90
3.8 $^{12}\mathrm{C}(\gamma, n)^{11}\mathrm{C}$ event 91
3.9 $^{12}\mathrm{C}(\gamma, n)^{11}\mathrm{B}$ event 92
3.10 Compton scattering event 93
3.11 Instrumental noise event 94
3.12 External event 95
3.13 Data reduction 97
3.14 Tracking procedures 99
3.15 Position dependence of time over threshold (TOT) 101
3.16 Time over threshold (TOT) 103
3.17 ΔE estimation 104
3.18 Selection analysis for the $^{4}\mathrm{He}(\gamma, n)^{3}\mathrm{He}$ events 108
3.19 Selection analysis for the $^{4}\mathrm{He}(\gamma, p)^{3}\mathrm{H}$ events 109
3.20 Pseudo $^{4}\mathrm{He}(\gamma, n)^{3}\mathrm{He}$ event generated with the simulation 111
3.21 Pseudo $^{4}\mathrm{He}(\gamma, p)^{3}\mathrm{H}$ event generated with the simulation 112

4.1 θ dependence of ^{4}He$(\gamma, n)^3$He cross sections 118
4.2 ϕ dependence of ^{4}He$(\gamma, n)^3$He cross sections 118
4.3 θ dependence of ^{4}He$(\gamma, p)^3$H cross sections 119
4.4 ϕ dependence of ^{4}He$(\gamma, p)^3$H cross sections 119
4.5 Experimental total cross sections 121

List of Tables

2.1 Specifications of the storage ring in NewSUBARU 52

2.2 Beam energy conditions 57

2.3 Specifications of the FE2009bal ASIC 64

2.4 Target thickness 69

3.1 Systematic uncertainties on the total beam flux 84

4.1 Experimental total cross sections 120

B.1 θ dependence of ϕ-averaged differential cross sections $\left\langle \frac{d\sigma_\theta}{d\Omega} \right\rangle$ (Eq. 4.1) of the ^{4}He$(\gamma, n)^3$He reaction at $\langle E_\gamma \rangle = 22.5$ MeV. 159

B.2 θ dependence of ϕ-averaged differential cross sections $\left\langle \frac{d\sigma_\theta}{d\Omega} \right\rangle$ (Eq. 4.1) of the ^{4}He$(\gamma, n)^3$He reaction at $\langle E_\gamma \rangle = 23.5$ MeV. 160

B.3 θ dependence of ϕ-averaged differential cross sections $\left\langle \frac{d\sigma_\theta}{d\Omega} \right\rangle$ (Eq. 4.1) of the ^{4}He$(\gamma, n)^3$He reaction at $\langle E_\gamma \rangle = 24.5$ MeV. 160

B.4 θ dependence of ϕ-averaged differential cross sections $\left\langle \frac{d\sigma_\theta}{d\Omega} \right\rangle$ (Eq. 4.1) of the ^{4}He$(\gamma, n)^3$He reaction at $\langle E_\gamma \rangle = 26.5$ MeV. 160

B.5 θ dependence of ϕ-averaged differential cross sections $\left\langle \frac{d\sigma_\theta}{d\Omega} \right\rangle$ (Eq. 4.1) of the ^{4}He$(\gamma, n)^3$He reaction at $\langle E_\gamma \rangle = 27.5$ MeV. 161

B.6 θ dependence of ϕ-averaged differential cross sections $\left\langle \frac{d\sigma_\theta}{d\Omega} \right\rangle$ (Eq. 4.1) of the ^{4}He$(\gamma, n)^3$He reaction at $\langle E_\gamma \rangle = 29.4$ MeV. 161

B.7 ϕ dependence of θ-averaged differential cross sections $\left\langle \frac{d\sigma_\phi}{d\Omega} \right\rangle$ (Eq. 4.2) of the ^{4}He$(\gamma, n)^3$He reaction at $\langle E_\gamma \rangle = 22.5$ MeV. 161

B.8 ϕ dependence of θ-averaged differential cross sections $\left\langle \frac{d\sigma_\phi}{d\Omega} \right\rangle$ (Eq. 4.2) of the ^{4}He$(\gamma, n)^3$He reaction at $\langle E_\gamma \rangle = 23.5$ MeV. 162

B.9 ϕ dependence of θ-averaged differential cross sections $\left\langle \frac{d\sigma_\phi}{d\Omega} \right\rangle$ (Eq. 4.2) of the ^{4}He$(\gamma, n)^3$He reaction at $\langle E_\gamma \rangle = 24.5$ MeV. 162

B.10 ϕ dependence of θ-averaged differential cross sections $\left\langle \frac{d\sigma_\phi}{d\Omega} \right\rangle$ (Eq. 4.2) of the ^{4}He$(\gamma, n)^3$He reaction at $\langle E_\gamma \rangle = 26.5$ MeV. 163

B.11 ϕ dependence of θ-averaged differential cross sections $\left\langle \frac{d\sigma_\phi}{d\Omega} \right\rangle$ (Eq. 4.2) of the ^{4}He$(\gamma, n)^3$He reaction at $\langle E_\gamma \rangle = 27.5$ MeV. 163

B.12 ϕ dependence of θ-averaged differential cross sections $\left\langle \frac{d\sigma_\phi}{d\Omega} \right\rangle$ (Eq. 4.2) of the ^{4}He$(\gamma, n)^3$He reaction at $\langle E_\gamma \rangle = 29.4$ MeV. 164

B.13 θ dependence of ϕ-averaged differential cross sections $\left\langle \frac{d\sigma_\theta}{d\Omega} \right\rangle$ (Eq. 4.1) of the ^{4}He$(\gamma, p)^3$H reaction at $\langle E_\gamma \rangle = 22.5$ MeV. 164

B.14 θ dependence of ϕ-averaged differential cross sections $\left\langle \frac{d\sigma_\theta}{d\Omega} \right\rangle$ (Eq. 4.1) of the ^{4}He$(\gamma, p)^3$H reaction at $\langle E_\gamma \rangle = 23.3$ MeV. 164

B.15 θ dependence of ϕ-averaged differential cross sections $\left\langle \frac{d\sigma_\theta}{d\Omega} \right\rangle$ (Eq. 4.1) of the ^{4}He$(\gamma, p)^3$H reaction at $\langle E_\gamma \rangle = 24.3$ MeV. 165

B.16 θ dependence of ϕ-averaged differential cross sections $\left\langle \frac{d\sigma_\theta}{d\Omega} \right\rangle$ (Eq. 4.1) of the ^{4}He$(\gamma, p)^3$H reaction at $\langle E_\gamma \rangle = 25.7$ MeV. 165

B.17 θ dependence of ϕ-averaged differential cross sections $\left\langle \frac{d\sigma_\theta}{d\Omega} \right\rangle$ (Eq. 4.1) of the ^{4}He$(\gamma, p)^3$H reaction at $\langle E_\gamma \rangle = 26.5$ MeV. 165

B.18 θ dependence of ϕ-averaged differential cross sections $\left\langle \frac{d\sigma_\theta}{d\Omega} \right\rangle$ (Eq. 4.1) of the ^{4}He$(\gamma, p)^3$H reaction at $\langle E_\gamma \rangle = 28.7$ MeV. 166

B.19 ϕ dependence of θ-averaged differential cross sections $\left\langle \frac{d\sigma_\phi}{d\Omega} \right\rangle$ (Eq. 4.2) of the ^{4}He$(\gamma, p)^3$H reaction at $\langle E_\gamma \rangle = 22.5$ MeV. 166

B.20 ϕ dependence of θ-averaged differential cross sections $\left\langle \frac{d\sigma_\phi}{d\Omega} \right\rangle$ (Eq. 4.2) of the ^{4}He$(\gamma, p)^3$H reaction at $\langle E_\gamma \rangle = 23.5$ MeV. 167

B.21 ϕ dependence of θ-averaged differential cross sections $\left\langle \frac{d\sigma_\phi}{d\Omega} \right\rangle$ (Eq. 4.2) of the ^{4}He$(\gamma, p)^3$H reaction at $\langle E_\gamma \rangle = 24.3$ MeV. 167

B.22 ϕ dependence of θ-averaged differential cross sections $\left\langle \frac{d\sigma_\phi}{d\Omega} \right\rangle$ (Eq. 4.2) of the ^{4}He$(\gamma, p)^3$H reaction at $\langle E_\gamma \rangle = 25.7$ MeV. 168

B.23 ϕ dependence of θ-averaged differential cross sections $\left\langle \frac{d\sigma_\phi}{d\Omega} \right\rangle$ (Eq. 4.2) of the ^{4}He$(\gamma, p)^3$H reaction at $\langle E_\gamma \rangle = 26.5$ MeV. 168

B.24 ϕ dependence of θ-averaged differential cross sections $\left\langle \frac{d\sigma_\phi}{d\Omega} \right\rangle$ (Eq. 4.2) of the ^{4}He$(\gamma, p)^3$H reaction at $\langle E_\gamma \rangle = 28.7$ MeV. 169

Chapter 1

Introduction

1.1 Photodisintegration and the IVGDR

1.1.1 Electromagnetic Probes for the Nuclear Physics

A photon is one of the promising probes to investigate the dynamics underlying atomic nuclei. On the contrary that low-energy dynamics of the strong interaction, which describe the interaction between hadronic probes and nuclei, is not fully understood, the electromagnetic interaction between photons and charged particles has already been settled. That allows us to regard the experimental studies by means of electromagnetic probes such as photons and electrons as a reliable basis of our understanding of the nuclear physics.

One can access various scale of nuclear structure via the electron scattering off nuclei by varying the energy of electron beams. From a naive perspective, a wave length of a virtual photon interchanged between an electron and a target object determines the length-scale involved with the scattering phenomena. Innumerable brilliant achievements have been completed with electron scattering so far. For example, an intensive study of electron elastic scattering conducted by Hofstadter *et al.* revealed the systematics of the charge-density distribution in various stable nuclei [2], and that brought him the Nobel prize in 1961. Moreover, finer structure inside nucleons was unveiled with the deep inelastic scattering on nuclei. This process was interpreted as the electron scattering off a point particle inside nucleons, and that proved the existence of the quarks [3]. In addition, electron inelastic scattering is also a powerful tool to investigate the low-lying collective excitation of nuclei such as the giant resonance. That will be discussed later in the context of the comparison with the photo-absorption reaction.

Emission and absorption of real photons by nuclei are the different key reactions to access the nuclear structure. Spectroscopic measurement of gamma-ray radiation from the nuclear transition is a typical and longstanding case of the utilization of the photo-reaction in the study of nuclear structure. By comparing the nuclear level scheme recon-

structed from the gamma-ray spectrum and theoretical predictions, one can extract the knowledge on various collective motion of nucleons such as deformation and vibration. Even today, the in-beam gamma ray spectroscopy is a one of the most reliable techniques to tackle with exotic unstable nuclei produced in radioactive isotope factories over the world [4, 5, 6]. Regarding the photoabsorption process, the response functions of various nuclei over the wide energy range of incoming photon energy were measured systematically. Those results were mainly argued in the context of the sum rule of the transition strength, and photodisintegration, which is the main topic of this thesis, is the pivotal reaction channel for this discussion.

Both electron scattering and photoabsorption are employed in the study of the nuclear response function. These two reactions are similar but not the same in some points. The difference is stem from whether photons that mediate the reactions are on their mass-shell or not. The quantity so-called virtuality Q^2 is the measure of the deviation from the mass shell. The virtuality is defined as

$$Q^2 = q^2 - \frac{\omega^2}{c^2}, \tag{1.1}$$

where $\hbar q$ and $\hbar\omega$ are the momentum and energy carried by a photon, respectively. The value of Q^2 is fixed to 0 in the case of a real photon. On the other hand, that for photons emitted in the electron scattering can take arbitrary negative values in the ultra-relativistic limit ($m_e \sim 0$).

Real-photon induced reactions are constrained by the spin selection rule and momentum scale correspond to the energy. However, those induced by virtual photons are not. This difference makes the electron inelastic scattering off the target nuclei both versatile and complicated, simultaneously. The electron inelastic scattering gives rise to the transition to final states with various isospins T and intrinsic spins. Thus, additional deliberations are required to decompose the transition strength with respect to isospin (ΔT), angular momentum (ΔL), and intrinsic spin (ΔS). On the other hand, the photoabsorption with several tens of MeV photon has a strong selectivity for the isovector dipole transition ($\Delta T = 1$, $\Delta L = 1$, and $\Delta S = 0$).

1.1.2 Energy Dependence of Photonuclear Reactions

Photoabsorption cross sections are experimentally determined from the summation of the cross sections resulting in various final states. Namely, the total photoabsorption cross section $\sigma_{\rm tot}(E)$ at the photon energy E is give as

$$\sigma_{\rm tot}(E) = \sigma(\gamma,\gamma') + \sigma(\gamma,n) + \sigma(\gamma,2n) + ... + \sigma(\gamma,p) + \sigma(\gamma,2p) + ..., \tag{1.2}$$

where the σs in the right hand side is sorted with the reaction channel: i. e. $\sigma(\gamma,n)$ means the cross sections to one-neutron final state. This summation runs over all the photonuclear reaction channels feasible under the given photon energy. When E is below the particle decay threshold of the target nuclei, only the photon-scattering cross sections

$\sigma(\gamma, \gamma')$ contribute to the photoabsorption cross sections. For E larger than the particle decay threshold, particle-decay cross sections such as $\sigma(\gamma, n)$ and $\sigma(\gamma, p)$ dominate the photoabsorption cross section. Especially in the heavy nuclei, neutron emission cross sections occupy sizable amount of the total photoabsorption cross section because the Coulomb barrier prevents charged-particle emission.

Energy dependence of photoabsorption cross sections shows the features common among all nuclei, and these features are explained from the nuclear degrees of freedom involving. Energy dependence of experimental photoabsorption cross sections are shown in Fig. 1.1. Mass-number (A) normalized cross sections for proton, Be, Pb, and Cu are shown together. The behavior of σ/A for nuclei $A > 1$ are similar, and they resemble proton cross section above the π meson production threshold (m_π). The energy dependence of the photoabsorption cross sections is associated with four mechanisms depending on the energy region.

First, the photoabsorption cross sections rise sharply from the particle decay threshold and peak around several tens MeV, then decrease. This trend is attributed to the giant resonance (GR) which is the main topic of this thesis. The giant resonance is considered as a collective motion of nucleons. More detailed explanation regarding the giant resonance will be remarked later.

Second, the energy interval between the GR and m_π is called the quasi-deuteron (QD) region. The cross sections therein are slowly decrease and its absolute value is proportional to the photodisintegration cross sections of deuterons σ_d as

$$\sigma_{\rm tot} \sim L\frac{NZ}{A}\sigma_d, \tag{1.3}$$

where L is the Levinger constant [7] which is the measure of the quasi-deuteron density in the nuclear medium. This behavior is described by a picture that incoming photon is absorbed by a deuteron-like nucleon pair stemming from the short range correlation.

Third, above the π meson production threshold, $\sigma_{\rm tot}$ is dominated by the transition between a nucleon to its excited states, namely nucleon isobars. This energy region is called the isobar region. Several peak structures seen in the proton spectrum are attributed to various N and Δ resonances [8], and the most prominent one corresponds to the $\Delta(1232)$ resonance. The moderate differences in the width and the amplitude of the spectral line shapes of proton and nuclei are ascribed to the Fermi motion and the Pauli blocking in the nuclear medium, respectively.

Forth, the high energy region above the isobar region is called the shadowing region. The features of the cross sections in this energy region are similar to those of the hadron absorption cross section such as $\sigma(\pi, p)$ except for their scale. This fact implies the transition therein is dominated by the absorption of virtual-hadron state of a photon. Because of the strong absorption of hadrons by nucleon, only nucleons on the surface of the nuclei are involved in the photoabsorption reaction. This effect is called the shadowing. The violation of the A scaling of the cross sections caused by the shadowing effect results in the reduction of nuclear cross sections compared to that of a proton.

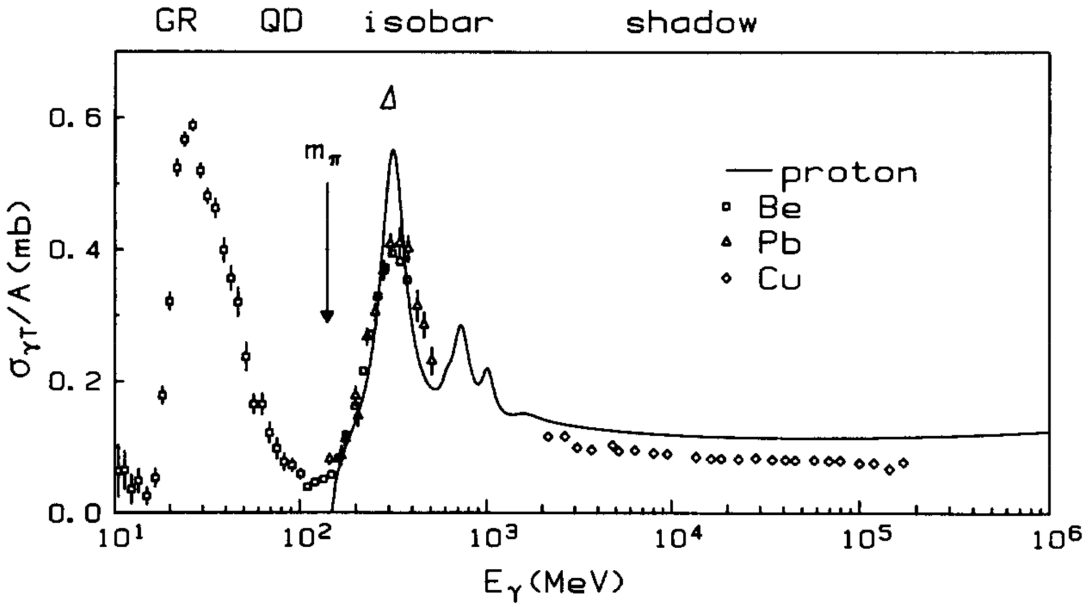

Figure 1.1: Photon energy dependence of $\sigma_{\rm tot}/A$ taken from Ref. [9]. The markers indicate the cross sections for Be, Pb, and Cu nuclei, whereas the solid line depicts the proton cross sections. The horizontal axis is segmented into four intervals depending on the feature of the phenomenon: giant resonance (GR), quasi-deuteron (QD), isobar, and shadowing (shadow). The production threshold of a π meson and a Δ baryon are also exhibited.

In terms of the (low-energy) nuclear structure study, the most important region of the photonuclear reaction is the GR region. Since the giant resonance is attributed to the collective motion of nucleons, its frequency and the width reflect the bulk properties of nuclear matter.

1.1.3 Photoabsorption in Low Energy Region

In the GR region explained in the former section, the resonance populated by photoabsorption is mostly limited to the isovector giant dipole resonance (IVGDR: $\Delta T = 1$, $\Delta L = 1$, and $\Delta S = 0$). This is due to the strong selectivity stemming from the mismatch between the photon wavelength and the nuclear radii.

Let us check the typical length scale of particles involved in a simple example. A nuclear charge radius R of nuclei of mass number A is approximated with the systematics

$$R \sim 1.2A^{\frac{1}{3}} \text{ fm} \tag{1.4}$$

as given in Ref. [10]. By substituting A with 300 as a edge case, the charge radius of a normal nucleus is at most 8 fm. On the other hand, the wavelength λ of a photon with

the energy E is given from

$$\begin{aligned} \lambda &= \frac{2\pi\hbar c}{E}, \\ &\sim \frac{1200}{E\ (\mathrm{MeV})}\ \mathrm{fm}. \end{aligned} \tag{1.5}$$

As for the typical energy region of the GR region, a nuclear radius R is less than 40 fm, which corresponds to 30 MeV. Judging from these two estimations, the wavelength of the photon is at least twice as large as the nuclear radius in the GR energy region. Therefore, the electric and the magnetic fields formed by a photon is approximately constant over the whole region of a nucleus. From a naive perspective, only protons in a nucleus are coupled with the electric field and they are altogether shook alternately synchronizing with the time dependent switching of the field. This situation is exactly the classical picture of the IVGDR.

The classical picture on the low-energy photoabsorption can be justified more rigorously at the long-wavelength limit, namely

$$qR \ll 1, \tag{1.6}$$

where q is a wave number of a photon [11, 12, 13]. This limit leads the general formula of photoabsorption cross section to the simple form, which consists only of the $E1$-transition amplitude described with the dipole-transition operator. That is the origin of the strong selectivity to the transition to the IVGDR.

At the long-wavelength limit, the cross sections of photoabsorption $\sigma_\gamma^{\mathrm{LWA}}$ induced by a photon of energy E_γ is reduced to,

$$\sigma_\gamma^{\mathrm{LWA}}(E_\gamma) \sim \frac{4\pi^2}{\hbar c} E_\gamma \left| \left\langle J_f \left| \hat{D}_z \right| J_i \right\rangle \right|^2 \delta(E_f - E_i - E_\gamma), \tag{1.7}$$

where the initial and final state of the nucleus are characterized with the energy E_i, E_f and the spin J_i, J_f [11]. In addition, $\hat{D}_z$ is the dipole transition operator. When we assume the point-like charge distribution of nucleons, the dipole operator is defined as

$$\hat{D}_z = \sum_{k=1}^{A} \chi_i e(\boldsymbol{r}_i - \boldsymbol{R})_z. \tag{1.8}$$

Here, χ_i is the effective charge of the i-th nucleons: that value is N/A for protons and Z/A for neutrons in the cerner-of-mass frame. $(\boldsymbol{r}_i - \boldsymbol{R})_z$ indicates the z-component of the displacement of the i-th nucleon with respect to the center of mass the $\boldsymbol{R}$. The derivation of Eq.(1.7) from the general formula Eq. (A.1) is shown in the Appendix A.

Comparison with Electron Scattering For comparison, the double-differential cross sections of the electron scattering off a nucleus [11] is derived as

$$\frac{d^2\sigma}{d\Omega dE} = 4\pi \frac{\sigma_{\mathrm{Mott}}}{e^2} \left[\frac{1}{2} \left\{ \frac{q^2 - \left(\frac{\omega}{c}\right)^2}{q^2} \right\}^2 F_L^2(q,\omega) + \left\{ \frac{1}{2} \frac{q^2 - \left(\frac{\omega}{c}\right)^2}{q^2} + \tan^2 \frac{\theta}{2} \right\} F_T^2(q,\omega) \right]. \tag{1.9}$$

This is the cross section of the transition with a momentum transfer $\hbar q$ and a energy transfer $\hbar\omega$. Here, F_L^2 and F_T^2 are the longitudinal (Coulomb) and the transverse form factors defined as,

$$F_L^2(q,\omega) = \frac{1}{2J_i+1}\sum_{J=0}^{\infty}\left|\left\langle J_f \left|\left|\hat{T}_J^C(q)\right|\right| J_i\right\rangle\right|^2 \delta(\hbar\omega+\epsilon_i-\epsilon_f), \tag{1.10}$$

$$F_T^2(q,\omega) = \frac{1}{2J_i+1}\sum_{J=1}^{\infty}\left\{\left|\left\langle J_f \left|\left|\hat{T}_J^E(q)\right|\right| J_i\right\rangle\right|^2 + \left|\left\langle J_f \left|\left|\hat{T}_J^M(q)\right|\right| J_i\right\rangle\right|^2\right\}\delta(\hbar\omega+\epsilon_i-\epsilon_f). \tag{1.11}$$

Here, $\hat{T}_J^C(q)$, $\hat{T}_J^E(q)$, and $\hat{T}_J^M(q)$ are Coulomb, electric, and magnetic multipole transition operators defined in Eqs. (A.5,A.3,A.4). In addition, the Mott cross section $\sigma_{\rm Mott}$ is the electron-scattering cross section off the point charge given as

$$\sigma_{\rm Mott} = \frac{e^4\cos^2\frac{\theta}{2}}{4E_e^2\sin^4\frac{\theta}{2}}. \tag{1.12}$$

It should be noted that the long-wavelength limit is not always valid for the electron scattering even for the transition to low-energy excited states. That is because of the arbitrariness of the relation between momentum transfer $\hbar q$ and the energy transfer $\hbar\omega$. This is the origin of the complexity of the electron scattering mentioned earlier.

1.1.4 Isovector Giant Dipole Resonance (IVGDR)

The giant resonances are the common excitation mode observed among various nuclei [14]. They are associated with the collective vibration of nucleons and categorized with their intrinsic spin and isospin characters. Giant resonances appear as larger and wider bump structures compared with the low-lying excited states in the nuclear excitation function. It was the first case of the discovery of the giant resonance that enormous ^{63}Cu(γ,n) cross section was observed in 1937 [15]: this resonance is later associated with the isovector giant resonance.

The isovector giant dipole resonance (IVGDR or GDR) is the best known giant resonance. The name of the resonance follows the nomenclature of the giant resonances and indicates their isospin (ΔT), orbital angular momentum (ΔL), and spin (ΔS) as 1, 1, and 0, respectively. These features are exactly the same to those of $E1$ transition. As one can understand by recalling the fact that the low-energy photoabsorption reaction is approximated as the $E1$ transition, this resonance is commonly observed by means of the photonuclear reactions. The total photoabsorption cross sections for ^{197}Au are shown in Fig. 1.2. The data shows a typical appearance of the GDR in heavy nuclei such that $A > 50$. In the photoexcitation function for the heavy nuclei, a remarkable peak structure that fit the Lorenzian resonance distribution

$$\sigma(E_\gamma) = \frac{\sigma_m\Gamma_m^2E_\gamma^2}{(E_\gamma^2-E_m^2)^2+\Gamma_m^2E_\gamma^2}, \tag{1.13}$$

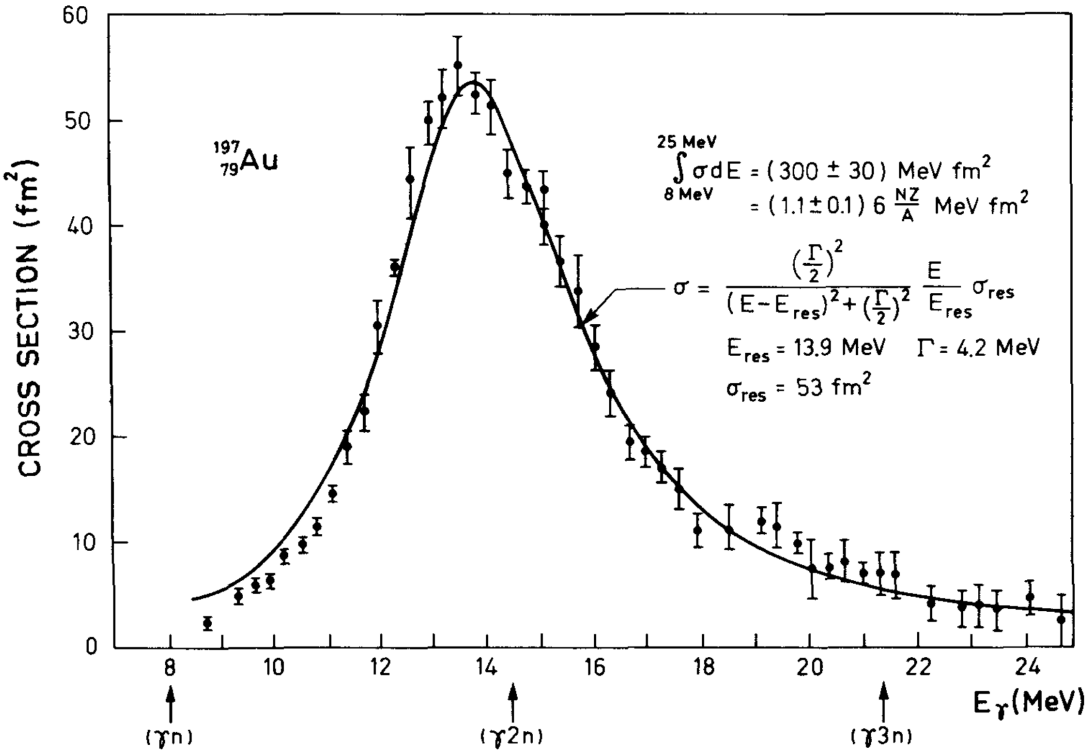

Figure 1.2: Total photoabsorption cross section of ^{197}Au taken from Ref. [16]. The experimental data are from Ref. [17]. The Breit-Wigner function that fits the data are shown by the solid curve.

can be seen above the (γ, n)-reaction threshold energy. Here, Γ_m, E_m, and σ_m are the parameters for a nuclear resonance indicating its width, resonance energy, and height. Among various nuclei, E_m is around 15 MeV, whereas Γ_m is the order of 2.5–5 MeV. Assuming the resonance as a harmonic oscillation, the typical E_m corresponds to a frequency of $\sim 3.5\times10^{21}$ Hz. Moreover, the lifetime of the resonance estimated from the representative Γ_m value is approximately the order of 10^{-22} s. This ratio implies that the resonance damps completely due to energy dissipation earlier than a few vibration [14].

The most outstanding character of the giant resonances is its collectivity deduced from the sum rules. As for the GDR, the Thomas-Reiche-Kuhn (TRK) sum rule [18, 19, 20] is the proverbial example. The TRK sum rule gives the upper limit of the energy integral of $E1$ cross sections as

$$\int_0^\infty \sigma_{E1}(E)dE \sim \frac{60NZ}{A} \text{ (MeV mb)}. \tag{1.14}$$

The sum-rule value on the right hand side is derived from the sum of the dipole excitation cross sections [Eq. (1.7)] of single-particle excitations for each individual particle based on the assumption that the long-wavelength approximation, or the Siegert's theorem Eq. (A.12), is valid over all energy region [13]. Even though this premise is not necessarily

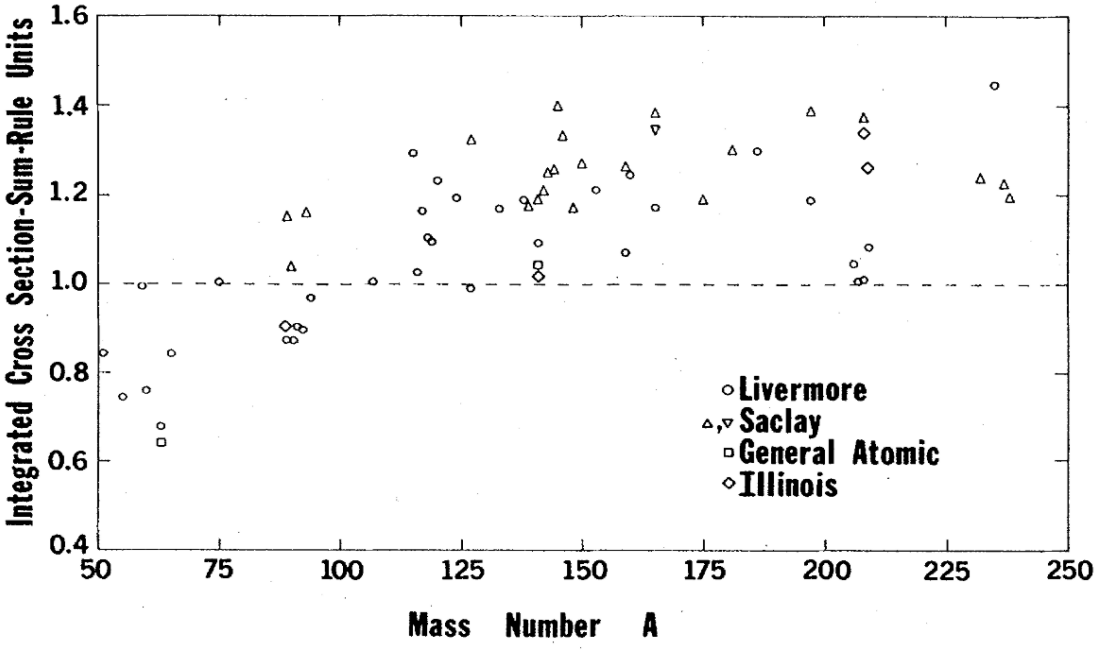

Figure 1.3: Energy integrated cross sections of the GDR measured by a unit of the TRK sum rule value [Eq. (1.14)] taken from Ref. [21]. The energy integrals derived from the Lorenzian [Eq. (1.13)]functions that fit the experimental data are shown by markers. The shapes of the markers correspond to the laboratories where the data were taken, and the sources of all the data are sorted in the references in Ref. [21]. The horizontal dashed line indicates the TRK sum-rule value.

valid in high-energy region, the value constrains the low-energy integral of the cross section as an upper limit. The GDR exhausts considerable part of this sum-rule value, and that occupation ratio reaches almost 100% especially in heavy nuclei. The energy integral values of the GDR cross sections are shown in Fig. 1.3. One can see the integrated GDR cross sections in the most of heavy nuclei have almost identical magnitude to the TRK sum rule value. Moreover, the integration exceeds the sum-rule value in some nuclei, which is considered to be due to the non-locality of the nucleon Hamiltonian ignored in the derivation of Eq. (1.14). In any case, the significant amplitude of the GDR cross section implies that numerous nucleons are coherently involved in the GDR. In other words, this resonance has collective character. That is contrasting against the low-lying excited states that exhaust at most a few % of the sum-rule value.

Based on the collectivity inferred from the TRK sum rule, the GDR is qualitatively interpreted as a collective motion of nucleons from a macroscopic perspective. One of the most famous pictures was proposed by Goldhaber and Teller [22]. In their model, the GDR is attributed to the linear oscillation of the rigid spheres composed of protons and neutrons. The proton sphere and the neutrons sphere move alternatively around the center of mass in opposite phase. This oscillation is driven by the resilience force

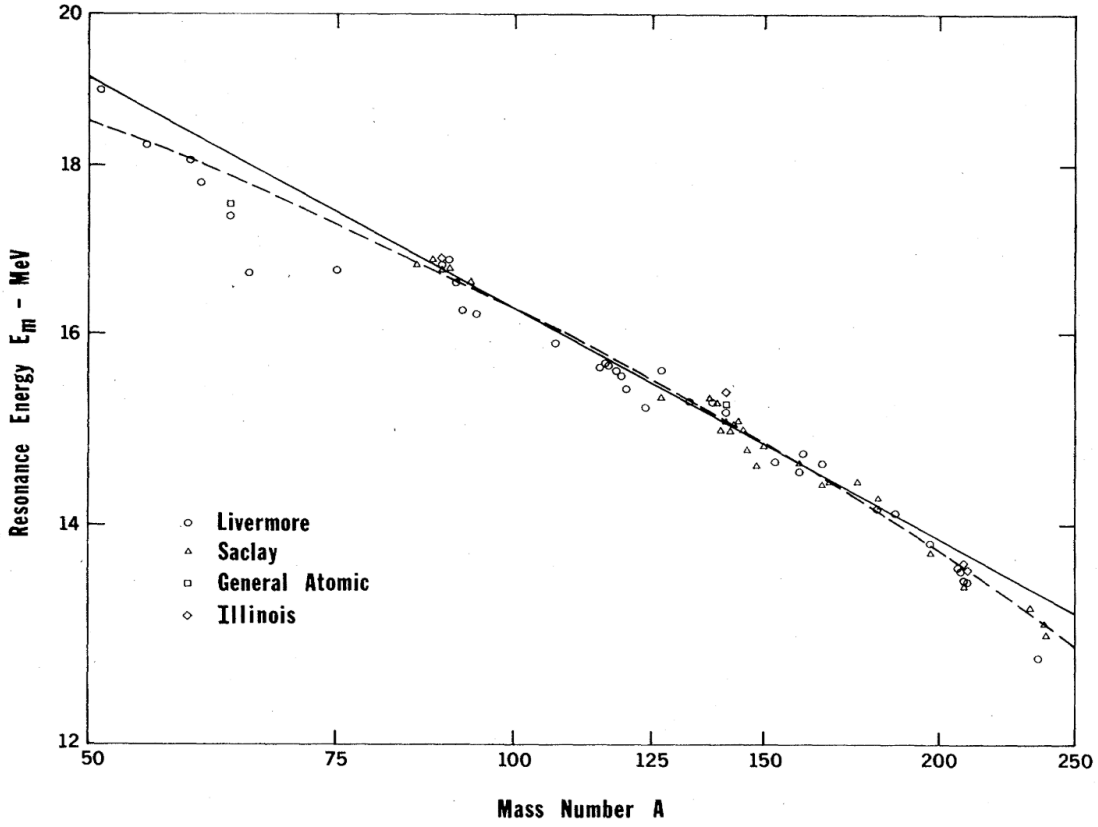

Figure 1.4: Resonance energy of the GDR taken from Ref. [21]. The sources of experimental data are indicated with the shape of markers. The solid line shows the trend described by Eq. (1.15), whereas the dashed line depict another trend formula proposed in Ref. [21].

stemming from the symmetry energy at the marginal region where only either protons or neutrons exist. This condition results in the hypothesis that the resonance energy of the GDR is proportional to $A^{-1/6}$. Another well known point of view regarding the GDR was the one described by Steinwedel and Jensen [23]. They portrayed the GDR as the convection of the proton and neutron fluids. These fluids were treated as hydrodynamic irrotational flows, and their densities varied while keeping their total density. From this consideration, the resonance-energy trend which obeys $A^{-1/3}$ is derived. In fact, the GDR in heavy nuclei is thought to be in the intermediate case of these two pictures. The resonance energy E_m for various nuclei are shown in Fig. 1.4. The trend of the E_m value is well approximated [21] by using the mass number A as

$$E_m \sim 3.12A^{-\frac{1}{3}} + 20.6A^{-\frac{1}{6}} \text{ (MeV)}, \tag{1.15}$$

which is shown with the solid line in Fig. 1.4. One can see the good agreement with the data and this formula in heavy nuclei.

The origin of the high collectivity of the GDR is explained from a microscopic point

of view. The schematic model [24] is quite simple but instructive one. The explanation below mainly owes to the descriptions in Refs. [12, 13, 14]. Therein, one-particle-one-hole (1p1h) excitation from a ground state of closed-shell nuclei is considered. The wave function of a 1p-1h state with a hole in a single-particle state m and a particle in a single-particle state i is written as,

$$\left|mi^{-1}\right\rangle = \hat{a}_m^\dagger \hat{a}_i \left|0\right\rangle, \tag{1.16}$$

where $|0\rangle$ is the ground-state wave function. $\hat{a}_i^\dagger$ and $\hat{a}_i$ are the creation and annihilation operators of a single particle state i. Such states are not eigenstates of the general two-body Hamiltonian

$$\hat{H} = \sum_{k_1,k_2} t_{k_1k_2} \hat{a}_{k_1}^\dagger \hat{a}_{k_2} + \frac{1}{2} \sum_{k_1k_2k_3k_4} v_{k_1k_2k_3k_4} \hat{a}_{k_1}^\dagger \hat{a}_{k_2}^\dagger \hat{a}_{k_3} \hat{a}_{k_4}. \tag{1.17}$$

By solving the variation problem

$$\delta \Big(\langle \Psi | \hat{H} | \Psi \rangle - E \langle \Psi | \Psi \rangle \Big) = 0 \tag{1.18}$$

for the 1p-1h excited states $|\Psi\rangle$ such that

$$|\Psi\rangle = \sum_{m,i} c_{mi} \left|mi^{-1}\right\rangle, \tag{1.19}$$

the Tamm-Dancoff equations

$$\sum_{jn} \left[(\varepsilon_m - \varepsilon_i)\delta_{mn}\delta_{ij} + \left\langle mi^{-1}\middle|\bar{v}\middle|nj^{-1}\right\rangle \right] c_{nj} = E c_{mi}, \tag{1.20}$$

is derived. Here, ε_i is a single particle energy of the state referred by i, and $\bar{v}$ symbolizes the antisymmetrized matrix element of the two-body residual interaction term v in Eq. (1.17). In the trial wave function Eq. (1.19), only the single-particle level above (below) the Fermi level is assigned to the particle state m (the hole state i). The Tamm-Dancoff equation Eq. (1.20) represents the net single-particle energy of the 1p-1h state ($|mi^{-1}\rangle$), namely $\varepsilon_m - \varepsilon_i$, is modified by couplings to the other 1p-1h configurations due to the residual interaction. Following the assumption in Ref. [24], the antisymmetrized matrix element is separated as

$$\left\langle mi^{-1}\middle|\bar{v}\middle|nj^{-1}\right\rangle \sim \lambda D_{mi}^* D_{nj}. \tag{1.21}$$

This approximation is equivalent to replacing the switching of the particle-hole pairs with sequential pair annihilation (D_{nj}) and pair creation (D_{mi}^*). The sign of the coefficient λ depends on the nature of the residual interaction: it is negative for attractive channels and positive for repulsive channels. Inserting Eq. (1.21) into the Tamm-Dancoff equation Eq. (1.20) an eigenvalue equation

$$\frac{1}{\lambda} = \sum_{mi} \frac{|D_{mi}|^2}{E - \varepsilon_m + \varepsilon_i}, \tag{1.22}$$

is finally obtained. Letting the number of possible combinations of the particle-hole levels be N, this equation has N eigenenergy solutions except for the case $\lambda = \pm\infty$. These solutions are grouped into the two categories. $N-1$ of them are trapped between the single-particle energy $\tilde{\varepsilon}_{i'}$ and $\tilde{\varepsilon}_{i'}+1$. Here, $\tilde{\varepsilon}_{i'}$ is defined as the particle-hole energy $\varepsilon_m - \varepsilon_i$ which is the i'-th smallest among the all possible combination of m and i. On the other hand, the other solution takes a value between $\tilde{\varepsilon}_N$ and $+\infty$ ($-\infty$ and $\tilde{\varepsilon}_1$) when the parameter λ is a positive (negative) value. This solution is attributed to the collective excited state. Especially in the case that all the particle-hole states ($|mi^{-1}\rangle$) degenerate, the eigenenergy of the collective state is

$$E = \varepsilon + \lambda \sum_{mi} |D_{mi}|^2 , \tag{1.23}$$

whereas those for the other $N-1$ states are ε. Here, ε is the particle-hole energy: $\tilde{\varepsilon}_{i'} = \varepsilon$ for every i'. As for the GDR, λ is positive because of the isospin $T = 1$, and energy of the collective state is larger than the particle-hole energy ε. That is consistent with the fact that the energy of the GDR is larger than the shell-gap energy. In addition, the collective state is written as

$$|\Psi^c\rangle = \sum_{mi} \frac{D_{mi}}{\sqrt{\sum_{nj} |D_{nj}|^2}} \left|mi^{-1}\right\rangle . \tag{1.24}$$

This equation manifests that the collective state Ψ^c is the coherent superposition of all the possible 1p-1h states. In fact, the transition probability from the ground state to the collective state is given as

$$\left| \langle \Psi^c | \hat{D} | 0 \rangle \right|^2 = \sum_{mi} |D_{mi}|^2, \tag{1.25}$$

where the transition operator $\hat{D}$ is defined as

$$\hat{D} \coloneqq \sum_{kk'} D_{kk'} \hat{a}^\dagger_k \hat{a}_{k'}. \tag{1.26}$$

This transition probability completely exhausts the sum of transition probabilities from the ground state to all the possible states This conclusion dovetails with the fact that the GDR uses up the TRK sum-rule value.

The discussions above are well applicable to the GDR in heavy nuclei. In contrast, the situation in lighter nuclei, say $A < 40$, is complicated a little [14, 25]. The resonance energy neither obeys the known trend Eq. (1.15), nor its line shape seems to be a single pronounced peak anymore. In light nuclei, the $E1$ transition-strength function splits into fine peak structures distributing over wider energy range, and thus the total photoabsorption cross section integrated up to 30 MeV no longer exhausts the TRK sum-rule value. These tendencies can be understood as rather the behavior of individual nucleons than the nuclear bulk property is relatively more important in light nuclei. As a matter of fact, the photoabsorption cross section drastically varies by adding a few nucleons to the system such as C and O isotopes [26]. The fragmentation of the excitation

strength function was quantitatively sketched by the configuration splitting scheme [25]. Therein, the origin of the fragmentation is explained from the single-particle-excitation-energy difference among the different configurations, such as $1p \rightarrow (sd)$ and $(sd) \rightarrow (fp)$. As a consequence, the complete degeneracy assumed in the schematic model is not achieved, and the strength stemming from the different configurations remains apart.

1.2 ^{4}He Photodisintegration

1.2.1 Profile of ^{4}He Nuclei

Atomic nuclei are the quantum many-body system existing isolated from the exterior, and its low-energy dynamics are mainly explained from their components, namely protons and neutrons. The nuclear force that acts among nucleons binds protons and neutrons together to form a nucleus. This self-binding nature is one of the distinguishable feature of nuclear system, which is different from the case of atomic system where electrons are trapped by a electric field of a nucleus. Similarly to atomic system, nuclear system also has a property that it is stabilized at the specific nucleon numbers, namely 2, 8, 20, 28, 50, 82, 126, and so on. They are called the nuclear magic number.

General features of the nuclear system, such as the magic numbers, are well explained by the jj-coupling shell model [27, 28, 29, 30]. Therein, nucleons are regarded as nearly free particles trapped in an effective mean-field potential. Mutually energetically apart quantum orbits of nucleons (shell) are defined in the potential, and they are categorized with their total spin j, orbital angular momentum l, and principal quantum number n. The energy gap between different shells are considered to provoke the stability at the magic number. That is to say the nuclear system is stabilized when the vacant energetically lowermost orbital get to be fully occupied. The strong spin-orbit force term in the mean field is essential to reproduce the nuclear magic numbers. The shell model would also be a good starting point to explain various features of nuclei other than the magic number.

^{4}He nucleus is the lightest nucleus of doubly-closed shell ($Z = N = 2$) in the context of the shell-model picture. The dominant nucleon configuration of ^{4}He is $(\pi 0s_{1/2})^2(\nu 0s_{1/2})^2$, or two protons and two neutrons fully occupy the lowest s-orbit ($l = 0$) with a principal quantum number $n = 0$ and a total spin $j = 1/2$. Nucleons in ^{4}He are bound by a binding energy of 28.30 MeV. The binding energy per nucleon of ^{4}He is by far the largest value among those of neighboring nuclei. According to the *ab-initio* calculations [31, 32], the tensor force caused by the one-pion exchange is a key ingredient of this tight binding. Therein, the binding energy of the ^{4}He was reproduced from the sum of the kinetic ($\sim +102$MeV) and potential (~ -128 MeV) energies, and the contribution of the tensor force to the potential energy was estimated to be approximately 68 MeV, which was more than a half of the expectation value of total potential energy. Taking into account a configuration mixing due to the tensor force [33], the ground state of ^{4}He

contains several % contributions from the 2p-2h configurations $[(0s_{1/2})^2_{10}(0p_{1/2})^2_{10}]_{00}$ that contain a *pn* pair occupying high energy orbits. Here, two subscripts of orbitals indicate spins and isospins, respectively. This situation is similar to the fact that the ^{2}H ground state are composed of both large amount of the S-wave component and a fraction of the D-wave component.

The excitation level of ^{4}He known so far is summarized in Fig. 1.5 [34]. Due to the tight binding between nucleons, the particle decay threshold energy is larger compared with that of the nuclei nearby in the nuclear chart. The excitation energies to the first excited state of closed-shell nuclei tend to increase because intra-shell transitions are forbidden by the Pauli blocking. As for ^{4}He, there are no low-lying excitation level observed below the decay threshold.

The GDR of ^{4}He is considered to exist in the excitation-energy region around several tens MeV. As seen in Fig. 1.5, the energy of the GDR is larger than the Q values of the particle decay reaction, which are $Q_n = 20.578$ MeV and $Q_p = 19.815$ MeV for (γ, n) and (γ, p) reactions, respectively. Thus, the photoabsorption cross sections in the energy region around the GDR is well approximated with

$$\sigma_{\rm tot}(E) \sim \sigma(\gamma, n) + \sigma(\gamma, p). \tag{1.27}$$

That is because the reaction channels competing with (γ, n) and (γ, p) channels, such as (γ, d) and more than three body channel, are hindered due to the isospin selection rule and the decay-phase space.

1.2.2 Topics Regarding Nucleon Few-Body Calculations

Precise theoretical calculations based on realistic nuclear interactions have recently been conducted in the light nuclear systems. Such computational techniques are referred to as *ab initio* methods. Low-energy photodisintegration reaction of light nuclei is a good research subject of the *ab initio* calculations. That is because the simplicity of the photoabsorption cross sections [Eq. (1.7)] in the long-wavelength approximation. Actually, theoretical photoabsorption and photodisintegration cross sections of ^{4}He obtained with the *ab initio* methods have been reported by many researchers. These results will be reviewed in Chap. 1.3. In the circumstances, reliable experimental cross sections play important roles to benchmark the computational methods and, moreover, the nuclear interaction adopted. Here, common knowledge on nuclear interactions and some computational methods applied in *ab initio* calculations will be introduced.

Nuclear 2-Body and 3-Body Interactions The Nucleon-Nucleon (NN) interaction, that binds nucleons together overcoming the Coulomb repulsive force, has been one of the long-standing research subjects in the field of nuclear physics. Yukawa presented the oldest theory of nuclear force in which a particle of a mass 2×10^2 times as large as the electron mass exchanged between nucleons was assumed [35]. Later, the particle

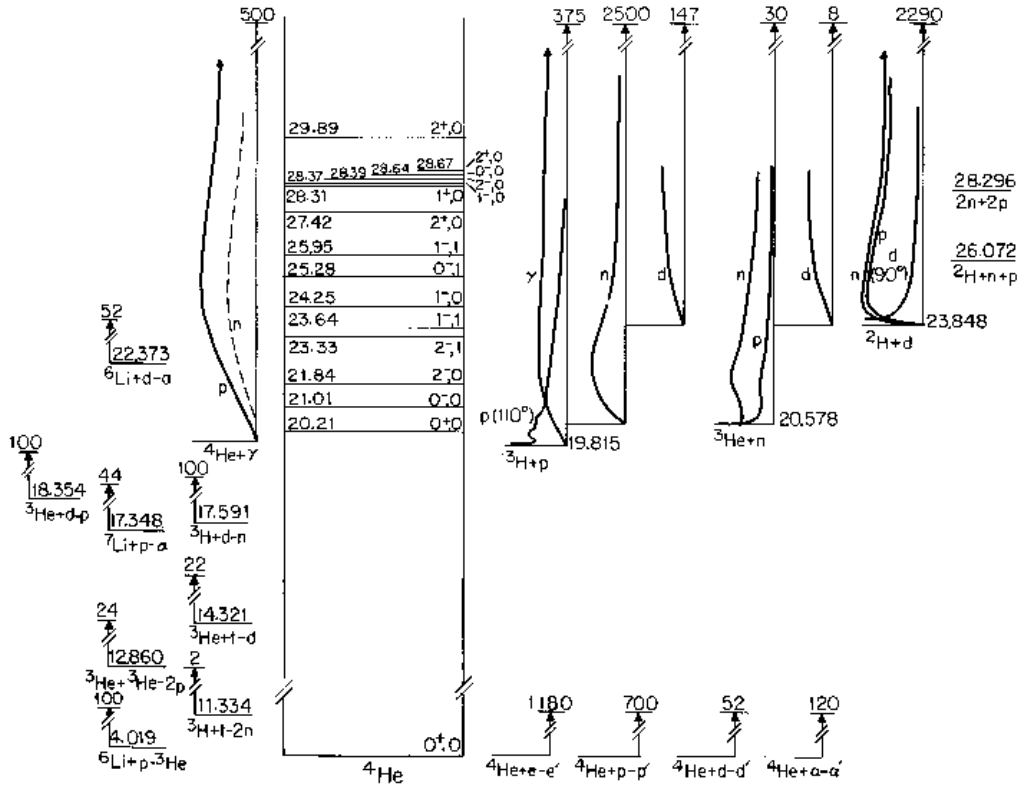

Figure 1.5: Known levels of ^{4}He compiled by the Nuclear Data Group at Triangle University Nuclear Laboratory (TUNL) [34]. The energy levels are plotted in a vertical scale giving the center of mass energy in MeV relative to the ^{4}He ground state. Each excitation level is labeled by its excitation energy, spin, parity (J^π), and isospin (T). Other horizontal lines mark the threshold energies of the ^{4}He formation reactions (left) and the decay to multi-particle sub-systems (right). Typical excitation function of some reactions are also depicted with the curves above the threshold-energy lines. Numbers at the tops of the vertical arrows indicate the highest energies in the laboratory system reached by experimental studies regarding the corresponding reaction performed before the publication of Ref. [34], or 1992. Note that the excitation function of the (γ, p) reaction (the solid curve over the ^{4}He+γ line) is about twice as large as that of the (γ, n) reaction (the dashed curve over the ^{4}He+γ line), which reflects the experimental status in 1980s. The situation will be explained later (see Fig. 1.13).

was attributed to the π-meson. This One-Pion-Exchange-Potential (OPEP) is commonly accepted picture of the long range behavior of the NN interaction, even today.

The NN interaction shows various aspects depending on the distance between two nucleons r. That is usually divided into three parts [37] as shown in Fig. 1.6.

(a) The long-range (LR) part: the attractive force in the region $r \geq 2$ fm is described by the OPEP. That leads the potential [36]

$$V_{\mathrm{OPEP}}^{(1)}(\boldsymbol{r}) = \frac{g_\pi^2}{3}(\boldsymbol{\tau}_1 \cdot \boldsymbol{\tau}_2)\left[\frac{e^{-\mu r}}{r}(\boldsymbol{\sigma}_1 \cdot \boldsymbol{\sigma}_2) + \left(1 + \frac{3}{\mu r} + \frac{3}{(\mu r)^2}\right)\frac{e^{-\mu r}}{r} S_{12}\right], \tag{1.28}$$

where the range parameter μ is relevant to the mass of π-meson as $\mu = m_\pi c/\hbar$. The tensor operator S_{12} is defined as

$$S_{12} = \frac{3\,(\boldsymbol{\sigma}_1 \cdot \boldsymbol{r})\,(\boldsymbol{\sigma}_2 \cdot \boldsymbol{r})}{r^2} - (\boldsymbol{\sigma}_1 \cdot \boldsymbol{\sigma}_2)\,. \tag{1.29}$$

Here, the spin and isospin of each nucleon are written with $\boldsymbol{\sigma}$ and $\boldsymbol{\tau}$, respectively, and the subscripts (1 or 2) indicate the particle indexes. In addition, $\boldsymbol{r}$ is the relative positions of nucleons, and g_π is the coupling constant obtained from meson-nucleon scattering experiments. As seen in Eq. (1.28), the typical interaction range of meson exchange is approximately given by $1/\mu = \hbar/\,(m_\pi c)$. Thus, the long-range part can be reasonably approximated by the OPEP originated from the lightest meson, or π meson, exchange.

(b) The medium range (MR) part: the attractive potential within the distance range of 1 fm $\leq r \leq$ 2 fm is ascribed to exchange of heavier mesons. The intermediate-range behavior is mainly attributed to scalar meson exchanges. The exchanged scalar meson with a mass of 500 MeV is attributed to so-called σ meson, or $f_0(500)$. The $f_0(500)$ is observed as a $\pi\pi$ S wave resonance with a very broad width ($\Gamma \sim 250$ MeV) [8], and the scalar meson exchange is occasionally interpreted as a two-pion exchange.

(c) The short range (SR) part: the vector boson exchange results in the short range repulsion in $r \leq 1$ fm. This process can also be attributed to a multi-pion exchange. The hard-core potential at the inner most region is considered to stem from the repulsion between quarks in nucleons.

Thanks to the high-precision experimental NN scattering data, the NN interaction below $T_{\mathrm{lab}} = 500$ MeV is well known both qualitatively and quantitatively. The NN interaction is expressed in formulations based on different standing-points. These formulation styles are classified with three categories.

(i) Phenomenological Model: the NN potential is represented by the sum of potentials allowed by the symmetry requirement, such as rotation, translation, and isospin. The potentials included in this summation are products of the r-dependent potential part and the rest parts, such as the central (I), spin-spin ($\boldsymbol{\sigma}_1 \cdot \boldsymbol{\sigma}_2$), spin-orbit ($\boldsymbol{L} \cdot \boldsymbol{S}$), and tensor ($S_{12}$) interactions. The potential parts are responsible to the behavior in different ranges: the OPEP is employed in the LR, whereas fully-phenomenological potential is used in the MR and SR. This kind of potentials have numbers of free parameters that

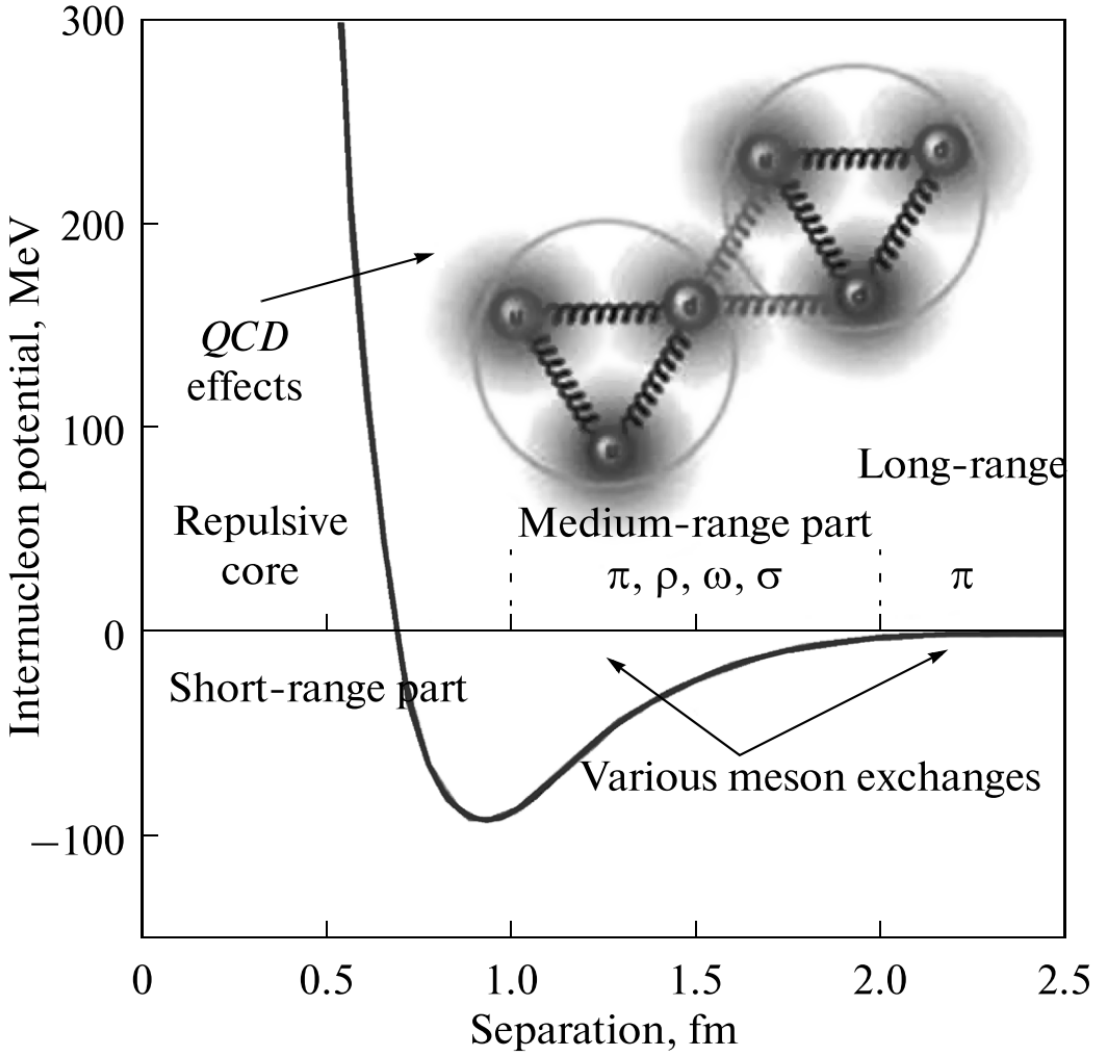

Figure 1.6: General scheme for Nucleon-Nucleon (NN) potential taken from Ref. [36]. The potential energy between two nucleons are plotted with respect to their separations. The behavior of the potential is sorted with the separation length into three parts: long-range, medium-range, and short-range parts. Each part is sectioned with the dashed vertical lines.

must be determined form experimental data. This flexibility is the strong point of this formalism, but the connection to the physical background is rather weak. Examples of the phenomenological models are the Hamada-Johnston potential [38], the Urbana-group potentials (e.g., UrbanaV14 [39]) , the Argonne-group potentials (e.g., ArgonneV14 [40], ArgonneV18 [41]), and so on. Recent high-quality phenomenological potentials achieved successes in fitting the NN-scattering data globally within the accuracy of a reduced χ^2 of nearly 1 (e.g. χ^2 per datum of 1.09 for 4301 pp and np data in the energy range of 0–350 MeV [41]) .

(ii) Boson Exchange Model: the NN potential is explained with various one boson exchanges (OBEP). In addition to π-mesons, which are the lightest pseudo-scalar mesons, the potential is built with the phenomenological exchange of other pseudo-scalar [$J^\pi = 0^-$: $\eta(549)$, $\eta'(958)$ etc.], vector [$J^\pi = 1^-$: $\rho(769)$, $\omega(783)$, $\phi(1020)$ etc.], and scaler mesons [$J^\pi = 0^+$: $f_0(500)$ etc.]. The basic features of the potential in the LR, such as tensor interactions, are mainly explained by π- and ϕ-meson exchanges, and the repulsive force and the spin-orbit force in the SR is understood from an ω-meson exchange. The attractive force in the MR is result from ρ- and σ-meson exchanges, or two-pion exchanges. Some examples of the potentials classified in this class are the one given by the Paris group [42], the Bonn group [43], and the Nijmegen group [44]. Although the agreement with the data is slightly inferior to those of the full phenomenological potentials and potentials derived from chiral-EFT, the experimental data for the LR and MR parts are reproduced well by the OBEP potential.

(iii) The model based on quantum chromodynamics (QCD): the NN potential is explained with the effective model based on QCD. One major example is one derived from the chiral perturbation theory (ChPT). Chiral symmetry, or the symmetry between the quarks with opposite helicities, is spontaneously broken in the energy below the energy scale $\Lambda_{\rm QCD} \sim 1$ GeV. Below $\Lambda_{\rm QCD}$, the effective field theory (chiral effective field theory: ChEFT) for pions and nucleons, rather than quarks and gluons, can be constructed as a low-energy limit of QCD [45]. Within this effective theory, the NN potential was derived from the perturbative expansion of the Feynman diagrams involving NN scattering with the order of $(Q/\Lambda_{\rm QCD})^\nu$, where Q is a momentum or pion mass [46, 47]. The reproductivity of NN data by the potential derived from ChPT improves when the order of chiral expansion increases. The high-quality NN-potential calculated taking into account the next-to-next-to-next-to-leading order (N^{3}LO) of the expansion is presented by several groups, for example the Idaho group [48], whose accuracy of the reproduction is comparable to the phenomenological high-precision ArgonneV18 potential [41].

The characteristics of the individual NN-interaction models are extensively discussed in Ref. [36].

As pointed out by Primakoff in 1939 [49], multi-body force such as three-nucleon force (3NF) also give significant contributions to the nuclear system with $A \geq 3$. One of the commonly accepted pictures of 3NF's effect in the nuclear system is the Fujita-Miyazawa force [50]. The process considered in the Fujita-Miyazawa force is originated from sequential exchanges of two π-meson via the intermediate state with a Δ baryon: a pion is

emitted from a nucleon is absorbed by another nucleon to form Δ baryon, the Δ baryon emits a pion again to decay into a nucleon, and the other nucleon absorbs the pion remaining a nucleon. This diagram is irreducible within the description by nucleon degrees of freedom. In fact, the 3NF plays essential roles in the nuclear structure calculations. It is well known that the 3 nucleon bound state, namely ^{3}H and ^{3}He, are theoretically unbound without 3NF [31]. Moreover, binding energies of light nuclei ($A \geq 3$) are underestimated compared to the experimental values from the Green's function Monte-Carlo method using the high-precision phenomenological NN interaction (ArgonneV18 [41]), but this discrepancy is resolved by adding 3NF [51]. In addition, the saturation density in nuclear matter is not reproduced without 3NF [52]. As examples of 3NF models, we mention the 2π-exchange Tucson Melbourne (TM) [53], its derivative model given by the Brazilian group [54], and the phenomenological model so called Urbana IX 3NF [55]. Furthermore, 3NF potentials are even able to be derived from the ChPT. The 3NF calculated with the chiral expansion up to next-to-next-to-leading order (N^{2}LO) was published by Kolck *et al.* [56] and Epelbaum *et al.* [57].

Even the NN anf 3N interactions are understood precisely, such realistic potentials are not normally employed in the nuclear structure calculations for many-body systems. Instead, the effective interactions, that are in quite simple forms compared to the bare NN interaction, are used as the interactions between nucleons in the nuclear medium. This prescription is taken mainly due to computational difficulty using the bare NN interaction and enjoys success in the nuclear structure calculations. In order to avoid divergence of the two-body matrix element due to the hard-core contained in realistic NN interaction, the NN interaction is divided into two parts: one is renormalized in the propagator as a one-body mean potential, and the rest part is the origin of the effective interaction. The effective interaction is systematically evaluated from the rest part of NN-interactions by using the G-matrix or the Brueckner-Bethe-Goldstone theory [58, 59, 60]. The derivation of the effective interaction and its application are reviewed in Ref. [61]. Some shell-model calculations [62, 63] are actually performed on the basis of the effective interaction derived from the realistic NN interactions, such as the Bonn potential [43] and the Paris potential [42]. However, in many case, more simplified effective interactions [64] which are not necessarily rigorously supported by underlying NN interaction are employed. It is obvious that the theoretical calculation performed with the realistic NN and 3N interactions are more preferable, if possible. Modern *ab initio* calculations meet that requirement.

Ab initio Calculations in Nuclear Few-Body System The *ab initio* calculation is also referred as the first principle calculation as it can be understood from the meaning of the latin word "*ab initio*", namely "from the beginning". In the context of the computational chemistry, the *ab initio* calculation originally implies that it is based on no experimental data other than the fundamental constants. However, this name is ambiguously used in the field of nuclear physics. According to definitions by some experts[1],

[1] "solve nuclear many-body problem based on realistic interactions using controlled and improvable truncations with quantified theoretical uncertainties" by Roth [65].

the essences of the nuclear *ab initio* calculation are summarized as follows [65, 66, 67].

- The calculation aims to solve many-body problems regarding nucleon degrees of freedom.
- As for the interaction among nucleons, the realistic NN and 3N interactions are employed. Especially, one derived from the chiral EFT is preferred.
- Attentions are paid to control the approximation or truncation applied in the calculation, thereby maximizing predictive capability.

As can be seen from the listing above, the *ab initio* calculation does not mean a specific theoretical framework.

The *ab initio* calculation is mainly performed in few-nucleon systems. Theoretical frameworks actually applied in the *ab initio* calculations for the few-nucleon systems are reviewed in Refs. [68, 69]. Here, some major frameworks therein are introduced in the point of view of application to the ^{4}He photodisintegration following the descriptions in Refs. [68, 69].

Generally speaking, dynamics of a system of A-nucleons with mass m is governed by the nuclear Hamiltonian

$$\hat{H} = \hat{T} + \hat{V} \tag{1.30}$$

$$= \sum_i^A \frac{\hat{\boldsymbol{p}}_i^2}{2m} - \frac{\hat{\boldsymbol{P}}_{\rm CM}^2}{2Am} + \sum_{i<j}^A \hat{V}_{ij} + \sum_{i<j<k}^A \hat{V}_{ijk}. \tag{1.31}$$

Here, $\boldsymbol{p}_i$ and $\boldsymbol{P}_{\rm CM}$ are the momentum of the i-th nucleon and the center of mass momentum. In addition, V_{ij} and V_{ijk} are realistic NN and 3N potentials. The dynamics of the system must fulfill the Schrödinger equation,

$$(\hat{H} - E)\,|\Psi\rangle = 0, \tag{1.32}$$

where E and $|\Psi\rangle$ denote one of the eigenenergies and eigenfunctions of $\hat{H}$. When the eigenenergy E is below the break-up threshold ($E_{\rm th}$) of the A-nucleon system, this function is solved as a mere eigenvalue equation regarding the localized function $|\Psi\rangle$. On the other hand, in case for $E > E_{\rm th}$, Eq. (1.32) must be solved under appropriate boundary conditions such as asymptotic boundary condition because $|\Psi\rangle$ is not localized around the origin ($\boldsymbol{r}_i - \boldsymbol{r}_j = \boldsymbol{0}$), or a continuum state. Only if $A = 2$, the Lippmann-Schwinger equation enable one to apply asymptotic boundary condition automatically. However,

"use nucleons as the relevant degrees of freedom, start from the realistic forces among nucleons, recently almost exclusively the chiral EFT interactions that describe accurately the two-nucleon system and three-nucleon bound states, and aim at predicting the properties of atomic nuclei" by Navratil *et al.* [66].

"employing Lagrangians, Hamiltonians, or energy density functionals based on EFT principles and with degrees of freedom chosen such that it maximizes our predictive capabilities" by Ekström *et al.* [67].

some kinds of techniques are necessary to solve the equation in the case for both $E > E_{\rm th}$ and $A \geq 3$. The photodisintegration reaction of ^{4}He is one of the typical cases of that.

The total photoabsorption cross section is given in the long-wavelength limit as

$$\sigma_\gamma = \frac{4\pi^2}{\hbar c} E_\gamma R(E_\gamma), \tag{1.33}$$

where R is the dipole response function,

$$R(E_\gamma) = \int df \left| \left\langle \Psi_f \left| \hat{D}_z \right| \Psi_i \right\rangle \right|^2 \delta(E_f - E_i - E_\gamma). \tag{1.34}$$

Here, $\hat{D}_z$ is the electric dipole operator, it is given as, for example, $\hat{D}_z(\boldsymbol{r}) = \sum_i^A e/2(1-\tau_3)\delta(\boldsymbol{r}_i - \boldsymbol{r})z$, if one assumes point-charge distribution of proton. The integral $\int df$ represents the summation over all the possible final states Ψ_f. This equation is equivalent to Eq. (1.7). In addition to Eq. (1.33), the coupling between nuclear final state Ψ_f and the exit channels must be taken into account to calculate the photodisintegration cross sections.

The complication in Eqs. (1.33) and (1.34) is the final state $|\Psi\rangle$ is inevitably a continuum state composed of four nucleons. This difficulty is solved by some computational techniques to transform the continuum problem to the eigenvalue problem for the localized basis.

The Lorentz integral transform (LIT) [70] is one promising trick to handle the continuum. This method is based on the transformation of $R(E_\gamma)$ with the Lorentz kernel defined by parameters σ_R and σ_I as

$$\begin{aligned}
L(\sigma_r, \sigma_I) &= \int dE_\gamma \frac{R(E_\gamma)}{(E_\gamma - \sigma_R)^2 + \sigma_I^2} && (1.35)\\
&= \int df \frac{\left| \left\langle \Psi_f \left| \hat{D}_z \right| \Psi_i \right\rangle \right|^2}{(E_f - E_i - \sigma_R)^2 + \sigma_I^2} && (1.36)\\
&= \langle \Psi_i | \hat{D}_z^\dagger \frac{1}{\hat{H} - E_i - \sigma_R + i\sigma_I} \frac{1}{\hat{H} - E_i - \sigma_R - i\sigma_I} \hat{D}_z | \Psi_i \rangle && (1.37)\\
&= \left\langle \tilde{\Psi} \middle| \tilde{\Psi} \right\rangle, && (1.38)
\end{aligned}$$

where

$$\left| \tilde{\Psi} \right\rangle := \frac{1}{\hat{H} - E_i - \sigma_R - i\sigma_I} \hat{D}_z \left| \Psi_i \right\rangle. \tag{1.39}$$

From the Eq. (1.39), $\left| \tilde{\Psi} \right\rangle$ can be obtained by solving the Schrödinger-like equation,

$$(\hat{H} - E_i - \sigma_R - i\sigma_I) \left| \tilde{\Psi} \right\rangle = \hat{D}_z \left| \Psi_i \right\rangle. \tag{1.40}$$

As for the transition from the grand state, the right hand side of Eq. (1.40) is the ground-state wave function transformed by the operator $\hat{D}_z$, and that result in a short

range function. Since $\left|\tilde{\Psi}\right\rangle$ vanishes at large distance, Eq. (1.40) is much simpler to solve than the continuum equation. Once $\left|\tilde{\Psi}\right\rangle$ is obtained, the integral transform L in Eq. (1.38) and its inverse transform $R(E_\gamma)$ is calculable. Difficulties stemming from the inversion transform and the prescription for it are discussed in Ref. [71].

The complex scaling method (CSM) [72] is another trick to avoid the difficulties relevant to continuum wave function. The CSM is based on the idea that asymptotic behavior of continuum wave function is localized if the transformation,

$$U(\theta): \ \boldsymbol{r} \to \boldsymbol{r}e^{i\theta}, \ \boldsymbol{p} \to \boldsymbol{p}e^{-i\theta} \tag{1.41}$$

is introduced. If one applies the rotational transformation $U(\theta)$ to the outgoing wave $\Psi^{sc} \sim \exp(ikr)/r$, where $k = \sqrt{2\mu E}/\hbar$, the corresponding wave function $\bar{\Psi}^{sc}$ dumps exponentially $\sim \exp(-kr\sin\theta)$ as r increases. This fact enables one to convert continuum problems into a bound-state problem. The summation for the final state leads the strength function Eq. (1.34) to

$$R(E_\gamma) = -\frac{1}{\pi}\mathrm{Im}\,\langle\Psi_\mathrm{i}|\hat{D}_z^\dagger\frac{1}{E_\gamma - \hat{H} + E_i + i\epsilon}\hat{D}_z|\Psi_\mathrm{i}\rangle\,. \tag{1.42}$$

Applying the transformation on Eq. (1.42), the response function leads to

$$\begin{aligned}
R(E_\gamma) &= -\frac{1}{\pi}\mathrm{Im}\,\langle\Psi_\mathrm{i}|\hat{D}_z^\dagger U^{-1}\frac{1}{E_\gamma - \hat{H}(\theta) + E_i + i\epsilon}U\hat{D}_z|\Psi_\mathrm{i}\rangle & (1.43)\\
&= -\frac{1}{\pi}\mathrm{Im}\,\langle\Psi_\mathrm{i}(\theta)|U\hat{D}_z^\dagger U^{-1}\frac{1}{E_\gamma - \hat{H}(\theta) + E_i + i\epsilon}U\hat{D}_z U^{-1}|\Psi_\mathrm{i}(\theta)\rangle & (1.44)\\
&= -\frac{1}{\pi}\mathrm{Im}\,\langle\Psi_\mathrm{i}(\theta)|\hat{D}_z^\dagger(\theta)\frac{1}{E_\gamma - \hat{H}(\theta) + E_i + i\epsilon}\hat{D}_z(\theta)|\Psi_\mathrm{i}(\theta)\rangle & (1.45)\\
&= -\frac{1}{\pi}\sum_{\lambda,\lambda'}\mathrm{Im}\,\langle\Psi_\mathrm{i}(\theta)|\hat{D}_z^\dagger(\theta)|\Psi_\lambda(\theta)\rangle\ \langle\Psi_\lambda(\theta)|\frac{1}{E_\gamma - \hat{H}(\theta) + E_i + i\epsilon}|\Psi_{\lambda'}(\theta)\rangle\\
&\quad\times\langle\Psi_{\lambda'}(\theta)|\hat{D}_z(\theta)|\Psi_i(\theta)\rangle & (1.46)\\
&= -\frac{1}{\pi}\sum_{\lambda}\mathrm{Im}\frac{\langle\Psi_\mathrm{i}(\theta)|\hat{D}_z^\dagger(\theta)|\Psi_\lambda(\theta)\rangle\ \langle\Psi_{\lambda'}(\theta)|\hat{D}_z(\theta)|\Psi_\mathrm{i}(\theta)\rangle}{\mathrm{E}_\gamma - \mathrm{E}_\lambda(\theta) + \mathrm{E}_\mathrm{i} + \mathrm{i}\epsilon}. & (1.47)
\end{aligned}$$

Here, the complex scaled operator $\hat{O}(\theta)$ is defined as

$$\hat{O}(\theta) \coloneqq U(\theta)\hat{O}U^{-1}(\theta), \tag{1.48}$$

and the transformed wave function is given as

$$|\Psi_\lambda(\theta)\rangle \coloneqq U(\theta)\,|\Psi\rangle\,. \tag{1.49}$$

The wave function is derived from the complex-Schrödinger-like equation

$$\left(\hat{H}(\theta) - E_\lambda(\theta)\right)|\Psi_\lambda(\theta)\rangle = 0. \tag{1.50}$$

Since the complex scaled function is localized, Eq. (1.50) can be solved as a eigenenergy problem of bound states. If θ is a positive value large enough, $E_\lambda(\theta)$ is independent from the choice of θ. In order to fulfill this condition, resonance poles on the complex energy plane must be covered by a semicircle integral path defined by the rotated momentum axis [73]. Practically, one must make a choice for a suitable scaling angle θ examining the response function.

By combining these methods and the realistic NN and 3N interactions, the dipole response function and then the photoabsorption cross sections can be derived without relying on any empirical parameters. Moreover, the *ab initio* method is applicable to more general problems that is experimentally difficult to be tackled with. Inversely, one can assess the reliability of the calculation methods and the knowledge on the nucleon interaction from the comparison with a reliable experimental cross section. The low energy photodisintegration cross section would be a suitable benchmark because the transition is approximately governed by a single dipole operator which is easy to handle theoretically.

1.2.3 Astrophysical Interests

Reliable experimental cross-sections of ^{4}He photodisintegration reactions are desperately needed not only from the perspective of nuclear structure but also from that of nuclear astrophysics. That is because the ubiquity of the ^{4}He in the universe. In this section, the importance of the ^{4}He in the universe will be first introduced. Then, some nuclear astrophysical impacts of ^{4}He photodisintegration will be reviewed.

^{4}He in the universe ^{4}He is the most abundant nucleus in the universe second to ^{1}H, and, as it were, an important building block of the universe. Roughly speaking, the mass fractions of the universe is viewed to be occupied by three forth of ^{1}H, one forth of ^{4}He, and about one order smaller fractions of other elements. Almost all the ^{4}He nuclei are considered to be produced in the very early phase of the universe, namely the Big Bang era. The Big Bang nucleosynthesis is reviewed in Sec. 23 in Ref. [8]. When approximately 10^{-4} s passed from the beginning of the universe, the temperature of the universe was cooled down to the QCD phase transition temperature. Thereafter, the universe had been filled with the leptons and baryons, not quarks and gluons. These particles were in a chemical equilibrium governed by the bidirectional reactions such as

$$n \leftrightarrow p + e^- + \bar{\nu}_e. \tag{1.51}$$

The neutrons to protons number ratio n_n/n_p was defined in the equilibrium defined with the temperature T as,

$$\frac{n_n}{n_p} = \exp\left(-\frac{\Delta m}{T}\right), \tag{1.52}$$

where Δm is the mass difference between a proton and a neutron, 1.293 MeV. The proton-neutron interconversion rate Γ_{pn} was approximately estimated to be $\Gamma_{pn} \sim G_F^2 T^5$. Here,

G_F is the Fermi coupling constant. While T was large enough, the number ratio was almost 1. As time passed, T dropped and consequently the neutron-to-proton ratio also decreased. The expansion rate of the universe H was evaluated as $H \sim \sqrt{g_* G_N} T^2$. Here, g_* and G_N are the numbers of relativistic particle species involving the energy density in radiation and the Newtonian constant of gravitation, respectively. When the speed of the expansion overwhelmed the interconversion rate, the equilibrium was no longer maintained. The critical temperature T_c would be approximately at the point that these rates got equal,

$$T_c \sim \left(\frac{g_* G_N}{G_F^4} \right)^{\frac{1}{6}} \sim 1 \text{ MeV}. \tag{1.53}$$

The neutron-to-proton ratio at $T = T_c$ was freezed out except for the spontaneous β decay of neutrons. By taking into account the β-decay, the ratio dropped to $n_n/n_p \sim 1/7$ by the time nuclear reactions began. Assuming all the neutrons left at that time were exhausted to produce ^{4}He nuclei combined with the same amount of protons, the mass ratio of ^{4}He over ^{1}H resulted in 1/3, and that is consistent with the present abundance ratio. This fact supports the perspective that almost all the ^{4}He nuclei was generated during the Big Bang nucleosynthesis (BBN).

In addition, ^{4}He nuclei produced via the proton-proton chain (pp-chain) reaction in stars have been one of the key ingredients in the nuclear reactions proceeding in the various sites. The most prominent example is the triple-alpha process in stars. This is a nuclear fusion process in which three alpha particles coalesce. This process is considered to proceed through three-steps: a merger of two ^{4}He nuclei composes a ^{8}Be nucleus, the other ^{4}He particle is sticked by the ^{8}Be nucleus to form a resonance state of ^{12}C, and the ^{12}C nucleus is de-excited to its ground state. In order this sequence to happen, each steps must finish in a very short time shorter than their inverse processes. Thus, the ^{4}He-rich environment at high-temperature and the circumstance of rich ^{4}He nuclei, which realizes only in heavy stars, not in the Big Bang, is essential. Elements heavier than ^{12}C is considered to produced via this process. In order to explain the abundance of heavy elements, a ^{12}C resonance state at the suitable excitation energy is required. This state was first predicted by Hoyle [74], and experimentally discovered later. This resonance, so-called the Hoyle state [75], is also of interest from a point of view of the nuclear structure because the state is considered to be a cluster state consisting of three ^{4}He nuclei [76].

Nuclear Astrophysical Phenomena Relevant to the ^{4}He photodisintegration
The cross section of the ^{4}He photodisintegration reaction in the GDR-energy region has recently attracted research interest because it is an important aspect for understanding nucleosynthesis in the universe. Here, three of them are introduced.

One example is the ν-process in the He-layer of core-collapse supernovae [77]. Core-collapse supernovae are explosive phenomena that occur at the end of the chemical evolution of massive stars [78]. Before the explosion, onion-like layers of elements are accumulated around the core of the stars. The layer structure evaluated with a supernovae model

is shown in Fig. 1.7. These layers are produced via nuclear fusion reaction process in the star as summarized below. At the beginning, hydrogens in the star coalesce to form a helium. Eventually, all the hydrogens in the star are exhausted, and then, the star starts to shrink because of the absence of the heat released from the hydrogen fusion. Due to the contraction, the temperature in the star is again raised to be high enough to allow helium fusions, which produces carbon and oxygen at the core of the star. Similarly, more heavy elements are produced via sequential fusion reactions, and they forms onion-like layers. In massive stars, the ^{56}Fe core is finally produced in the innermost region of the star. Since ^{56}Fe has the largest binding energy per nucleon among all the nuclei, there exists no room to produce energy from fusion reactions. Therefore, the star is squeezed onto the iron core under huge gravitational pressure. When the mass of the core exceeds the Chandrasekhar limit, gravitational pressure overcomes the degeneracy pressure of electrons force the core to collapse catastrophically. As the density of the core increases, electrons and protons are merged together to from neutrons via inverse beta decay, and, at the same time, huge amount of neutrinos are produced. Due to the weakness of the interaction of neutrinos with matters, neutrinos can escape from the core. Meanwhile, a fraction of neutrinos flux interact with the element, and elements are transmuted via neutrino-nucleus reactions. When the density of the core reaches the nuclear density, outer layers falling inward bounces back to outward by the incompressibility of nuclear matter. The shock wave that stems from the bounce ultimately triggers the supernova explosion. Then, the elements around the core are sprayed over the space.

The ν-process is driven by a huge amount of neutrinos released from supernovae explosion and occurs at the outer layer of the onion-like structures. In this process, rare elements such as ^{7}Li and ^{11}B are produced through a series of nuclear reactions in the helium layer. The reaction path of the process is schematically shown in Fig. 1.8. That reaction flow is initiated by the ^{4}He(ν,$\nu' n$) and ^{4}He(ν,$\nu' p$) reactions [79, 80] in the helium layer. The giant resonances, such as GDR and spin-dipole resonances, make a dominant contribution to these reactions because the ^{4}He(ν,ν') reaction primarily excites these resonances with an angular-momentum transfer of $\Delta L = 1$ [81]. The Gamow-Teller resonance is approximately forbidden in ^{4}He due to the system's double magicity.

The neutrino-scattering cross sections on nuclei are also proportional to the sum of the square of the nuclear matrix elements given from a multipole expansion similar to the electron and photonuclear cross sections [82]. There are two measure difference between electromagnetic and neutrino cross sections. One is neutrino cross section consists also of the matrix element of the longitudinal transition operators [Eq. (A.6)]: the four classes multipole operators, namely electric [Eq. (A.3)], magnetic [Eq. (A.4)], Coulomb [Eq. (A.5)], and longitudinal operators [Eq. (A.6)], contribute all together. As for photonuclear (electron) cross section [Eqs. (A.1, 1.9)], that is described only with the matrix elements of the electric and magnetic transition operators (electric, magnetic, and Coulomb transition operators). The other is the matrix elements are composed with axial-vector nuclear currents besides those with vector nuclear currents. That is contrasting to the case of electromagnetic process where only the vector nuclear current are involved with the cross sections. Since all the terms in the neutrino cross section

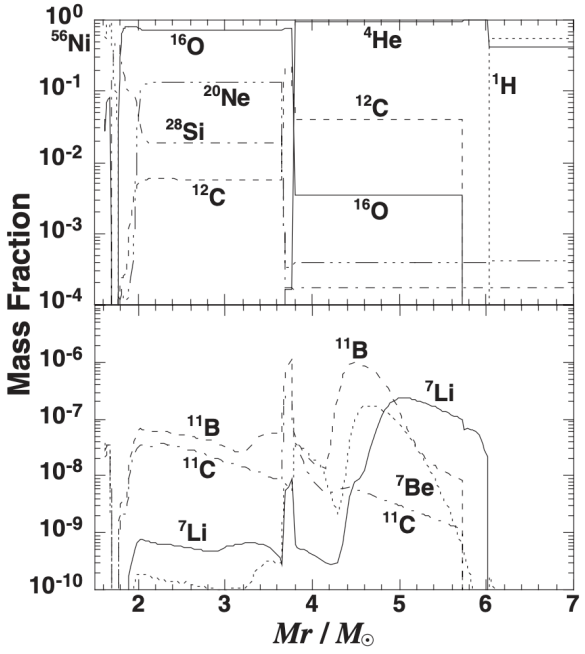

Figure 1.7: Mass fraction distribution of main elements (upper panel) and rare elements (lower panel) in SN 1987A evaluated with a supernovae model taken from Ref. [79]. The vertical axis denotes the cumulative mass coordinate measured from the center in the solar mass unit ($M_\odot$). The helium layer is between 3.8-6.0$M_\odot$.

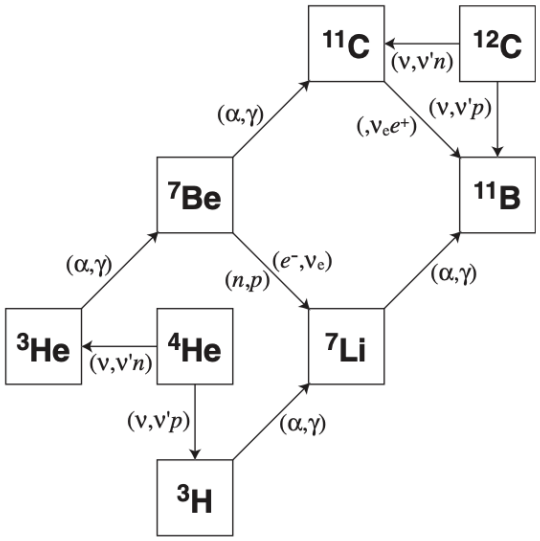

Figure 1.8: Nuclear reaction flow-path of ν-process in the helium layer around the super novae explosion taken from [79].

other than the matrix elements can be derived precisely, nuclear structural information is, therefore, a main source of uncertainty with regard to the theoretical neutrino cross sections.

Because of technical difficulties in measuring neutrino-nucleus reactions, estimation of neutrino-nucleus reaction cross sections for examining the ν-process relies on nuclear structure theories. However, by using the analogy between electromagnetic responses and weak responses of nuclei [83, 84], part of the matrix elements, namely the vector current electric transition carrying $\Delta L = 1$, can be evaluated directory from the experimental photo absorption cross section. Therefore, the experimental cross sections of the ^{4}He photodisintegration reaction can provide a criterion to test the validity of the estimated cross sections of ^{4}He(ν,$\nu'n$) and ^{4}He(ν,$\nu'p$) reactions.

Second, a relationship was also discussed between the ^{4}He photodisintegration and the lithium problem in BBN [85]. The lithium problem is an unsolved discrepancy between the primordial abundances of lithium isotopes estimated from the astronomical observation and those predicted from the BBN calculation. According to spectroscopic measurements on the metal-poor halo stars, the primordial abundance or abundance at BBN of ^{7}Li was evaluated [86]. The result of the spectroscopic measurement on ^{7}Li and ^{7}Be is shown in Fig. 1.9. In contrast to the ^{9}Be abundance, the ^{7}Li abundance is constant over the wide region, that is called the spite plateau. Since the horizontal axis correspond to the time at the star was formed, one can anticipates that ^{7}Li produced in BBN remained unchanged over time. Therefore, the primordial ^{7}Li abundance would be 10^{-10} with respect to the hydrogen abundance.

The lithium problem that the standard BBN facing to is shown in Fig. 1.10. This

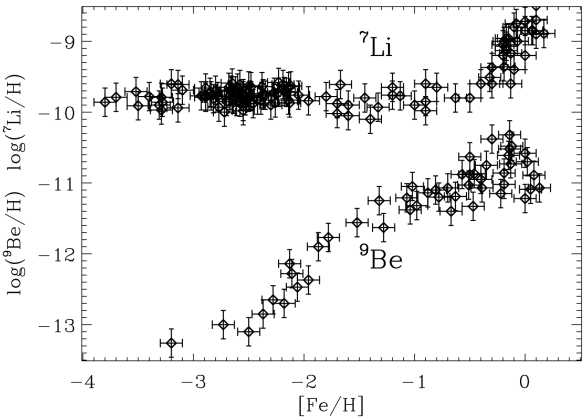

Figure 1.9: ^{7}Li and ^{9}Be abundances as a function of the iron abundance of stars taken from ref. [86]. Data are taken from references therein. The horizontal axis denotes relative abundance of Fe with respect to H, Fe/H. This relative abundance corresponds to the time when the star was formed in order of left to right. In the ^{9}Be case, abundance of the beryllium is proportional to the time. That means ^{9}Be has constantly been produced over time in the universe. In contrast, ^{7}Li abundance is almost constant in the F/H region below 0. This region is called the spite plateau. The existence of the plateau implies the ^{7}Li once produced in the beginning of the universe, namely the Big Bang era, remains unchanged until the time corresponds to Fe/H = 1. In addition, the primordial abundance of ^{7}Li would be that constant value.

figure shows primordial abundances of light elements including ^{7}Li. The curved bands show the standard BBN predictions, whereas boxes indicate the results evaluated from observations. In case of ^{4}He and D, the prediction and observation regions are overlapping. However, those of ^{7}Li are not, which means the primordial abundance of ^{7}Li is deficient with regard to the standard BBN prediction by a factor of three [87, 88]. In addition, the possibility of an overabundance of ^{6}Li at the level of approximately three orders of magnitude was also suggested from the spectroscopic measurements [89].

It was proposed that the extended BBN modified with non-thermal photons produced through radiative decays of unstable relic neutral massive particles X might solve the lithium problem [85]. Additional source of the photons in the early phase of the universe can increase (decrease) the abundance of the light elements via photodisintegration reactions of light elements, such as helium. Therefore, this model is sensitive to the photodisintegration reaction cross sections. Although the relic particles X have not yet been observed, their possible masses, abundances, and lifetimes are constrained by the cross sections of the ^{4}He photodisintegration reaction. In Ref. [85], the parameter region that could solve the lithium problems was surveyed with then-current compilation of the experimental cross sections of ^{4}He photodisintegrations. The constraints on the lifetime τ_X and the abundance parameter ζ_X for X particles considered in the model is shown in Fig. 1.11. Here, the abundance parameter ζ_X is defined as $\zeta_X = (n^0_X/n^0_\gamma)E_{\gamma 0}$, where n^0_X, n^0_γ, and $E_{\gamma 0}$ are the present X density, the present photon density, and the energy of the photon from the radiative decay of X. The shaded regions below the thick solid line is the allowed parameter regions. The solid (dotted) lines are the boundary of the allowed region originating from the abundances of individual elements based on the then-current (conventional) cross sections. As seen in the figure, two allowed regions from the different cross sections are not completely overlapped, which manifests the cross section dependence of the model. The reliable cross sections are essential to give a efficient constraint on the relic-particle properties.

Third, the photodisintegration reaction cross sections of light nuclei are crucial to explain the propagation of ultra-high-energy cosmic rays (UHECR), the cosmic ray whose energies are above 10^{18} eV [91]. The energy distribution and nuclear species of the UHECR are modified through the travel from their origin to observatories on the earth. The interaction with the cosmic microwave background (CMB) photons is the one key feature of the propagation process of the UHECR. The so-called GZK cut-off [92, 93], or the steep dropping of the population of the cosmic rays with energies above 10^{19} eV, is understood from the effect by the photo-π-meson-production reaction. Due to the large Lorentz factor of the UHECR, the collision between a UHECR and a CMB photon ($\sim 10^{-3}$ eV) in the rest frame is equivalent to the bombardment of a high energy photon with a energy that is enough to open th π-meson production channel on a nuclei in the nuclear reference frame. This process decreases the total energy of the UHECR for 10–20% per collision, and this results in the cut off.

The composition of the UHECR is becoming to be clarified from the recent observations. According to Refs. [94, 95], heavier element contributions other than protons are strongly favored for the UHECR. The sizable contribution from the complex nuclei (A=2

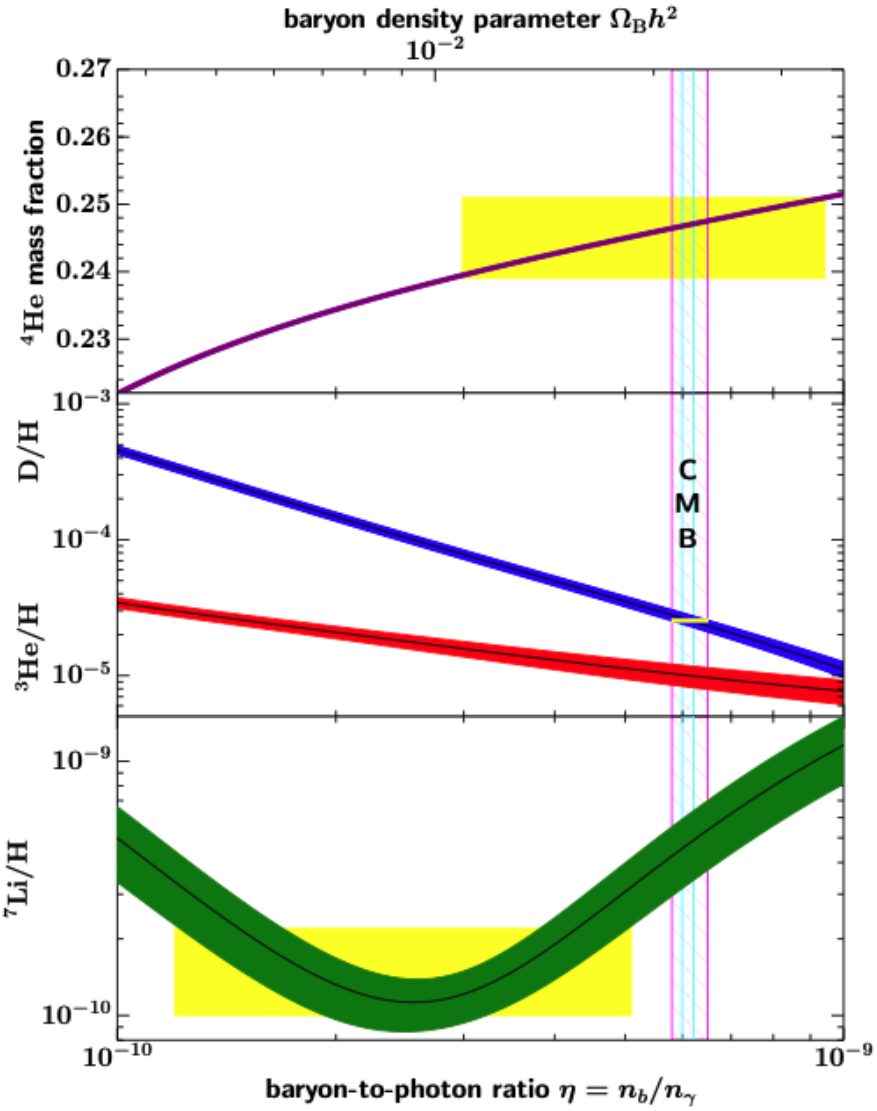

Figure 1.10: Primordial abundance of ^{4}He, D, ^{3}He, and ^{7}Li predicted by the standard BBN taken from Ref. [8]. The curved bands show the 95% CL range of the abundances as functions of cosmic baryon content taken from Ref. [90]. The narrow vertical band is the parameter range inferred from the CMB measurements. The boxes indicate the primordial abundances evaluated from observations.

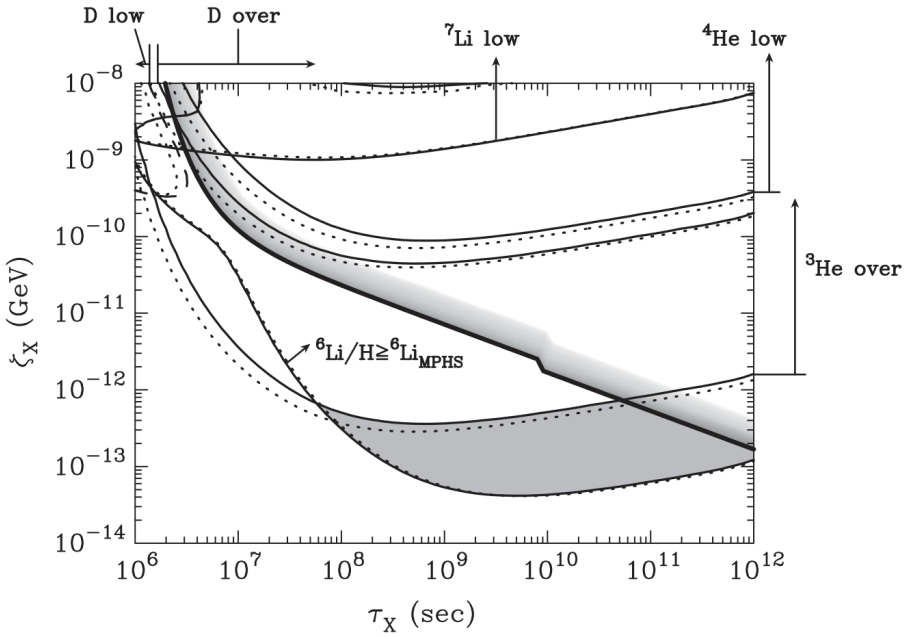

Figure 1.11: Constraints on the lifetime τ_X and the abundance parameter ζ_X for X particles considered in the no-standard BBN model taken from Ref. [85]. The abundance parameter ζ_X is defined as $\zeta_X = (n_X^0/n_\gamma^0)E_{\gamma 0}$, where n_X^0, n_γ^0, and $E_{\gamma 0}$ are the present X density, the present photon density, and the energy of photons from the radiative decay of X. The solid lines are the constraints given from abundances based on then-current experimental cross sections, which is smaller than the value expected before. The displacement between these two lines shows the dependence on the ^{4}He photodisintegration cross sections. The dotted line is the constraints based on the conventional cross sections. In addition, thick solid line is another consistency requirement from the CMB with a blackbody. The shaded contour below the thick line is the parameter region which can solve the lithium problems.

and heavier) implies the UHECRs are accelerated in some astrophysical sites rather than produced directly via elementary processes. In order to search for the possible source of the UHECR, the mean free paths of the elements are the essential inputs for the calculation. As for the nuclei, the excitation of the GDR is the most important process to asses the mean free path in the universe, because it has the largest cross-section and lowest energy threshold. Therefore reliable experimental nuclear photoreaction data are desired. At present, the propagation distance of ^{4}He UHECR was estimated to be 3.5 Mpc based on the experimental cross sections [96]. However, it would be modified if the cross-section data were wrong.

In short, the enrichment of the ^{4}He nucleus makes them to be involved with various nuclear reactions in the universe. The knowledge on some of them, such as the ν-process, the BBN, and the propagation of UHECR, is depending on the cross sections of the ^{4}He photodisintegration in the GDR energy region. Therefore, reliable experimental inputs are mandatory to improve our understanding on such astrophysical phenomena.

1.3 Theoretical Works

Even prior to the *ab initio* calculation had come into play, the photodisintegration cross section had been a subject of theoretical studies mainly motivated by the large asymmetry between experimental proton and neutron cross sections [97] [See Fig. (1.13)]. Until late 1990's, then-current best practice for the calculation was employing semi-realistic NN forces, such as the Malflieit-Tjon (MT) potential [98]. For instance, Wachter *et al.* [99] performed the calculation using the resonating group method by means of a semi-realistic potential [100]. They claimed the asymmetry is unlikely to be as large as reported, but rather around 1.1. Similarly, Sofianos *et al.* carried out their calculation based on the (Faddeev type) integrodifferential equation approach (IDEA) with the MT I + III potential, and claimed the ratio would be 1.05 [101]. Subsequently, Ellerkmann *et al.* [102] published theoretical ^{4}He$(\gamma, n)^3$He cross sections below the three-body-decay-threshold energy by solving the Alt-Grassberger-Sandhas (AGS)-type integral equation, which is a more rigorous treatment similar to the IDEA. They compared the cross sections given with two kind of potentials, the MT I + III and the Yamaguchi potential [103], and concluded these results were in the similar trend. Meanwhile, the LIT technique taking into account the full final-state interaction was applied on the total ^{4}He photodisintegration cross sections for the first time by Efros *et al.* [104]. They considered the use of the MT I + III potential and the trento (TN) potential [105, 106] and observed a pronounced peak structure around 30 MeV in both cases. As for the peak hight of the cross sections at that time, there were two distinct trends: ones from Refs. [99, 104] (LIT and RGM) reached maximal value of approximately 2 mb around $E_\gamma \sim 30$ MeV, whereas ones from Refs. [101, 102] (IDEA and AGS) increased to at most about 1.3 mb and were kept almost constant up to 40 MeV.

Afterwards, a benchmark calculation on the three-nucleon system (^{3}H and ^{3}He) was set by Golack *et al.* [107]. They studied the influence of various effects, such as (1) the

calculation methods (LIT and the Faddeev type equation), (2) the long-wavelength limit, (3) Coulomb force, and (4) the treatment of the MEC effect. Their major conclusions were follows.

- The resultant cross sections from the different frameworks (LIT and the Faddeev type equation) were qualitatively agreed as long as the same potential was used.
- The long-wavelength was valid within a precision of a few % up to $E_\gamma \sim$ several tens MeV.
- Without the Coulomb force, the cross sections near the decay threshold were overestimated by up to several tens %, but those at more than few MeV above the threshold were affected negligibly.
- The difference between the cross sections derived from the calculation with an explicit inclusion of MEC but no 3N force, and those obtained by the method with an implicit treatment of MEC (using the Siegert theorem) was as large as 10% around the GDR peak region but less significant in the higher-energy region. Note that a large part of three-nucleon MEC effect is automatically taken into account only by including the 3N force in calculation.

Since this remarks would be valid even in four-body system, many theorists were prompted to study further by using the more realistic nucleon potentials.

In 2000's, the theoretical studies by means of the LIT were performed actively. Quaglioni *et al.* [108], first, published their results on the exclusive two-body cross sections based on the MT I + III potential. Gazit *et al.* [109] presented the total photoabsorption cross sections by using the realistic two-body and three-body potentials, namely the Argonne V18 (AV18) NN potential [41] + the Urbana IX (UIX) 3NF [55]. Moreover, considerations regarding the even better 3NF were attempted. Bacca *et al.* [110] tried to substitute the phenomenological 3NF with one derived from AV18 potential by using the unitary operator method (UCOM). In the framework of the UCOM, non-local a two-body potential emerged from the transformation acts as an effective "three-body" interaction. Their resultant cross sections qualitatively reproduced the effect by adding 3NF, reduction near the threshold and the enhancement in high energy, but did not succeed to fit the experimental data very much compared to the AV18 + UIX result [109]. Especially, the disagreement was larger in near-threshold region in ^{4}He, and this trend suggested that the higher density of the ^{4}He made it sensitive to short-range properties of 3NF. Quaglioni *et al.* [111], again, computed the cross section with NN and 3N potentials derived from another manner, namely by the chiral effective field theory (ChEFT). Both the NN potential at N^{3}LO [48] and the 3N potential at N^{2}LO [56, 57] were applied in the calculation. Their results showed a peak around $E_\gamma = 27.8$ MeV. In spite of the disagreement between their results solely with the NN and ones obtained only based on the AV18 potential [109], their full results were in good agreement with those obtained with the AV18 + UIX potential [109] within a few %.

Thereafter, a comprehensive study on the ^{4}He photodisintegration was performed by Horiuchi *et al.* [112]. They studied the reaction based on two kind of frameworks, the CSM and the microscopic R-matrix method (MRM), taking into account the final state interactions and two- and three-body decay channels. The Argonne $v8'$ (AV8$'$) [55] and the G3RS potentials [113] were employed as the NN interaction, whereas a phenomenological potential was adopted for the 3NF [114]. The validity of exclusive two-body cross sections obtained with MRM was confirmed from the comparison with the inclusive photoabsorption cross sections given from the CSM. Their inclusive cross sections fairly agreed with the result of the LIT with the AV18 + UIX potential [109]. The exclusive cross sections published by them are shown in Fig. 1.12. These results were similar to the cross sections by the LIT calculation with the semi-realistic NN potential [108]. However, the peak hight (the resonance width) was slightly lower (broader) than those from Ref. [108]. It is interesting to mention that this characteristics is exactly the one realized by adding 3NF as pointed out in Ref. [110].

In summary, the recent state-of-the-art calculation techniques enabled one to perform *ab initio* calculations by using realistic NN and 3N interactions. The results obtained from various frameworks, finally, are getting converged within a fair degree of agreement among each other, and are quantitatively agrees various experimental data. However, not all recent data obey the trend, and this may potentially endanger the theoretical understanding seemed to be settled.

1.4 Experimental Review

^{4}He photodisintegration reactions in the GDR region are intensively studied for a long time. Various experimental studies are reviewed in this section.

1.4.1 Overview

Studies of the ^{4}He photodisintegration reactions near the decay threshold energy have been continuously performed since 1950s. Since its beginning, there have been typically two approaches to tackle with the reaction for a long time. One major strategy was measuring decay particles from the photodisintegration caused with continuous-energy photon beam, and the other one was deducing the cross section from the photon yield from the inverse reaction.

In order to perform the photodisintegration experiments, photon beams generated somehow is required. The characteristics of ideal photon beam was outlined in Ref. [120]:

- A good enough energy resolution to matches the requirements from the target object;

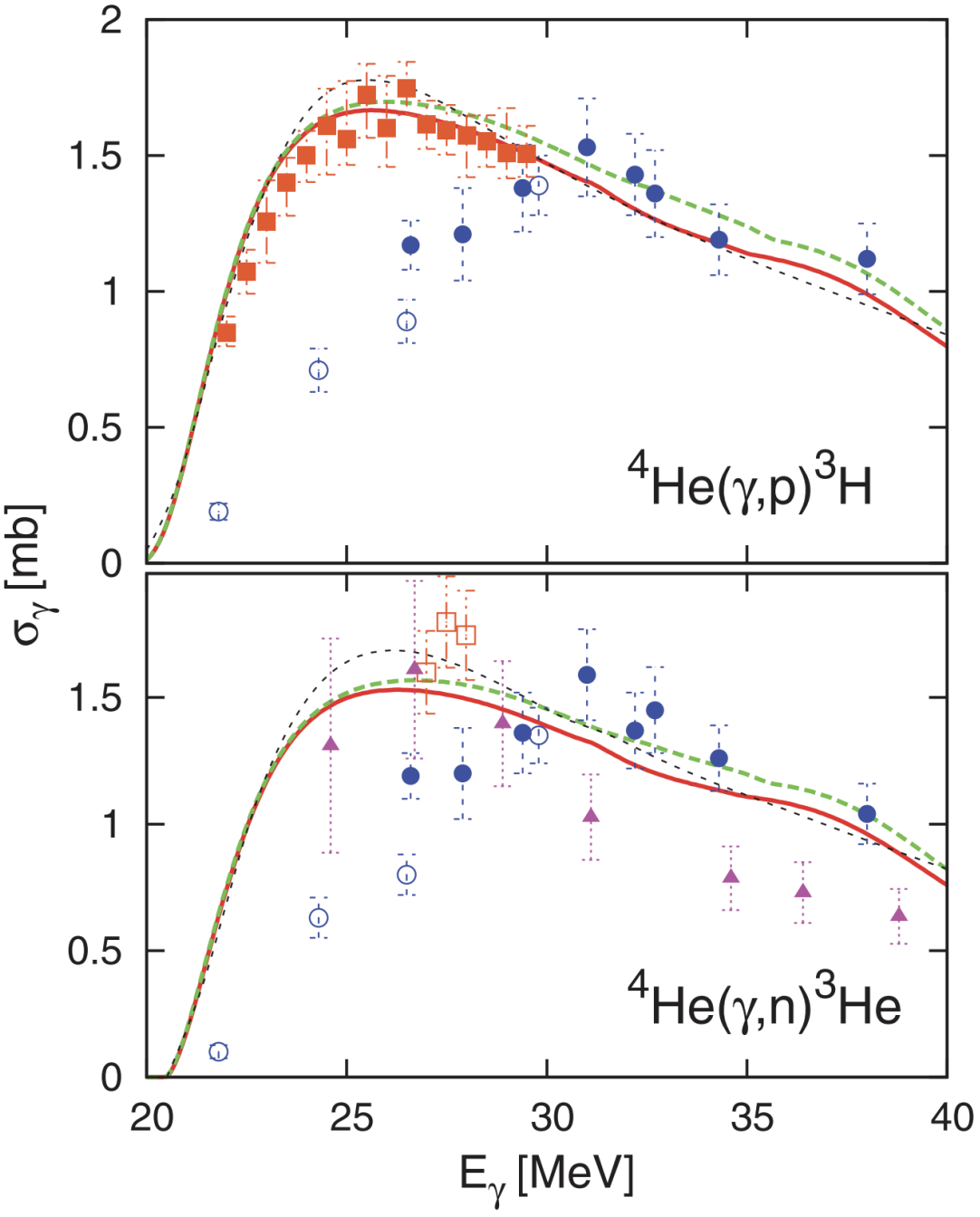

Figure 1.12: Theoretical photodisintegration cross sections of ^{4}He taken from Ref. [112]. The solid curve and the dashed curve are the result computed with the AV8′ and the G3RS potentials, respectively. The thin dotted curve is the LIT calculation with the MT I + III potential [108]. The experimental data are also plotted. They are taken as follows: open circles [115], closed squares [116], closed circles [117], open squares [118], and triangles [119].

- A highest possible beam flux without deteriorating the energy resolution;
- A lowest possible count rate of background photons;
- A good tunability of the beam energy;
- A good emittance.

Various experimental techniques aiming at an ideal photon beam apparatus have been developed over several decades.

The bremsstrahlung photon beam from an electron beam laid the foundation in the study of photonuclear reactions [21]. This is the radiation from the electron beam from an accelerator bombarded on a target made of a high-Z material. As the electron decelerated by the collision with a target atom, the kinetic energy lost at the collision is converted to a photon. That yield a radiation with a continuous energy spectrum, and this energy spreading is too large to decompose the nuclear level structures. On the other hand, this technique has good tunability of the maximal photon energy by varying the incident electron energy. Due to the insufficient energy resolution, the "unfolding" of the data, or subtracting the reaction yields with different incident electron energy varied in steps, is mandatory to obtain the reaction yield at a certain photon energy. Since this procedure heavily counts on the stability of in the accelerator parameters, enormous counting statistics, knowledge of the bremsstrahlung flux and spectrum, this potentially be a source of systematic uncertainty of the measurement.

To recover the drawback of bremsstrahlung photon source, namely the worse selectivity in a beam energy, mono-energetic photon sources have been invented. Here, three of them that adopted to the ^{4}He photodisintegration measurements are briefly mentioned.

The annihilation-photon method is one of the options of the mono-energetic photon source. This method takes advantage of in-flight annihilation of fast positrons. This phenomenon was first discovered in 1951 [121], and its application was proposed in 1957 by Tzara [122]. A fast positron beam are produced by pair production at a thick high-Z converter radiated by intense high-energy electron beam. Then, suitable energy component in the positron beam is selected either by a secondary accelerator or a magnetic spectrometer. Finally, the positron beam strikes a thin low-Z target to produce a mono-energetic annihilation photons in the forward direction and is swept away from the photon beam line by a dipole magnetic field. The energy of the highest possible energy of photon is given as $T_{e^+} + \frac{3m_ec^2}{2}$ in the relativistic limit, where T_{e^+} and m_e are the incident kinetic energy of the positron and the mass of electron (positron), respectively [120]. Since the annihilation is two-body reaction, a photon beam with a good energy resolution is produced by limiting the emission angle. The major source of the background photon is the bremsstrahlung of the positron whose probability scales with Z^2, whereas the annihilation probability is proportional to Z. That is why a low-Z material is preferred as an annihilation target to reduce the contamination of unwanted continuous energy photons. Even though, a considerable amount of continuous-energy background photon ranging

from the low-energy side is still unavoidable. Thus, it is necessary to subtract the yield measured with a electron beam from the one obtained with the positron beam.

The tagged bremsstrahlung method is a straight-forward extension of the bremsstrahlung method initiated by Weil and McDaniel in 1953 [123]. This method enable one to tag energy of the radiation photon by measuring the momentum of post-bremsstrahlung photon in coincidence with photoreaction products. The intensity and resolution of the resultant photon beam are comparable to those those of the annihilation photon technique. However, the requirement of the coincidence measurement constrains the usable detector type to a fast small-solid-angle detector (such as an organic scintillator) and the maximal acceptable count rate to small enough value that contribution of the pile-up event is ignorable.

The Laser Compton scattering (LCS), which is a back scattering of intense laser photon off relativistic electrons, could be utilized as a source of mono-energetic photon beam source. LCS is also known as a synonym, Compton back scattering (CSB), and was first investigated in 1963 [124, 125]. The principle of the LCS is energy amplification of laser photon by the large Lorentz factor of the incident electron. That result in highly directive photon beam with a narrow energy distribution. Simultaneously, this method have high manipulability of the beam energy by tuning the energy of both the incident electron and the laser photon. However, very precisely collimated incident electron and laser beams, an maximal spatial overlap between two beams, and an extremely well collimated photon beam, are required to realize a mono-energetic photon facility by using the LCS.

The inverse reaction of the photodisintegration is the radiative capture reaction. The principle of detail of balance

$$\sigma_{\rm abs}(E_\gamma) = \frac{2k^2_{N+3N}}{k^2_{^4{\rm He}+\gamma}}\sigma_{\rm rad}(T_N) \tag{1.54}$$

enables one to determine the photodisintegration cross section $\sigma_{\rm abs}$ from the radiative-capture cross section $\sigma_{\rm rad}$. Here, k_{N+3N} and $k_{^4{\rm He}+\gamma}$ represent wave numbers of proton (neutron) and photon, respectively. Factor 2 is originated from the ratio between spin statistical factors of initial and final states. The energy of photon beam E_γ of the photodisintegration reaction corresponding to the kinetic energy of proton (neutron) beam T_N of the radiative capture reaction is given as

$$E_\gamma = \frac{(m_N + n_{3N})^2 - m^2_{^4{\rm He}} + 2m_{3N}T_N}{2m_{^4{\rm He}}}. \tag{1.55}$$

Eq. (1.54) can be derived from the Breit-Wigner formula [126]

$$\sigma_{cc'} = \frac{\pi}{k_c^2}\frac{2J+1}{(2I_{c1}+1)(2I_{c2}+1)}\frac{\Gamma_{\lambda c}\Gamma_{\lambda c'}}{(E-E_\lambda)^2 + \Gamma^2_\lambda/4}, \tag{1.56}$$

where $\sigma_{cc'}$ is cross section of the reaction whose initial and final states are represented as c and c', respectively. This reaction proceeds via a intermediate resonance state (λ) of spin J, resonance energy E_λ, and the total width Γ_λ. The partial widths of the initial

and final channels are give as $\Gamma_{\lambda c}$ and $\Gamma_{\lambda c'}$. Parameters mentioned so far are in common for the normal and the inverse reactions. The spins of particle 1 and 2 in the initial state are denoted by I_{c1} and I_{c2}. In addition, k_c indicates the wave number of particles in the initial state. By substituting c and c' in Eq. (1.56), $\sigma_{\rm abs}$ and $\sigma_{\rm rad}$ are obtained. Finally, Eq. (1.54) is given from the ratio of $\sigma_{\rm abs}$ and $\sigma_{\rm rad}$.

Note that the conversion factor in Eq. (1.54) include a wave-number-dependence term, and this term monotonically increases in the energy region where the kinetic energy is far smaller than the mass of particles. Due to this energy dependence nature, the converted excitation function of photodisintegration reaction is more suppressed in the lower energy region. Therefore, the peak position of the excitation function of the photodisintegration reaction locates higher than that of the radiative capture reaction.

1.4.2 Prehistory until 1980s

The oldest study of the photodisintegration included in the EXFOR compilation [127] was published by A. N. Gorbunov *et al.* in 1957 [128, 129, 130]. Their measurement was conducted with a cloud chamber with the continuous-energy photon beam generated from bremsstrahlung. A magnetic field applied on the cloud chamber allowed them to determine the momentum of the decay charged particles from their curvature of the recorded trajectories. They presented the beam energy dependence of the (γ, n) and (γ, p) cross section from the decay threshold to 170 MeV. These cross sections peaks near the decay threshold, but the peak positions were vague due to the beam energy resolution.

Experimental studies of the photodisintegration were performed consecutively mainly by the bremsstrahlung beam. In 1965, Clerc *et al.* presented the ^{4}He$(\gamma, p)^3$H cross sections in the photon beam energy range from 24 to 56 MeV [131]. They measured charged particles from a He gas target bombarded by bremsstrahlung photon beam. Charged particles emitted from the target were analyzed by quadruple magnets and detected by a semiconductor detector. Their cross sections agreed to those by Gorbunov *et al.* and peaks around 28 MeV. Sanada *et al.* published the result of their measurement performed at the betatron of the Tokyo University of Education in 1970 [132]. Nuclear emulsion plates were employed to detect proton from the ^{4}He$(\gamma, p)^3$H reaction caused by bremsstrahlung photon beam in the energy range up to 32 MeV. The excitation function was deduced from the energy spectrum of photo-protons. Their data implied two broad peak structures at 24 and 17 MeV existed in the excitation function. As for (γ, n) channel, Berman *et al.* reported cross sections for the ^{4}He$(\gamma, n)^3$He reaction in the beam energy range between 22 and 32 MeV in 1972 [133]. The cross sections were determined from a energy spectrum of photoneutron from liquid a He target measured by the time-of-flight technique. Their cross sections peaked around 28 MeV but were about half of those by Gorbunov *et al.* [129]. In 1973, Irish *et al.* issued the ^{4}He$(\gamma, n)^3$He reaction cross section for excitation energy between 22 and 37 MeV [134]. They pointed out that photoneutron yield from the target largely varied depending on the physical state of target mater.

Considering this systematics, they evaluated the cross section by combining the results obtained with liquid and gas targets. Their results, in turn, were about twice as those by Berman *et al.* [133]. In the same year, Malcom *et al.* also presented the ^{4}He$(\gamma, n)^3$He cross section from threshold to 110 MeV [135]. Their results agreed well with Gorbunov *et al.* and was approximately a factor of two greater than those by Berman *et al.* A simultaneous measurement of both (γ, n) and (γ, p) channels was published by Arkatov *et al.* in 1973 [136] and 1974 as well [137]. The (γ, n) and (γ, p) cross sections up to 50 MeV determined from charged particle tracking by using a diffusion chamber were presented. Balestra *et al.* also issued a result of the simultaneous measurement with a diffusion cloud chamber [138]. Ratios of (γ, n) to (γ, p) cross sections deduced from these two simultaneous measurements at each beam energy were almost unity over their measurement range. In 1980, Berman *et al.* presented their follow-up measurement by using gaseous He target [139]. It should be noted that they employed mono-energetic photon beam generated by in-flight-annihilation method. The new results agreed to their former results obtained with liquid He target, but disagree with other results.

Besides, studies taking advantage of the inverse reaction were also started since 1950s. The photon yield from the ^{3}H(p, γ) ^{4}He reaction was measured by Willard *et al.* in 1953 [140]. This reaction is the inverse reaction of the ^{4}He$(\gamma, p)^3$H reaction, and thus the cross section of the photodisintegration reaction could be evaluated from the principle of detailed balance. A tritium gas target was bombarded with proton beams from a Van de Graaff accelerator, and gamma radiation from the target was detected by an NaI(Tl) scintillation detector. Their measurement covered the energy region of E_p from 1 to 5 MeV which corresponds to $E_\gamma \sim 20.6$ – 23.6 MeV. The total cross section deduced from their result peaked at E_p=3 MeV which was equivalent tot $E_\gamma \sim 22$ MeV.

As for the ^{3}H(p, γ) ^{4}He channel, subsequent inverse-reaction studies covered wider energy region around the GDR. Almost all the studies below are performed in the setup similar to that of Willard *et al.* Perry *et al.* presented their measurement with proton beams of the energy range 0.1 to 6.2 MeV (corresponds to $E_\gamma \sim 19.9$ – 24.5 MeV) in 1955 and observed the cross section peaks at $E_p \sim 4$ MeV [141]. The result of Gardner *et al.* published in 1962 covered higher energy region ranging between $E_p = 5.8$ – 9.2 MeV ($E_\gamma \sim 24.2$ – 26.8 MeV) [142] . Their cross sections monotonically decreases with respect to the beam energy and consistent with the result by Perry *et al.* In the same year, Gemmell *et al.* also reported the result of their measurement with $E_p = 4$–11 MeV ($E_\gamma \sim 22.9$ – 28.2 MeV), which agreed to that of Perry *et al.* as well [143]. The energy range of the cross section was broadened up to $E_p = 18$ MeV ($E_\gamma \sim 33.4$ MeV) in 1970 by Meyerhof *et al.* [144]. The photodisintegration cross sections deduced from their result was roughly in accordance with those by Gorbunov *et al.* [130], which peaked at $E_\gamma \sim 26$ MeV. In 1982, McBroom *et al.* [145] measured this reaction for incident proton energies from 8 – 30 MeV ($E_\gamma \sim 25.9$ – 42.5 MeV) and confirmed their results could be smoothly connected to the low energy results by Perry [141], Gemmell [143], and Meyerhof *et al.* [144]. Afterwards, Calarco *et al.* presented their results at E_p= 8.34 and 13.6 MeV ($E_\gamma \sim$ 26.1 and 30.1 MeV) and reviewed previously published results for both ^{3}H $(p, \gamma)^4$He and ^{4}He$(\gamma, p)^3$H channels.

On the other hand, few studies regarding the ^{3}He(n,γ) ^{4}He channel was published until 1980's. One reason is this is a technical difficulty for handling neutron beam which is inevitably a secondary product of ion beams. In 1963, Zurmuehle *et al.* performed the measurement making use of neutron beam at $E_n = 4.6$ MeV ($E_\gamma \sim 24.1$ MeV) generated via $d(d,n)^3$He reaction [146]. Ward *et al.* presented their results for E_n between 6.0 and 17.0 MeV ($E_\gamma \sim 25.2$ – 33.4 MeV) in 1981 [147]. The ^{4}He(γ,n) ^{3}He cross sections derived from their results were compared with ^{4}He(γ,n) ^{3}He [139] and $^4(\gamma,p)$ ^{3}H [138, 144] cross sections available at that time. Their result well reproduced the result of Berman *et al.* [139] and supported the claim (γ,p) to (γ,n) cross section ratio is between 1.6 and 1.9.

The results yield from these early experimental attempts had gotten attentions in terms of the charge symmetry breaking of the nuclear force. There were significant discrepancies between the exclusive cross sections of the ^{4}He$(\gamma,n)^3$He and the ^{4}He$(\gamma,p)^3$H reactions in the GDR region. The situation was reviewed by Calarco *et al.* in 1983 [97]. They proposed a recommendation of the cross section deduced from the experimental data sets available at that time [139, 147, 148]. The recommendation is shown in Fig. 1.13. If the charge symmetry of the nuclear force holds, the cross section of the mirror reactions behave similar except for corrections due to the Coulomb force. However, in contrast to the (γ,p) cross section, which sharply rises at the reaction-threshold energy and has a pronounced peak structure, the (γ,n) cross section obeys a flatter distribution with a peak height of a half of the (γ,p) cross sections.

1.4.3 Experimental Attempts before 2000s

A serious disagreement of ^{4}He$(\gamma,n)^3$He and ^{4}He$(\gamma,p)^3$H cross sections pointed out by Calarco *et al.* urged many researchers to perform further experimental studies. Hereafter, experimental attempts performed in various methods are shown in the chronological order.

In 1988, Bernabei *et al.* introduced a new kind of beam source, the laser compton scattering (LCS) technique, into the ^{4}He photodisintegration measurement [149]. The LCS technique enabled them to perform the experiment using a mono-energetic beam with smaller amount of background compared to measurements using in-flight-annihilation method. They measured the ^{4}He$(\gamma,p)^3$H cross section in the photon beam energy region between 28.6 and 58.1 MeV by detecting protons from a gaseous He target with a NE213 liquid scintillator. Their cross sections showed flat peak around 30 MeV and disagreed with those of Calarco *et al.* [148]. Their peak structure, however, was similar to the ^{4}He$(\gamma,n)^3$He cross sections recommended by Calarco *et al.* [97] shown in Fig. 1.13. They claimed (γ,p) to (γ,n) cross section ratio estimated from the comparison with that (γ,n) cross sections were about 1 between 28.6 and 42.4 MeV, and there seemed to be no indications of charge symmetry breaking.

Following the results by Bernabei *et al.*, Feldman *et al.* presented their measurement of ^{3}H$(p,\gamma)^4$He reaction for E_p =2.0–15.0 MeV (E_γ=21.3–31.1 MeV) in 1990 [150]. Their results were consistent with those by Bernabei *et al.* [149] but disagreed with those by

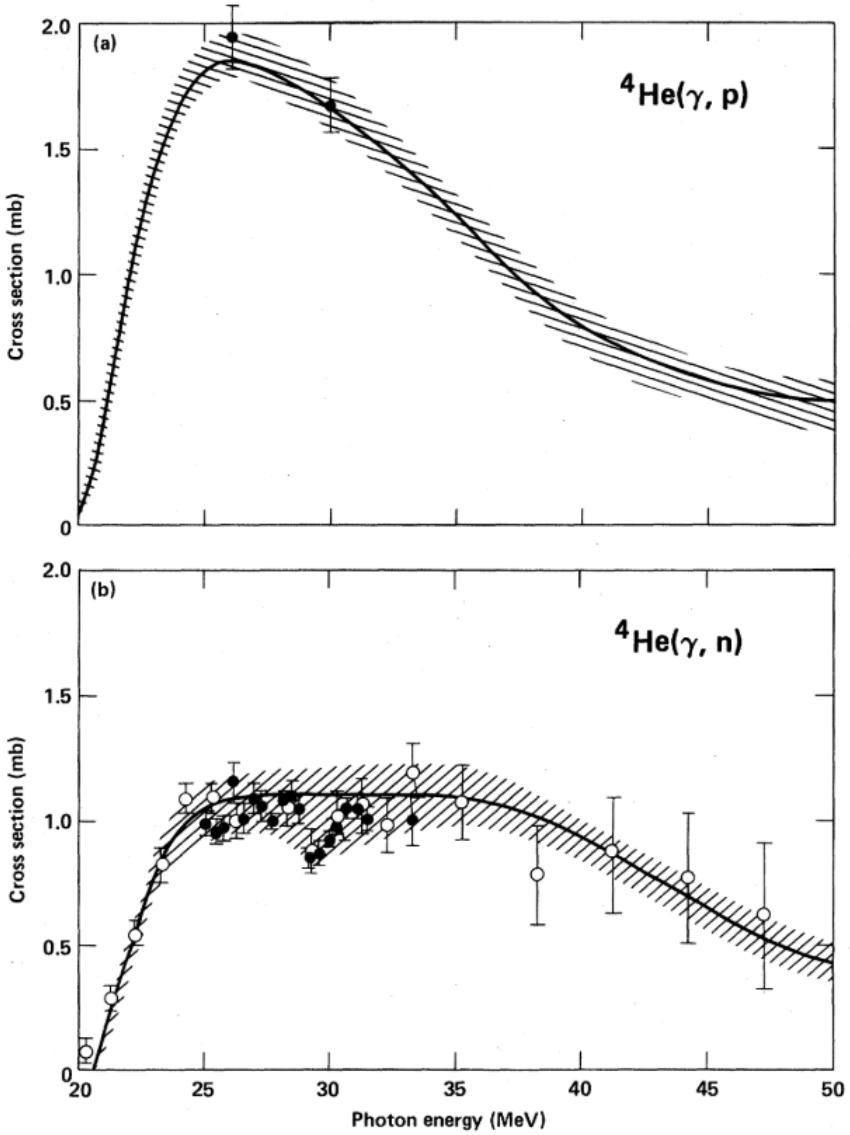

Figure 1.13: ^{4}He$(\gamma, n)^3$He and ^{4}He$(\gamma, p)^3$H cross sections recommended by Calarco *et al.* taken from Ref. [97]. Evaluated cross sections are shown by solid lines, and the shaded bands indicate their estimate of the uncertainty. The experimental data they thought reliable was shown as well: closed circles in (a), open circles in (b), and closed circles in (b) are taken from Calarco *et al.* [148], Berman *et al.* [139], and Ward *et al.* [147]. Among three datasets, ones shown with closed circles (Calarco and Ward) were the data deduced from the inverse-reaction measurements, and one depicted with open circles (Berman) was the data acquired by a photodisintegration measurement.

earlier evaluation by Calarco *el al.* [97] shown in Fig. 1.13. Consequently, they supported the claim regarding the charge symmetry posed by Bernabei *et al.*

Meanwhile, Wells *et al.* took an approach different from previous studies in evaluating the photoabsorption cross sections in 1992 [151]. They measured cross sections of elastic photon scattering off ^{4}He using the tagged photon technique. In the context of the charge symmetry, they pointed out there existed two kind of perspectives: one was standing on the datasets before 1983 [139, 145, 147, 148]. evaluated by Calarco, Berman, and Donnelly (CBD) [97], and the other was based on the (γ, n) cross sections in CBD [139, 147] and the (γ, p) cross sections newly obtained by TUNL (TL) [149, 150]. From the CBD point of view, the (γ, p) cross sections were much larger than the (γ, n) cross sections, and therefore the charge symmetry was broken in this energy region. On the contrary, from the TL perspective, the (γ, p) cross sections was smaller than expected earlier, and the charge symmetry was valid. They compared their results with the sum of (γ, n) and (γ, p) cross sections derived from TL and CBD taking advantage of the relationship between complex forward scattering amplitude and the total photo absorption cross section through the optical theorem and a dispersion relation. They concluded that the TL cross sections were unlikely valid because they were too small compared to their estimation.

Hoorebeke *et al.* presented the result of their measurement of $^4\mathrm{He}(\gamma, p)^3\mathrm{H}$ reactions in the energy between 28 and 33 MeV using bremsstrahlung photon beams in 1993[152]. They compared their cross sections with then-current studies. Their (γ, p) cross sections were consistent with, in the notation by Wells [151], the CBD (γ, p) cross sections [145, 148].

In 1993, Komar *et al.* lowered the lower energy limit of the $^3\mathrm{He}(n, \gamma)^4\mathrm{He}$ cross sections [153]. A ^{3}He gas target was irradiated with fast neutron beams at five energies between E_n =0.14–2.0 MeV (E_γ=20.7–22.0 MeV) produced via the $^7\mathrm{Li}(p, n)^7\mathrm{Be}$. γ-rays emitted from the target were detected with a bismuth germanate oxide (BGO) scintillator. Their cross sections were along with those measured by Berman *et al.* [139] and Ward *et al.* [147] and supported the (γ, n) cross sections recommended by Calarco *et al.* [97].

Hahn *et al.* revisited the $^3\mathrm{H}(p, \gamma)^4\mathrm{He}$ cross sections for E_p=0.1–6.0 MeV (E_γ=19.9–24.3 MeV) [154]. The energy dependence of their cross sections were similar to those by previous studies, which peaked at $E_p \sim 4$ MeV. Regarding the peak hight, their data sets supported earlier data by Perry *et al.* [141], Gemmell *et al.* [143], and Gardner *et al.* [142] rather than newer data by Feldman *et al.* [150].

In short, numerous experimental works motivated by the epoch-making review paper by Calarco *et al.* [97] did not achieve a success in terms of the charge symmetry breaking. A hypothesis that the (γ, p) cross sections were smaller than expected, and as a consequence, the charge symmetry was kept in this reaction had been posed by Bernabei *et al.* [139] and supported by Feldman *et al.* [150] once. However, other measurements performed subsequently [151, 152, 154] multilaterally confirmed that lowered (γ, p) cross sections were unreasonable. These sequence of researches made the situation go back to its start.

1.4.4 Recent Measurements

The puzzling situation regarding the charge symmetry breaking was not settled even in 2000's. Hereafter, recent measurements have been performed since 2000's are reviewed in terms of two perspectives. One perspective is an improved method for the (γ, n) channel measurements. Although the then current experimental results [139, 147, 154] supported the flat (γ, n) cross sections as recommended by Calarco *et al.* [97], several theoretical studies [99, 101] struggled to explain the cross-section discrepancy in vain. Thus, reconfirmation of the (γ, n) cross sections in reliable manners was required in the circumstance. The other point is an importance of the simultaneous measurement of the (γ, n) and the (γ, p) channel. Up to then the cross-section ratio had mainly been argued based on different datasets from experiments performed timely and spatially apart. However, this treatment is possibly problematic, because, in general, experimental results obtained separately has individually different systematic errors that can not be fully controlled. The simultaneous measurement could be a remedy for this issue. That is because part of its systematic errors such as those resulted from the target density, the beam intensity are cancelled in the cross-section ratio. In addition to those two perspectives, determination of the total photo absorption cross sections of ^{4}He is also a valid approach to constrain the (γ, n) and (γ, p) cross sections.

It should be noted that experimental works since 2000's have been performed with mono-energetic photon sources. In terms of the reaction probe, mono-energetic photon beams are more preferable than continuous-energy beams generated with bremsstrahlung since the unfolding procedure can be a source of the systematic errors on the cross sections otherwise stability of the accelerator, sufficient counting statistics, and knowledge of the beam-energy spectrum are guaranteed. The LCS technique enabled one to handle photon beams with far smaller energy spread than bremsstrahlung. Moreover, the bremsstrahlung-tagging technique made it possible to determine energy of bremsstrahlung photon. This enabled one to treat a bremsstrahlung facility as a mono-energetic photon source.

Shima *et al.* 2005 In 2005, a result of the measurement using modern setup was presented by T. Shima *et al.* [115]. Both the ^{4}He(γ, n)^{3}He and ^{4}He(γ, p)^{3}H reactions were simultaneously measured using an active target system based on a time projection chamber (TPC) [155]. In general, a particle detector whose detection medium is also served as the reaction target is called an active target. In this case, the He gas filled in the TPC played not only a role of the operation gas of the gaseous detector but also a target of the photodisintegration reaction. This mechanism contributed to lower the instrumental low-energy-limit of charged-particle detection. They measured the trajectories of charged-decay particles and their energy depositions in the target medium.

Their experiment was performed at the TERAS electron storage ring in the AIST facility [156]. Quasi-monochromatic photon beams were generated using the Laser Compton scattering technique in the intensity of 10^4 photons per second. The photon beams were directed to the TPC filled with a mixed gas of 80% He and 20 % CH_4 with a total pres-

sure of 1000 Torr. The reaction cross sections at the beam energy of E_γ = 22.3, 25, 28, 32 MeV were examined. Their data sets are plotted with open circles in Fig. 1.14 and compared with results by then-current experimental and theoretical studies.

As seen in Fig. 1.14, their cross sections of the (γ, n) and the (γ, p) reactions didn't peak within their measurement energy region. Their cross sections ratio $\sigma(\gamma, p)/\sigma(\gamma, n)$ were consistent with 1 except for one beam energy near the reaction threshold, and no onset of the charge symmetry breaking were observed in their dataset. However, their results were contradictory to those by any other experimental studies so far. They claimed the validity of their method was proved by the accordance between their $^2\mathrm{H}(\gamma, p)n$ and $^4\mathrm{He}(\gamma, pn)^2\mathrm{H}$ cross sections and the literature values. Moreover, they published their preliminary results of a follow-up measurement in 2010 [117]. The newly presented result was consistent with the former datasets and implied the $^4\mathrm{He}(\gamma, n)^3\mathrm{He}$ and $^4\mathrm{He}(\gamma, p)^3\mathrm{H}$ cross sections became maximum at around E_γ =32–33 MeV.

Shima *et al.* had deliberately planned their experiment based on a number of previous studies, and their experimental set up has clear advantages compared to the previous ones. Therefore, the discrepancies between their datasets and the results by other experimental and theoretical studies posed a new issue in the research field.

Nilsson *et al.* 2005 New result of the $^4\mathrm{He}(\gamma, n)^3\mathrm{He}$ cross section measurement was reported by Nilsson *et al.* in 2005 [158]. They remarked that the few studies about the near-threshold (γ, n) cross sections were published [115, 153] and performed the measurement with energy-tagged bremsstrahlung photons from E_γ = 23 – 42 MeV at the MAX-lab facility [159]. Subsequently, they published a full article including the result up to E_γ = 70 MeV in 2007 [119].

Quasi-mono-energetic photon beams were generated by post-bremsstrahlung-electron tagging. Energy of a bremsstrahlung photon was reconstructed from the momentum of the corresponding post-bremsstrahlung electrons measured with a magnetic spectrometer. Single count rate of the tagging counter was 0.5 MHz in average, and the tagging efficiency was about 25%. The photon beams were directed to a liquid He target. Photoneutrons from the target were detected with a liquid scintillator array located 2.6 m away from the target. Neutrons were discriminated from other particles by means of its time-of-flight and the pulse-shape discrimination technique.

Their results are shown in Fig. 1.15. A clear resonance peak structure was observed in their data around E_γ = 28 MeV. This trend could be connected smoothly with the low-energy data set by Komar *et al.* [153] but was contradictory to the data sets by Shima *et al.* [115, 160] and the CBD evaluation [97] in the energy region below 30 MeV. Up to the resonance region, two theoretical calculations shown in Fig. 1.15 were in good agreement with their cross sections. Their cross sections indicated the possibility that the (γ, p) to (γ, n) cross-section ration in the GDR region was approximately equal to unity because the (γ, n) cross sections were larger than as expected since Calarco *et al.* [97].

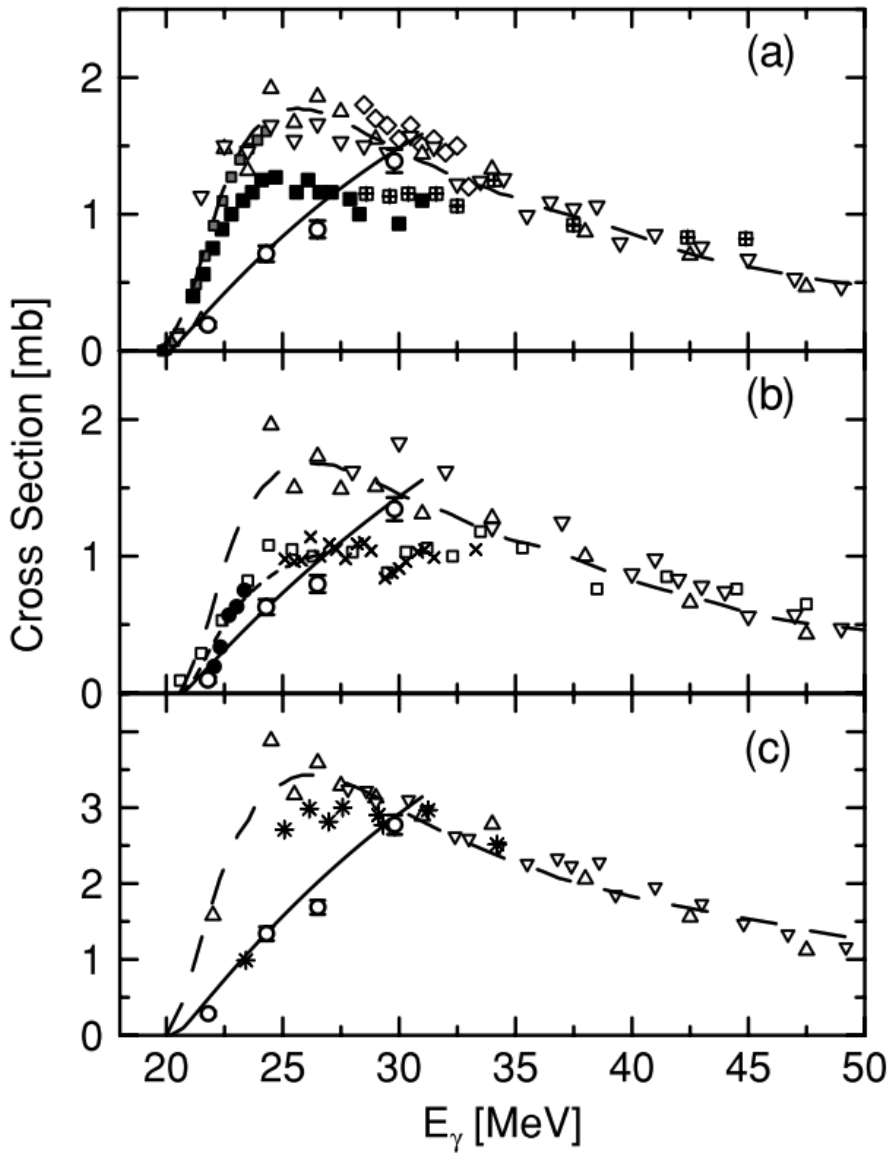

Figure 1.14: ^{4}He photodisintegration cross sections evaluated by Shima *et al.* taken from Ref. [115]. Their datasets are shown in open circles, and the solid curves are the most probable functions of the cross sections obtained from their analysis. (a) (γ, p) cross sections. The data taken by Gorbunov [128, 130] (open upward triangles), Arkatov [137] (open downward triangles), Bernabei [149] (crossed squares), Feldman [150] (filled squares), Hoorebeke [152] (open diamonds), and Hahn [154] (Gray squares) are presented. (b) (γ, n) cross sections. The data taken by Gorbunov [129, 130] (open upward triangles), Arkatov [137] (open downward triangles), Berman [139] (open squares), Ward[147] (diagonal crosses), and Komar [153] (filled circles) are presented. (c) Total photoabsorption cross sections. The data taken Gorbunov [157] (open downward triangles), Arkatov [137] (open downward triangles), and Wells [151] (asterisks) are presented. Theoretical cross sections presented in Ref. [108] and Ref. [102] are also shown in the long-dashed curves and the short dashed-curve, respectively.

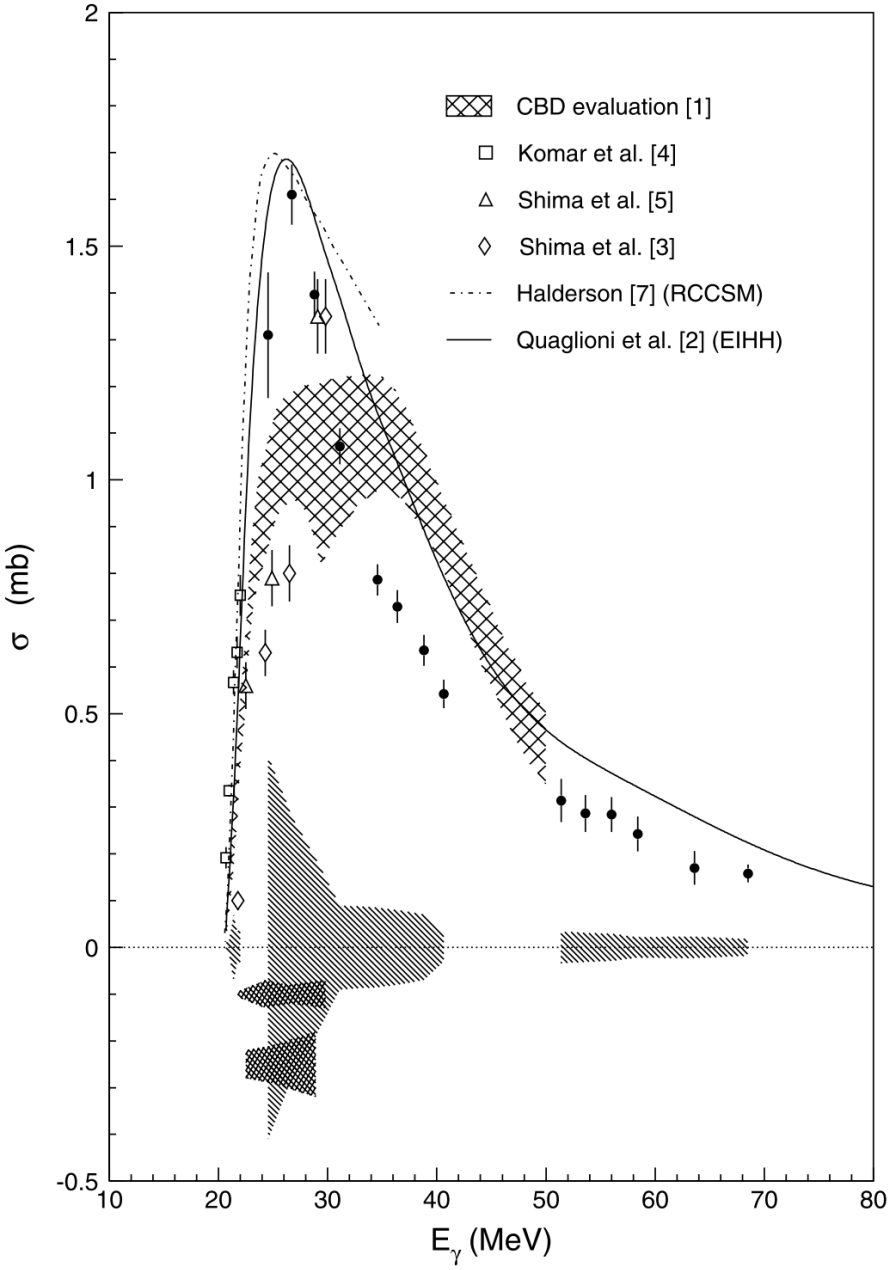

Figure 1.15: ^{4}He$(\gamma, n)^3$He cross sections reported by Nilsson *et al.* taken from Ref. [119]. Their data are shown in closed circles. A cross-hatched region is the cross section evaluated by Calarco, Berman, and Donnelly (CBD) [97]. The data from Komar *et al.* [153], Shima *et al.* in 2001 [160], Shima *et al.* in 2005 [115] are plotted in open squares, open triangles, and open diamonds, respectively. The results of theoretical cross sections are shown with lines: recoil corrected continuum shell model (RCCSM) calculation [161] (dashed-dotted line); effective interaction hyper-spherical harmonic (EIHH) expansion calculation [108] (solid line). The statistical and systematic uncertainties associated with each experimental data are represented by error bars and bands at the bottom of the panel.

Nakayama *et al.* 2007 In 2007, a new constraint on the ^{4}He photodisintegration cross sections was given by Nakayama *et al.* [162]. They deduced the photoabsorption cross section of ^{4}He via the ^{4}He(^{7}Li ^{7}Be) reaction.

The experiment was performed at the Research Center for Nuclear Physics, Osaka University. A He gas target was irradiated with ^{7}Li beam at an energy of $E = 455$ MeV. Scattered ^{7}Be particles were momentum analyzed with the Grand RAIDEN spectrometer [163] and detected with focal plane detectors. The spin transfer ΔS through the ^{4}He(^{7}Li ^{7}Be) reaction was tagged by measuring the gamma transition between the first excited state (1/2-, 0.43 MeV; ^{7}Be$_1$) and the ground state (3/2-; ^{7}Be$_0$) of the scattered particle. The ^{7}Be$_0$-final-state is populated through the transition with either ΔS=0 or ΔS =1, whereas the ^{7}Be$_1$-final-state is excited by the reaction with ΔS=1. In addition, the angular distribution of the differential cross sections was attributed to the transition with a orbital angular momentum transfer ΔL=1. Thus, the reaction to the final state with a ^{7}Be$_1$ was interpreted as the transition to the ^{4}H in the state which was analogue to the spin-dipole-resonance (SDR; ΔL=1, ΔS=1), and that to the final state with a ^{7}Be$_0$ was, on the other hand, attributed to the superposition of the transitions to the state analogue to the SDR and the GDR (ΔL=1, ΔS=0). By substituting the excitation functions obtained with the ^{7}Be$_1$ tagging from the singles spectrum, the $E1$ photoabsorption cross sections of ^{4}He was derived from the proportionality between the double differential cross section $d^2\sigma/d\Omega dE$ and the electric transition probability $dB(E1)/dE$.

The photoabsorption cross sections presented by Nakayama *et al.* are shown in Fig. 1.16. According to their result, the photoabsorption cross sections have a pronounced peak due to the GDR at $E_x \sim 27$ MeV. Their results were in good agreement with the recommended cross sections by Calarco *et al.* [97] and the twice of the (γ, n) cross sections by Nilsson *et al.* [158]. However, they were in serious contradiction with the result given by Shima *et al.* [115].

Raut *et al.* and Tornow *et al.* 2012 In 2012, the (γ, n) and the (γ, p) cross sections measured with the identical setup were published by Raut *et al.* [116] and Tornow *et al.* [118]. The measurement was conducted in the HIγS facility with a high-pressure ^{4}He-Xe gas scintillator [164], which was an active target.

A mono-energetic photon beams were produced via Compton back-scattering of free-electron laser photons from relativistic electrons in the Duke University electron storage ring [165] and directed to the active target in a typical flux of 10^6 /s. The mixture ratio of the gas component in the active target was optimized correspondingly to the beam energy and the reaction channels with keeping the total pressure of 51 atm. Thanks to the high filling-pressure of the active target, the charged particles resulting from the beam irradiation were stopped within the target vessel with a diameter of 5.1 cm. From the total energy deposition by charged particles in the final state, the photodisintegration events were clearly discriminated from the background events caused by Compton scattered electrons. Moreover, the (γ, n) events and the (γ, p) events were mutually distinguishable as well. The thick target and intense beam allowed them to obtain statistically high-

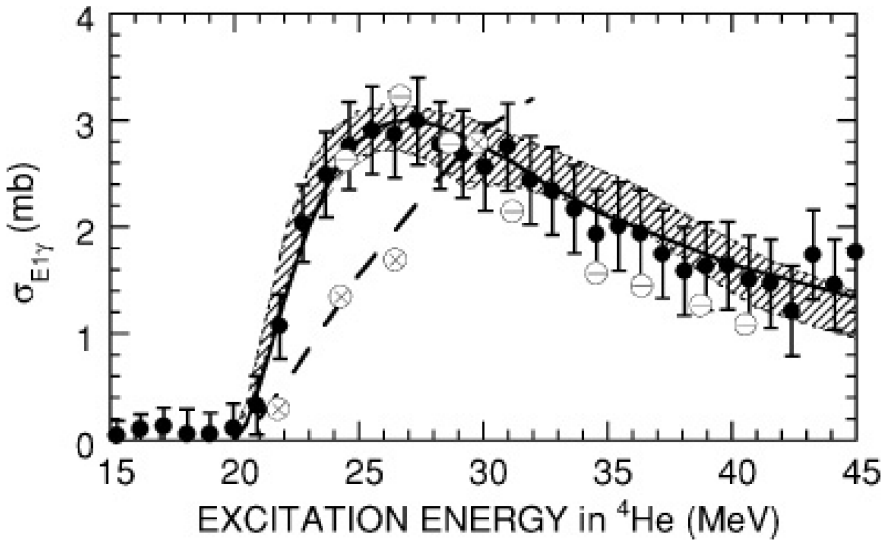

Figure 1.16: $E1$ photodisintegration cross sections evaluated by Nakayama *et al.* taken from Ref. [162]. Their results are shown in closed circles. The hatched area is the sum of (γ, n) and (γ, p) cross sections recommended by Calarco *et al.* [97]. The photoabsorption cross sections measured by Shima *et al.* [115] ($\otimes$) and the doubled (γ, n) cross sections obtained by Nilsson *et al.* [158] ($\ominus$) are also depicted. The dashed curve is a guide to the eye drawn for the dataset by Shima *et al.*, and the solid line indicates the theoretical calculation by Gazit *et al.* [109].

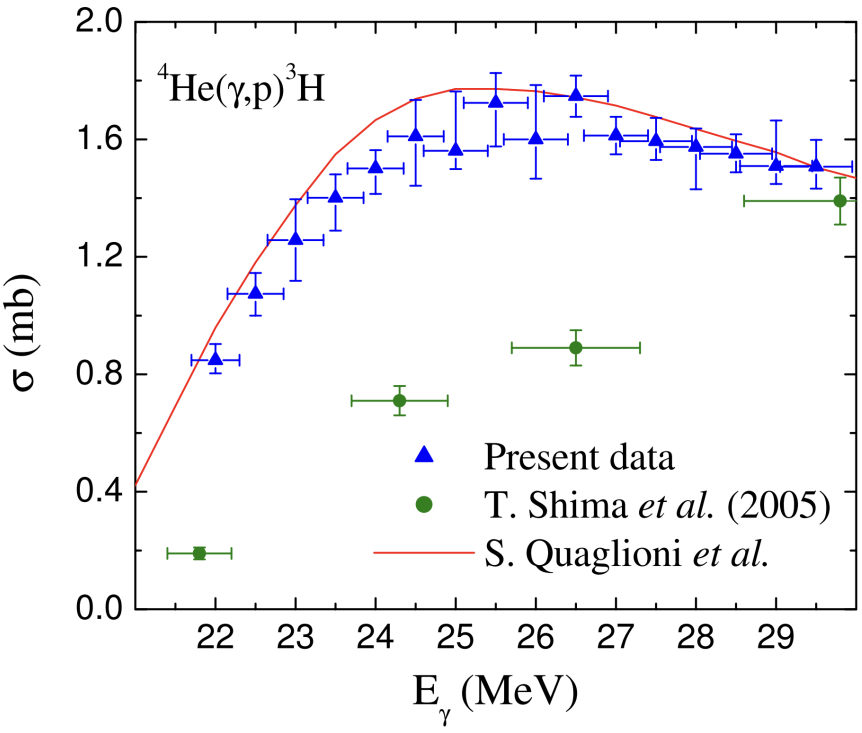

Figure 1.17: ^{4}He$(\gamma, p)^3$H cross sections evaluated by Raut *et al.* taken from Ref. [116]. Their results are shown with upward triangles and the data set given by Shima *et al.* [115] are also represented with closed circles. The line indicates the theoretical calculation by Quaglioni *et al.* [108].

precision data.

Their ^{4}He photodisintegration cross sections are shown in Fig. 1.17 and Fig. 1.18. They were in good agreement with the theoretical prediction of Quaglioni *et al.* [108] that had a pronounced GDR peak at 26 MeV. Consequently, they were inconsistent with the data given by Shima *et al.* [117]. It should be noted that they did not report the cross sections of the (γ, n) reactions below 27.0 MeV. Therefore, one can not conclude the energy dependence of the cross sections of the (γ, p) and (γ, n) channels solely from their result.

1.5 Aim of Present Work

Photodisintegration of ^{4}He nucleus in the GDR region is theoretically somehow tractable due to its few body nature and the long wave length approximation, and simultaneously could be a key input for models of the several astrophysical phenomena. Recent advancement of *ab initio* calculation made it possible to treat this phenomena by means of a realistic nuclear interaction based on well controlled manners. Supported by knowledge

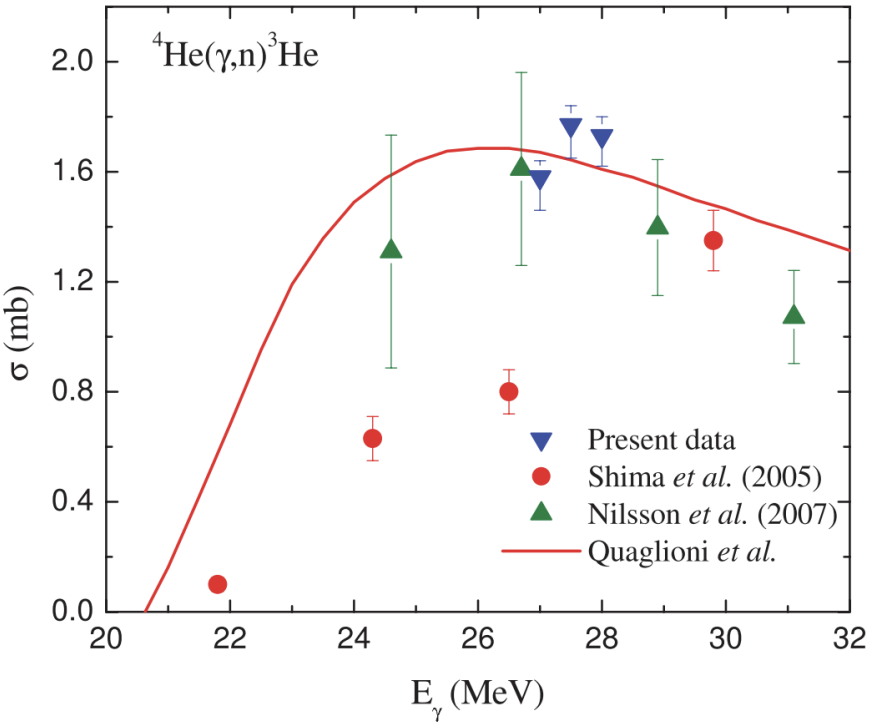

Figure 1.18: ^{4}He$(\gamma, n)^3$H cross sections evaluated by Tornow *et al.* taken from Ref. [118]. Their results are shown with downward triangles. The data sets obtained from the previous studies by Shima *et al.* [115] (closed circles) and Nilsson *et al.* [119] are also depicted. The line indicates the theoretical calculation by Quaglioni *et al.* [108].

accumulated so far, results from state-of-the-art calculations regarding the ^{4}He photodisintegration are reaching a consensus.

On the other hand, the situation regarding experimental photodisintegration cross sections of ^{4}He nucleus is still controversial. As for the recent results obtained with monoenergetic photon beams, all but one data are in accordance with the theoretical consensus. The measurement resulting in the distinctive cross sections, which was performed by Shima *et al.*, was planned deliberately and implemented with a highly versatile detector system based on TPC. Moreover, the validity of the data was also verified with the different reaction channels. Thus, it is hard to point out any flaws in their work, and there is no reason not to treat this result on an equal basis with others.

In view of the contradiction among the experimental results and potential tension between theoretical and experimental studies, we planned a new experiment presented in this thesis. The aim of the new measurement is publishing the new exclusive cross sections of the $^4\mathrm{He}(\gamma, n)^3\mathrm{He}$ and the $^4\mathrm{He}(\gamma, p)^3\mathrm{H}$ reaction evaluated in a solid manner, and give a criteria to discuss on the discrepancy. In order to achieve the purpose, this measurement was performed in the similar but improved fashion to the work by Shima *et al.*

First, the present measurement was also done with the active target system based on TPC. However, its sensitivity to short-range particles such as ^{3}He was improved because of following points. Thanks to the introduction of the micro-pixel chamber (μ-PIC), the pitch of read-out electrodes increased up to 400 μm, which was formerly 2 mm. In addition, the target thickness was optimized depending on beam energy to keep the particle trajectories visible.

Second, quasi-monoenergetic photon generated using the laser Compton scattering (LCS) method was similarly utilized as a beam for the experiment. Present experiment was performed at the next generation LCS facility, namely NewSUBARU. The performance of the beam source, such as the intensity and energy spread, was more highly specified compared to the facility constructed in former times. Moreover, auxiliary apparatuses, such as the beam monitor, were better than that used in the previous research.

In the following chapters, details of the experiment and the analysis will be explained. Then, the differential and total cross sections obtained from the present study will be presented. Finally, these results will be compared with the previous experimental and theoretical results.

Chapter 2

Experimental Setup

The experiment was carried out at the BL01 beam line in the NewSUBARU synchrotron radiation facility. Photon beams generated with Laser Compton Scattering (LCS) were irradiated on the MAIKo active gas target system. ^{4}He nuclei in MAIKo absorbed incident photons and decayed via photodisintegration process. We employed the MAIKo active target to measure charged particles emitted from the decay. Throughout the measurement, beam flux punched through MAIKo was monitored using an NaI (Tl) scintillation detector at downstream. The details of the experimental setup are described in this chapter.

2.1 BL01 NewSUBARU

2.1.1 NewSUBARU Synchrotron Radiation Facility

NewSUBARU [166] is a synchrotron radiation facility constructed in the SPring-8 site [167]. This facility is constructed as a light source in Extreme Ultraviolet (EUV) to soft X-ray region. Photon provided by the NewSUBARU facility offers opportunities for researches in various fields, such as micro-machining, investigations of new materials, and X-ray microscopy. The layout of the facility is shown in Fig. 2.1.

The main facility of NewSUBARU is the 1.5 GeV electron storage ring. The parameters of the storage ring are summarized in the Table 2.1. The storage ring has the form similar to race track, which consists of the two straight section between the curved sections. The circumference of the storage ring is 119 m long, and the straight sections are 14 m long. An undulator and an optical klystron are installed as insertion devises at the straight sections. Electron beams accelerated in the SPring-8 injector LINAC are delivered to the storage ring at the energy of 1 GeV. By using the RF cavity in the storage ring, electron beams are accelerated or decelerated on demand to the energy between 0.5 GeV and 1.5 GeV. The absolute value of the electron beam energy is well calibrated in the accuracy of 10^{-5} [169].

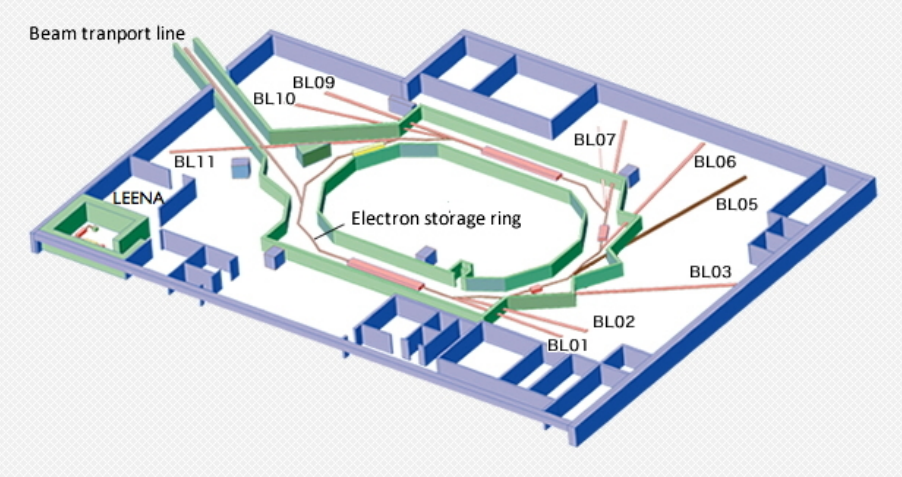

Figure 2.1: Bird's-eye-view of the NewSUBARU synchrotron radiation facility taken from Ref. [168]. Electron beam is provided via the beam transport line toward the electron storage ring show at the center. Wide energy range of photons generated with various techniques, such as the synchrotron radiation, undulation, and the laser Compton scattering, by means of the electron beam stored in the ring are delivered apparatuses placed on the numbers of beam lines from BL01 to BL11.

Table 2.1: Specifications of the storage ring in the NewSUBARU [168].

Injection energy	1 GeV
Stored current	<500 mA
Circumference	118.731 m
RF frequency	499.955 MHz
Harmonic number	198
Bunch length (σ)	33 ps (Normal operation)

This facility offers two modes of operation: one is top-up operation mode, and another is decay mode. In the top-up operation, electron beams are continuously injected from the LINAC during the operation to keep the stored current 220 mA. This mode is only capable for the 1.0 GeV operation, whereas beams with energy other than 1.0 GeV can not be stored in the top-up mode since accelerated or decelerated beams can not be refilled from the LINAC. Therefore, these beams are handled in the decay mode, instead. In the decay mode operation, beams with energy of 1.0 GeV from the LINAC are accumulated up to 400 mA, and its energy is ramped up (down) to the desired value. Due to various reasons, the beam current decays exponentially in a typical life time of 10 hours (18 hours for 1.5 GeV 100 mA).

There are eleven radiation-photon beam lines (BL01 – BL11) around the NewSUBARU storage ring. Synchrotron radiation produced at the bending magnet and insertion devises are utilized as light sources at ten out of eleven beam lines (BL02 – BL11). The radiations produced with bending magnets have continuous energy distributions ranging from IR to soft X-ray, and those produced with the insertion devises have narrower energy distributions in lower energy region. Among the beam lines in the NewSUBARU facility, BL01 has the unique feature. Here, a quasi-monochromatic gamma-ray beam generated by laser Compton scattering (LCS) is available.

2.1.2 BL01

BL01 [170] is the only beam line designed for gamma-ray beam production in the NewSUBARU facility. It is located on the extension of one of the straight line of the storage ling. A schematic drawing of BL01 is shown in Fig. 2.2. The experimental setup for the present study is also drawn. In the BL01 beam line, gamma-ray beams are generated from relativistic electron beams and visible (or infrared) laser photons by using the laser Compton Scattering (LCS) technique.

Laser Compton Scattering

The Laser Compton Scattering (LCS) technique is a powerful method that can be utilized to obtain intense photon beams with small energy and angular spread. As seen in a conceptual diagram of LCS shown in Fig. 2.3, the head on collision of electron and laser photon is used in this technique.

In the case of head on collision between a relativistic electron and a laser photon, energy of photon (E_γ) scattered to very-backward angle ($\theta \sim 0$) is approximated as

$$E_\gamma = \frac{E_L\gamma^2/(1+R)}{1+\gamma^2\theta^2/(1+R)}, \qquad R = \frac{4E_L\gamma}{m_e c^2}, \tag{2.1}$$

where E_L, γ, θ are the laser photon energy, the Lorentz factor of an electron, and the angle of scattered photon measured from electron beam axis respectively. Here, m_e and

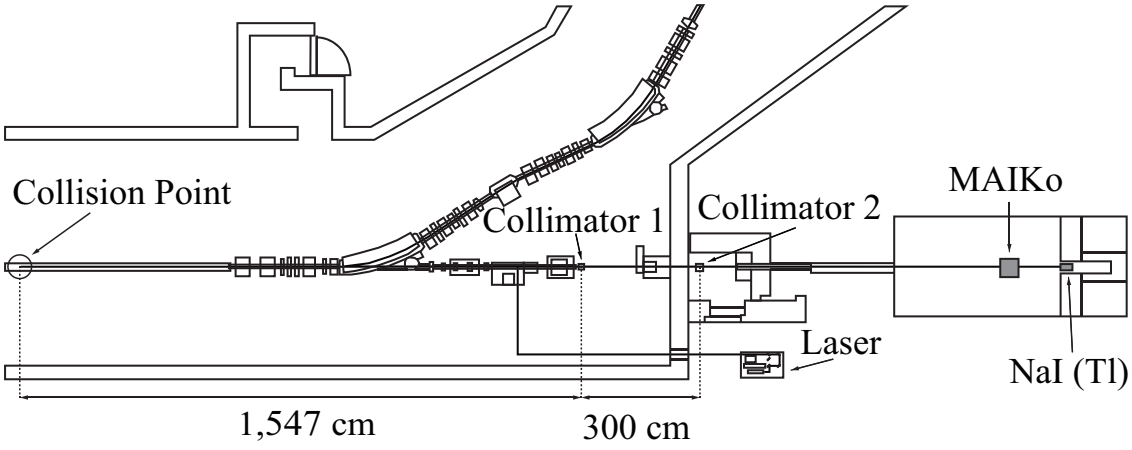

Figure 2.2: Top view of the BL01 beam line at NewSUBARU synchrotron radiation facility taken from Ref. [1]. Infrared photon beams generated with the $NdYVO_4$ laser modules were guided into the electron storage ring after two times of reflections. Back-scattered photons off head-on collision with relativistic electron beams coming from left were straightly guided to the experimental hatch at the right most of the figure in which the MAIKo active target and the NaI (Tl) beam monitor were installed. On the way to the hatch, photons were sieved with the two collimators to be monochromatic photon beams.

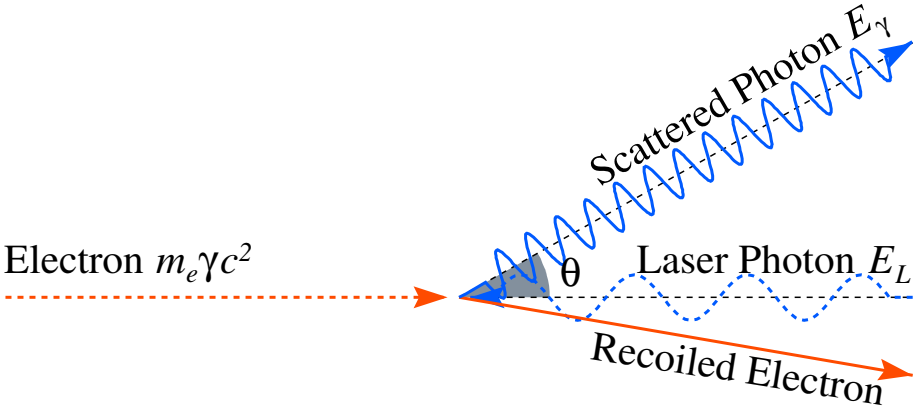

Figure 2.3: Laser Compton scattering (LCS) in the laboratory frame. An incident electron and laser photon are shown in the red dotted line and blue dotted wavy line. The scattering angle of the photon θ is defined with respect to the direction of the incident electron.

c denote the rest mass of electron and the speed of light. This formula means the energy of incident photon is amplified after the Compton scattering. The energy amplification factor in the typical experimental condition is large enough (on the order of 10^6 – 10^7) to create MeV-gamma-ray from the laser photons with an energy order of eV.

According to Eq. (2.1), the value of E_γ depends on θ and become maximal when $\theta = 0$. Thus, it is important to select the photons scattered to very backward angle ($\theta \sim 0$) for producing the gamma-ray beams of narrow energy spreading. This condition is realized by collimators placed on the way of scattered photon sufficiently apart from the collision point.

Beam Line Elements

The beamline elements drawn in Fig. 2.1 are explained along the beam generation sequence. As for the primary photon generator, various laser modules are available depending on the purpose in BL01. In the present measurement, the Nd:YVO_4 laser module was user for the primary photon generation. The wave length of photon from Nd:YVO_4 is 1064 nm, which corresponds to 1.165 eV, and the maximum power of the laser module is 30 W. The oscillation of the laser module synchronized with square wave pulses of 8 ns width repeated in 20 kHz. Moreover, the laser was repeatedly operated with an cycle of 80 ms on amd 20 ms off. This corresponded to a duty cycle ratio of 80%. Namely, the averaged frequency of laser pulse was 16 kHz.

Photons generated by the laser module were linearly polarized with nearly 100% polarization. The polarization vector of the laser photon can be rotated by a half-wave plate directly downstream of the laser output port. Thereby, nearly 100% linearly polarized photons of arbitrary polarization direction were obtained. From the view point of tracking efficiency of the MAIKo active target, photons linearly polarized in the direction tilted 10 degrees from the vertical axis were mainly used for the present experiment. Because the polarization of the LCS γ rays is maximum at the scattering angle of 180° [171], highly polarized beams were obtained at the GACKO beam hutch.

Photons led through the half-wave plate were, then, transported by the mirrors toward the storage ring. Finally, photons were injected into the vacuum duct to a collision point in the straight section in the storage ring. Photons back scattered at the collision point were employed as gamma-ray beam. The alignment of the optical elements were checked by using the He-Ne laser beam. We confirmed that the He-Ne laser beam send from the opposite side of the straight section was led through the straight section and the mirror system in the opposite direction onto the output port of the Nd:YVO_4 laser.

As shown in Fig. 2.1, the two collimators were consecutively installed on the extension of the straight section. These collimator was made from thick lead slab, and the diameters of their circular aperture on their center were 3 mm and 2 mm respectively in the order from the upstream of the beam. The one in the downstream, which was located 1847 cm away from the collision point, effectively limited the scattering angle of photons. The alignments of the collimators were optimized by tuning the x-y position and the tilt of

the collimators to the conditions that the maximal beam intensity was achieved.

The instruments for the measurement were installed in the GACKO (Gamma collaboration hutch of Konan University) beam hutch behind the collimators. For the present experiment, the MAIKo active target was introduced in the GACKO hutch. In addition, the NaI (Tl) scintillation detector based beam monitor was placed just before the radiation shield at the end of the hutch.

Beam Monitor

Gamma ray beams punched through the MAIKo active target were measured using the beam monitor at the downstream end of the GACKO beam hutch. A large cylindrical-shaped NaI (Tl) detector was employed as the beam monitor. The dimension of the detector was 6 inches (15.24 cm) in diameter and 12 inches (30.48 cm) thick, which is sufficiently large compared to the radiation length (2.588 cm) and the Molière radius (4.105 cm) of NaI [8].

Scintillation light from the NaI (Tl) crystal was collected by four photomultiplier tubes (PMT) fixed on the backend of the crystal. Charge outputs from the PMT were first amplified by preamplifiers (Model 113, ORTEC), then combined by a sum and invert amplifier (Model 533, ORTEC), and finally pulse-shaped by a spectroscopy pile-up amplifier (Model 572A, ORTEC).

Pulse height of processed signal was recorded by a high rate multi channel analyzer (APU8208, Techno AP). The input-signal dynamic range of the MCA was 0 – 10 V, and the resolution of ADC was 16 bits. The amplifier gain was selected so that the largest signal pulse did not exceed the dynamic range of the MCA.

2.1.3 Beam Conditions

Present measurement was performed with the six different beam energies. The summary of the beam energy is shown in Table 2.2. The electron beam energy (K_e) shown in the table is the calibrated one based on the formula in Ref. [169], where systematic deviation of nominal beam energy from the true value was corrected. The gamma-ray energy (E_{max}) is maximum energy in the energy spectrum. These conditions were selected to cover the energy region where the results of previous studies contradicts.

Bunches of gamma-ray beam arrived in a frequency of 16 kHz, which is the average frequency of laser pulse. In a typical operation condition od the present measurement, several to a dozen photons were contained within a beam bunch. Namely, the intensity of the gamma-ray beam was few ten to few hundred kHz.

The storage ring was operated in the decay mode because beams with energy other than 1 GeV were required for the present measurement. Electron beams injected from the LINAC were accelerated in the storage ring to the desired energy. After the accel-

Table 2.2: Beam energy condition of the present measurement. K_e, λ, E_{max} denotes the kinetic energy of electron beam, the wave length of the laser, and the maximal energy of the gamma-ray beam.

	K_e (MeV)	λ (nm)	E_{max} (MeV)
1	1145.90	1064	23.0
2	1170.81	1064	24.0
3	1195.14	1064	25.0
4	1242.55	1064	26.0
5	1265.77	1064	27.0
6	1310.98	1064	30.0

eration process, the current in the storage ring gradually decayed in a life time of a few hours. Beam instability sometimes caused sudden loss of beam current by half during the acceleration or the measurement. While the measurement, the current of electron beam in the storage ring was between 50 and 300 mA. When the current become lower than about 50 mA, we discarded the remaining beam in the storage ring to the beam dump and resumed beam injection process.

The laser module was operated at a power of approximately 10–20 W. As the electron current decreased, the laser power was adjusted to compensate for decrease of electron current. The power was limited to the extent that optical devices are not heated too much. This was because thermal deformation of the mirrors caused decrease of the transport efficiency of laser photons, and consequently the photon beams.

2.2 MAIKo Active Target

2.2.1 Overview

We developed the Time Projection Chamber (TPC) based target system named MAIKo. The schematic view of the MAIKo active target is shown in Fig. 2.4. The system is a type of the detector commonly known as the active target, where the medium of the detector also plays a role of the reaction target. As for the MAIKo active target, the gas mixtures whose main component is the target of nuclear reaction are employed as the detection gas of the TPC. The MAIKo active target is very versatile enough to operate with various compositions of gas mixtures of a various thicknesses: for instance, the detector performances with He (93%) + iso-C_4H_{10} (7%) at 430 hPa [172], He (93%) + CO_2 (7%) at 430 hPa [172], He (98%) + CF_4 (2%) at 2000 hPa [173], H_2 at 1000 and 1500 hPa [174], H_2 (86%) + CH_4 (14%) at 1450 hPa [174], He (96%) + CO_2 (4%) at 500 and 1000 hPa [175], and H_2 (90%) + iso-C_4H_{10} (10%) at 100 hPa [176] were studied so far. The detector is sensitive to the charged particles going through the cubic-shaped volume shown in Fig. 2.4. When the beam injected into the sensitive volume triggers the desired reaction with the target nuclei inside, the scattered, recoiled, and decay particles from the

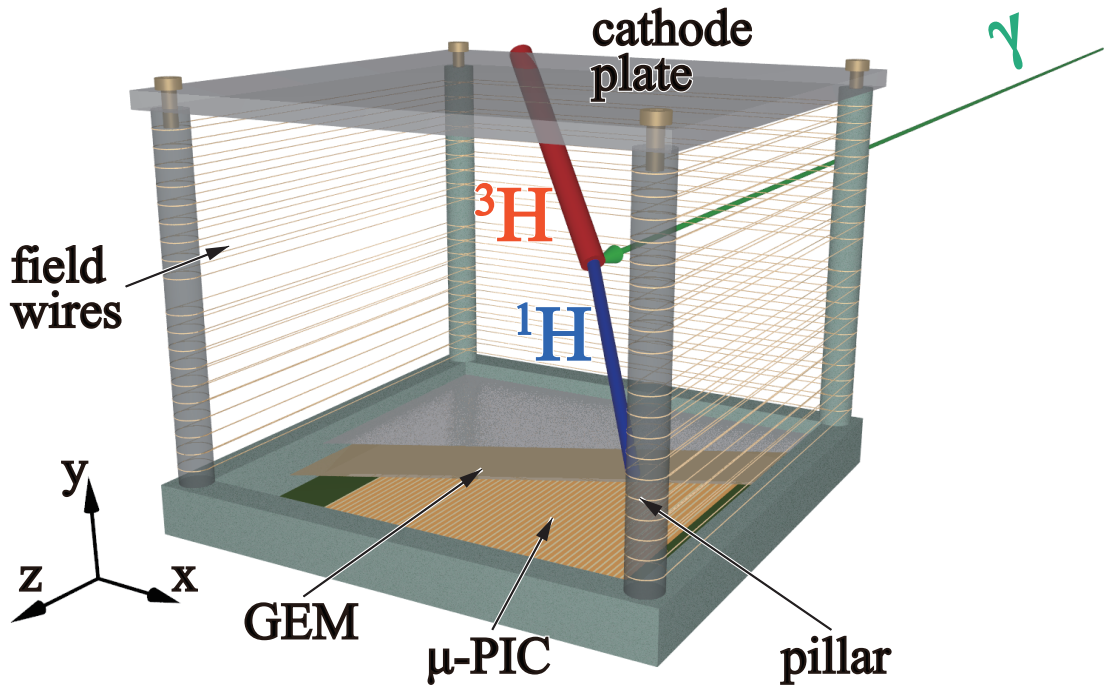

Figure 2.4: Schematic picture of MAIKo active target taken from Ref. [1]. This figure displays a typical ^{4}He (γ, p)^{3}H event, in which a ^{4}He nucleus absorbs a photon (thin green arrow coming from the opposite direction) to break up into a proton (the thickest red line) and a ^{3}H (thicker blue line). Electrons generated along the trajectories of the decay particles were drifted with the uniform electric field to the μ-PIC at the bottom. For good visibility, potential wires on the front side and the lower half of GEM are not drawn in the figure.

reaction were detected by MAIKo. This detector was originally developed to perform missing-mass spectroscopy of unstable nuclei, and we have successfully performed the measurement of alpha-(in)elastic scattering off ^{10}C with MAIKo [175].

There are two major advantages of the active target system in terms of decay particle measurement. First, it lowers the detection limit of the low energy particles. This factor is critical in the measurement of both photodisintegration and scattering under inverse kinematics condition. Especially in case of the photodisintegration study, the detection limit of low energy particle constrains the accessibility to the low energy region near the reaction threshold. In the case of conventional gaseous target, target gas is filled in a container having a pair of windows which is hermetically sealed with thin films, and the decay particle detectors are installed outside the window. Therefore, lower-energy charged decay particles can not reach the detector because they lose all of their kinetic energy as they penetrate the target and encapsulating material. In contrast, the use of active target allows measurement to be made without the influence of materials in between. Second, it improve the geometrical detection efficiencies. In the conventional case, the angular coverage of the particle detector is limited, which decrease the detection efficiency of decay particles. By using active target, all the areas around the reaction point can be covered by the sensitive volume. Thus, a full solid-angle detection acceptance is ideally realized.

As stated earlier, MAIKo is operated as a TPC. TPC is a gaseous tracking device, which allows one to reconstruct the three-dimensional trajectory of charged particles passing through the sensitive volume. When a charged particle traverses the drift region of MAIKo, it ionizes target gas molecules and form electron cloud along its path. These Electrons are guided by strong electric field applied in the drift region. Thanks to the uniformity of the electric field, electrons are led downward to the multiplication region in the MAIKo without changing their relative positions. Electrons arrived to the multiplication region are amplified via avalanche multiplication process firstly at gas electron multiplier (GEM) [177], then at micro pixel chamber (μ-PIC) [178]. The electric signals induced on electrodes in the μ-PIC are readout via dedicated circuits named the Iwaki board [179].

2.2.2 Detector Structure and Readout

Structure The detectors shown in Fig 2.4 is installed in a stainless-steel vacuum chamber with a volume of approximately 30L, which is filled with the detection gas. In the present experiment, the gas mixtures composed of He + CH10 at 500, 1000, 2000 hPa were used as the detection gas. There exist apertures on upstream and downstream side of the chamber, which are entrance and exit windows for the beam. Thin films of 125 μm-thick Kapton®seal the aperture and insulate the chamber from the atmosphere.

The volume of the sensitive volume of MAIKo is 100 $\times$ 100 $\times$ 110 mm^3 in the order of width, depth, and height. The width and depth are limited by the area of GEM, and height are defined by the height of the drift cage. The supporting frames for the drift

cage are made from glass epoxy laminate (G10). In order to reduce the deterioration of the detector performance due to outgassing from detector materials, the gas mixture in the detector are constantly replaced by the gas circulation system. The detail of the gas handling system is explained later.

Fig. 2.5 shows the electric circuit of the MAIKo active target. The sensitive volume is the area between the cathode plate and the grid mesh. Electrical connection between detector elements are depicted schematically.

Drift cage The sensitive volume of MAIKo is surrounded by the drift cage. The drift cage was optimized and newly constructed for the present experiment, which was smaller than tha employed in the previous experiment [175] with respect to its height . The outer dimension of the drift cage is 151 $\times$ 151 $\times$ 115 mm^3, in the order of width, depth, and height. The top and bottom of the drift cage are defined by the cathode plate and grid mesh. The dimension of the cathode plate is 151 $\times$ 151 $\times$ 5 mm^3, and its surface was buff-polished to avoid electric discharges from fine scratches on the plate. The grid mesh is composed of the wire with a diameter of 150 micro meter aligned in the interval of 0.85 mm. The mesh was pasted on an outer frame made of The electric field formed around the grid mesh behave like a semipermeable membrane for electrons and ions. In other words, it allows electrons produced in the sensitive volume to pass through and blocks ions produced in the GEM and the μ-PIC.

The distance between the cathode plate and the grid mesh, which defines the height of the sensitive volume, is kept at 110 mm by the for pillars standing at the corner of the cathode plate. The pillars are cylindrical shape with crosswise grooves curved in the side at 5 mm interval. Field wires are doubly wound onto the grooves on the pillars. The wires are made from Be-Cu and 125 μm in diameter. These wires are electrically connected to adjacent ones through the metal film resistor of 10 MΩ, Similarly, the wire on the topmost and the bottommost are connected to the cathode plate and grid mesh through the resistor of the same electrical resistivity, respectively. By applying negative high voltage between on the cathode plate, upward electric field are uniformly formed inside the drift cage. Thanks to the doubly layered field wires, non-uniformity of the electric field inside the sensitive volume is reduced within 0.4% [180].

Before the present measurement, the drift cage was aligned so that the beam passes through the center of the sensitive volume. The electrons produced in the sensitive volume are led downward to the amplification region composed of the GEM and the μ-PIC.

GEM A photograph of a GEM is shown in Fig. 2.6 [181]. GEM is a thin insulating film with periodically aligned through holes, and the surface of the GEM are covered by metal conductor. A high voltage is applied between the front and back of the GEM to form a strong electric field in the holes. That field triggers an avalanche amplification of incoming electrons and results in the signal amplification. Consecutively, these electrons are led out of the GEM guided by the field.

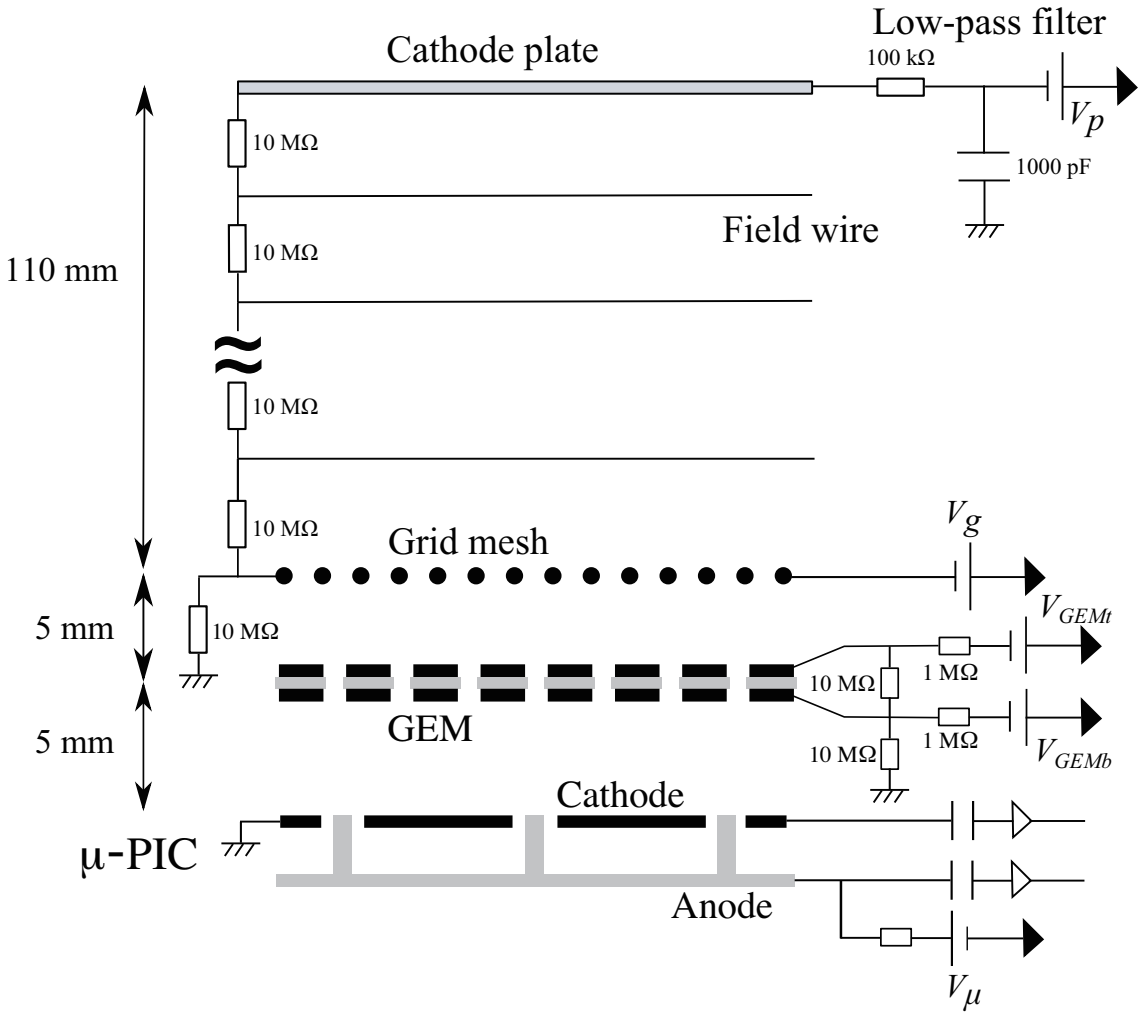

Figure 2.5: Circuit diagram of the MAIKo active target.

A gas electron multiplier (GEM) is installed in the middle of the grid mesh and the μ-PIC in MAIKo for the purpose of electron pre-amplification. The dimension of the GEM placed in MAIKo is 100 $\times$ 100 mm^2, and the polymer insulator sheet in between conductor sides is 100 μm thick. The 70 μm-diameter holes are drilled on the GEM in the 140 μm-pitched equilateral triangular pattern. The electrical wiring around the GEM are shown in Fig. 2.5.

μ-PIC μ-PIC is fine-pitched double-sided stripped electrode implemented on a printed circuit board (PCB). The schematic structure of μ-PIC is illustrated in Fig. 2.7. A pixel of μ-PIC is composed of concentric anode and cathode, and electrodes of same polarity on consecutive pixels are electrically connected to form strips. Cathode strips are implemented on the front side and anode strips are implemented on the back side. The direction of anode and cathode strips are crosswise. During its operation, a positive high voltage is applied to the anode electrodes, whereas the cathode electrodes are grounded. That results in an electric field between the electrodes, which is strong enough to trigger an electric avalanche in the vicinity of the anode. Therefore, incoming electrons are first guided toward the anode pixels and amplified by avalanche process near the anode. Then, positive ions and secondary-electrons produced via the gas multiplication are attracted to electrodes. Consequently, electric signals are induced on the electrodes by the motion of these charged particles.

In MAIKo, the μ-PIC is in charge of electron amplification and signal read-out. That is placed after the GEM and electron multiplied in the GEM are led to μ-PIC. The μ-PIC installed in MAIKo is a square 102.4 cm on a side and consists of 400 μm-pitched 256 $\times$ 256 pixels. Each strips of the anode and cathode are connected to the read-out board. Therefore, total number of readout channel is 512 (anode: 256 + cathode: 256). The PCB, on which μ-PIC is implemented, is attached on the top flange of the vacuum chamber. Thus, the drift direction of electrons is anti-parallel to the gravity direction. The anode (cathode) strips are oriented parallel (perpendicular) to the beam direction. Therefore, side (front) view of the charged-particle trajectory is reconstructed from signals induced on the anode (cathode) strips.

Front-end electronics The electrodes of the μ-PIC are first connected to the capacitor and resistor (CR)circuit boards. The CR circuit board act as a high-pass filter. One CR circuit board can process signals from 256 channels, therefore 2 CR circuit boards are attached to MAIKo. Each signal line from μ-PIC is connected to the read-out board through the coupling capacitor of 100-pF and to the high voltage input. The line from the high voltage input are first distributed into 16 lines. Each of the divided lines is connected to a 1 G Ω resistor. Finally, it is again distributed into 16 lines and connected to the signal line via a 1 M Ω resistor.

The analog signals processed through the filter circuit are then processed by the dedicated readout electronics called Iwaki board. Each Iwaki board can process signals from 128 channels, ths the for Iwaki boards are used in MAIKo. The block diagram of the

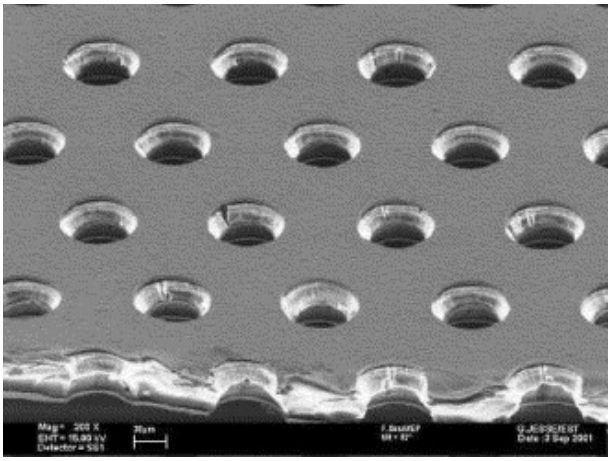

Figure 2.6: Photograph of a gas electron multiplier (GEM) taken from Ref. [181]

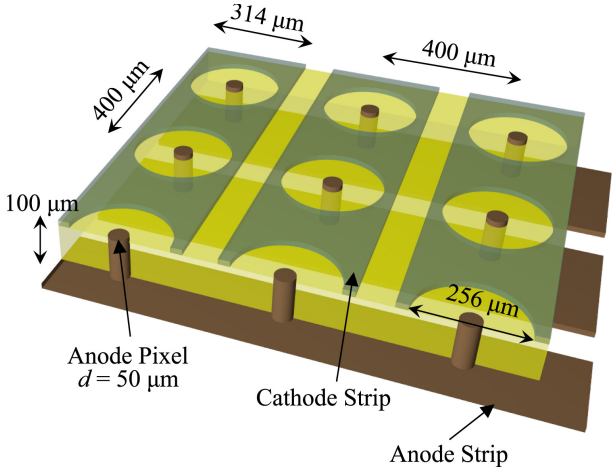

Figure 2.7: Schematic picture of a micro pixel chamber (μ-PIC) taken from Ref. [172]

Table 2.3: Specifications of the FE2009bal ASIC

Number of Channels	16
Peaking Time	30 ns
Gain	800 mV/pC
Dynamic Range	-1 – $+1$ PC
Cross Talk	$< 0.5\%$
Noise	$\sim$ 6000 electrons
Power Consumption	18 mW/ch

board is shown in Fig. 2.8. Signals are pre-amplified, shaped, and discriminated by the application specific integrated circuit (ASIC) chips named FE2009bal. The performance of the chip is shown in Table 2.3. The chip provides 16 digital out put and 1 analog output. The digital signal indicates the high or low status of each discriminator, whereas the analog signal is a sum of shaped analog signals.

The status of the digital signals from FE2009bal are sampled to be encoded synchronized with a 100-MHz clock. In addition, the analog signals from the chip for 32 adjacent strips of μ-PIC are summed and digitized by the 25-MHz 8 bit flash analog-to digital converters (FADC). These data are continuously written in a internal memory implemented in a field-programmable gate-array (FPGA) chip on the Iwaki board. They are stored in a circular buffer of with a capacity of 10.24 μs. When a Iwaki board receives a trigger signal, the data in the buffer is transferred to the first-in-first-out (FIFO) buffer. Subsequently, that data is transferred to the VME memory modules as the board received a transfer signal.

Gas handling system A dedicated gas handling system was designed for MAIKo. This system maintains the mixture ratio and density of the detector gas by controlling the gas flow both at the inlet and the outlet of the detector chamber. A schematic

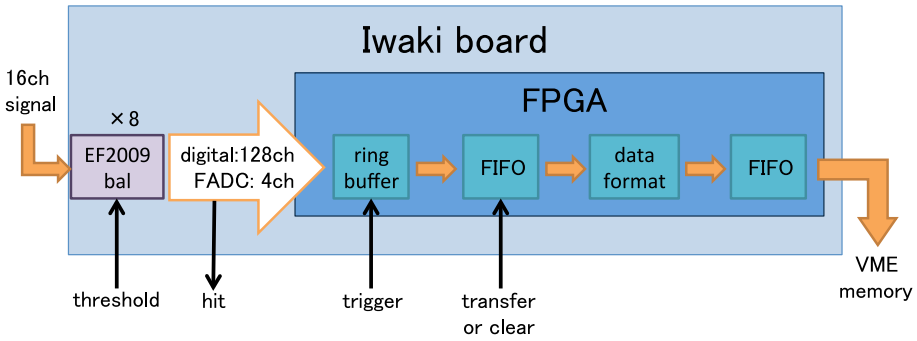

Figure 2.8: Block diagram of the data processing in the Iwaki board. The data flow is depicted with the orange thick arrows. The control input and analog output of the board are shown by the thin solid arrows.

diagram of the gas handling system is shown in Fig. 2.9.

The stability of the gas condition is certified with the dedicated monitor system. As shown in Fig. 2.9, the pressure, temperature, and dew point (equivalent to humidity) inside the detector chamber are continuously measured. These physical quantities are converted to the analog voltage output by the sensors, and converted again to the digital value by the analog to digital converter (ADC) module of the programable logic controller (PLC). The digitized values are periodically readout by a monitoring server and recorded in a text file.

Gases from the gas cylinders are first gated by mass flow controllers (MFC), and then supplied into the detector chamber through its inlet. Since the flow rates of the individual gasses are controlled by the MFCs, the mixture ratio and the total flow rate of mixed gas are kept constant. The outlet of detector chamber is connected to a scroll vacuum pump via a Piezo actuator valve. The density of the chamber gas is maintained by controlling the aperture ratio of the valve. The valve is equipped with a proportional-integral-derivative (PID) controller, where a voltage output of the pressure gauge is given as a process variable. In order to compensate the gas-density variation due to fluctuation of the room temperature, set value for the PID controller is corrected using the temperature T as

$$P'_{\mathrm{set}} = \frac{T}{300\ (\mathrm{K})} P_{\mathrm{set}}, \tag{2.2}$$

where P'_{set} and P_{set} are corrected and original chamber pressure, respectively. This correction ensures to keep the gas density constant at the density at $P = P_{\mathrm{set}}$ and $T = 300$ K. This on-line conversion is done in the PLC. After that, P_{set} is converted to the analog voltage output by the digital to analog converter (DAC) module and send to the PID controller.

The gas evacuation line is designed to minimize a risk of fire. If gas from the Piezo actuator valve is released inside the experimental hutch, the hutch would be filled with the gas including burnable component, namely CH_4. That increases the risk of fire. In order to prevent that burnable gas to be spread over the sealed hutch, the evacuated gas from the valve is, first, diluted with nitrogen gas immediately to the mixture ratio sufficiently lower than the explosion limit of the burnable component. Then, the diluted gas is guided with the piping toward the exhaust duct of the experimental hall and released there.

2.2.3 Operating Condition

The MAIKo active target was operated with the He (90%) + CH_4 (10%) mixture gas. This composition of operating gas was designed to achieve high signal to noise ratio and stable operation at the same time. Although pure helium gas is ideal as a target when considering the S/N ratio of the yield, organic gas as a quencher is essential to obtain the desired operating conditions for a gaseous particle detector. CH_4 was selected as the quenching gas in the present measurement. In case of MeV-photon beam experiments,

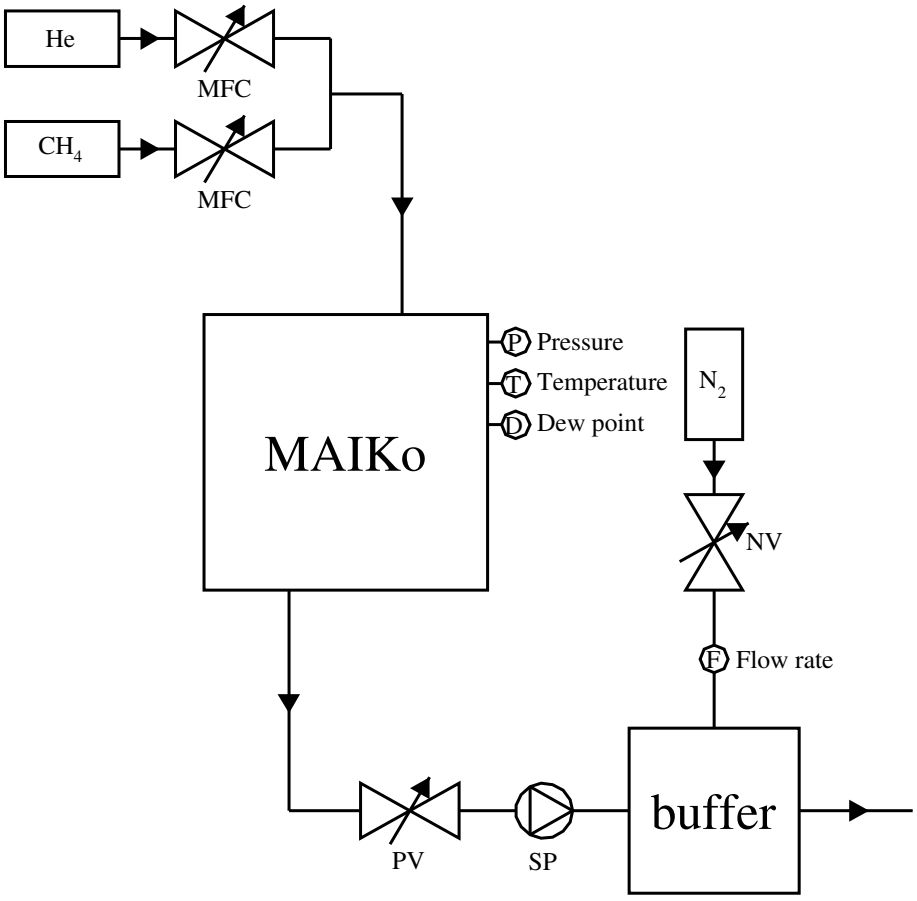

Figure 2.9: Schematic diagram of the gas handling system. The flow direction of the piping is shown by the triangles on the lines. Some pipe elements such as bypass lines and normally open valves are not shown in the picture because they are not used while in operation. He and CH_4 gases reserved in the gas cylinders are extracted via the mass flow controllers (MFC) with their flow rate controlled and released in the MAIKo chamber. Physical circumstance within the chamber, namely the pressure, temperature, and dew point (equivalent to humidity), are monitored periodically. The chamber gas is continuously sucked out by the scroll pump (SP). This gas evacuation rate is controlled by the aperture of the Piezo actuator valve (PV) on the way, and thus the gas density in the chamber is kept constant. The exhaust gas of the pump, is released in the buffer chamber. Therein, N_2 gas is constantly provided via the needle valve (NV) and the flow rate meter. Incoming chamber gas, that is burnable due to CH_4, is diluted by the inert N_2 gas and released at the exhaust duct safely.

the main source of the background event stems from the photodisintegration of elements heavier than ^{1}H. On the other hand, ^{1}H atoms do not contribute to the background, because photodisintegration and photoproduction are not allowed energetically. CH_4 molecules does not contains the heavier elements other than carbons, and its composition ratio of carbons over hydrogens are the least in all the available hydrocarbons. Thus, the CH_4 is one of the good choice in this situation.

The target thickness was optimized for the measurement of the charged particles from the ^{4}He$(\gamma, n)^3$He and ^{4}He$(\gamma, p)^3$H reactions. The range of decay charged particles are determined from the total energy and energy deposit of the particles. That is why the range is important information for particle identification. The range can be reconstructed only if the particle stops inside the sensitive volume. However, the energy deposit of decay particles take on a wide range of value, and therefore, it is realistically impossible to stop all the charged particle inside the sensitive volume while keeping the shortest range long enough to detectable length. Thus, the decision criteria of the target thickness was settled based on the range of the decay particles as follows;

1. The range of ^{3}He is short enough to stop in the sensitive volume of the active target.
2. The ranges of protons and ^{3}H are long enough to punch through the sensitive volume.

These conditions were fulfilled in the certain target thickness since the ranges of protons and ^{3}H are far longer than that of the ^{3}He. This is because the ratio of the amount of the kinetic energy shared by the decay particles from two-body photodisintegration is approximately equal to the inverse ratio of the particle mass ratio, and the energy deposit (dE/dx) of charged particles is proportional to the square of its electric charge and inverse of its kinetic energy.

In addition, the suitable target thickness depends on the beam energy. For simplicity, three measurement conditions, 500 hPa, 1000 hPa, and 2000 hPa were employed in the present measurement. The ranges of the decay particles under these conditions are shown in the panels (a) – (c) in Figs. 2.10. The energy dependence of the range for the decay particles from both ^{4}He and ^{12}C photodisintegration are shown together. In order to fullfil the ideal condition for the range measurement, the ^{3}He should stop inside the range sensitive region of the MAIKo active target, and p and ^{3}H should not. That can be judged in the panels (d) – (f) in Figs. 2.10. Therein, the beam energy dependence of the decay particle range are shown. The correspondence between beam energy and the target thickness is summarized in Table 2.4. As can be seen in the panels (d) – (f) in Figs. 2.10, these combination pass the requirements. The target gas was supplied in the flow rate of 100 cc/min, and its thickness was kept constant by the dedicated gas handling system described before.

The electric field inside the sensitive volume was set so that the electron drift velocity was about 1.5 cm/μs. This value was determined from the record time length of the Iwaki board (10.24 μs) and height of the sensitive volume (110 mm). If the drift velocity

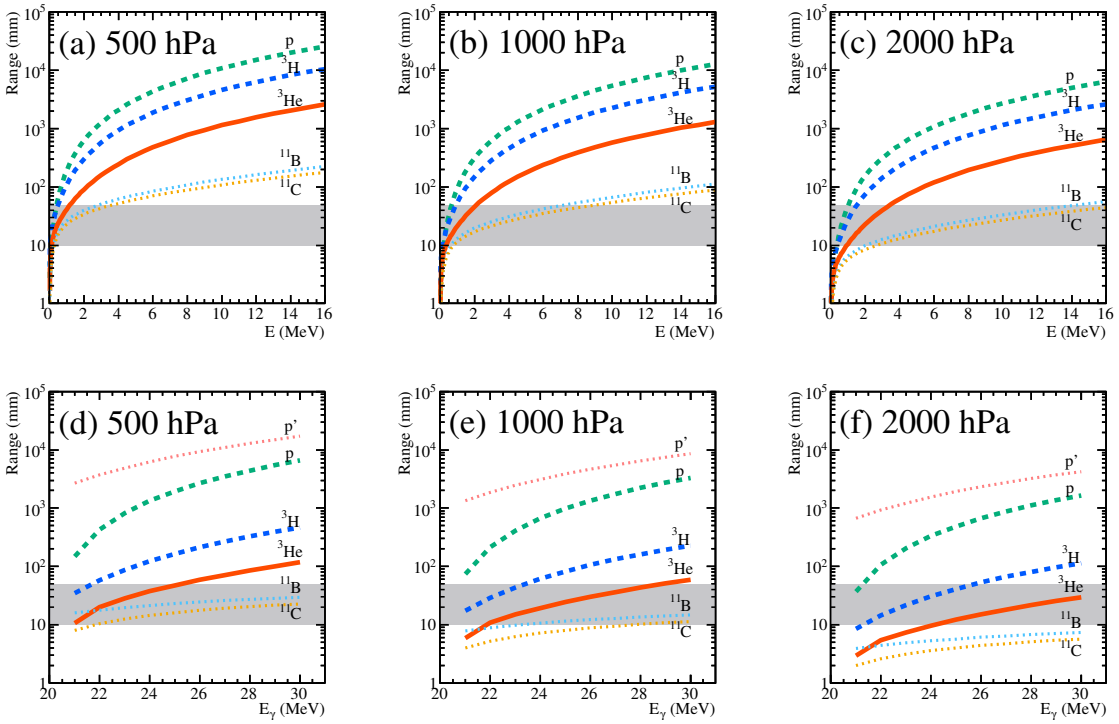

Figure 2.10: Ranges of the decay particles in the medium gas of the MAIKo active target, namely He (90%) + CH_4 (10%) at 500, 1000, and 2000 hPa. (a) – (c) Kinetic energy dependence of the ranges of the decay particles from ^{4}He photodisintegration (p, ^{3}H, ^{3}He), and those from ^{12}C photodisintegration (p, ^{11}B, ^{11}C). The range sensitive region of the MAIKo active target is shown with the filled area. (d) – (e) Beam energy dependence of the decay particles from the photodisintegration reactions, $^4\mathrm{He}(\gamma, n)^3\mathrm{He}$, $^4\mathrm{He}(\gamma, p)^3\mathrm{H}$, $^{12}\mathrm{C}(\gamma, n)^{11}\mathrm{C}$, $^{12}\mathrm{C}(\gamma, p)^{11}\mathrm{B}$. Here, the p from the decay of ^{12}C nuclei is denoted by p'. The kinetic energy of the decay particles are estimated from the case that the particle is emitted to the θ =90 degrees in the center of mass system.

is v and the time measurement range is T, the measurable height range is given by vT. Therefore, the measurable height with the drift velocity of the 1.5 cm/μs was about 150 mm and was enough to cover the whole sensitive volume (110 mm). The trend of the drift velocity with respect to the strength of the drift field was calculated using the Magboltz code [182], and the high voltage applied to the cathode plate of the drift cage was optimized based on the result. As shown in Table 2.4, the drift velocity was set to 1.53, 1.78, and 1.66 cm/μs for the measurements with the target pressures of 500, 1000, and 2000 hPa, respectively. These actual drift velocity was confirmed roughly from events triggered by cosmic rays, in which the electrons were generated throughout the top and the bottom of the sensitive volume along with the trajectories of cosmic rays punching through the sensitive volume vertically. In that case, the time duration of signal would be equal to the product of the drift velocity and the height of the drift cage. We confirmed this relation held within few %, and the nominal velocity was used in the further analysis.

Table 2.4: Target thickness for each beam condition. k is the index of the condition. The thickness is expressed with its pressure at $T = 300$ K.

k	E_γ (MeV)	Target thickness (hPa)	Drift velocity (cm/μs)
1	23.0	500	1.53
2	24.0	500	1.53
3	25.0	1000	1.78
4	27.0	1000	1.78
5	28.0	1000	1.78
6	30.0	2000	1.66

2.3 Data Acquisition

2.3.1 Overview

The data acquisition system based on the VME modules was employed in the present measurement. The system was composed of the front-end electronics, the NIM logic circuit, and the VME based backend electronics. The signal from the MAIKo active target was first processed by the front-end electronics, i.e. the Iwaki board. Part of the processed signals were then transported to the NIM logic circuit for the trigger decision. When the trigger was fired from the NIM logic circuit, the data transfer request signal was sent to the IWAKI board, and the data stored in the board were delivered to the VME memory board modules. After this data transfer ended, the data in the memory modules and other VME modules were read out through the VMEbus by the VME CPU module, and then written in the data disk. After the data writing finished, the system resumed to accept the trigger. These process resulted in the dead time of the data acquisition. The VME modules were controlled using the babirl software suite [183] which is commonly

used in the experiment at the RI beam factory (RIBF) in RIKEN. The dead time of the system were managed by the back-end software and that was fed back as a VETO signal for the NIM logic circuits which was in charge of the trigger decision.

2.3.2 Trigger

The trigger signal for the data acquisition was generated by the NIM logic circuits based on the analog output from the Iwaki boards. As mentioned earlier, each board has 4 analog output channels which emit the summed signals from 32 adjacent strips in the μ-PIC. Analog signals from anode strips of the μ-PIC were originally positively polarized pulses. These signals were inverted to the negative polarization by the inverter amplifier module, and input to the leading edge discriminator module combined with the analog signals from the cathode which has negative polarity. The threshold voltages of the discriminator modules were set low enough so as not to miss the photodisintegration events. The logical sum of the output from all the discriminator channels was employed as the trigger decision. The typical trigger rate in the present measurement was less than 100 Hz. At that time, the data acquisition efficiency was higher than 99%. That means the dead time of the system hardly deteriorated the performance of the data acquisition.

Chapter 3

Data Analysis

3.1 Overview

The aim of the present work was to determine the cross section of the $^4\mathrm{He}(\gamma, n)^3\mathrm{H}$ and $^4\mathrm{He}(\gamma, p)^3\mathrm{H}$ reactions over the photon beam energy range between 23.0–30.0 MeV. In this section, the procedure we performed on the data obtained from the present measurement is described.

The reaction cross sections were calculated from the total beam flux and the number of the photodisintegration events. The total beam flux was estimated from the fitting analysis on the energy spectrum measured with the beam monitor, whereas the number of events was counted from the tracking analysis on the acquired data. In addition, the tracking efficiency owing to the detector geometry and the algorithm of the tracking analysis must be taken into account to correct measurement yields to estimate the number of the events.

The analysis on the beam particles is described in Ch. 3.2. The total flux was derived from the template fitting analysis on the energy spectrum measured with the beam monitor. A Monte Carlo simulation for the beam-energy-profile estimation is also explained. In Ch. 3.3 , the analysis on the decay particles is expressed. From the decay particle trajectories measured with the MAIKo active target were tracked and sorted in a certain algorithm. The events of the $^4\mathrm{He}(\gamma, n)^3\mathrm{H}$ and $^4\mathrm{He}(\gamma, p)^3\mathrm{H}$ reactions were extracted. Details of a Monte Carlo simulation for tracking efficiency estimation is also given here. Finally, the procedure to derive the cross sections is presented in Ch. 3.4.1. The differential cross sections were first derived, and the total cross sections for each reaction channel were then determined.

3.2 Analysis of Beam Particles

The beam particles were measured with the NaI(Tl) beam monitor installed on the downstream end of the BL01 beam line (Fig. 2.2). During the decay-particle measurement using the MAIKo active target, the energy deposition spectrum by the photon beams was recorded with the data acquisition system independent of that of the MAIKo active target.

Since several incident beam photons were injected into the beam monitor at once, the measured energy spectrum was the superposition of the response functions to n-photon injection event. The unfolding analysis to obtain the probability distribution function of the photon multiplicity was necessary to obtain the total flux. For this purpose, we have measured the one-photon response function and then produced n-photon response functions. The energy spectra acquired with the physics data are fitted with the response template functions run by run. Finally, the total flux and its uncertainties were estimated for each run. The validity of these procedures had been studied in Ref. [184]. The one used in the present study is the extension of the technique to the general cases where the number distribution of incident photon does not necessarily to be regarded as the Poisson distribution.

In addition, the beam energy profile was deduced for all the beam conditions. This was done by fitting the energy spectrum generated with a Monte Carlo simulation to that measured in the present experiment. The energy profile information was used to deduce the cross sections as described later.

3.2.1 Timing Structure and Energy Spectra

In the NewSUBARU BL01 beam line, the photon beams are generated from the Compton scattering of the laser photon off the relativistic electron beams in the storage ring. Therefore, the time structure of the laser and the electron beam determine that of the photon beam, and this structure requires an analysis to deduce the beam flux.

The timing structure of the various element relevant to the beam production are shown in Figs. 3.1. As stated in Ch. 2.1.2, the Nd:YVO_4 solid state laser which we employed for the present measurement was operated pulse-wise: the oscillation was turned on for 8 ns every 50 μs (20 kHz). In addition, the module was operated at 80% duty cycle, or the module was turned on for the duration of 80 ms, and then turned off for 20 ms. Therefore, the repetition frequency of the laser photon was effectively 16 kHz.

On the other hand, according to the specification of the storage ring (Table 2.1), it takes approximately 396 ns an electron bunch to run one lap of the ring. This time is equivalent to a repetition in 2.53 MHz, namely the RF frequency divided by the harmonic number. The repetition frequency of the electron beam varies depending on the filling pattern of electron beam bunch, and it is at most in the RF frequency 499.955 MHz (every 2 ns).

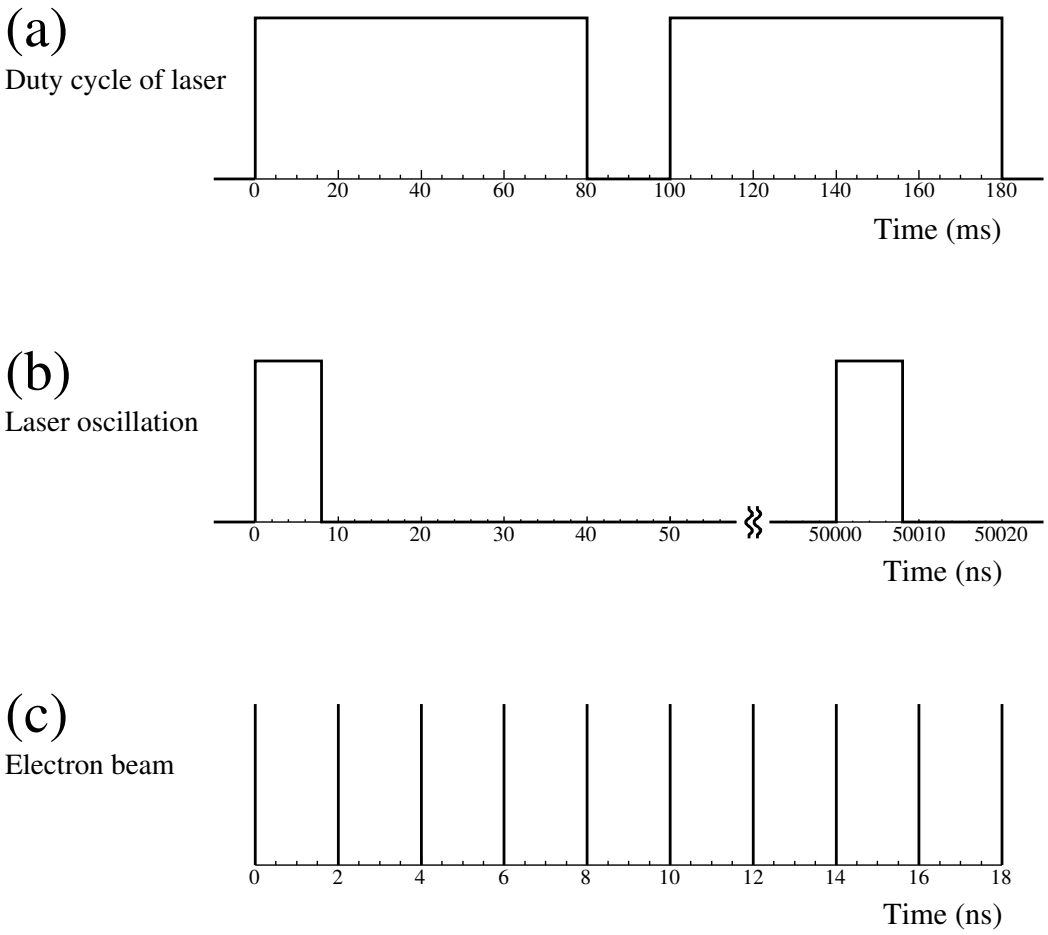

Figure 3.1: Schematic diagrams of the timing structures of the beam. (a) Duty cycle of the laser module. (b) Oscillation of the laser module. (c) Electron beam bunches.

Due to the difference between the time scale of the laser photons and electrons, the resultant photon beams follows the hierarchical timing structure. First, the beams had the finest timing structure owing to the electron beam frequency at most 499.955 MHz. Second, the finer timing structures were included in the repetition of the laser emission at 20 kHz with the duration of 8 ns. Third, the coarsest timing structure was due to the duty cycle of the laser module.

From the measurement side, the decay time constant of the scintillation light emission in NaI(Tl) crystals is on the order of 1 μs. Therefore, the finest timing structure of 2 ns interval can not be decomposed with the beam monitor. On the other hand, the medium structure of 50 μs interval is able to be distinguished. In consequence, the signal pulses synchronizing with the laser oscillation is counted one by one using the beam monitor. The pulse height of processed signals were recorded with the MCA. Since the throughput of the MCA is high enough to process every signals, the counting loss due to the data acquisition was ignorable.

A typical energy spectrum measured during the physics measurement is shown in the panel (a) in Figs. 3.2. In the present measurement, the typical intensity of the photon beam was about 10^5 cps, whereas the effective frequency of the beam bunch was 16 kHz. This meant several to ten photons were arrived at the "same" time in a beam bunch. Because of this multi-hit event, the measured energy spectrum exhibited the complicated pattern as shown in the panel (a) in Figs. 3.2. The approximately equally spaced peak structures were observed in the spectrum. This pattern could be understood by the assumption that the energy spectrum is a superposition of the multi-photon responses. Namely, the each peak structure corresponds to the one, two, and more photon injection event from left to right.

In addition to the physics runs, the energy spectra under the different beam conditions were also recorded. One is the spectrum obtained with a low intensity beam, and shown in the panel (b) in Figs. 3.2. The vertical axis in the panel is drawn in the logarithmic scale, whereas the inset panel depicts the same spectrum but with the linear scale. This spectrum can be approximately regarded as the one-photon response of the beam monitor. However, it contains a small fraction of backgrounds that can not be attributed to the one-photon injection as can be seen in the external panel. The treatment on these contaminating components will be described in the next section. Moreover, the spectra with no LCS beam was also recorded. That condition was realized by stopping the laser module that is in charge of the production of the primary photon for the LCS. A typical spectrum from this condition is shown in the panel (c) in Figs. 3.2. That spectra can be interpreted as the background spectra due to the electron beam in the storage ring.

3.2.2 Response Functions

In order to know the total beam flux, this multi-hit events observed in the energy spectrum must be handled properly. When the response functions of the beam monitor to n-photons injection are given as $t_n(x)$ at channel x, the observed energy spectrum should

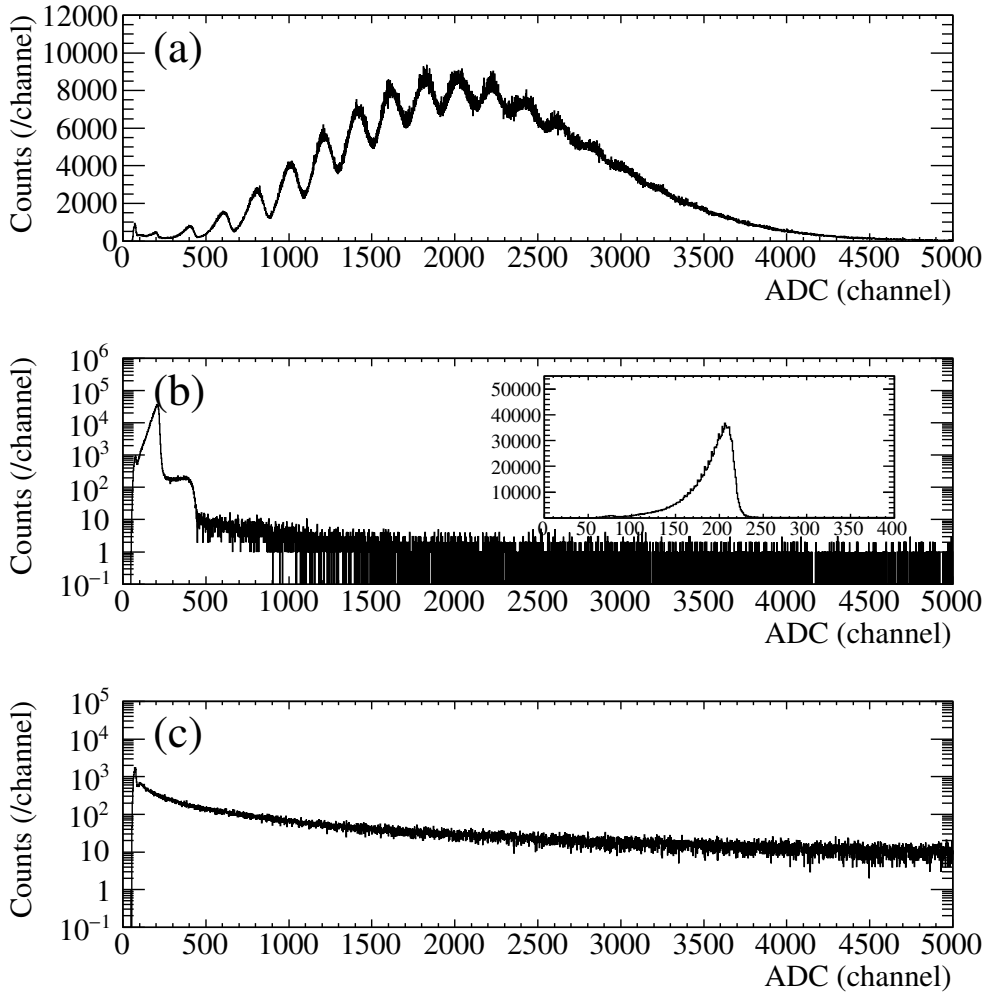

Figure 3.2: Typical beam energy spectra obtained under three different beam conditions. (a) Spectrum from the measurement with the high intensity beam. The peaks in the spectrum are attributed to the multi photon injection at the "same" time. (b) Spectrum from the measurement with the low intensity beam. The inset panel shows the same spectra but with the linear scale. (c) Spectrum from the measurement with no LCS beam.

ideally be fitted with the template function $T_0(x)$ shown below,

$$T_0(x) = \sum_{n=1}^{\infty} w_n t_n(x). \tag{3.1}$$

Here, w_n stands for the weight factors for n hit events. All the response functions $t_n(x)$ are normalized so that their integral values are equal to unity.

The response function to one photon event $t_1(x)$ was deduced from the energy spectrum measured with a low-intensity beam, such as the one shown in the panel (b) in Figs. 3.2. If the beam intensity is low enough, w_ns for all the $n > 1$ is almost zero, and the resultant spectrum is approximately proportional to $t_1(x)$. Fig. shows the typical energy spectrum measured with low intensity beam. As seen in Fig. , that spectrum is incomplete to be regarded as $t_1(x)$ in three points: (1) contaminating background event in the high-energy region, (2) small fractions of multi-photon contributions, and (3) instrumental cut-off in the low-energy side.

$t_1(x)$ was deduced from the following procedures. First, the amount of the contamination of the background was estimated from the template fitting using the background spectrum, and its contribution was subtracted from the measured histogram. The energy spectrum originating from the background events was measured with the laser module turned off. That spectrum was shown in the panel (c) in Figs. 3.2. The result of this template fitting is shown in tha panel (a) in Figs. 3.3. The shaded region of the raw energy histogram depicted with the black line is fitted to the background spectrum shown by the red line. The scaled template spectrum was subtracted from the raw spectrum.

Second, small contribution from multi-photon events in higher energy region were fitted with the function

$$f_{\rm mul}(x) = \exp(p_0 + p_1 x) \tag{3.2}$$

and subtracted from the spectrum. The best $f_{\rm mul}(x)$ to fit the background subtracted histogram is shown with the red line in the panel (b) in Figs. 3.3. That is overlaid on the background subtracted histogram depicted with the black line. The parameters P_0 and P_1 of $f_{\rm mul}(x)$ were determined from the fitting analysis regarding the spectra in the shaded region. The best fit spectra was subtracted from the background subtracted histogram.

Third, the missing low-energy-side tail in the spectrum was extrapolated with the function

$$f_{\rm low}(x) = \exp(p_2 + p_3 x) + p_4. \tag{3.3}$$

That is shown in the panel (c) in Figs. 3.3. The red line is indicating the $f_{\rm low}(x)$ reproducing the result of the former process. The part of spectrum to the left of the shaded region was substituted with the best $f_{\rm low}(x)$. Next, the high-energy side tail was truncated above the lowest bin ($x_{\rm max}$) whose entry was less than its error. The low energy end of this truncation is shown by the light vertical dashed line in (c) in Figs. 3.3. The result of the procedures mentioned so far, or the background-free spectrum $\tilde{H}_1(x)$ is shown in tha panel (d) in Figs.3.3.

Finally, the $t_1(x)$ was obtained from

$$t_1(x) = \frac{\tilde{H}_1(x)}{\sum_{x'=0}^{x_{\max}} \tilde{H}_1(x')}, \tag{3.4}$$

where $\tilde{H}_1(x)$ was the background-free spectrum. Thanks to the low-energy and high-energy end processing done on $\tilde{H}_1(x)$, $t_1(x)$ takes positive value only within the x range $[0, x_{\max}]$, and is set to zero otherwise. In addition, the integration over the x is normalized because of Eq. 3.4.

Based on the $t_1(x)$, the multi-photon response functions $t_n(x)$ were produced from the iterative convolutions. Since $t_1(x)$ was normalized to unity, it could be regarded as the probability mass function of the response to one photon injection. Under the assumption that the detector lineally responded to multi photons, the two photon response function $t_2(x)$ was written as

$$t_2(x) = \sum_{x'} t_1(x - x')t_1(x'). \tag{3.5}$$

In addition, the n-photon response was also obtained inductively from $(n-1)$-photon response t_{n-1} as

$$t_n(x) = \sum_{x'} t_{n-1}(x - x')t_1(x'). \tag{3.6}$$

In the present work response functions for the photon number up to n=60 was produced for each measurement condition.

It is known that the detector does not respond lineally to the multi photon injection, and its response quenches as the multiplicity increases [185]. This effect was taken into account in the fitting procedure described in the following section.

3.2.3 Template Fitting

We performed the template fitting of the measured spectrum by using the response functions defined in the previous section. We employed the template function $T(x)$ expressed in the following formula

$$T(x) = \sum_{n=1}^{60} w_n t_n(x) + w_{\mathrm{BG}} t_{\mathrm{BG}}(x). \tag{3.7}$$

Compared with the $T_0(x)$ shown before, the photon-multiplicity n were limited within the range $n \leq 60$, and the response function due to the background event t_{BG} was added.

In addition, the quenching effect for the multi photon injection was also considered. The quenching of this beam monitor was studied in Ref [185], where a empirical formula describing the light output quenching was given. We used the modified version of the empirical formula given below

$$y = ax^{\eta} + d. \tag{3.8}$$

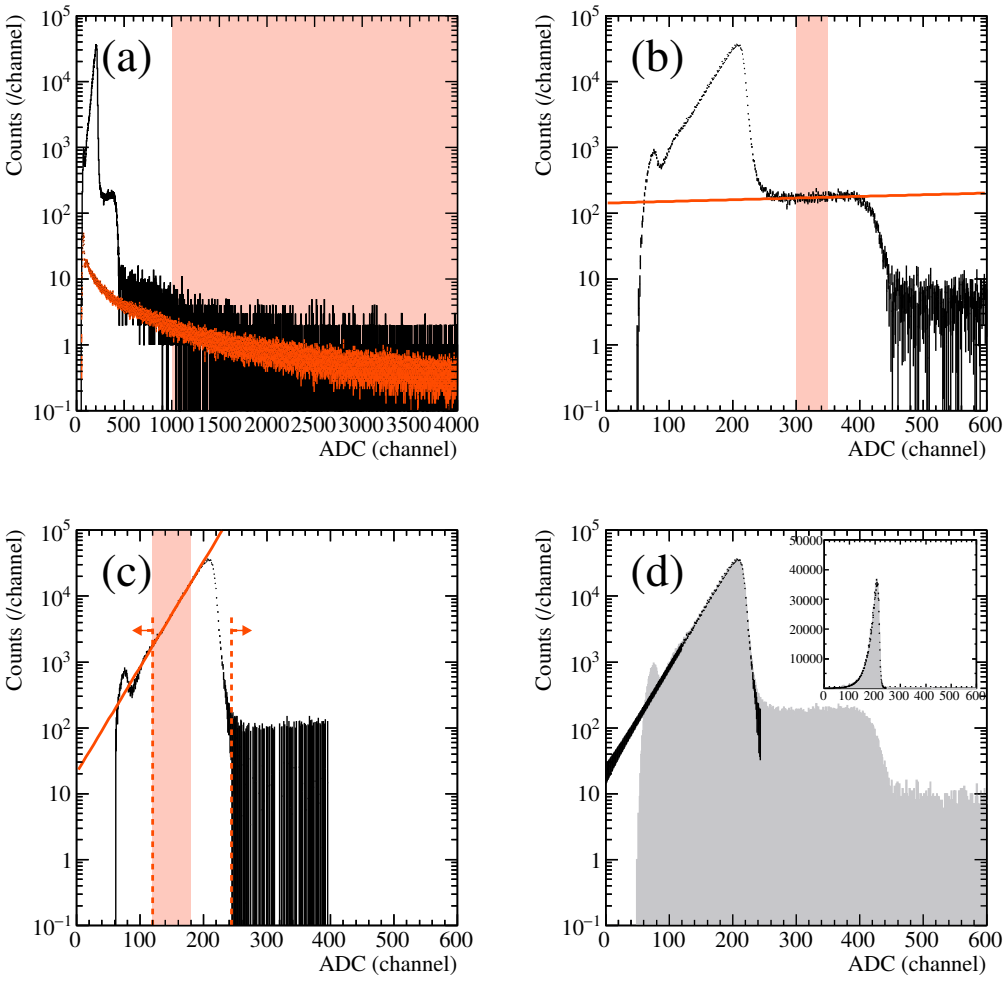

Figure 3.3: Procedures for estimating the one-photon response function $t_1(x)$. (a) Background subtraction. The raw energy spectrum obtained from the low-beam-intensity measurement is shown with the black histogram, and the contribution from the background estimated from the template fitting is overlaid on the spectrum. The energy region considered in the fitting analysis is indicated with the filled region. (b) Multi-photon event elimination. The background subtracted energy spectrum is shown with the black histogram. The tail of the multi-photon response approximated with Eq. 3.2 is indicated with the red line. (c) Low-energy and high-energy ends processing. The black histogram shows the energy spectrum resulting from the multi-photon event elimination. The part of the spectrum to the left of the left vertical dashed line is substituted with a function described by Eq. 3.3, which is shown with the red line. In addition, the other part of the spectrum to the right of the right vertical dashed line is truncated. (d) Spectra obtained after the subtractions and end processing. The resultant spectra $\tilde{H}_1(x)$ is drawn with the black histogram. The raw energy spectrum is also shown by the filled region. The inset figure is the same one but drawn with the linear scale. $t_1(x)$ is finally obtained after the normalization following Eq. 3.4.

Here, x and y are the channel number before and after saturation, respectively. d is the parameter we added to the original formula. η is defined as follows,

$$\eta = (1 - c) \cdot \exp(-bx) + c. \tag{3.9}$$

There are four parameters a, b, c, and d in this model. According to the Ref. [185], these parameters varied with respect to the various beam conditions such as the intensity. Therefore, we did not adopt single parameter set to all the measured spectra. Instead, we estimated the best parameters for the each spectrum.

We defined the n-photon template functions distorted by using Eq. (3.8) as $\tilde{t}_n(x)$ as,

$$\tilde{t}_n(x) = \sum_{x'} R_{x,x'} t_n(x'), \tag{3.10}$$

where $R_{x,x'}$ was the conversion coefficient given from the Eq. (3.8). Then, the equation (3.7) was rewritten as

$$\tilde{T}(x) = \sum_{n=1}^{60} w_n \tilde{t}_n(x) + w_{\mathrm{BG}} t_{\mathrm{BG}}(x). \tag{3.11}$$

Here, we did not apply Eq. (3.8) to the background template $t_{\mathrm{BG}}(x)$. The term $t_{\mathrm{BG}}(x)$ contributed to the measured spectrum only when the no photons were included in a beam pulse. We assumed this situation was totally identical to the background measurement, and the quenching in this situation was already included in the measured background template $t_{\mathrm{BG}}(x)$. In addition, during the physics run, the average photon number in a beam pulse was high enough that we could regard the influence of the $t_{\mathrm{BG}}(x)$ on the fitting result was minor.

The parameters w_n, w_{BG}, and a–d which reproduced the measured spectrum best were searched by using the computational minimization package MINUIT [186] implemented in the ROOT library [187]. The object of the minimization was the chi-square defined by considering the error of the template functions as follows,

$$\chi^2 = \sum_{x=x_{\min}}^{x_{\max}} \frac{(H_{\mathrm{tgt}}(x) - \tilde{T}(x))^2}{\Delta H_{\mathrm{tgt}}(x)^2 + \Delta \tilde{T}(x)^2}. \tag{3.12}$$

Here, $H_{\mathrm{tgt}}(x)$ stands for the measured energy spectrum to be fitted, and the variables begin with Δ are the statistical uncertainties. $x_{\min}$ and $x_{\max}$ are the minimum and maximum boundary for the fitting range.

Since the dimension of the parameter is large, we divided the minimization the procedure to search for the best parameter that minimize Eq. (3.12) in three steps. First, chi-square were minimized varying w_ns. In this process, the w_ns were optimized individually starting from the largest w_n in the descending order. Next, the best ratio of w_{BG} over the sum of w_ns was searched. This search was constrained that this ratio was less than tha value when the energy region lower than the one photon peak, where the background template took the larger value, was totally explained with the background

template. Then, the parameters for the quenching effect were optimized. By iteratively repeat these three steps of minimization for 100 times, the chi-square converged to the best parameter set.

It should be noted that we did not assume that the w_ns obeyed the Poisson distribution. It is true that these parameters must follow the Poisson distribution with the mean of the average photon number in a beam bunch in the case of a short-time measurement. However, in the present measurement, the measurement time of 1 hour was not necessarily short compared with the decay time of the electron beam, and the average photon number in a beam bunch also decayed over time. For the reason, we searched the best w_ns in more general cases rather than limiting them in the single Poisson distribution.

The statistical uncertainties of w_ns were estimated from the interval of each w_n where the chi-square becomes 1 larger than the best-fit chi-square value at its boundary. For simplicity, we assumed that the w_ns were the approximately independent, and the limit of the interval was determined for each w_n individually. The chi-square calculated from Eq. (3.12) should ideally be the same to the number of degrees of freedom (NDF) ν, but the chi-square tended to be larger than the NDF in the present result. This suggested that our model might be insufficient to fit the measured spectrum completely, and the uncertainties adopted in the denominator in Eq. (3.12) was underestimated. We defined the corrected chi-square ($\tilde{\chi}^2$) as follows

$$\tilde{\chi}^2 = \frac{\nu}{\chi^2_{\rm best}}\chi^2, \tag{3.13}$$

where $\chi^2_{\rm best}$ is the chi-square evaluated by substituting parameters with the best fit results. The uncertainty intervals were estimated based on the corrected chi-square, or the upper and lower limit of the uncertainty interval for each w_n were defined at the point where $\tilde{\chi}^2 = \nu + 1$.

The total photon flux Φ was determined from the best fit parameters as,

$$\Phi = \sum_{n=1}^{60} n w_n. \tag{3.14}$$

Since all of the template functions $\tilde{t}_n(x)$ were normalized to be unity, w_n was equal to the most probable number of event with photon multiplicity of n. Therefore, Φ was obtained from the weighted mean of the w_n.

A typical result of the template fitting is shown in Figs. 3.4. The raw energy spectrum which is subject to the fitting is shown in the panel (a) in Figs.3.4. That is fitted with the model described in Eq. (3.11). The corrected response functions $\tilde{t}_n(x)$ based on the best quenching parameter are shown with the dashed lines in the panel (b) in Figs. 3.4. Each peak corresponds to individual $\tilde{t}_n(x)$ from left to right in the ascending order of the index n. The best parameters of the quenching model Eq. (3.8) and (3.9) were $(a, b, c, d) = (1.07, 8.77 \times 10^{-7}, 0.50, 0.00)$. The result of the fitting is shown in the panel (c) in Fig. 3.3. The model function with the best parameters is overlaid on the raw spectrum. The response functions $\tilde{t}_n(x)$ scaled by the weight factors w_n are also drawn with the dashed lines.

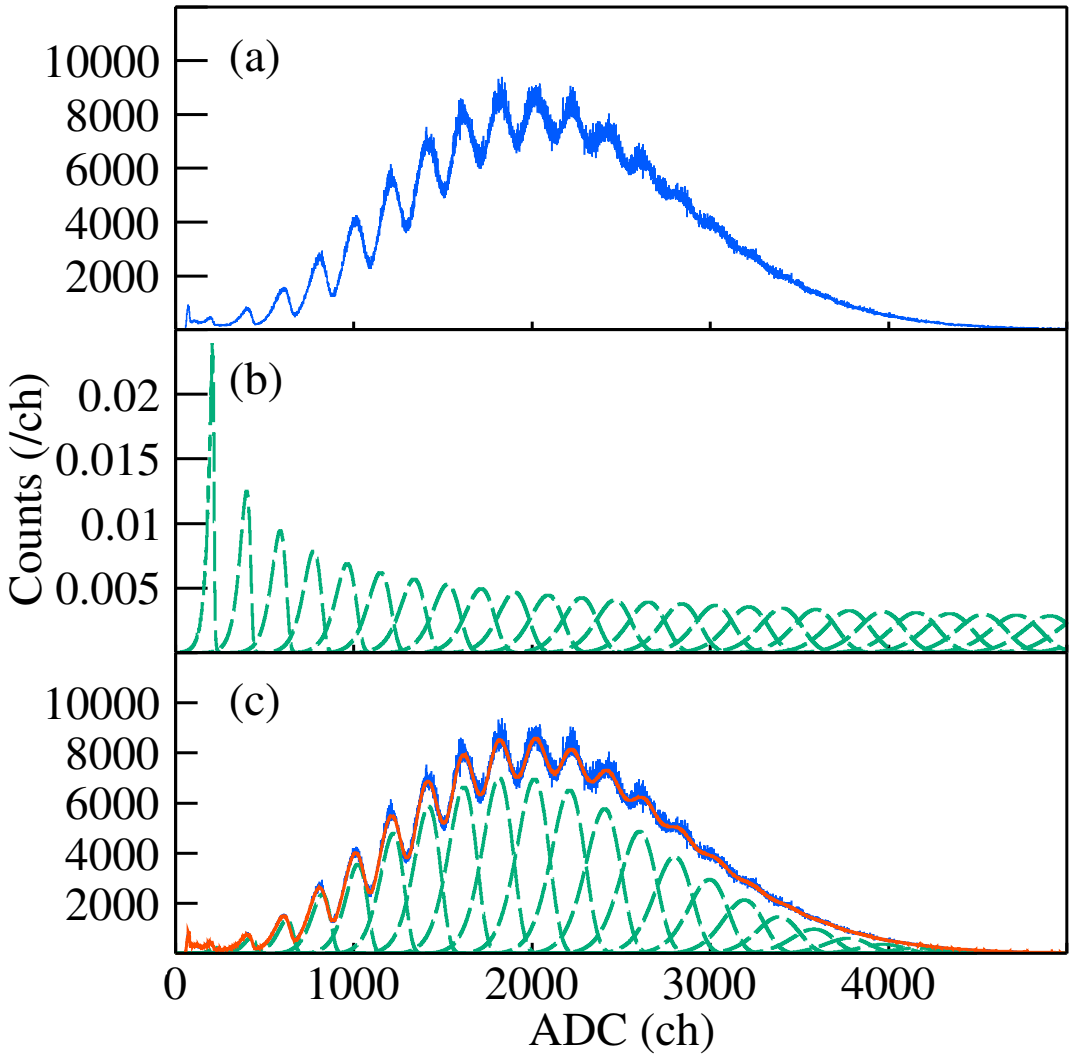

Figure 3.4: Procedure for beam flux estimation taken from Ref. [1]. (a) is the energy distribution measured with the NaI (Tl) beam monitor, and each peak structure in the histogram is correspond to energy deposit by several photons injected at the same time. (b) and (c) are the detector response templates for fitting analysis and the result of fitting analysis respectively. In (c), the best fit result (thick red line) overlaid on the measured distribution and template functions multiplied with weight factors (green dashed line) are overlaid on the measured energy distribution.

3.2.4 Uncertainties

The statistical uncertainty of the total photon flux $\Delta\Phi_{\rm stat}$ was evaluated from the propagation from those of w_n as

$$\Delta\Phi_{\rm stat} = \sqrt{\sum_{n=1}^{60} n^2 \Delta w_n^2}, \tag{3.15}$$

where the Δw_n is the average of the upper and lower uncertainties of w_n. $\Delta\Phi_{\rm stat}$ was at 0.2% for each measurement in average.

The systematic uncertainties on the total photon flux evaluated from Eq. (3.14) was estimated from the total photon flux evaluated by the various methods. We employed six alternative methods for the total flux evaluation, and we denoted them as $\Phi_1, ...\Phi_6$. Three of them (Φ_1, Φ_2, Φ_3) were based on the assumption that the average number of photons in a beam bunch m was obtained by the average channel number of the multi- and single-photon spectra. Then, the total flux was evaluated from the product of m and the total events of multi-photon spectrum. This method was one adopted in Ref. [185]. In another method (Φ_4), the number of beam bunch evaluated from the product of the measurement time and the repetition frequency of the laser was employed instead of the total events od multi-photon spectra. The last two method (Φ_5, Φ_6) was the correction to Eq. (3.14) with respect to the contribution from the higher multiplicity events.

First, as described in Ref. [185], the total flux was the product of the average photon number m and the total number of beam bunch N_γ as

$$\Phi_i = m_i \times N_\gamma, \ (i = 1, 2, 3). \tag{3.16}$$

i is the index of the evaluation method that takes value from 1 to 3. Here, the average photon number was obtained as

$$m_i = \frac{\bar{N}_m^i}{\bar{N}_s^i}, \tag{3.17}$$

where $\bar{N}_m^i$ and $\bar{N}_s^i$ were the average channel number of the multi- and single-photon spectrum for i th method. The average channel number of the spectra $H(x)$ was defined as,

$$\bar{N}_{m/s}^i = \frac{\sum x H_{m/s}^i(x)}{\sum H_{m/s}^i(x)}. \tag{3.18}$$

The photon spectrum defined below were employed,

$$H_m^1(x) = \sum_{x'} R_{x,x'}^{-1} \left(H_m(x') - w_{\rm BG} t_{\rm BG}(x')\right) \tag{3.19}$$

$$H_m^2(x) = \sum_{x'} R_{x,x'}^{-1} H_m(x') \tag{3.20}$$

$$H_m^3(x) = H_m(x') - w_{\rm BG} t_{\rm BG}(x') \tag{3.21}$$

$$H_s^1(x) = H_s^2(x) = H_s^3(x) = t_1(x) \ (= \sum_{x'} R_{x,x'}^{-1} \tilde{t}_1(x')). \tag{3.22}$$

Here, $R^{-1}_{x,x'}$ was the coefficient of the inverse matrix of quenching effect $R_{x,x'}$ defined in Eq. (3.10). By multiplying the matrix, nonlinearity due to the quenching effect is canceled. In other word, the multi-photon spectrum after the background subtraction and the quenching correction was used in the first method (Φ_1), and that after the quenching correction and after the background subtraction were used in the second and third method (Φ_2, Φ_3), respectively. The first method should be the most reliable result. The aim of the comparison among these results was quantitatively assessing the fluctuation due to the treatment of the background and the quenching effect.

Second, the forth candidate of the total flux Φ_4 was evaluated from the number of beam pulse estimated in another way. The number of beam pulse $\tilde{N}_\gamma$ could be obtained as,

$$\tilde{N}_\gamma = f_{\text{laser}} \times T, \tag{3.23}$$

where f_{laser} and T were the effective repetition frequency of the laser (=16 kHz) and the measurement time, respectively. It should be noted that $\tilde{N}_\gamma$ was the number of the timings that the Compton scattering can occur, whereas the N_γ was the number of the events when the photons were detected by the detector. Thus, we must properly treat the possibility of the zero-photons-injection event to obtain the total flux from $\tilde{N}_\gamma$. Since the probability mass function of the photon multiplicity was approximately equivalent to the Poisson distribution, we assumed this distribution to deduce the probability of the zero-photons-injection event. The probability mass function of the Poisson distribution $P_\lambda(n)$ with the mean of λ was written as,

$$P_\lambda(n) = \frac{\lambda^n}{n!} e^{-\lambda}. \tag{3.24}$$

We assumed the weight factor w_n was proportional to $P_\lambda(n)$. The weighted mean of w_n, $\tilde{m}$ was given as

$$\tilde{m} = \sum_n n w_n. \tag{3.25}$$

Then, the relation below held between λ and $\tilde{m}$

$$\tilde{m} = \frac{\lambda}{1 - e^{-\lambda}}. \tag{3.26}$$

The λ was uniquely determined by numerically solving this formula, because the right hand side was the single-valued function of λ. Finally, the total flux Φ_4 was obtained as

$$\Phi_4 = \tilde{N}_\gamma \times \tilde{m}. \tag{3.27}$$

The aim of the comparison with Φ_4 was the evaluation of the possible counting loss due to the data acquisition system.

Third, the last two candidates for the total flux, Φ_5 and Φ_6 were calculated as the corrected version of the Φ given from Eq. (3.14). The contribution from the events with higher photon-multiplicity was considered here. The number of basis employed in the template fitting procedure was 60, and the multiplicity more than 60 was ignored in Eq.

Table 3.1: Summary of Φ_i. The average of the difference between Φ^i and Φ normalized with Φ is displayed in the second column. The systematic uncertainty involved with the assumption adopted for the derivation of Φ should be at most within these values.

i	$\langle \Delta\Phi^i/\Phi \rangle$	note
1	+0.3%	m w/ BG & quenching corr.
2	+2%	m w/ quenching corr.
3	+4%	m w/ BG corr.
4	+4%	$\tilde{m}$ and # of the Compton scat.
5	+0.4%	higher n corr. 1
6	+0.3%	higher n corr. 2

(3.14). The correction was made from asymptotic behavior of w_n deduced from w_n at the region of $n \sim$60. w_n were fitted with the exponential function

$$f_{\rm asym}(n) = \exp(p_0 + p_1 n). \tag{3.28}$$

The interval of n involved in this fitting was widely (narrowly) chosen for Φ_5 (Φ_6), thus p_0 and p_1 for Φ_5 and Φ_6 were different. By adding the contributions of the asymptotic behavior of w_n, the total photon flux expressed in the Eq. (3.14) was corrected as,

$$\begin{aligned} \Phi_{5/6} &= \sum_{n=1}^{60} n w_n + \sum_{n=61}^{\infty} n w_n \\ &\sim \Phi + \int_{61}^{\infty} x f_{\rm aym}(x) dx \\ &= \Phi + \frac{1 - 61 p_1}{p_1^2} \exp(p_0 + 61 p_1). \end{aligned} \tag{3.29}$$

The aim of the comparison with Φ_5 and Φ_6 was check the fluctuation originated by adding the w_n at higher n in Eq. (3.14).

We examined the difference for each measurement and evaluate the ratio of the difference over Φ, namely $(\Phi_i - \Phi)/\Phi$. The results are summarized in Table 3.1. $\langle \Delta\Phi^i/\Phi \rangle$ are the normalized difference normalized over the all measurements. As shown in Table 3.1, the averages took positive values, whereas the this value took negative values for some runs. The averaged difference had the largest value of +4% with Φ^3 and Φ^4. This meant that the Φ tended to be 4% smaller value than those obtained from the procedures in which the quenching effect or the average number of photons treated under the different assumptions. The systematic uncertainty on Φ would be less than the difference between Φ_i and Φ itself. Thus, we conclude that the systematic uncertainty on Φ was at most within $\pm$ 4%. This uncertainty is similar magnitude with one estimated in the previous study [184], which was 3.5%.

3.2.5 Energy Profile Estimation

The energy profile of the beam particle was essential to obtain the cross section. A Monte Carlo simulation was performed to estimate the energy profile of the photon beam. The simulation incorporated the effect of the random production of the beam particles, the process of their interaction with the material on the beam line, and the response of the beam monitor. The Geant4 toolkit [188] was used to implement the particle tracking process in the simulation. The version of the Geant4 employed in the study was 4.10.04.

In the simulation process, the photon beam was randomly generated based on the realistic situation. First, the position of the Compton scattering between a laser photon and a electron was randomly generated. The z (longitudinal) -position was generated within the interval around the waist of the electron beam, and the x- (horizontal) y- (vertical) positions were then generated by taking the z-dependence of the spot size of the electron and laser into account. Finally, the Compton scattered photon beam was generated at the position by simulating the Compton scattering based on the Klein-Nishina formula.

In order to track the interacting process of the photon beams, the beam line elements were virtually positioned in the simulated geometry to reproduce the configuration of the present measurement. As mentioned earlier, the pair of collimators made of lead played the main role to limit the angle of the Compton scattering. In addition, the the beam shutter and the absorber for the radiation lights were also taken into account. Since their aperture were much larger than that of the collimators, their effect on the beam particle tracking were minor. The beam monitor was virtually installed at the downstream end of the beam line. We adopted the physics list provided as "EM Standard Physics" in the Geant4 library in which the electromagnetic interaction of electrons and photons in the energy range up to 10 TeV was covered.

The total beam energy deposit E in the beam monitor was counted for each event. The information of the total energy was deteriorated due to finite resolution of the detector. We adopted the normal distribution $\mathcal{N}(E, a\sqrt{E})$ to generate the output of the beam monitor, where $\mathcal{N}(\mu, \sigma)$ meant the normal distribution of the mean of μ and the standard deviation of σ. As the parameter a, 0.1 ($\mathrm{MeV}^{1/2}$) was adopted so as to reproduce the measurement result.

The parameters for the simulation was tuned to reproduce the energy spectra obtained by the measurement with the low-intensity beam. In the present work, we adjusted the electron beam emittance in the x direction for each measurement condition. The incident energy spectrum of the LCS photons estimated by the simulation is shown in the upper panel of Fig. 3.5, and its deduced energy-deposit spectrum folded with the finite energy resolution of the NaI (Tl) detector is shown in the lower panel of Fig. 3.5. Energy spectrum measured with the beam monitor was reproduced by the deduced energy-deposition spectrum. Therefore, we could deduce the raw-energy spectrum of the incident beams.

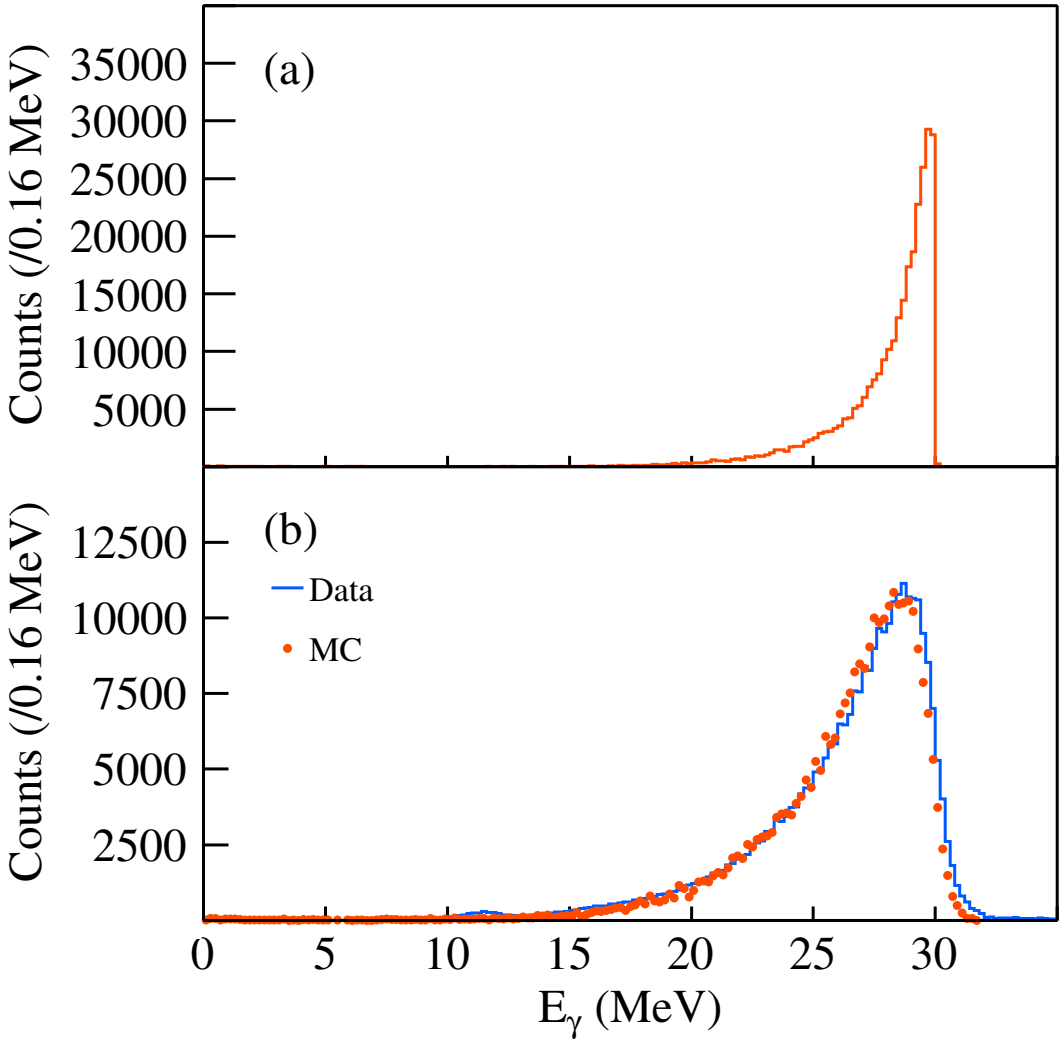

Figure 3.5: Energy spectrum of the LCS photons estimated by the Monte Carlo simulation (a), and the energy-deposit distribution measured with the NaI (Tl) beam monitor (b). when the maximum LCS-photon energy was 30.0 MeV. The solid line in (b) shows the measured spectrum whereas the solid circles are obtained by the Monte Carlo simulation. These figures are taken from Ref. [1].

3.3 Analysis of Decay Particles

The decay particles from the photodisintegration were measured with the MAIKo active target installed in the GACKO beam hutch on the BL01 beam line. The decay particle information, namely the image of the particle trajectories and the energy deposition in the sensitive volume, was acquired event by event. The trigger for the data acquisition was decided based on the signals induced on the MAIKo active target, which was independent from the data acquisition timing by the beam monitor.

A tracking analysis was performed to obtain the physical quantity of the event from the acquired image. Vast numbers of the background events were included in the acquired data set because the trigger condition was set loosely. Moreover, the acquired images were occasionally contaminated with the instrumental noise event in the photodisintegration event. Therefore, the noise pixels were removed by the data cleansing analysis before the tracking analysis. Then, the tracking analysis was performed on the processed data. Finally, most of the background events were cut out from the analyzed event set based on the robust criteria.

More detailed analysis based was performed on the data set to extract and sort the $^4\mathrm{He}(\gamma, n)^3\mathrm{He}$ and $^4\mathrm{He}(\gamma, p)^3\mathrm{H}$ events. In this process, the cut conditions dedicated to each reaction were established based on the geometry of the trajectories and energy deposits along those. The events passed the cut conditions were sorted with the emission angle from the event vertex.

The detection efficiency for the $^4\mathrm{He}(\gamma, n)^3\mathrm{He}$ and $^4\mathrm{He}(\gamma, p)^3\mathrm{H}$ reactions were evaluated by using a Monte Carlo simulation. Pseudo data set generated with the simulation was processed with both tracking and selection analysis. The efficiencies were estimated at each emission angle and in each division of the beam energy.

3.3.1 Preprocessing and Tracking Analysis

There are two purposes for the tracking analysis. One was roughly selecting the photodisintegration-event candidates from the vast event set acquired, and another was extracting the physical quantity such as shape (length, angle) of the trajectories and the energy deposit. In this section, the explanation follows the timeline of the analysis. First, the typical data obtained from the various origins will be displayed. Next, the data cleansing method we applied to remove noise pixels in the obtained in the trajectory images will be explained. Then, the tracking algorithm will be described. Finally, the criteria for the data reduction will be given.

Recorded Events

Since the trigger for the data acquisition was set loose, various types of events were recorded in addition to the $^4\mathrm{He}$ photodisintegration event. Each type of events had

the distinctive features. The typical data originated from various types of events are displayed in the following paragraphs and Figs. 3.6–3.12. These figures include the digital hit pattern images and analog signal shapes. The filled regions in the hit pattern images indicate the time-over-threshold (TOT), or the time duration when the signal pulse from the strip is higher than the threshold value.

Here after, we call the hit pattern of anode (cathode) strips as the ZY (XY) image. The direction of the photon beams are parallel to the Z axis and normal to the XY image. The horizontal center of the beam was located above the strip electrode at $X = 124$ in XY image. On the other hand, the vertical position of the track images are depend on events, since the time difference between the trigger and the beam injection, which determines the vertical position of the trajectories in the image, varies depending on the vertical extension of the trajectories towards the bottom of the image.

First, a typical event data interpreted as ^{4}He$(\gamma, n)^3$H is shown in Fig. 3.6. There is a thick short line extending from the beam position on the XY image. This line is the trajectory of ^{3}H from the ^{4}He photodisintegration, whereas the neutron does not make any trace in the image because the active target is insensitive to neutral particles. The energy deposit (dE/dx) of ^{3}He is relatively large in the particles detected in the present experiment. This fact is recognized in the recorded signal shape. The amplitude of the signal induced by the ^{3}He is the largest among the decay particles (p, ^{3}H, ^{3}He) emerging from the ^{4}He photodisintegration reaction. Thanks to the optimization of the target thickness, the length of the ^{3}He trajectory is short enough to stop inside the sensitive volume.

Second, an example of the event data recording the ^{4}He$(\gamma, p)^3$He is displayed in Fig. 3.7. There are two long lines. The thicker one is the trajectory of the ^{3}H, whereas the thinner one is that of the proton. The difference of dE/dx between the proton and the ^{3}H can be seen in the signal shape. Since the dE/dx of both the proton and the ^{3}H is smaller than that of the ^{3}He, the trajectories of them are long enough to escape from the sensitive volume.

Third, two background events attributed to the ^{12}C$(\gamma, n)^{11}$C and ^{12}C$(\gamma, p)^{11}$B reactions are shown in Figs. 3.8 and 3.9. In Fig. 3.8, only one very short thick line interpreted as the trajectory of ^{11}C is seen. On the other hand, in Fig. 3.9, one can see both the long thin and short thick line: the trajectory of proton and that of ^{11}B. The property of the acquired image involving the length of the trajectories is greatly different from those of ^{4}He photodisintegration reactions. Therefore, the contamination of these events can be removed by the property given from the particle tracking analysis.

Forth, another background events caused by the Compton scattered electrons is displayed. The thin zigzag traces of the electrons are recorded in Fig. 3.10. Since, the dE/dx of the electrons are far smaller than that of nuclei, these events are distinguishable from the photodisintegration events based on the amount of the energy deposit.

Fifth, an image produced by the instrumental noise is shown in Fig. 3.11. Electric noise was occasionally induced on the μ-PIC by the short term discharges. The noise

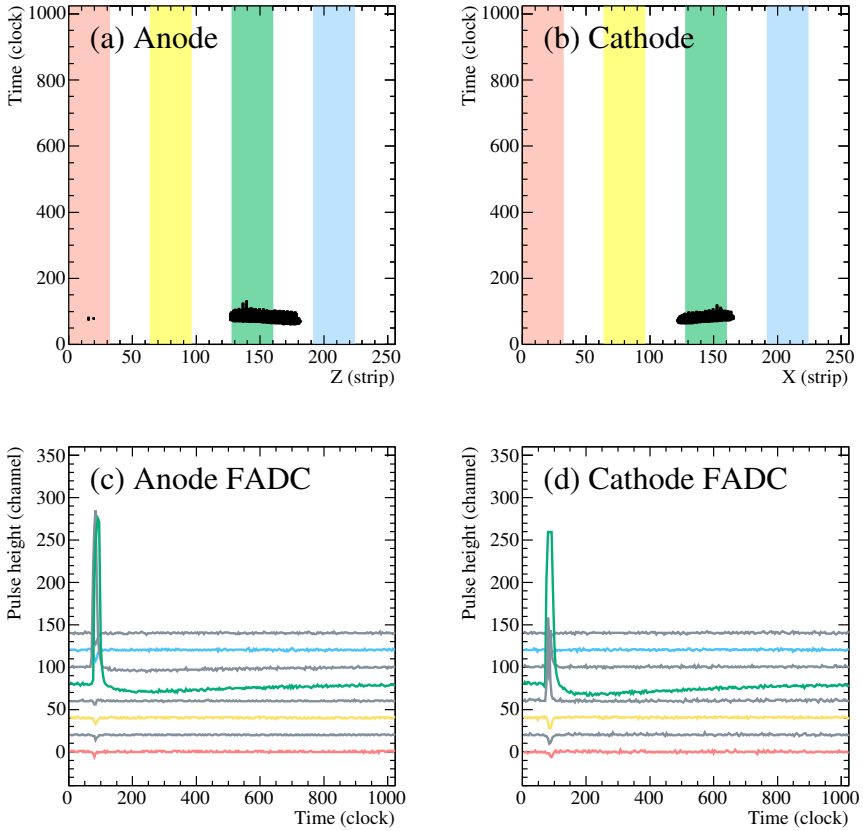

Figure 3.6: Typical event attributed to the ^{4}He$(\gamma, n)^3$He reaction obtained from the measurement at $E_\gamma = 30.0$ MeV. Upper panels show digital hit pattern readout from the anode (a) and cathode (b) electrodes. Blacked out areas indicate the time over threshold (TOT) of the signals, and highlighted regions show the channel division for the FADC readout. The lower panel (c) and (d) display the analog signal shape from the anode and cathode electrode, respectively. Signals in the panels are shifted upwards for visibility: the lowest line is the signal from the strips whose index is within [0,31]. The colors of the colored lines correspond to the color of highlighted regions in the upper panels.

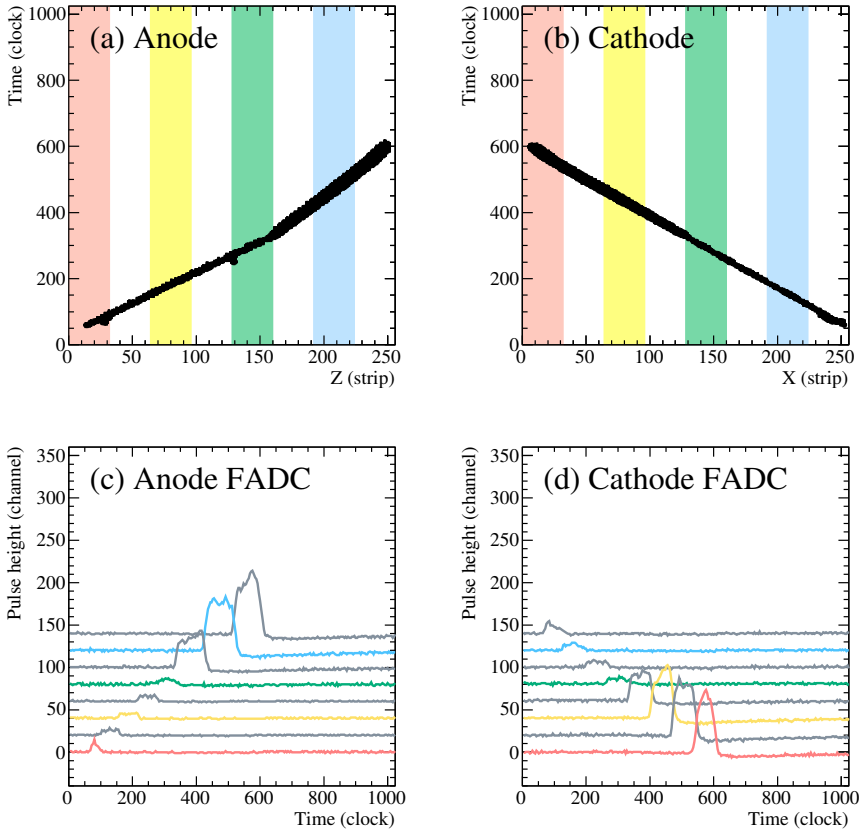

Figure 3.7: Typical event attributed to the $^4\mathrm{He}(\gamma, p)^3\mathrm{H}$ reaction obtained from the measurement at $E_\gamma = 30.0$ MeV. The definitions of the panels are same as Fig. 3.6.

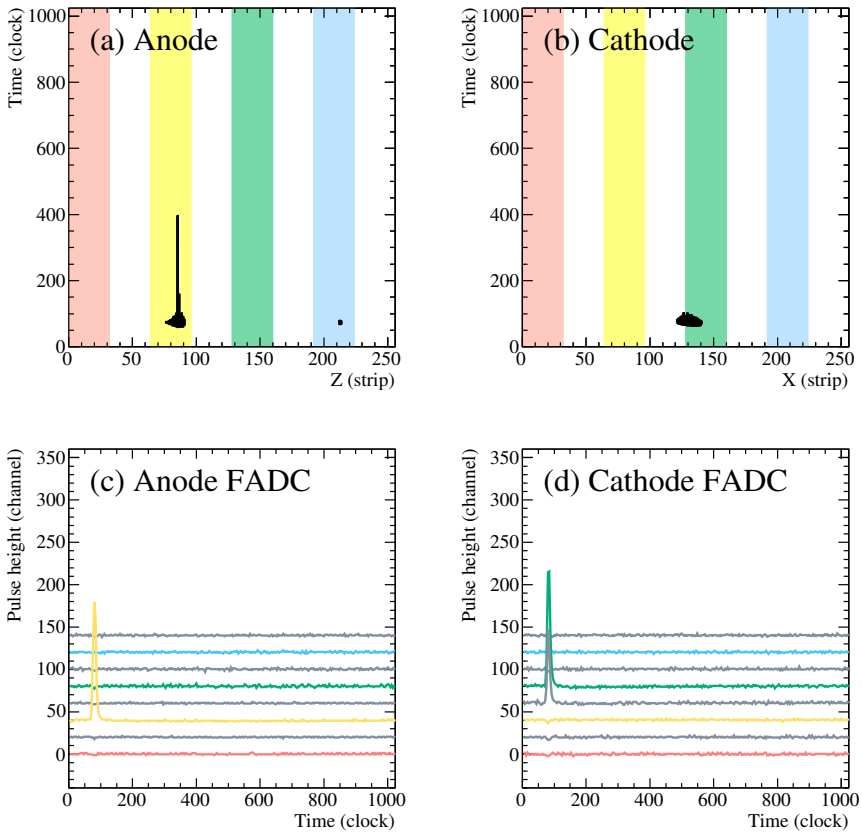

Figure 3.8: Typical event attributed to the $^{12}\mathrm{C}(\gamma, n)^{11}\mathrm{C}$ reaction obtained from the measurement at $E_\gamma = 30.0$ MeV. The definitions of the panels are same as Fig. 3.6.

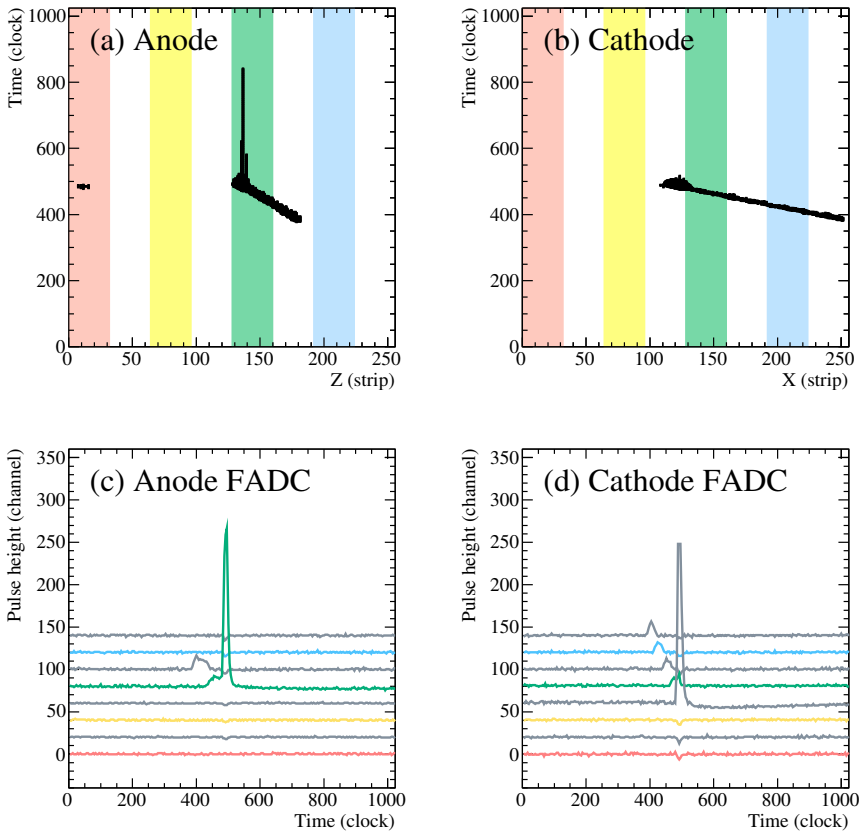

Figure 3.9: Typical event attributed to the $^{12}\mathrm{C}(\gamma, n)^{11}\mathrm{B}$ reaction obtained from the measurement at $E_\gamma = 30.0$ MeV. The definitions of the panels are same as Fig. 3.6.

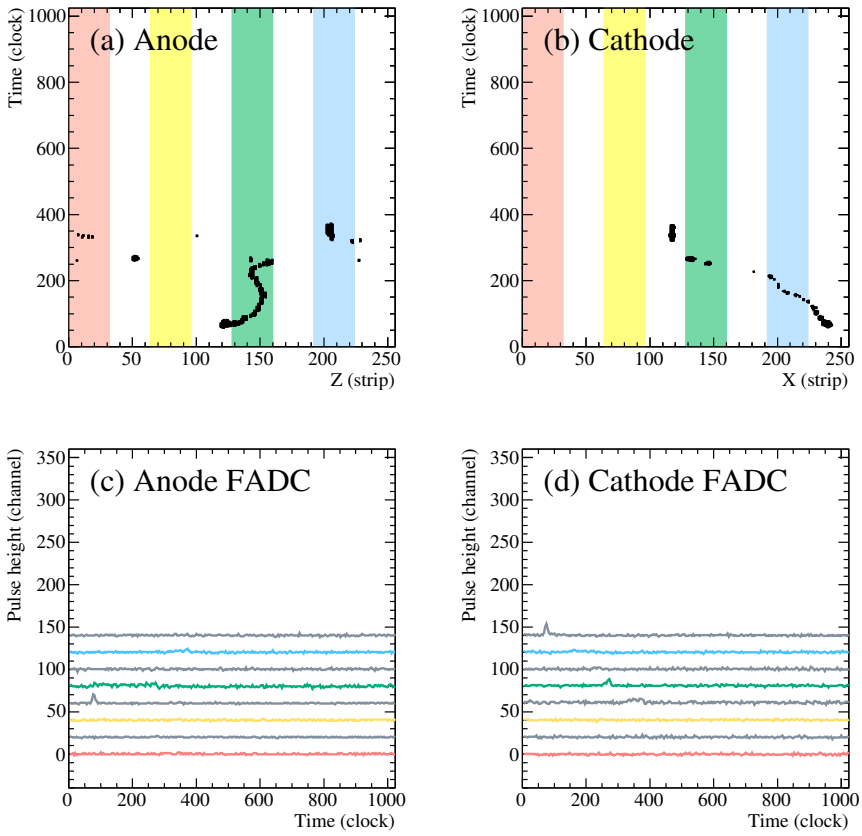

Figure 3.10: Typical event attributed to the Compton scattering obtained from the measurement at $E_\gamma = 30.0$ MeV. The definitions of the panels are same as Fig. 3.6.

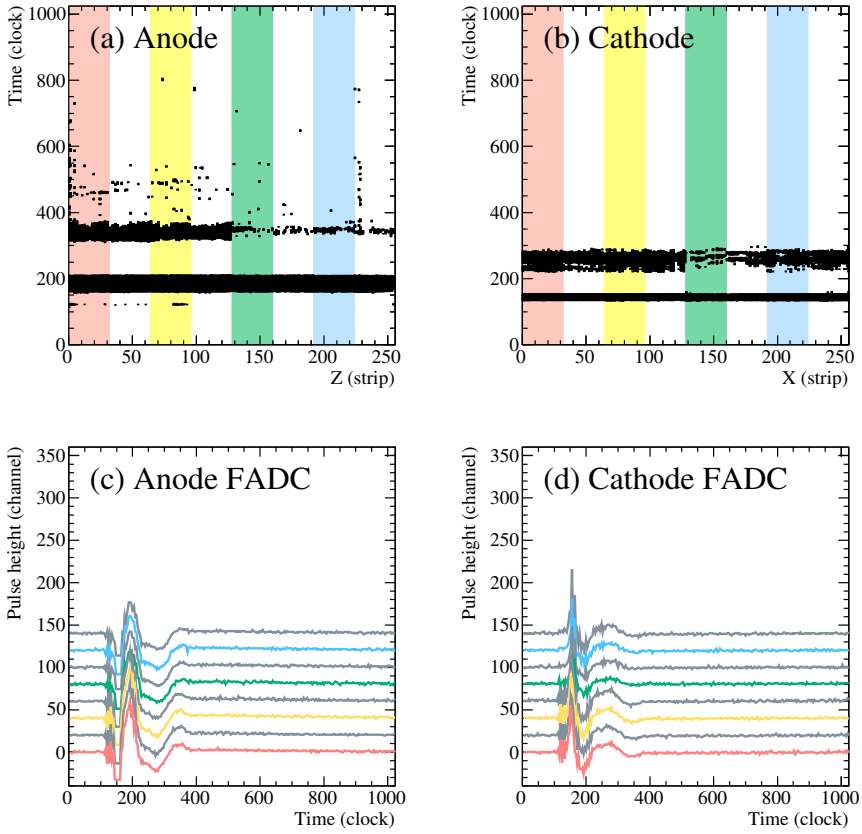

Figure 3.11: Typical event attributed to instrumental noise obtained from the measurement at $E_\gamma = 30.0$ MeV. The definitions of the panels are same as Fig. 3.6.

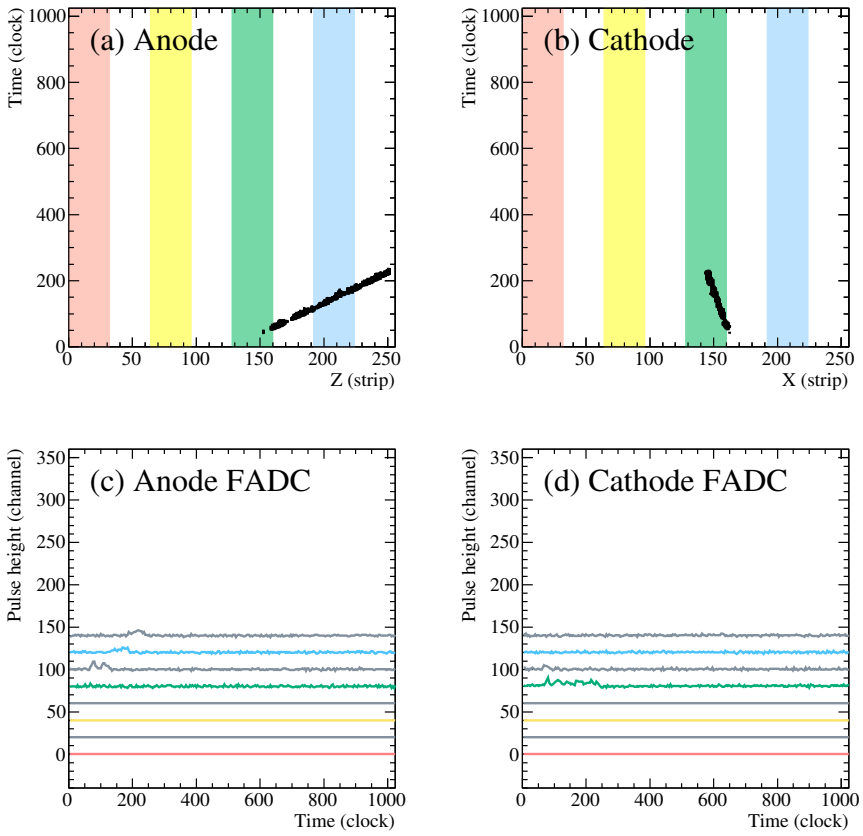

Figure 3.12: Typical event attributed to reactions occurred outside the sensitive volume obtained from the measurement at $E_\gamma = 30.0$ MeV. The definitions of the panels are same as Fig. 3.6.

also produce the trigger system when its pulse height is higher than the threshold. The images are covered by the large noise signals. The large undershoot can be seen in the signal shape, which is the unique feature associated with the noise event. Thus, the signal with a large amplitude toward the opposite polarity can be utilized to reject this events.

In addition to the event described above, the events triggered by the charged particles from the photodisintegration occurred out of the sensitive volume were also recorded (Fig. 3.12). In most cases of these events, no trajectories are detected within the region in the vicinity of the beam axis that extends parallel to the axis. Conversely, the all the trajectories extend from the beam region in the proper events. Therefore, the contamination of these events can be reduced by using the signal amplitude around the beam position in the XY plane.

Data Pre-processing

Several quantities were calculated from the raw data before the following analysis. Hereafter, we define signal on an individual strip as a hit.

First, the hit information in strips, namely leading edge and the time over threshold (TOT), were calculated. The acquired pixel data in the black-and-white pattern were sorted and grouped into the timely (vertically in the image) neighboring pixels in the same strip. Each group corresponds to one signal induced on the strip. The height of the lowest pixel in the group is defined as the position of the leading edge of the signal, and the vertical distance between leading edge and the highest pixel in the group was defined as the TOT of the signal.

Second, the energy deposit is calculated from the wave form. The integration of a pulse is proportional to the amplitude of the energy deposit. This integration was performed over the time interval where the signal height is larger than the threshold value. In order to define the integration interval robust against noises, signal smoothened with the moving average filter was compared with the threshold. The interval from when the signal height exceeded the threshold to when it fell below the threshold again was defined as the integration interval. All the energy deposit values were sorted by the timing and the channels of FADC. Hereafter, the energy deposit on the j th FADC segment (from $32j$ th to $32j+31$ th strips of μ-PIC) is denoted as ΔE_j, and the energy deposit summed over all the segments is indicated as E.

Third, the correspondence between the hits and energy deposits was determined. If an energy-deposit signal both timely and spatially overlaps a his on a strip, this energy deposit is associated with the hit. Since the FADC signals are the sum of the adjacent 32 strips, one energy deposit information is associated to multiple hits on the strips.

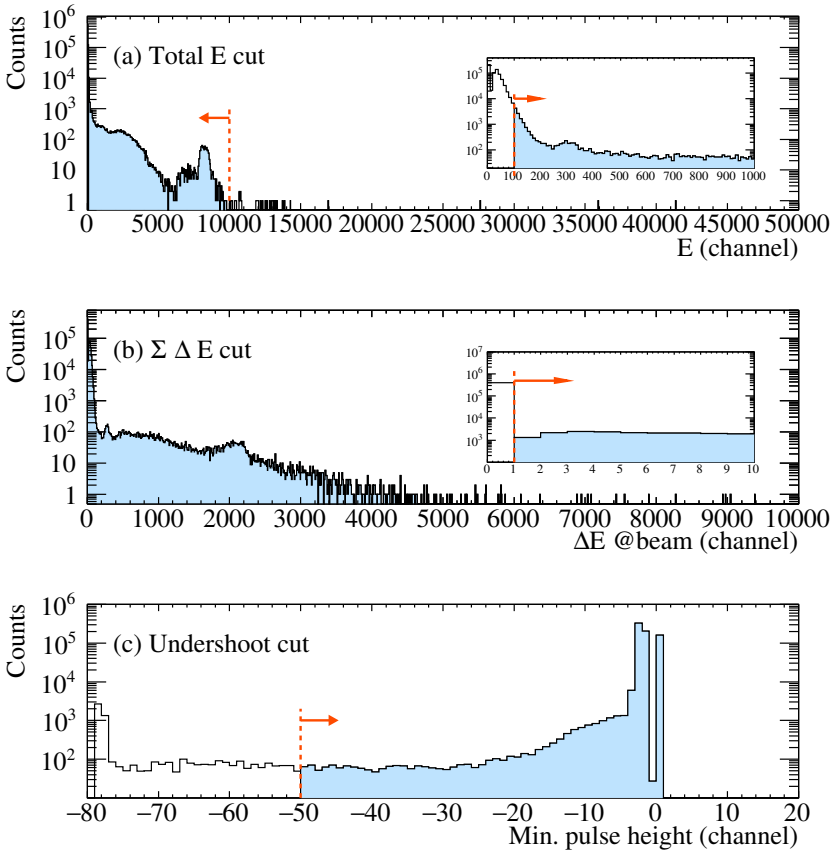

Figure 3.13: Cut condition imposed in the data reduction procedure: each panel shows the cut condition regarding (a) total E, (b) $\Sigma\Delta E$, and (c) undershoot of the signal. Insets are the enlargements of the corresponding panels. The data are results of the measurement at $E_\gamma = 30.0$ MeV. The selected parameter regions are shown with the filled areas in the panels.

Data Reduction

The event set acquired in the present measurement contains the vast number of background. It is desirable to remove these events without affecting true events. We imposed three conditions to reduce background events. These conditions are shown in Fig. 3.13.

First one is related to the sum of energy deposits E (the upper panel in Fig. 3.13). Events with smaller total energy deposit and larger total energy deposit are removed. The total energy deposit of events induced by the Compton scattering (See Fig. 3.10) is smaller than that of photodisintegration events, whereas the energy deposit of events induced by the discharge is larger (See Fig. 3.11) . Second one is related to the energy deposit summed over the region around the beam axis $\Sigma\ \Delta E_j$ (the middle panel in Fig. 3.13). Events of no energy deposit associated with the FADC channels around the beam axis are removed. Photodisintegration events occurring inside the sensitive volume have finite energy deposit around the beam axis, whereas those occurring outside do not

necessarily have energy deposit in this region (See Fig. 3.12). Third one is related to the minimum pulse height of signals observed with FADC (lower panel in Fig. 3.13). Events with signal of large undershoot are removed. Noise events induced by the discharge tend to have signal of large undershoot (See Fig. 3.11).

These criteria of event selection were set loose enough so as not to exclude the ^{4}He photodisintegration events. After this selection procedure, the number of events was reduced one order of magnitude.

Data Cleansing

Before tackling with the tracking analysis, the data cleansing on the XY and ZY images was performed. The purpose of this procedure is remove the obviously false-hit pixels included in the images by using a simple algorithm.

In the present measurement, false-hit pixels caused by two different origins were observed (See for example (a) in Figs. 3.6, 3.8, and 3.9). That is caused due to the cross talk in the electric lines on the readout board. Signal lines that are 128 channels (half of the full width of the images) apart are fabricated close to each other on the read-out board. When a significantly large signal passes thorough a signal line, the crosstalk occurs on the signal line that is 128 channels away from it. Signals originating from crosstalk are observed as a signal pulse of opposite polarity than that of ordinary one. Occasionally, these signal make a hit in images. The other factor is electric noise cased in other reasons. Hits originating from noises have smaller TOT than that of ordinary one.

Hits caused by the noises should be removed before tracking analysis. In order to achieve the purpose, we performed the data cleansing of the hit images using energy deposits and the TOTs. The hits originating from crosstalk spawn a certain distance away from the real hit and is not associated with the energy-deposit. When a hit overlaps other hit 128 channels away and no energy deposit information are associated with either one, the hit of no-energy-deposit is removed. In addition, the hits originating from electric noise has smaller TOT than that of ordinary one. When the TOT of a hit is smaller than the threshold, that hit is removed from the images.

Tracking

Trajectories of decay particles are reconstructed from the processed ZY and XY-image by a certain tracking algorithm. The algorithm consists of five steps described below. In these steps, only the leading edges of the pixels were used because the TOTs of signals varied drastically depending on the reaction channels and occasional discharges. These steps is designed to work correctly for "good" events containing 2 or less trajectories, and to actively eliminate other events. If processing for an event fails during any of these steps, processing for that event is terminated. The tracking procedures described below are schematically shown in Figs. 3.14.

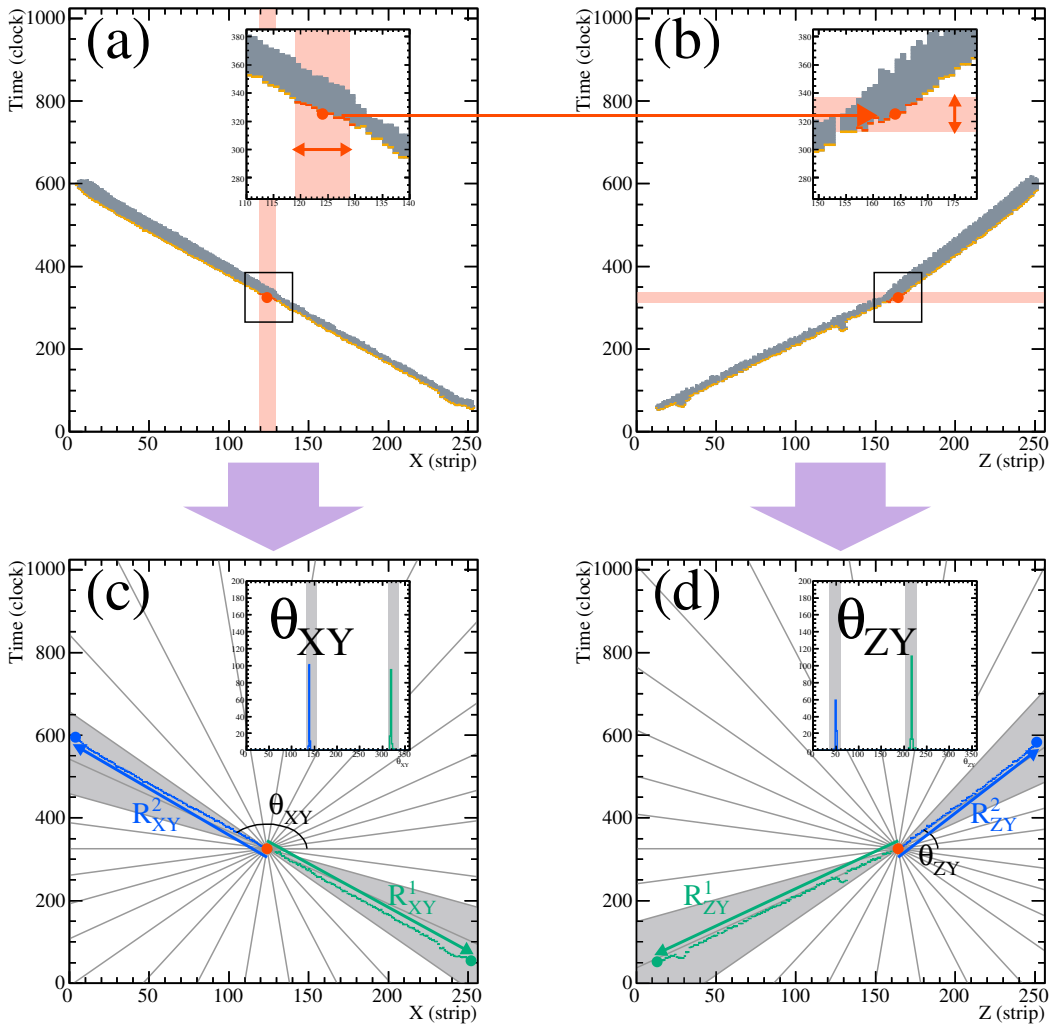

Figure 3.14: Tracking procedures. The vertex search in XY image (a) and that in ZY image (b) are shown in the upper panels. Filled regions in the panels are the hit pattern and their leading edges on their bottom are highlighted. In addition, the inset panels are the enlargement of the region near the vertex. The vertex positions in each panel are shown with the filled circles. First, the vertex position in XY image (a) is determined within the region spanning ± 2mm from the beam position. Then, the vertex in ZY image (b) is obtained using the Y position of the vertex. The tracking in XY image (c) and that in ZY image (d) are shown in the lower panels. The hits in the panels are sorted with the angular divisions shown with the radial lines from the vertex. The populations of the angles θ_{XY}, θ_{ZY} are shown in the inset panels. There exist two localized peaks, and these clusters are attributed to the trajectories.

First, the position of the reaction point (vertex) in the image is determined. This procedure is first done for the XY image and then the ZY image, they are shown in the panels (a) and (b) in Figs. 3.14. The horizontal position of the beam center is regarded as the X position of the vertex in the XY image. This value is fixed at $X = 124$ for all the events acquired. This position was determined from the TOT distribution shown in Fig. 3.15. The Y position of the vertex is determined from hits in the XY image (a). Median of Y positions of all hits within $\pm$ 2 mm to the left and right of the X position of the vertex is used as the Y position of the vertex. This region is shown with the vertically elongated highlighted region in the panel (a) in Figs. 3.14. Based on the Y position, all the hits within 2 mm to the below and above the Y position of the vertex in the ZY image (b) are extracted. This region is shown with the horizontal highlighted region in the panel (b) in Figs. 3.14. The Z position of the vertex is set to the z position of the hit which is the nearest to the vertex in the Y direction.

Next, the maximal number of trackable trajectories are counted in the XY image. This step is done by counting the number of hits more than 10 mm apart from the vertex in XY image. When the number of these hits in both the left and the right halves of the XY image is more than one, the number of trackable trajectories of the event is two. If the number of these hits in either the left or the right halves of the image is more than one, the number of trackable trajectories of the event is one. Otherwise, the number of the trackable trajectories is set to zero. The events is rejected if the number of the trackable trajectories is zero.

Then, the hits that exist radially around the vertex into groups that are aligned in a straight line. This procedure is schematically shown in the panels (c) and (d) in Figs. 3.14. All the hits in the XY and ZY image are classified by the angle of a line between the vertex and the hit. These angles are stored in a histogram with the bin-width of 12 degrees. These histograms for the XY image (c) and ZY image (d) are shown in the insert panels in the corresponding panels. As for the event shown in Figs. 3.14, there are two distinct peaks in the histograms, and they are attributed to the two trajectories. The hits in the bin of the maximal entry and the bins adjacent are extracted as the hit cluster candidate. The hits in the candidate group are checked sequentially in the ascending order of the distance from the vertex. If the distance of the vertex of the hit is much larger than that of the previous hit, the subsequent hits are excluded from the candidate group. After that, the candidate group are categorized as a hit cluster. If the number of trackable trajectories are two, this procedure is repeated for the hits which are not included in the hit cluster nor excluded. Eventually, hits clusters in the same number as the trajectories are found if this step succeeds.

After that, the trajectories in the XY and XZ images are reconstructed independently. The direction of a trajectory (θ_{XY} and θ_{ZY}) is determined by minimizing the sum of the square of the distance between the trajectory and hits in the clusters, whereas the length of the trajectory (R_{XY} and R_{ZY}) is set as the distance from the vertex of the farthest hit in the cluster. In addition, the TOT averaged over the hits in a cluster is associated with the trajectory. As seen in the inset panel in Fig. 3.16, the averaged TOT value $\tilde{T}^i_{XY/ZY}$ of the i th trajectory in XY or ZY image had the correlation with the direction of the

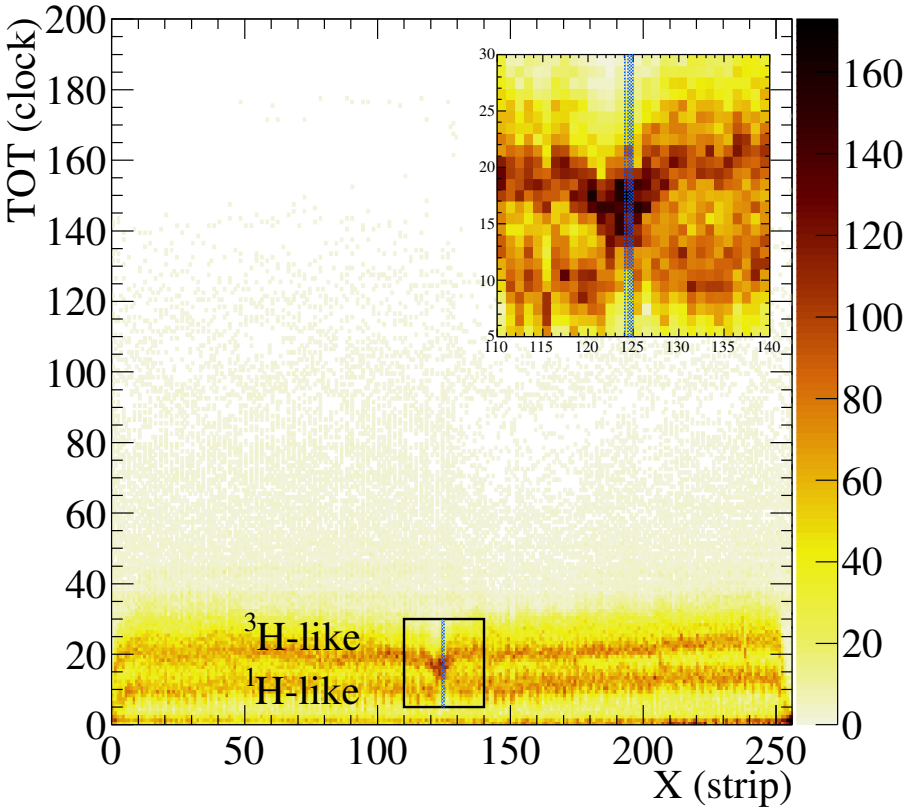

Figure 3.15: Position dependence of the TOT in cathode signals, which was used for the beam position estimation. The TOT of all the hits in the selected events from the from $E_\gamma = 30.0$ MeV measurement are shown. Events fulfilling the cut conditions, (1) smallest X among hits is less than 10, (2), largest X among hits is more than 240, and (3) E is not so small, were selected so as to choose select the events that having horizontally elongated tracks, which is the characteristic of ^{3}He$(\gamma, p)^3$H events. Because of the difference in the energy deposit profile, there exist two horizontal loci in the panel: locus above (below) is attributed to the tracks of ^{3}H (^{1}H). These loci would cross at the beam position where the reactions occur. As seen in the inset figure indicating the enlargement, that crossing point is on the highlighted square placed at $X = 124$ strip. Thus, the beam position in the present measurement was approximated to be at $X = 124$.

trajectory. That is corrected using the direction of the trajectory in the image $\theta_{XY/ZY}$ by

$$\tilde{T}^i_{XY/ZY} = T^i_{XY/ZY} |\cos\theta_{XY/ZY}|, \tag{3.30}$$

where $T^i_{XY/ZY}$ is an averaged raw TOT value in XY or ZY image. The result of the correlation is shown in Fig. 3.16. We can see sharp peaks associated with the specific particles in the corrected TOT. The ^{1}H-like component contaminating 1-track events implies the necessity of the further selection analysis described later.

Finally, the trajectories are reconstructed in three-dimensional space by matching the trajectories in the XY and ZY images. The matching criteria is based the Y positions of the end point of trajectories. A pair of trajectories in XY and ZY images having similar end point height (within 10 mm) is regarded as a candidate of the matching. However, no pairs are made between trajectories going upward and downward. If this pairing is uniquely determined for a XY trajectory, a three-dimensional trajectory is reconstructed from the pair of trajectories. If the pair candidates of a XY trajectory are duplicated, the ZY trajectory associated with the TOT value similar to that of the XY trajectory is adopted as the true pair. The direction (θ, ϕ) and length R and of the trajectory in three-dimensional space are calculated from the information of the matched trajectories as

$$(\theta, \phi) = \left(\tan^{-1}\left(\frac{\tan\theta_{ZY}}{\sin\theta_{XY}} \right), \theta_{XY} \right), \tag{3.31}$$

and

$$R = \frac{R_{XY}}{|\sin\theta|}. \tag{3.32}$$

Here after, the direction of the trajectory is represented with the polar angle θ and the azimuthal angle ϕ.

Some additional quantity is calculated for each reconstructed track. First, the polar angle of the decay particle in the center of mass frame $\theta_{\rm cm}$ is calculated by using the average beam energy calculated from the energy profile estimated by the simulation. Hereafter, this $\theta_{\rm cm}$ is simply denoted as θ, unless otherwise noted. Second, the information whether the endpoint of the trajectory is inside the sensitive volume or not is associated with trajectories. If the endpoint is inside the sensitive volume, the measured trajectory length is equal to the range of the decay particle, which is related to the kinetic energy of that particle.

Moreover, the energy deposit dE^i of the i th trajectory is calculated by fitting the FADC distribution along the trajectory. The pulse height distribution of a ^{4}He$(\gamma, p)^3$H event is shown in the panel (a) in Fig. 3.17. The intensity of the color is proportional to the pulse height measured by the FADC. The energy deposit ΔE^i on the strip segment associated with the FADC chanel i is obtained from the integral of the signal. The resultant value is shown in the panel (b) in Fig. 3.17. Here, we made a simple approximation that the depth x dependence of the energy deposit of particles associated with the i the trajectory obeys a linear function,

$$\frac{dE}{dx}^i(x) = P^i_0 + P^i_1 x, \tag{3.33}$$

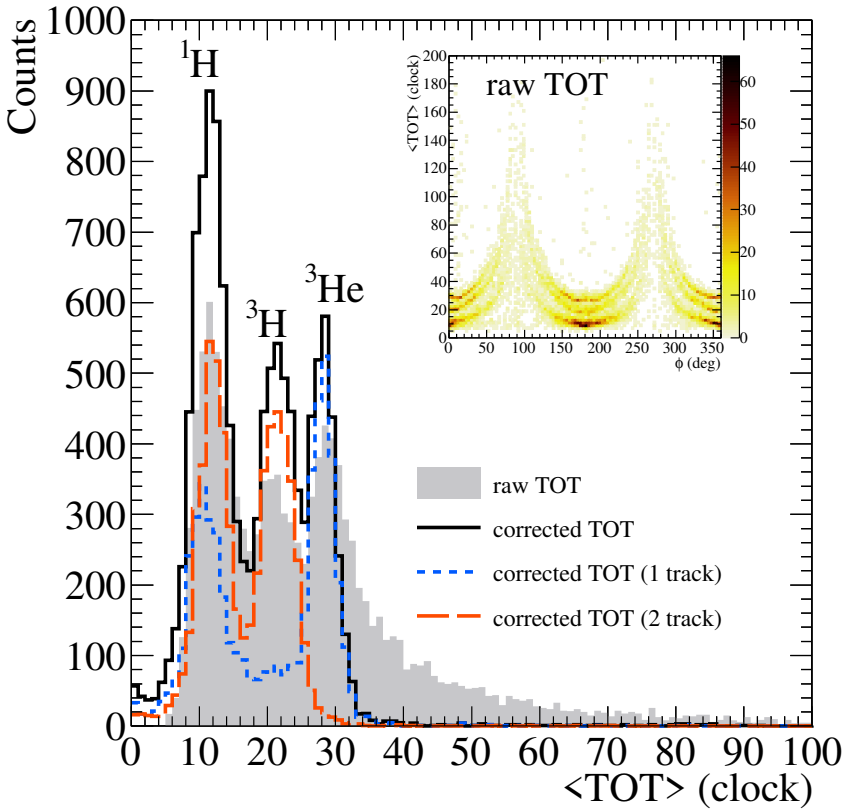

Figure 3.16: Time over threshold (TOT) associated with the trajectory obtained from the measurement at $E_\gamma = 30$ MeV. T^i_{XY}, or averaged TOTs from XY image are shown in the panels. The inset panel shows the angular dependence of T^i_{XY} with respect to the trajectory direction projected on the XY-plane θ_{XY}, namely ϕ. One can see a correlation between T^i_{XY} and θ_{XY}, and that is corrected using Eq. 3.30 to be $\tilde{T}^i_{XY}$. Tha main panel shows the distribution of the raw TOT T^i_{XY} and the corrected one $\tilde{T}^i_{XY}$. The distributions for both 1-track events and 2-track events are also displayed. Three peaks in these distributions are associated with the track of ^{1}H, ^{3}H, and ^{3}He, respectively. There exists ^{1}H-contaminations in 1-track events. They will be excluded by the selection analysis described later.

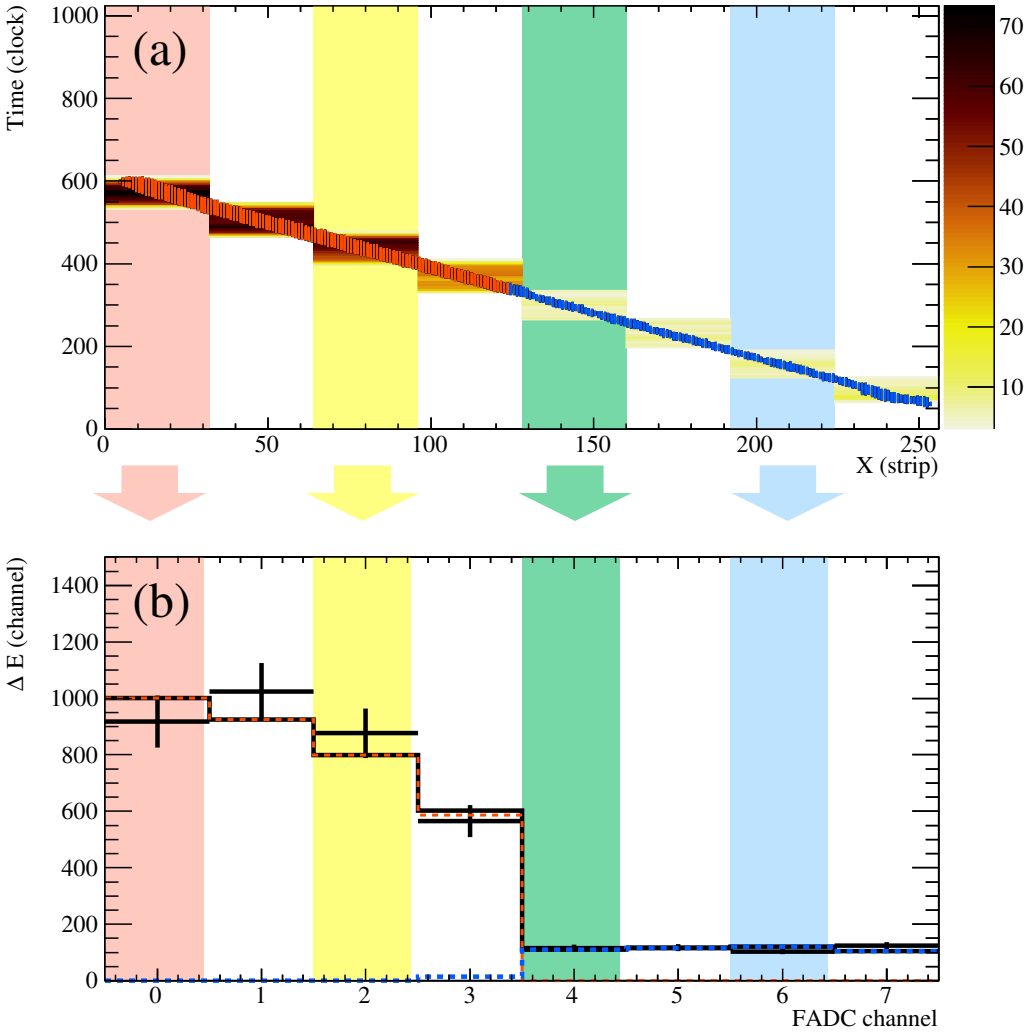

Figure 3.17: (a) Pulse height distribution of a ^{4}He$(\gamma, p)^3$H event and (b) its ΔE distribution. In the upper panel, the pulse heights of the measured signals are shown by the intensity of the color. The XY track image is also shown with colored region where hits attributed to the ^{3}He track (p track) going left (right) is colored in red (blue). In the lower panel, The energy deposits ΔE_j on each strip segments (j) calculated from the integral of the signals are shown. ΔE_js are depicted by cross-shaped markers, and the correspondence with the signals shown in the upper panel is displayed by background colors and the vertical arrows. ΔE_js estimated by the fitting based on Eq. 3.34 is shown with the solid line. Fractions of the contribution from each decay particle is also shown with the dashed lines.

where P_0 and P_1 are free parameters. In consequence, the total energy deposit ΔEj on a j th FADC segment (from $32j$ th to $32j+31$ strips) are approximately given as

$$\begin{aligned} \Delta E_j &= \sum_{i=1}^{n_{\rm track}} \left\{ \frac{dE}{dx}^i (x_j^i) \right\} \Delta x_j^i \\ &= \sum_{i=1}^{n_{\rm track}} \left\{ P_0^i + P_1^j x_j^i \right\} \Delta x_j^i, \end{aligned} \tag{3.34}$$

where $n_{\rm track}$, x_j^i, and Δx_j^i are the number of trajectories, the depth of the i th trajectory on the j th FADC segment, and the length of the trajectory on the j th FADC segment. The depth x_j^i is measured between the reaction point to the mid point of the trajectory segment on the j th FADC segment. Observed energy deposit on all the FADC strip is fitted to the formula Eq. (3.34) optimizing the free parameters. Finally, the energy deposit dE^i of the i th trajectory is calculated as

$$\begin{aligned} dE^i &= \int_0^{L_{\rm seg}} \left\{ P_0^i + P_i^j x \right\} dx \\ &= P_0^i L_{\rm seg} + \frac{1}{2} P_1^i L_{\rm seg}^2. \end{aligned} \tag{3.35}$$

Here, $L_{\rm seg}$ is the width of a FADC segment (32 strips = 12.8 mm). dE^i is equivalent to the energy deposit of decay particle i as it travels 12.8 mm from the reaction point.

3.3.2 Selection Analysis

In order to count number of the ^{4}He$(\gamma, n)^3$He and ^{4}He$(\gamma, p)^3$H events acquired, a selection analysis was performed on the tracking results. As a result of the tracking analysis, events of successful tracking analysis are categorized with the number of reconstructed trajectories. The main component of events including one reconstructed trajectory is the ^{4}He$(\gamma, n)^3$He events, whereas that including two trajectories is the ^{4}He$(\gamma, p)^3$H events. However, there still remains some contribution of the ^{12}C$(\gamma, n)^{11}$C and ^{12}C$(\gamma, p)^{11}$B events. These contaminating events are excluded by the selection analysis described here.

For the ^{4}He$(\gamma, n)^3$He candidates, we required the five conditions below.

- The number of reconstructed trajectory is one.
- The reaction point is at least 1 cm distant from the edge of the sensitive volume.
- The end point of the trajectory is inside the sensitive volume.
- The correlation between E and the trajectory length is consistent with that of ^{3}He.
- Kinematically reconstructed beam energy is in the range between $E_{\rm max} - 1$ and $E_{\rm max}$ MeV.

These conditions are illustrated in Figs. 3.18. The purpose for the second criterion is rejecting events resulting from reaction occurred near the edge of sensitive volume. This is because the events near the edge are contaminated with some events occurred outside of the sensitive volume. The vertex reconstructed from the data are shown in the panel (c) in Figs. 3.18. The intention of the third criterion is rejecting events resulting from $^{12}\mathrm{C}(\gamma, p)^{11}\mathrm{B}$ reaction, which occasionally misclassified as an event including one trajectory due to shortness of ^{11}B trajectory. The proton trajectory contained in this kind of event is long enough to penetrate through the sensitive volume. The forth criterion aims at simply rejecting some events in which the tracking analysis failed somehow. The correlation between the total E and the range R reconstructed from the data are shown in the panel (a) in Figs. 3.18. The events in the slanting locus in the panel is attributed to the well tracked events, whereas the large population distributing along the horizontal axis are the events caused by intruder protons from the external region (see 3.12). The latter are the origin of the low TOT events in Fig. 3.16. The last criterion plays an essential role to select the $^{4}\mathrm{He}(\gamma, n)^{3}\mathrm{He}$ events. $^{12}\mathrm{C}(\gamma, n)^{11}\mathrm{C}$ events, which is the main source of background events, contain one short trajectory of ^{11}C. Since the range of ^{11}C is far shorter than that of ^{3}He in the desired events, this kind of background events are safely excluded by using the kinematic correlation. The reconstructed beam energy is shown in the panel (b) in Figs.3.18. The width of the accepted region was set narrow. That is because the ^{11}C particles from the $^{12}\mathrm{C}(\gamma, n)^{11}\mathrm{C}$ events could not be separated from the ^{3}He particles solely using the E-R correlation due to the insufficient dynamic range of the electronics.

For the$^{4}\mathrm{He}(\gamma, p)^{3}\mathrm{H}$ candidates, we required five conditions below.

- The number of reconstructed trajectories is two.
- The reaction point is at least 1 cm distant from the edge of the sensitive volume.
- The two trajectory reach the edge of the sensitive volume.
- dE of one trajectory is consistent with that of a proton, and dE of the other trajectory is consistent with that of ^{3}H.
- The two trajectories are oriented in a back-to-back direction in the XY image.

These conditions are illustrated in Figs. 3.19. The second criterion is completely same to that of the former one. The vertex depth distribution is shown in the panel (d) in Figs. 3.19. The third criterion, in contrast, requires the both trajectories are long enough to punch through the sensitive volume. This requirement is automatically fulfilled for $^{4}\mathrm{He}(\gamma, p)^{3}\mathrm{H}$ events thanks to the target thickness optimization. The forth criterion is the strongest condition among them. Only $^{4}\mathrm{He}(\gamma, p)^{3}\mathrm{H}$ events can show the proper dE-dE correlation, and background events resulting from various causes such as ^{12}C photodisintegration and the high-energy proton emitted outside the sensitive volume are excluded by this selection. The dE correlation is shown in the panel (a) in Fig. 3.19. These energy deposit is sorted with their amplitude in the descending order. The last

one is for rejecting the events of more than 3 decay particles. The angle between two trajectories in the center-of-mass system are shown in the panels (b) and (c) in Figs. 3.19. Two trajectories originated from binary reactions must be oriented to the opposite direction due to the momentum conservation. In contrast, events of more than 3 decay particle such as ^{12}C(γ, 3α) and ^{4}He(γ, *pnd*) reactions seldom contains two trajectories going back-to-back direction. The distribution of the relative θ (b) is broader than that of relative ϕ (c). That is because the mean beam energy is adopted to the derivation of *theta*s.

Finally, we defined events satisfying these conditions as true photodisintegration events. These true events are sorted with respect to its decay particle orientation θ and ϕ. Obviously, all the photodisintegration events occurred during the measurement are not contained in the true event group, because some of them are rejected by the tracking and selection analysis. The reaction cross sections are calculated from the measurement yield corrected with the efficiency of the analysis. The efficiency is evaluated by using a Monte Carlo simulation as descried in the next section.

3.3.3 Efficiency Estimation

Efficiency

The efficiency of the analysis is defined as the ratio of the successfully selected events and the all the ^{4}He$(\gamma, n)^{3}$He and ^{4}He$(\gamma, p)^{3}$H events occurred in the target. In this analysis procedure, some true events are rejected in the tracking analysis, and others are excluded in the selection analysis. Therefore, the the efficiency can be evaluated by analyzing the generated data in the same manner as the real data. Then, the survival ratio of the generated data after all the analysis procedure is equal to the efficiency. This efficiency has beam energy and particle-emission angle dependence. The efficiency are evaluated for each polar and azimuthal angular bins with steps of $\Delta\theta = \Delta\Phi = 20^{\circ}$ and beam-energy bins with step of ΔE_{γ}=500 keV over 19–30 MeV.

$$\epsilon(\theta, \phi, E_{\gamma}) = \frac{\#\text{ of selected events at } (\theta, \phi, E_{\gamma})}{\#\text{ of all events at } (\theta, \phi, E_{\gamma})} \tag{3.36}$$

Simulation

A Monte Carlo simulation is developed to evaluate the efficiency of the analysis. The binary photodisintegration events are randomly generated. In the event generation procedure, first, the reaction point was randomly selected in the cylindrical region along the beam direction. The probability distribution function, which was utilized for the reaction point generation, had no longitudinal position dependence, whereas it laterally follows the Gaussian distribution. Next, the emission-angle and kinetic energy of the decay particle is randomly determined. These parameters are selected as it satisfies the momentum and energy conservation.

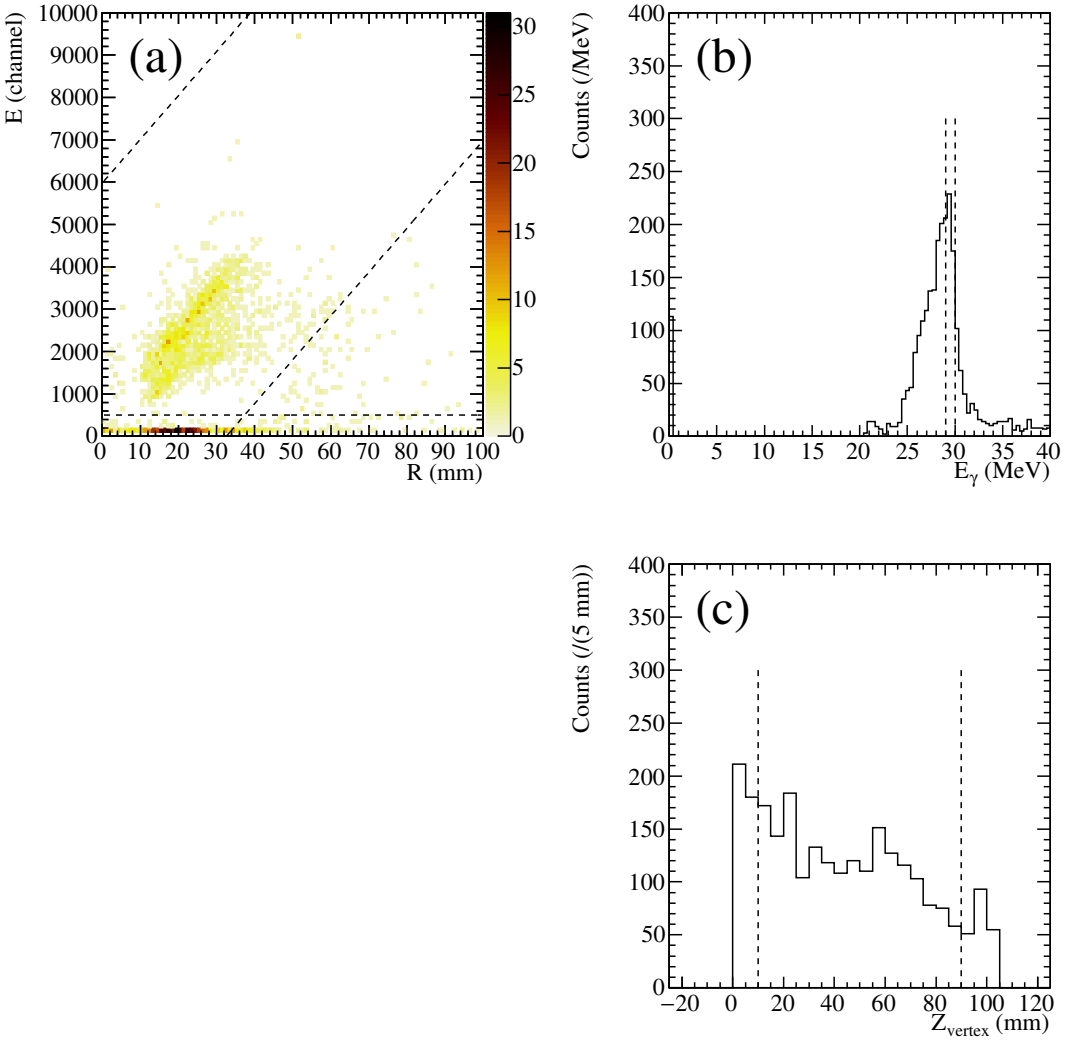

Figure 3.18: Selection analysis for the ^{4}He$(\gamma, n)^3$He event candidates from the measurement at $E_\gamma = 30.0$ MeV. (a) The correlation between the total E and the range R, (b) the beam energy reconstructed from kinematics, and (c) the Z coordinate of the vertex. All the events which contains only one trajectory stopping in the sensitive volume are included in these plots. The conditions imposed on these variables are shown with dashed lines.

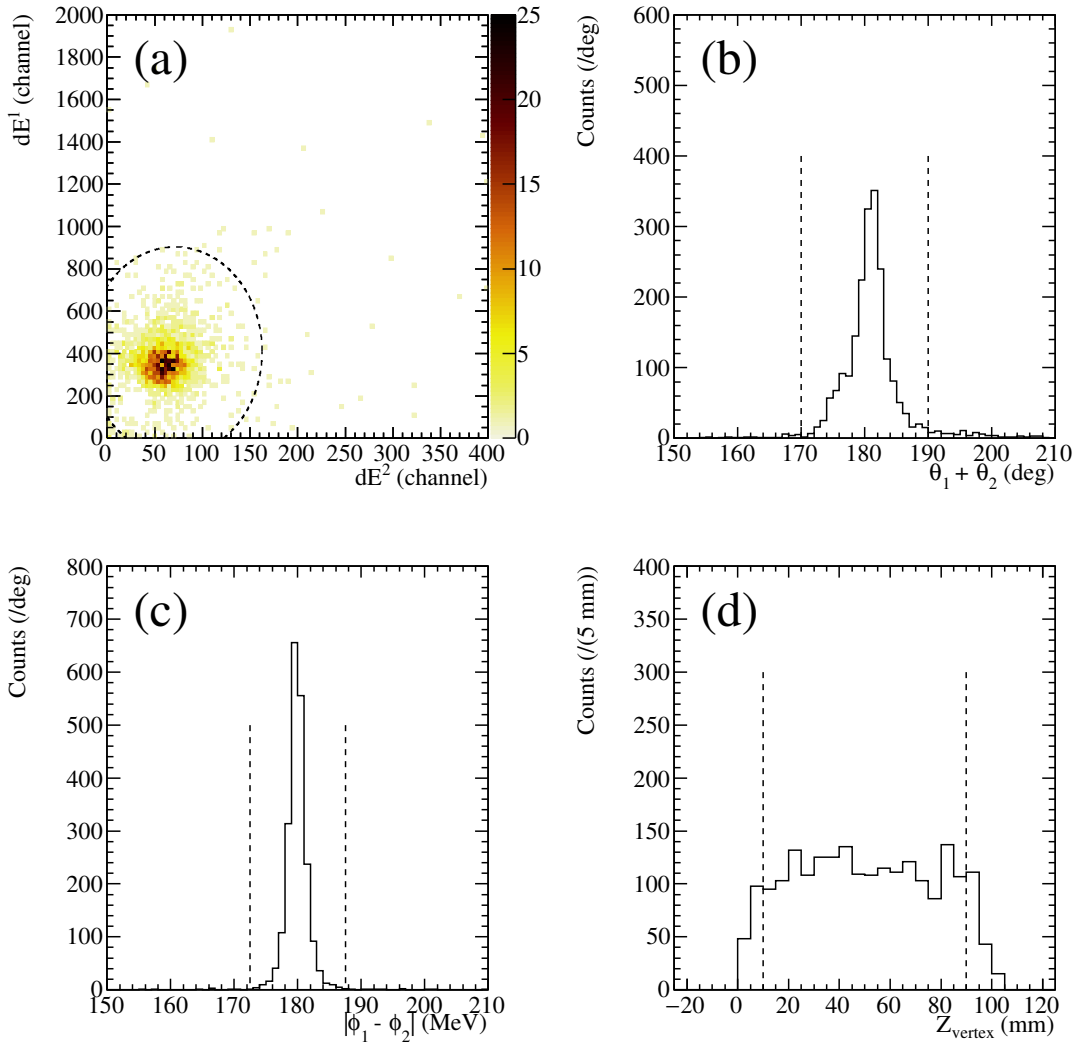

Figure 3.19: Selection analysis for the ^{4}He$(\gamma, p)^3$H event candidates from the measurement at $E_\gamma = 30.0$ MeV. (a) The correlation between dEs, (b) the polar angle θ between two trajectories, (c) the azimuthal angle ϕ between two trajectories, and (d) the Z coordinate of the vertex. All the events which contains two trajectories reaching the edge of the sensitive volume are included in these plots. The conditions imposed on these variables are shown with dashed lines.

Ionization process caused by charged-decay particles are simulated based on the SRIM code [189]. This algorithm was newly developed because the ionization simulator class built in the Garfield++ [190] did not work well. The algorithm requires many samples of the history of the ionization caused by one ion injection are generated using the TRIM code built in the SRIM software suite. A sample of ionization contains the history of the collision between ion and the electrons in the gaseous medium over the interval till ions lose all of their kinetic energy. When this algorithm is called, one of the samples are randomly selected. Electrons kicked off from the molecules in the gaseous medium are generated at the collision position in the sample. The number of generated electrons at the collision are calculated from the ratio of the energy loss of the ion and the average work function of the molecules. In addition, ionization histories are mixed among samples having the collision records at approximate kinetic energy. Thanks to this mixing algorithm, the variety of the ionization process can be generated from finite samples.

The electrons generated along the particle trajectory are transported by the electric field inside the sensitive volume of the detector. We assumed that the electric field, that drive electron transport, is perfectly uniform, because the uniformity of the electric field inside the drift cage was studied already. Because of the molecules in the medium, electrons are transported in the zig-zag trajectory in the certain drift velocity in average. This diffusion coefficient and the drift velocity vary depending on the strength of the electric field and the type of medium. In this simulation, these properties calculated by the Magboltz code is employed. The stochastic process regarding electron transport is calculated one by one by the class provided by the Garfield++ library [190]. This calculation was proceeded until electrons reach at the bottom most of the drift region.

The electron delivered to the GEM and μ-PIC is amplified by electron avalanche. In this simulation, this process is emulated by a simple model. We assumed the probability mass function of the electron-amplification factor is given by a single Pólya distribution. Amplification factor is randomly calculated for every electron reaches at the bottom most of the drift region, and it is recorded with its position and timing information. The mean amplification factor is a parameter that is optimized to reproduce the real data. The criteria for the parameter determination will be described later.

The signal read-out from μ-PIC strips are calculated based on the signal template shown in Ref. [191]. The signal pulse is calculated by the convolution of the signal template and arrival-timing distribution of electrons at each pixel of the μ-PIC. The signals on pixels are summed in the same manner as the real read-out circuit, and pulse shape for a strip is obtained. This pulse shape is compared with the threshold, and the hit pattern of XY and ZY images are generated. In addition, the signal measured by FADCs are calculated by adding the signal for 32 adjacent strips. The threshold value, which is set to the common value for all strips, is also a parameter of this simulation.

Two parameters, namely the mean amplification factor and the threshold value, are optimized for each measurement conditions to reproduce the real data. First, the amplification factor is determined to reproduce the dE for ^{3}He, ^{3}H, and ^{1}H from the $^4\mathrm{He}(\gamma, n)^3\mathrm{He}$ and the $^4\mathrm{He}(\gamma, p)^3\mathrm{H}$ reactions. The dE for ^{3}H and ^{1}H are reproduced with an accuracy of

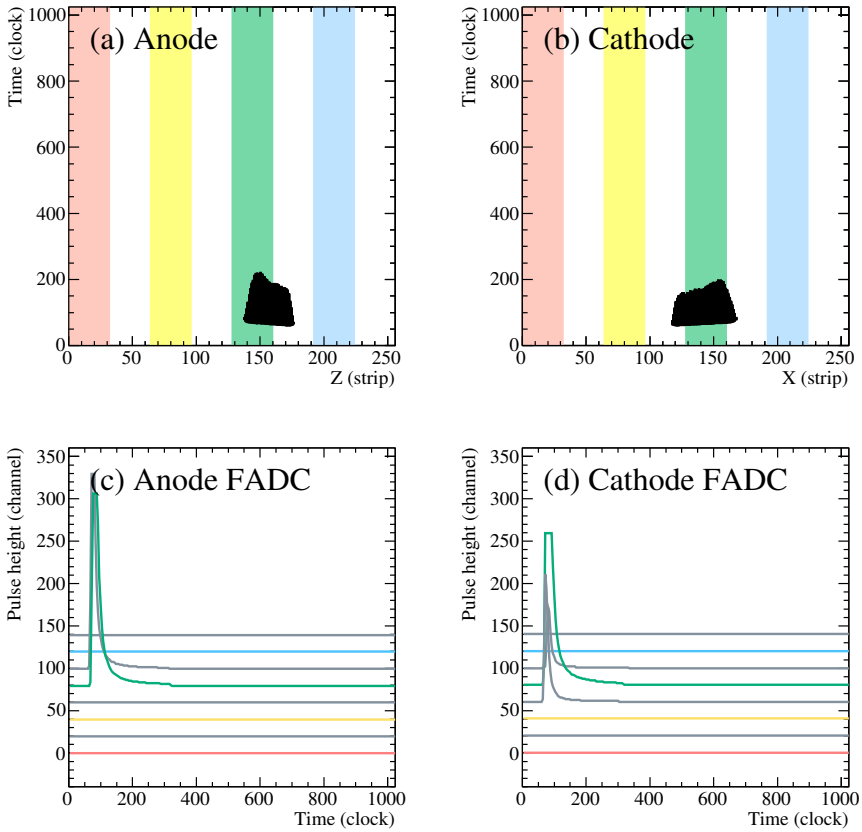

Figure 3.20: Typical ^{4}He$(\gamma, n)^3$He event generated with the Monte Calro simulation. The detector condition in the simulation was set to the one used in the measurement at E_γ = 30.0 MeV. The definitions of the panels are same as Fig. 3.6.

less than 10%, but the agreement regarding dE for ^{3}He is about 10%. Next, the threshold is optimized to reproduce the TOT of the trajectory. However, we gave up reproducing the TOT of the trajectories other than ^{1}H (^{3}He and ^{3}H), because all of them could not be reproduced by a single optimal parameter. Since the TOT of ^{1}H is the smallest one, that is the most critical to evaluate the tracking efficiency.

Typical events obtained from the simulation are shown in Figs. 3.20, and 3.21. These are the ^{4}He$(\gamma, n)^3$He and ^{4}He$(\gamma, p)^3$H events, respectively. The definition of each panel is same as Figs. 3.6. Compared to the real event shown in Figs. 3.6 and 3.7, the TOTs of the trajectories in Figs. 3.20, and 3.21 are larger. However, the TOTs of the trajectories were not directory referred in the event selection criteria. Thus, that would not be matter in the efficiency estimation.

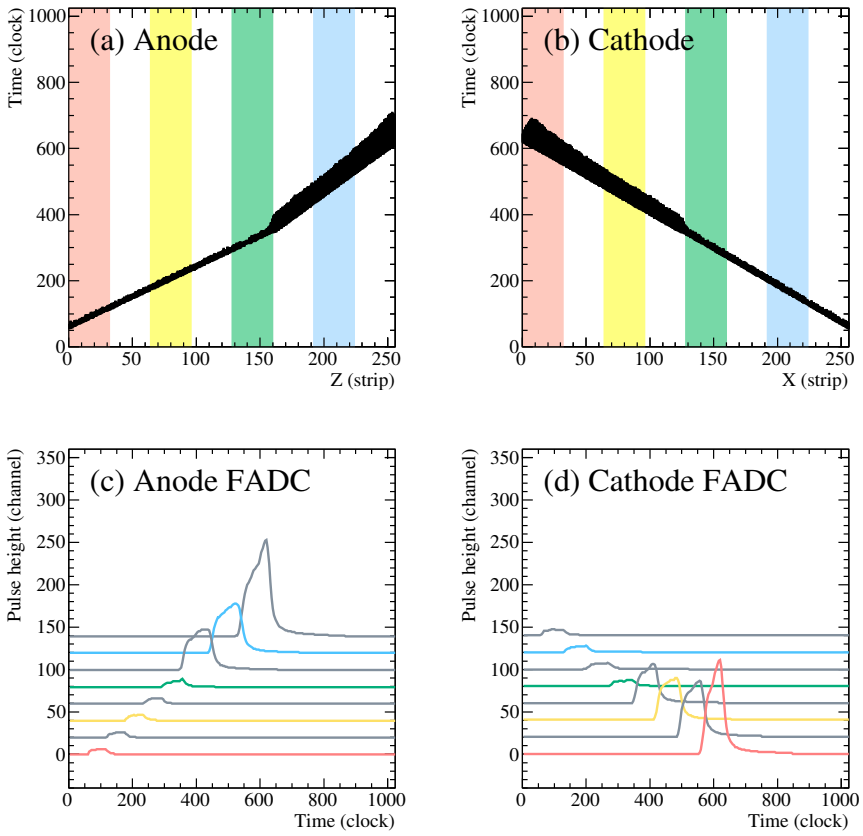

Figure 3.21: Typical ^{4}He$(\gamma, p)^3$H event generated with the Monte Calro simulation. The detector condition in the simulation was set to the one used in the measurement at E_γ = 30.0 MeV. The definitions of the panels are same as Fig. 3.6.

3.4 Cross Sections

3.4.1 Overview

Here, the analysis method to determine the cross sections of the ^{4}He$(\gamma, n)^3$He and the ^{4}He$(\gamma, p)^3$H reactions is described. Due to the finite energy spread of the photon beam generated by the LCS technique, what one can determine from the measurement is the cross section averaged over the beam-energy distribution. The averaged total cross section was derived as follows: the differential cross sections averaged over each angular bin were determined from the measurement yield, and the total cross section was, then, obtained from the integral of the differential cross sections over the full solid angle. In addition, the average energy of each measurement was determined as well.

Hereafter, the bins of the polar angle (θ) bins, the polar angle (ϕ) bins of decay particle, and the measurement condition are indexed with the character i, j, and k, respectively. Since there are six measurement conditions as summarized in Table 2.4, the index k varies in a range between 1 and 6. The bin width of the decay-particle emission angle is 20 degrees, i (j) varies in a range between 1 and 9 (18). The i th bin defines the θ interval from $20(i-1)$ and $20i$ degrees, and the j th bin is the similar ones for ϕ interval. Hereafter, we represent i th and j th bin as θ_i and ϕ_j. The solid angle of the bin (θ_i, ϕ_j) is denoted as $\Delta\Omega_{i.j}$. The target thickness of k th condition is represented by τ_k.

The measurement yield of k th condition at the bin (θ_i, ϕ_j) determined by the selection analysis is represented as $Y_{i,j,k}$. The beam energy profile function of k th condition is written as $f_k(E)$ at the beam energy E. The $f_k(E)$ is based on the energy profile determined in Ch. 3.2, and its energy integral of this function is normalized as

$$N_{\gamma,k} = \int_0^{E_{\max,k}} dE f_k(E). \tag{3.37}$$

Here, $N_{\gamma,k}$ and $E_{\max,k}$ are the total photon flux determined in Chap. and the maximum energy of the photon beam, respectively. The efficiency determined in Ch. 3.3.3 is written as $\epsilon_{i,j,k}(E)$.

3.4.2 Differential Cross Section

The differential cross section of k th condition at the bin (θ_i, ϕ_j) is calculated using following formula. In preparation for determining the total cross sections, we first evaluated the differential cross section at each angular bin using the following formula

$$\left\langle \frac{d\sigma}{d\Omega} \right\rangle_{\theta_i,\phi_j,k} = \frac{Y_{i,j,k}}{\left[\int_0^{E_{\max,k}} dE\ f_k(E)\epsilon_{i,j,k}(E)\right]\ \tau_k \Delta\Omega_{i,j}}. \tag{3.38}$$

The integral in the denominator is in fact approximated by a summation over the beam energy

$$\int_0^{E_{\max,k}} dE\ f_k(E)\epsilon_{i,j,k}(E) \sim \sum_l \epsilon_{i,j,k}(E_l) \int_{E_l-\Delta E/2}^{E_l+\Delta E/2} dE f_k(E), \tag{3.39}$$

where E_l is the midpoint of energy bin with a step of ΔE (=500 keV).

3.4.3 Total Cross Section

In principle, the total cross section is obtained by integrating the differential cross sections Eq. (3.38) over the full solid angle of 4π. In the present analysis, however, the cross sections in the angular bins with lower detection efficiencies was removed from the integration because those angular bins caused larger systematic uncertainties amplified by the efficiencies.

Hereafter, we define $\Delta\tilde{\Omega}_k$ as the angular range in which the differential cross sections are reliable and included in the analysis. Angular bins of the efficiency larger than a certain threshold value are included in $\Delta\tilde{\Omega}_k$. The detail of this bin selection criteria is discussed later.

In order to obtain the total cross section, it is necessary to deduce the correction factor for converting the cross section integrated over the partial solid angle $\Delta\tilde{\Omega}_k$ into that over 4π. For this purpose, we assume the photodisintegration reactions in the present energy region are primarily induced through the $E1$ transition, and model the angular distribution of the differential cross sections at $E_\gamma = E$ by the following formula

$$\left(\frac{d\sigma_M}{d\Omega}\right)_k = \sigma_M(E)\left\{\frac{3}{8\pi}\sin^2\theta\left[1+\alpha_k\cos 2(\phi-\tilde{\phi})\right]\right\}, \tag{3.40}$$

where θ and ϕ are the polar and azimuthal angles of the decay particles in the center of mass frame. $\tilde{\phi}$ and α_k are the polarization direction of the linearly polarized photon beam and the azimuthal asymmetry parameter, respectively. σ_M corresponds to the total cross section obtained by integrating the modeled differential cross section over 4π. In addition, we assume that the energy dependence of the modeled total cross section $\sigma_M(E)$ is given by

$$\sigma_M(E) = \begin{cases} \sum_{l=1}^{4} p_l (E - E_{\rm th})^l & (E \geq E_{\rm th}) \\ 0 & (E < E_{\rm th}), \end{cases} \tag{3.41}$$

where $E_{\rm th}$ is the threshold energy of the photodisintegration reactions.

Based on the cross section model described above, the expected yield $\tilde{Y}$ at a certain angular bin is estimated as

$$\tilde{Y}_{\theta_i,\phi_j,k} = \tau_k \int d\Omega \int_0^{E_{\max,k}} dE \left[I_{\Delta\Omega_{i,j}} \left(\frac{d\sigma_M}{d\Omega}\right)_k f_k \epsilon_{i,j,k} \right]. \tag{3.42}$$

Here, for the sake of simplicity, the arguments (E, θ, and ϕ) of the functions in the integrand are omitted. I_A is an indicator function on the angular range which is defined as,

$$I_A(x) = \begin{cases} 1 & (x \in A) \\ 0 & (x \notin A). \end{cases} \tag{3.43}$$

Therefore, the angular integration in Eq. (3.42) was done within an angular bin $\Delta\Omega_{i,j}$ with $\Delta\phi = \Delta\theta = 20^\circ$ around θ_i and ϕ_j. This angular bin is the same as that employed in Eq. (3.38). The unknown parameters, α_k and p_l in Eqs. (3.40) and (3.41), were optimized to maximize the likelihood of the expected yields $\tilde{Y}$ by comparing them with the measured yields Y at all angular bins and beam energies while $\tilde{\phi}$ was fixed at $\tilde{\phi} = 10^\circ$. The log likelihood function $\ln \mathcal{L}(Y)$ is defined by the formula

$$\ln \mathcal{L}(Y) = \sum_{\{\theta_i,\phi_j\}\in\Delta\tilde{\Omega}_k} \ln P_{\tilde{Y}_{\theta_i,\phi_j,k}}(Y_{\theta_i,\phi_j,k}), \tag{3.44}$$

where the summation symbol means the log likelihood functions at the angular bins included in the selected region $\Delta\tilde{\Omega}_k$ are accumulated. Moreover, $P_\lambda(x)$ is the probability mass function of the Poisson distribution with the average λ given by

$$P_\lambda(x) = \frac{\lambda^x e^\lambda}{x!}. \tag{3.45}$$

The averaged beam energy $\langle E\rangle_k$ was calculated from the weighted mean of the beam energy defined as follows:

$$\langle E\rangle_k = \frac{\int_0^{E_{\max,k}} dE \int d\Omega \left\{E\left[I_{\Delta\tilde{\Omega}_k}\left(\frac{d\sigma_M}{d\Omega}\right)_k f_k \epsilon_{i,j,k}\right]\right\}}{\int_0^{E_{\max,k}} dE \int d\Omega \left[I_{\Delta\tilde{\Omega}_k}\left(\frac{d\sigma_M}{d\Omega}\right)_k f_k \epsilon_{i,j,k}\right]}. \tag{3.46}$$

Finally, the measured cross sections were corrected to obtain the experimental total cross section at the average beam energy $\langle E\rangle_k$ by the following formula

$$\langle\sigma\rangle_k = C_k \langle\sigma\rangle_{\Delta\tilde{\Omega}_k} \tag{3.47}$$

$$= C_k \sum_{\{\theta_i,\phi_j\}\in\Delta\tilde{\Omega}_k} \left[\left\langle \frac{d\sigma}{d\Omega}\right\rangle_{\theta_i,\phi_j,k} \Delta\Omega_{i,j}\right] \tag{3.48}$$

where the correction factor C_k is given as

$$C_k = \frac{\sigma_M(\langle E\rangle_k)}{\int d\Omega \left[I_{\Delta\tilde{\Omega}_k}\left(\frac{d\sigma_M}{d\Omega}\right)_k (\langle E\rangle_k)\right]}. \tag{3.49}$$

The second factor in Eq. (3.47), $\langle\sigma\rangle_{\Delta\tilde{\Omega}_k}$ is the integration of the differential cross section in Eq. (3.38) over the angular bins adopted in the analysis. The correction factor C_k corresponds to the ratio of the modeled cross section integrated over 4π to that over $\Delta\tilde{\Omega}_k$.

Bin-Seletion Criteria

The angular bins employed in the analysis, $\Delta\tilde{\Omega}_k$, was selected based on the efficiency at the most frequent beam energy for each measurement. The lower limit of the efficiency $\epsilon_{\rm min}$ was defined, and bins whose efficiency ϵ is higher than $\epsilon_{\rm min}$ were included in the selected angular region $\Delta\tilde{\Omega}$.

Results given from $\epsilon_{\rm min} = 0.05, 0.1, ..., 0.6$ were compared together. If $\epsilon_{\rm min}$ was lower than a suitable value, total cross sections largely deviates the energy dependence given from Eq. 3.41 due to contribution from statistical fluctuation in low-efficiency bins amplified by the efficiency. On the other hand, if $\epsilon_{\rm min}$ was higher than the good value, statistical uncertainty ratio associated with the total cross sections become large. Thus, $\epsilon_{\rm min}$ should be chosen with considering that balance. In the present study, the best $\epsilon_{\rm min}$, which was attributed to the most probable value of the total cross section, was chosen based on the best agreement with the model cross section given from Eq. (3.47). Other results with the similar degree of agreement were also considered as candidates of probable results. The variation among these candidates were included in the systematic uncertainty of the total cross section.

Altanative Model

It is possible that the reaction cannot be regarded as the pure $E1$ transition. The theta dependence of the differential cross section with inclusion of the contribution of the electric and magnetic transition is given as

$$\left(\frac{d\sigma_M}{d\Omega}\right)_k = \sigma_{M,k}(E,\phi)C(\beta_{2,k},\beta_{3,k})\left\{\sin^2\theta(1+\beta_{1,k}\cos\theta+\beta_{2,k}\cos^2\theta)+\beta_{3,k}\right\}, \quad (3.50)$$

where $\sigma_{M,k}(E,\phi)$ is the product of total cross section Eq. (3.14) and the ϕ-dependence in Eq. (3.40). $C(\beta_{2,k},\beta_{3,k})$ is the normalization factor for θ integral. This formula is based on Ref. [192]. The series of analysis was done by using this formula instead of Eq. (3.40) as well.

We adopted the result obtained with this alternative model as not the most probable result but a measure of the systematic error originating from the model selection. It it because the parameters $\beta_{1,k}$–$\beta_{3,k}$ could not be determined precisely due to the insufficient statistics of the measurement. Moreover, the dominance of the $E1$ transition seems to be a more robust assumption than allowing large contribution from the transitions of higher multi-polarity. The bin selection criteria was considered independently from that for the pure-$E1$ model, and the variation among the result candidates were also included in the systematic uncertainty of the total cross sections.

Chapter 4

Results & Discussions

4.1 Differential Cross Section

The differential cross sections of ^{4}He$(\gamma, n)^3$He and ^{4}He$(\gamma, p)^3$H are shown in appendix. These cross sections integrated with respect to θ and ϕ are shown in Figs. The ϕ-averaged differential cross section $\langle d\sigma_\theta/d\Omega \rangle$ at $\theta = \theta_i$ and θ-averaged differential cross section $\langle d\sigma_\phi/d\Omega \rangle$ at $\phi = \phi_j$ are written as

$$\left\langle \frac{d\sigma_\theta}{d\Omega} \right\rangle_k = \frac{\int_{\Delta\Omega_{\theta_i}} d\Omega \left[I_{\Delta\tilde{\Omega}_k} \left\langle \frac{d\sigma}{d\Omega} \right\rangle_{i,j,k} \right]}{\int_{\Delta\Omega_{\theta_i}} d\Omega \left[I_{\Delta\tilde{\Omega}_k} \left(\frac{d\sigma_M}{d\Omega} \right)_k \right]} \frac{\int_{\Delta\Omega_{\theta_i}} d\Omega \left(\frac{d\sigma_M}{d\Omega} \right)_k}{\Delta\Omega_{\theta_i}} \tag{4.1}$$

and

$$\left\langle \frac{d\sigma_\phi}{d\Omega} \right\rangle_k = \frac{\int_{\Delta\Omega_{\phi_j}} d\Omega \left[I_{\Delta\tilde{\Omega}_k} \left\langle \frac{d\sigma}{d\Omega} \right\rangle_{i,j,k} \right]}{\int_{\Delta\Omega_{\phi_j}} d\Omega \left[I_{\Delta\tilde{\Omega}_k} \left(\frac{d\sigma_M}{d\Omega} \right)_k \right]} \frac{\int_{\Delta\Omega_{\phi_j}} d\Omega \left(\frac{d\sigma_M}{d\Omega} \right)_k}{\Delta\Omega_{\phi_j}} \tag{4.2}$$

respectively. Here, $\Delta\tilde{\Omega}_k$ denotes the angular region included in the selected bins for kth beam energy. The angular regions $\Delta\Omega_{\theta_i}$ and $\Delta\Omega_{\phi_j}$ are defined as

$$\Delta\Omega_{\theta_i} = \left[\theta_i - \frac{\Delta\theta}{2}, \theta_i + \frac{\Delta\theta}{2} \right] \times \left[0, 2\pi \right] \tag{4.3}$$

and

$$\Delta\Omega_{\phi_j} = \left[0, \pi \right] \times \left[\phi_j - \frac{\Delta\phi}{2}, \phi_j + \frac{\Delta\phi}{2} \right], \tag{4.4}$$

respectively. The θ (ϕ) averaged cross section as the average beam energy are superimposed on Figs. These averaged cross sections are well be described by the assumption that the photodisintegration in this energy region is induced by the pure $E1$ transition.

As seen in Figs. 4.1 and 4.3, the θ dependence of the differential cross sections are peaks at θ= 90°. In addition, the ϕ dependence of the differential cross sections drawn

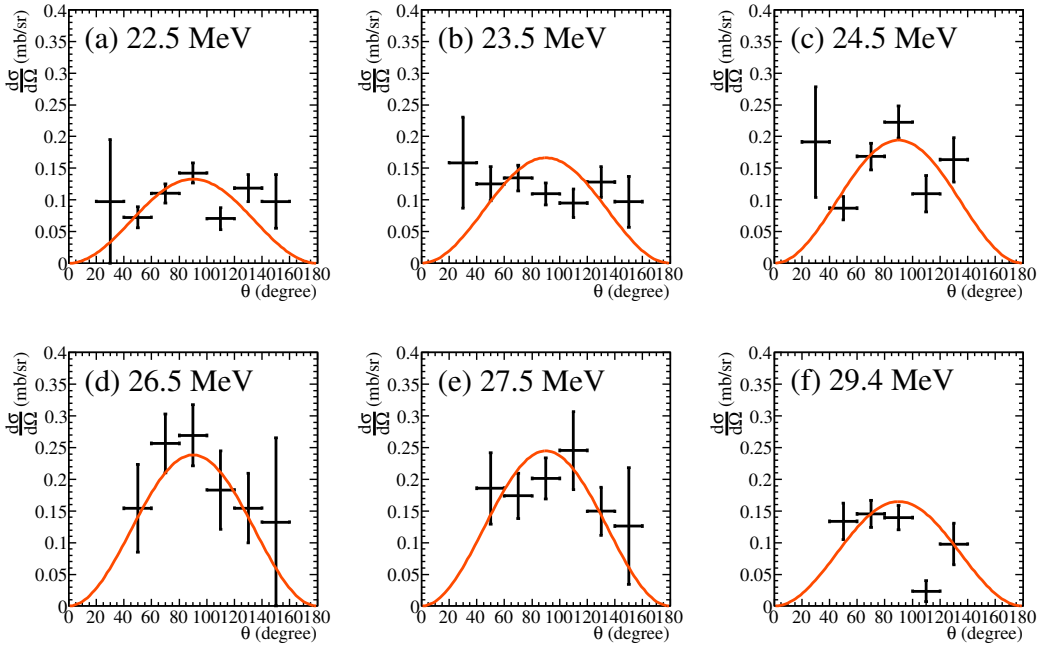

Figure 4.1: θ dependence of ϕ-averaged differential cross sections $\left\langle \frac{d\sigma_\theta}{d\Omega} \right\rangle$ (Eq. 4.1) of the ^{4}He$(\gamma, n)^3$He reaction and their statistical errors. The averaged beam energy evaluated with Eq. 3.46 is written at the top of each panel. The model cross sections (Eq. 3.40) at the beam energy are shown with the red solid lines.

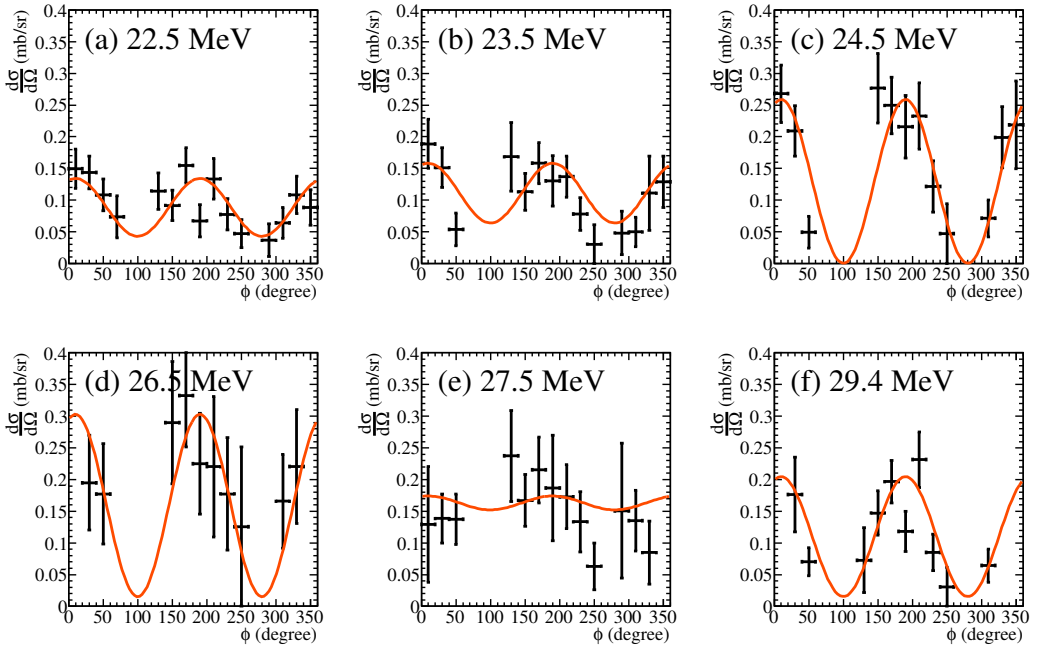

Figure 4.2: ϕ dependence of θ-averaged differential cross sections $\left\langle \frac{d\sigma_\phi}{d\Omega} \right\rangle$ (Eq. 4.2) of the ^{4}He$(\gamma, n)^3$He reaction. The definitions of the panels are same as Fig. 4.1.

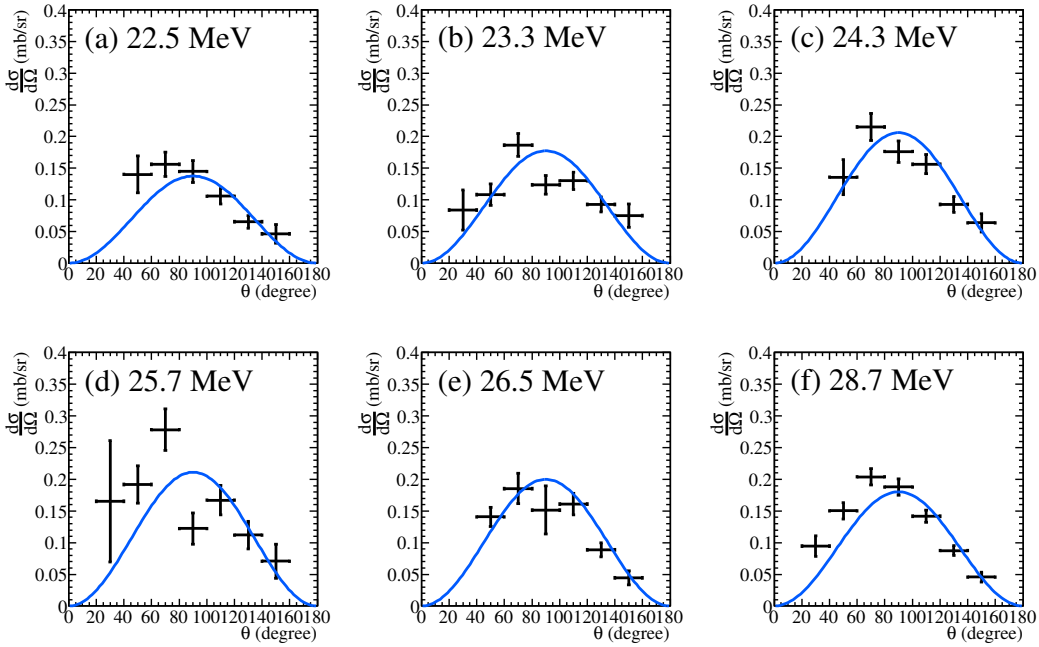

Figure 4.3: θ dependence of ϕ-averaged differential cross sections $\left\langle \frac{d\sigma_\theta}{d\Omega} \right\rangle$ (Eq. 4.1) of the $^4\mathrm{He}(\gamma, p)^3\mathrm{H}$ reaction and their statistical errors. The averaged beam energy evaluated with Eq. 3.46 is written at the top of each panel. The model cross sections (Eq. 3.40) at the beam energy are shown with the blue solid lines.

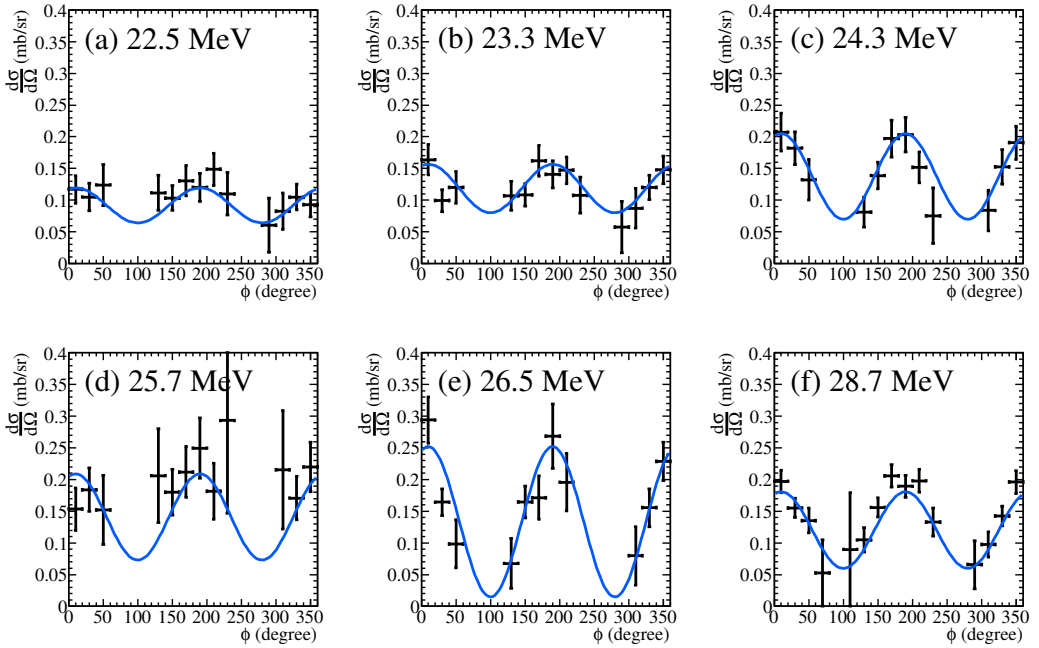

Figure 4.4: ϕ dependence of differential θ-averaged cross sections $\left\langle \frac{d\sigma_\phi}{d\Omega} \right\rangle$ (Eq. 4.2) of the $^4\mathrm{He}(\gamma, p)^3\mathrm{H}$ reaction. The definitions of the panels are same as Fig. 4.3.

Table 4.1: Experimental total cross sections for the $^4\mathrm{He}(\gamma,n)^3\mathrm{He}$ and $^4\mathrm{He}(\gamma,p)^3\mathrm{H}$ reactions. The average beam energies $\langle E\rangle_k$ obtained from Eq. (3.46) and the statistical and systematic uncertainties are also presented. k is an index of beam energy defined in Table 2.2.

		$^4\mathrm{He}(\gamma,n)^3\mathrm{He}$				$^4\mathrm{He}(\gamma,p)^3\mathrm{H}$			
k	$E_{\max}$ (MeV)	$\langle E\rangle_k$ (MeV)	$\langle\sigma\rangle_k$ (mb)	$\Delta\sigma_{\mathrm{stat}}$ (mb)	$\Delta\sigma_{\mathrm{sys}}$ (mb)	$\langle E\rangle_k$ (MeV)	$\langle\sigma\rangle_k$ (mb)	$\Delta\sigma_{\mathrm{stat}}$ (mb)	$\Delta\sigma_{\mathrm{sys}}$ (mb)
1	23.0	22.5	1.15	$\pm$ 0.08	$+0.13-0.13$	22.5	1.25	$\pm$ 0.08	$+0.56-0.40$
2	24.0	23.5	1.31	$\pm$ 0.10	$+0.14-0.15$	23.3	1.41	$\pm$ 0.07	$+0.28-0.28$
3	25.0	24.5	1.66	$\pm$ 0.12	$+0.18-0.18$	24.3	1.64	$\pm$ 0.08	$+0.25-0.22$
4	27.0	26.5	2.26	$\pm$ 0.25	$+0.25-0.24$	25.7	1.93	$\pm$ 0.13	$+0.34-0.42$
5	28.0	27.5	1.94	$\pm$ 0.19	$+0.21-0.24$	26.5	1.59	$\pm$ 0.09	$+0.63-0.21$
6	30.0	29.4	1.26	$\pm$ 0.11	$+0.16-0.19$	28.7	1.67	$\pm$ 0.05	$+0.19-0.23$

in Figs. 4.2 and 4.4 peaks twice at ϕ= 10° and 190°, which are the direction of the linear polarization axis of the incident photon beam. These tendencies are consistent with our assumption that the reaction is purely via the $E1$ transition. The model differential cross sections (Eq. 3.40) estimated with the best-fit parameters at the averaged beam energy of the measurement are also shown with solid lines. They reproduced the angular dependence and the amplitude of the cross sections.

As for the $^4\mathrm{He}(\gamma,n)^3\mathrm{He}$ reaction, the statistical error entailed in the differential cross sections are rather larger compared to the results on the $^4\mathrm{He}(\gamma,p)^3\mathrm{H}$ reaction. That would be due to the selection criteria on the beam energy, which is inevitable to exclude back ground events. On the other hand, because no explicit beam energy selection criterion are imposed on the $^4\mathrm{He}(\gamma,p)^3\mathrm{H}$ events, the statistical precision on the $^4\mathrm{He}(\gamma,p)^3\mathrm{H}$ cross sections are better. As a result of such processing on the beam energy, the averaged beam energy at the same condition but the different reactions differed slightly. resulted in the different averaged beam energy.

4.2 Total Cross sections

The results of simultaneous measurements using mono-energetic photon beams are shown in Fig. 4.5. The triangular markers indicates the data from the present study. Their statistical and systematic uncertainties are shown by the bars and the bands, respectively. Both the $^4\mathrm{He}(\gamma,n)^3\mathrm{He}$ and $^4\mathrm{He}(\gamma,p)^3\mathrm{H}$ cross sections peaked around $E_\gamma \sim 26$ MeV.

The systematic uncertainties considered in the present study are summarized below. The uncertainty, which is primarily due to the correction of the solid angle and the model selection, is estimated to be varying between ten and a few tens of percentages, depending on the measurement conditions. In addition, the uncertainty from the efficiency estimations due to the incompleteness of the Monte Carlo simulations was approximately 10%,

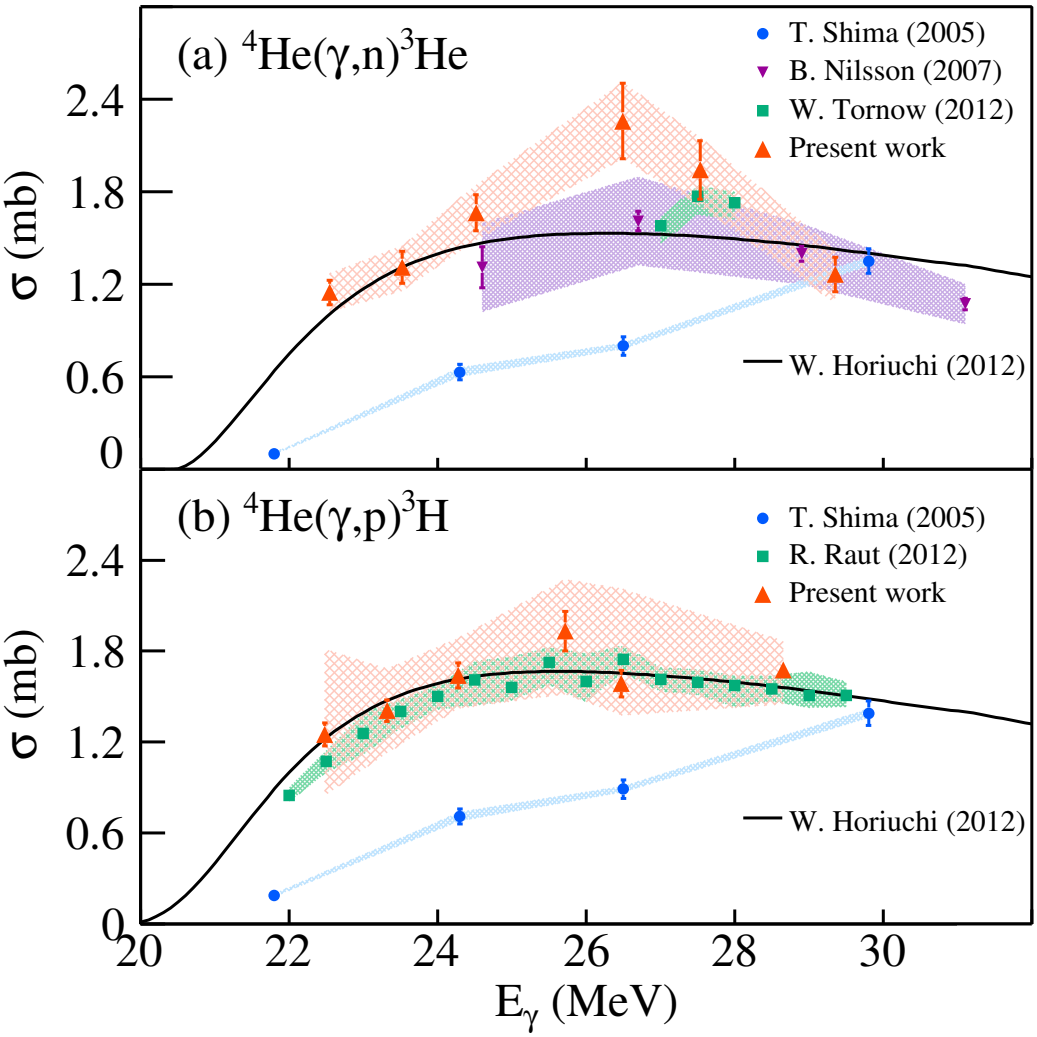

Figure 4.5: Experimental cross sections of the (a) ^{4}He$(\gamma, n)^3$He and (b) ^{4}He$(\gamma, p)^3$H reactions taken from Ref. [1]. The present result (upward triangles) is compared with those from previous studies ([115]: circles, [119]: downward triangles, [118] and [116]: squares). Systematic uncertainties of the cross sections are indicated with hatched regions. The theoretical predictions taken from Ref. [112] are shown by the solid lines.

which is taken from Ref. [175]. As discussed in Ch. 3.2, the uncertainty of the incident photon number was 4%. We controlled and monitored the density of the target gas, and uncertainty originated from that was 0.1% or less. These uncertainties from different sources were combined together, and the square root of their quadratic sum are shown by the red hatched region in the vicinity of the data points.

4.3 Comparison with the Previous Studies

The experimental total cross sections measured with the quasi-mono-energetic photon beams [115, 116, 118, 119] were selected from numerous previous studies in Ch. 1.4 and compared with the present results in Fig. 4.5. The present results showing the GDR peak structure around $E_\gamma = 26$ MeV in both the ^{4}He$(\gamma, n)^3$He and ^{4}He$(\gamma, p)^3$H reactions do not support those reported by Shima *et al.* [115], but are consistent with those from the HIγS group [116, 118]. The uncertainties in the present results are slightly higher than those in previous studies, but smaller than the difference between the results by Shima *et al.* and those by the HiγS group. Notably, the present ^{4}He$(\gamma, n)^3$He result also agrees with that by the MAX-lab group [119], which was obtained by using energy-tagged bremsstrahlung photons. The GDR peak energy is in accord with the theoretical calculation [112] shown by the solid lines in Fig 4.5. In addition, the absolute values of our data support the theoretical calculations within the uncertainty except for some points of the ^{4}He$(\gamma, n)^3$He reaction whereby their statistical uncertainties are higher than those of others.

As described in Ch. 1.2.3, the cross sections of the ^{4}He photodisintegration reactions in the GDR energy region are important to elucidate the certain processes in the nucleosynthesis in the universe. Because cross sections theoretically calculated from the nuclear structure theory are generally employed for the astrophysical calculation, one would have to revise the theoretical frameworks and the scenario of the nucleosynthesis if the theoretical predictions largely deviate from the experimental cross sections. The striking experimental results reported by Shima *et al.* challenged the conventional view of the ^{4}He photodisintegration reactions that the GDR peak was located around $E_\gamma = 26$ MeV. However, the present results support the conventional view and do not force one to revise the physical pictures on the nucleosynthesis drawn by the nuclear structure theories.

Chapter 5

Summary

The photodisintegration reactions, ^{4}He$(\gamma, n)^3$He and ^{4}He$(\gamma, p)^3$H in the GDR energy region are very fundamental and important reactions from a view of nucleosynthesis in the universe. From the theoretical side, the cross sections of the ^{4}He photodisintegrations were precisely calculated [112] based on the realistic nuclear forces. Both the $\sigma_{(\gamma,n)}$ and $\sigma_{(\gamma,p)}$ cross sections peak around E_γ =26–27 MeV, and they are approximately 1.5 mb and 1.7 mb at the peak, respectively.

There existed a serious contradiction in the experimental cross sections regarding their energy dependence, especially the peak position. One was reported by Shima *et al.* [115]. No peak structures were found in their $\sigma_{(\gamma,n)}$ and $\sigma_{(\gamma,p)}$ within the energy region below E_γ = 30 MeV, and the cross sections were about a half of the theoretical predictions. The other experimental studies were conducted at the HIγS facility [116, 118]. Their results were in fair agreement with the theoretical predictions, but near-threshold $\sigma_{(\gamma,n)}$ was not reported in the articles.

We performed the simultaneous measurement of ^{4}He$(\gamma,\ n)^3$He and ^{4}He$(\gamma, p)^3$H reactions at the BL01 in the NewSUBARU synchrotron radiation facility by using the TPC based gaseous active target, MAIKo. The quasi-monochromatic photon beams at E_γ = 23.0, 24.0, 25.0, 27.0, 28.0, and 30.0 MeV, which were closed to the GDR energy in ^{4}He, were irradiated on the MAIKo active target. With the information on charged decay particles measured with the active target, we selected the ^{4}He photodisintegration events. The tracking efficiencies of the MAIKo active target were estimated with the result of the Monte Carlo simulation in which the response of the detector was considered. The total flux and energy distribution of photon beams were evaluated from the energy distribution measured with NaI (Tl) scintillator based beam monitor. Finally, we determined the cross sections of the ^{4}He$(\gamma, n)^3$He and ^{4}He$(\gamma, p)^3$H reactions.

The cross sections obtained from the present measurement showed GDR peaks at around E_γ = 26 MeV. The peak position was consistent with the prediction by the recent theoretical calculation [112] and results from the HIγS facility [116] [118], and the $\sigma_{(\gamma,n)}$ and $\sigma_{(\gamma,p)}$ cross sections were also in fair agreement with these studies within

errors except for a few data points in $\sigma_{(\gamma,n)}$. As a consequence, our results didn't follow the result by Shima *et al.* [115]. Therefore, our result supported the conventional view of the ^{4}He photodisintegration reactions, and did not force one to revise the theoretical frameworks.

This work proved the applicability of the MAIKo active target, which was originally designed for the in-beam spectroscopy of the unstable nuclei, to the study of the nuclear photoreactions. This expand our possibility to contribute to the nuclear astrophysics by providing reliable data on important reactions measured with the MAIKo active target.

Acknowledgement

The present thesis would not have been completed without the dedicated and kind supports from many people. I would like to take this opportunity to express my sincere thanks to them.

First of all, I owe my sincere gratitude to Professor Takahiro Kawabata, who served as my supervisor and the director of this dissertation research for many years. I learned from him not only substantial skills but also a mental attitude as a professional researcher. Thanks to his flexible supervisory style, I could enjoy years pursuing what I was interested in. In addition, countless times was I encouraged by his witful and heartwarming personality. Without his constant support, I could not complete the arduous path toward a PhD.

I thank Professor Tatsuya Furuno for offering on-site training opportunity for experimental technique. I spent considerable part of my PhD-candidate years with him developing the MAIKo active target and participating many experiments conducted at RCNP. Meanwhile, he has been a both a teacher and a role model to me, simultaneously. If it were not for his devotion, I could not manage the beam time at the NewSUBARU nor even launch the experiment.

I am really grateful to Professor Hidetoshi Akimune. He gave me invaluable advices on the experiment at NewSUBARU and voluntarily undertook overnight shifts during the experiment despite being extremely busy. Moreover, he offered me a teaching job opportunity at Konan University over tha last few years. The course I taught was a wonderful experience for me and helped to relieve the tension of writing a dissertation.

I would like to express my gratitude to Professor Shuji Miyamoto and Professor Sho Amano, who were the senior staffs administrating the NewSUBARU. They supplied me essential information regarding the beamline since the planning period of the experiment. The successful completion of the experiment doubtlessly owed to their thorough operation and maintenance on the facility.

I gratefully acknowledge Professor Hiroaki Utsunomiya. As a skillful expert of the photonuclear reaction measurement, he generously shared me the great amount of know-how accumulated in his carrier. It cannot be overemphasized that analysis on the photon beam described in the thesis is deeply indebted on his advice.

I would like to thank Professor Toshiki Kajino, Professor Toshio Suzuki, Professor Wataru Horiuchi, and Professor Tatsushi Shima for fruitful discussions. They willingly offered the discussion opportunity even on our short notice and gave me profound advices based on their specialty, which were indispensable to clarify the situation surrounding the reaction dealt in the thesis.

I wish to thank the present and post members of our research group who cooperated in the experiment: Professor Satoshi Adachi, Ms. Miho Tsumura, Mr. Yuki Ishii, Dr. Kento Inaba, and Dr. Yuki Fujikawa. They and Prof. Furuno were my colleague when I was a graduate student in Kyoto University. I would like to credit their hard work and

contribution of their expertise as experimentalists during the beam time.

I express gratitude to the NewSUBARU synchrotron radiation facility and Research Center for Nuclear Physics, Osaka University, for providing their facilities and supports for the present work.

I thank the staffs at the Experimental Nuclear and Hadronic Physics Laboratory (NH) in Kyoto University: Professor Tomofumi Nagae, Professor Megumi Naruki, Professor Tetsuya Murakami, Professor Hiroyuki Fujioka, Professor Masayuki Niiyama, and Professor Toshiyuki Gogami. I spent, in total, six years in their laboratory as a graduate student. They are all the specialists in various research fields and gave me instructive suggestions from various aspects based on their expertise. I also thank colleagues in the laboratory. Discussions with them always stimulated my intellectual curiosity. Thanks to all the members in the laboratory, my graduate-studenthood became one of the unforgettable memories in my whole life.

I am grateful to all of the staffs and students in NP-1A group in RCNP. I have moved from Kyoto University to the NP-1A group five years ago. I really enjoyed the discussion with them. Especially, I was influenced a lot from Professor Nori Aoi, Professor Atsushi Tamii, Professor Eiji Ideguchi, Professor Tatsushi Shima, Professor Shinsuke Ota, and Dr. Harutaka Sakaguchi. In addition, I was really cheered up from the conversation with my colleague, in the NP-1A group, namely Dr. Yasutaka Yamamoto, Dr. Azusa Inoue, Mr. Keita Kawata, Mr. Takashi Sudo, Mr. Asahi Kohda, and Dr. Fumitaka Endo. Pleasant moments with them enabled me to endure the hard path to a PhD degree.

I thank to my dissertation committee members: Professor Nagae Tomofumi, Professor Takahiro Kawabata, Professor Juzo Zenihiro, Professor Yoshiko Kanada, and Professor Osamu Tajima. I am confident that their constructive feedback improved the thesis.

I appreciates the support of Grant-in-Aid for JSPS Research Fellow No. JP16J05592. This work was also supported by JSPS KAKENHI Grants No. JP23340068 and No. JP15H02091.

Finally, I would like to express my sincere appreciation to my family, namely Mineo Murata, Tomoe Murata, Masaru Murata, Takashi Ikeda, Teruyo Ikeda, Hirokazu Ikeda, Tomoya Murata, and Kazuaki Murata. I managed to continue my research activity for a long time owing to their understanding and seamless supports both from logistical and emotional aspects. I would not be where I am today if it were not for any of them.

Bibliography

[1] M. Murata, T. Kawabata, S. Adachi, H. Akimune, S. Amano, Y. Fujikawa, T. Furuno, K. Inaba, Y. Ishii, S. Miyamoto, M. Tsumura, H. Utsunomiya, Photodisintegration cross section of ^{4}He in the giant dipole resonance energy region, Phys. Rev. C 107 (2023) 064317. doi:10.1103/PhysRevC.107.064317.
URL https://link.aps.org/doi/10.1103/PhysRevC.107.064317

[2] R. Hofstadter, Electron scattering and nuclear structure, Rev. Mod. Phys. 28 (1956) 214–254. doi:10.1103/RevModPhys.28.214.
URL https://link.aps.org/doi/10.1103/RevModPhys.28.214

[3] E. M. Riordan, The Discovery of quarks, Science 256 (1992) 1287–1293. doi:10.1126/science.256.5061.1287.

[4] P. Doornenbal, In-beam gamma-ray spectroscopy at the RIBF, Progress of Theoretical and Experimental Physics 2012 (1) (2012) 03C004. arXiv:https://academic.oup.com/ptep/article-pdf/2012/1/03C004/11597694/pts076.pdf, doi:10.1093/ptep/pts076.
URL https://doi.org/10.1093/ptep/pts076

[5] S. Akkoyun, A. Algora, B. Alikhani, F. Ameil, G. de Angelis, L. Arnold, A. Astier, A. Ataç, Y. Aubert, C. Aufranc, A. Austin, S. Aydin, F. Azaiez, S. Badoer, D. Balabanski, D. Barrientos, G. Baulieu, R. Baumann, D. Bazzacco, F. Beck, T. Beck, P. Bednarczyk, M. Bellato, M. Bentley, G. Benzoni, R. Berthier, L. Berti, R. Beunard, G. Lo Bianco, B. Birkenbach, P. Bizzeti, A. Bizzeti-Sona, F. Le Blanc, J. Blasco, N. Blasi, D. Bloor, C. Boiano, M. Borsato, D. Bortolato, A. Boston, H. Boston, P. Bourgault, P. Boutachkov, A. Bouty, A. Bracco, S. Brambilla, I. Brawn, A. Brondi, S. Broussard, B. Bruyneel, D. Bucurescu, I. Burrows, A. Bürger, S. Cabaret, B. Cahan, E. Calore, F. Camera, A. Capsoni, F. Carrió, G. Casati, M. Castoldi, B. Cederwall, J.-L. Cercus, V. Chambert, M. El Chambit, R. Chapman, L. Charles, J. Chavas, E. Clément, P. Cocconi, S. Coelli, P. Coleman-Smith, A. Colombo, S. Colosimo, C. Commeaux, D. Conventi, R. Cooper, A. Corsi, A. Cortesi, L. Costa, F. Crespi, J. Cresswell, D. Cullen, D. Curien, A. Czermak, D. Delbourg, R. Depalo, T. Descombes, P. Désesquelles, P. Detistov, C. Diarra, F. Didierjean, M. Dimmock, Q. Doan, C. Domingo-Pardo, M. Doncel, F. Dorangeville, N. Dosme, Y. Drouen, G. Duchêne, B. Dulny, J. Eberth, P. Edelbruck, J. Egea, T. Engert, M. Erduran, S. Ertürk, C. Fanin, S. Fantinel, E. Farnea,

T. Faul, M. Filliger, F. Filmer, C. Finck, G. de France, A. Gadea, W. Gast, A. Geraci, J. Gerl, R. Gernhäuser, A. Giannatiempo, A. Giaz, L. Gibelin, A. Givechev, N. Goel, V. González, A. Gottardo, X. Grave, J. Gre˛bosz, R. Griffiths, A. Grint, P. Gros, L. Guevara, M. Gulmini, A. Görgen, H. Ha, T. Habermann, L. Harkness, H. Harroch, K. Hauschild, C. He, A. Hernández-Prieto, B. Hervieu, H. Hess, T. Hüyük, E. Ince, R. Isocrate, G. Jaworski, A. Johnson, J. Jolie, P. Jones, B. Jonson, P. Joshi, D. Judson, A. Jungclaus, M. Kaci, N. Karkour, M. Karolak, A. Kaşkaş, M. Kebbiri, R. Kempley, A. Khaplanov, S. Klupp, M. Kogimtzis, I. Kojouharov, A. Korichi, W. Korten, T. Kröll, R. Krücken, N. Kurz, B. Ky, M. Labiche, X. Lafay, L. Lavergne, I. Lazarus, S. Leboutelier, F. Lefebvre, E. Legay, L. Legeard, F. Lelli, S. Lenzi, S. Leoni, A. Lermitage, D. Lersch, J. Leske, S. Letts, S. Lhenoret, R. Lieder, D. Linget, J. Ljungvall, A. Lopez-Martens, A. Lotodé, S. Lunardi, A. Maj, J. van der Marel, Y. Mariette, N. Marginean, R. Marginean, G. Maron, A. Mather, W. Me˛czyński, V. Mendéz, P. Medina, B. Melon, R. Menegazzo, D. Mengoni, E. Merchan, L. Mihailescu, C. Michelagnoli, J. Mierzejewski, L. Milechina, B. Million, K. Mitev, P. Molini, D. Montanari, S. Moon, F. Morbiducci, R. Moro, P. Morrall, O. Möller, A. Nannini, D. Napoli, L. Nelson, M. Nespolo, V. Ngo, M. Nicoletto, R. Nicolini, Y. Le Noa, P. Nolan, M. Norman, J. Nyberg, A. Obertelli, A. Olariu, R. Orlandi, D. Oxley, C. Özben, M. Ozille, C. Oziol, E. Pachoud, M. Palacz, J. Palin, J. Pancin, C. Parisel, P. Pariset, G. Pascovici, R. Peghin, L. Pellegri, A. Perego, S. Perrier, M. Petcu, P. Petkov, C. Petrache, E. Pierre, N. Pietralla, S. Pietri, M. Pignanelli, I. Piqueras, Z. Podolyak, P. Le Pouhalec, J. Pouthas, D. Pugnére, V. Pucknell, A. Pullia, B. Quintana, R. Raine, G. Rainovski, L. Ramina, G. Rampazzo, G. La Rana, M. Rebeschini, F. Recchia, N. Redon, M. Reese, P. Reiter, P. Regan, S. Riboldi, M. Richer, M. Rigato, S. Rigby, G. Ripamonti, A. Robinson, J. Robin, J. Roccaz, J.-A. Ropert, B. Rossé, C. Rossi Alvarez, D. Rosso, B. Rubio, D. Rudolph, F. Saillant, E. Şahin, F. Salomon, M.-D. Salsac, J. Salt, G. Salvato, J. Sampson, E. Sanchis, C. Santos, H. Schaffner, M. Schlarb, D. Scraggs, D. Seddon, M. Şenyiğit, M.-H. Sigward, G. Simpson, J. Simpson, M. Slee, J. Smith, P. Sona, B. Sowicki, P. Spolaore, C. Stahl, T. Stanios, E. Stefanova, O. Stézowski, J. Strachan, G. Suliman, P.-A. Söderström, J. Tain, S. Tanguy, S. Tashenov, C. Theisen, J. Thornhill, F. Tomasi, N. Toniolo, R. Touzery, B. Travers, A. Triossi, M. Tripon, K. Tun-Lanoë, M. Turcato, C. Unsworth, C. Ur, J. Valiente-Dobon, V. Vandone, E. Vardaci, R. Venturelli, F. Veronese, C. Veyssiere, E. Viscione, R. Wadsworth, P. Walker, N. Warr, C. Weber, D. Weisshaar, D. Wells, O. Wieland, A. Wiens, G. Wittwer, H. Wollersheim, F. Zocca, N. Zamfir, M. Zie˛bliński, A. Zucchiatti, Agata—advanced gamma tracking array, Nuclear Instruments and Methods in Physics Research Section A: Accelerators, Spectrometers, Detectors and Associated Equipment 668 (2012) 26–58. doi:https://doi.org/10.1016/j.nima.2011.11.081.
URL https://www.sciencedirect.com/science/article/pii/S0168900211021516

[6] S. Paschalis, I. Lee, A. Macchiavelli, C. Campbell, M. Cromaz, S. Gros, J. Pa-

van, J. Qian, R. Clark, H. Crawford, D. Doering, P. Fallon, C. Lionberger, T. Loew, M. Petri, T. Stezelberger, S. Zimmermann, D. Radford, K. Lagergren, D. Weisshaar, R. Winkler, T. Glasmacher, J. Anderson, C. Beausang, The performance of the gamma-ray energy tracking in-beam nuclear array gretina, Nuclear Instruments and Methods in Physics Research Section A: Accelerators, Spectrometers, Detectors and Associated Equipment 709 (2013) 44–55. doi:https://doi.org/10.1016/j.nima.2013.01.009.
URL https://www.sciencedirect.com/science/article/pii/S0168900213000508

[7] J. S. Levinger, The high energy nuclear photoeffect, Phys. Rev. 84 (1951) 43–51. doi:10.1103/PhysRev.84.43.
URL https://link.aps.org/doi/10.1103/PhysRev.84.43

[8] R. L. Workman, Others, Review of Particle Physics, PTEP 2022 (2022) 083C01. doi:10.1093/ptep/ptac097.

[9] J. Ahrens, The total absorption of photons by nuclei, Nuclear Physics A 446 (1) (1985) 229–239. doi:https://doi.org/10.1016/0375-9474(85)90591-3.
URL https://www.sciencedirect.com/science/article/pii/0375947485905913

[10] B. A. Brown, C. R. Bronk, P. E. Hodgson, Systematics of nuclear rms charge radii, Journal of Physics G: Nuclear Physics 10 (12) (1984) 1683. doi:10.1088/0305-4616/10/12/008.
URL https://dx.doi.org/10.1088/0305-4616/10/12/008

[11] C. Ciofi degli Atti, Electron scattering by nuclei, Progress in Particle and Nuclear Physics 3 (1980) 163–328. doi:https://doi.org/10.1016/0146-6410(80)90032-0.
URL https://www.sciencedirect.com/science/article/pii/0146641080900320

[12] P. Ring, P. Schuck, The nuclear many-body problem, Springer-Verlag, New York, 1980.

[13] W. Greiner, D. Bromley, J. Maruhn, Nuclear Models, Springer Berlin Heidelberg, 2012.
URL https://books.google.co.jp/books?id=UcLsCAAAQBAJ

[14] M. Harakeh, A. Woude, Giant Resonances: Fundamental High-frequency Modes of Nuclear Excitation, Oxford science publications, Oxford University Press, 2001.
URL https://books.google.co.jp/books?id=ux0JhIdbGT8C

[15] W. Bothe, W. Gentner, Atomumwandlungen durch γ-strahlen, Zeitschrift für Physik 106 (3) (1937) 236–248. doi:10.1007/BF01340320.
URL https://doi.org/10.1007/BF01340320

[16] A. Bohr, B. Mottelson, Nuclear Structure II, Benjamin Inc., 1975.

[17] S. C. Fultz, R. L. Bramblett, J. T. Caldwell, N. A. Kerr, Photoneutron cross-section measurements on gold using nearly monochromatic photons, Phys. Rev. 127 (1962) 1273–1279. doi:10.1103/PhysRev.127.1273.
URL https://link.aps.org/doi/10.1103/PhysRev.127.1273

[18] W. Thomas, Über die zahl der dispersionselektronen, die einem stationären zustande zugeordnet sind. (vorläufige mitteilung), Naturwissenschaften 13 (28) (1925) 627–627. doi:10.1007/BF01558908.
URL https://doi.org/10.1007/BF01558908

[19] W. Kuhn, Über die gesamtstärke der von einem zustande ausgehenden absorptionslinien, Zeitschrift für Physik 33 (1) (1925) 408–412. doi:10.1007/BF01328322.
URL https://doi.org/10.1007/BF01328322

[20] F. Reiche, W. Thomas, Über die zahl der dispersionselektronen, die einem stationären zustand zugeordnet sind, Zeitschrift für Physik 34 (1) (1925) 510–525. doi:10.1007/BF01328494.
URL https://doi.org/10.1007/BF01328494

[21] B. L. Berman, S. C. Fultz, Measurements of the giant dipole resonance with monoenergetic photons, Rev. Mod. Phys. 47 (1975) 713–761. doi:10.1103/RevModPhys.47.713.
URL https://link.aps.org/doi/10.1103/RevModPhys.47.713

[22] M. Goldhaber, E. Teller, On nuclear dipole vibrations, Phys. Rev. 74 (1948) 1046–1049. doi:10.1103/PhysRev.74.1046.
URL https://link.aps.org/doi/10.1103/PhysRev.74.1046

[23] H. Steinwedel, J. D.Jensen, Zeitschrift für Naturforschung A 5 (8) (1950) 413–420 [cited 2023-09-20]. doi:doi:10.1515/zna-1950-0801, [link].
URL https://doi.org/10.1515/zna-1950-0801

[24] G. E. Brown, M. Bolsterli, Dipole state in nuclei, Phys. Rev. Lett. 3 (1959) 472–476. doi:10.1103/PhysRevLett.3.472.
URL https://link.aps.org/doi/10.1103/PhysRevLett.3.472

[25] R. Eramzhyan, B. Ishkhanov, I. Kapitonov, V. Neudatchin, The giant dipole resonance in light nuclei and related phenomena, Physics Reports 136 (4) (1986) 229–400. doi:https://doi.org/10.1016/0370-1573(86)90136-5.
URL https://www.sciencedirect.com/science/article/pii/0370157386901365

[26] D. J. McLean, M. N. Thompson, D. Zubanov, K. G. McNeill, J. W. Jury, B. L. Berman, ^{14}C photoproton cross section, Phys. Rev. C 44 (1991) 1137–1147. doi:10.1103/PhysRevC.44.1137.
URL https://link.aps.org/doi/10.1103/PhysRevC.44.1137

[27] M. G. Mayer, On closed shells in nuclei. ii, Phys. Rev. 75 (1949) 1969–1970. doi:10.1103/PhysRev.75.1969.
URL https://link.aps.org/doi/10.1103/PhysRev.75.1969

[28] O. Haxel, J. H. D. Jensen, H. E. Suess, On the "magic numbers" in nuclear structure, Phys. Rev. 75 (1949) 1766–1766. doi:10.1103/PhysRev.75.1766.2.
URL https://link.aps.org/doi/10.1103/PhysRev.75.1766.2

[29] M. G. Mayer, Nuclear configurations in the spin-orbit coupling model. i. empirical evidence, Phys. Rev. 78 (1950) 16–21. doi:10.1103/PhysRev.78.16.
URL https://link.aps.org/doi/10.1103/PhysRev.78.16

[30] O. Haxel, J. H. D. Jensen, H. E. Suess, Modellmäßige deutung der ausgezeichneten nukleonenzahlen im kernbau, Zeitschrift für Physik 128 (2) (1950) 295–311. doi:10.1007/BF01333077.
URL https://doi.org/10.1007/BF01333077

[31] A. Nogga, H. Kamada, W. Glöckle, Modern nuclear force predictions for the α particle, Phys. Rev. Lett. 85 (2000) 944–947. doi:10.1103/PhysRevLett.85.944.
URL https://link.aps.org/doi/10.1103/PhysRevLett.85.944

[32] H. Kamada, A. Nogga, W. Glöckle, E. Hiyama, M. Kamimura, K. Varga, Y. Suzuki, M. Viviani, A. Kievsky, S. Rosati, J. Carlson, S. C. Pieper, R. B. Wiringa, P. Navrátil, B. R. Barrett, N. Barnea, W. Leidemann, G. Orlandini, Benchmark test calculation of a four-nucleon bound state, Phys. Rev. C 64 (2001) 044001. doi:10.1103/PhysRevC.64.044001.
URL https://link.aps.org/doi/10.1103/PhysRevC.64.044001

[33] T. Myo, S. Sugimoto, K. Katō, H. Toki, K. Ikeda, Tensor Correlation in 4He with the Tensor-Optimized Shell Model, Progress of Theoretical Physics 117 (2) (2007) 257–274. arXiv:https://academic.oup.com/ptp/article-pdf/117/2/257/5283549/117-2-257.pdf, doi:10.1143/PTP.117.257.
URL https://doi.org/10.1143/PTP.117.257

[34] D. Tilley, H. Weller, G. Hale, Energy levels of light nuclei a = 4, Nuclear Physics A 541 (1) (1992) 1–104. doi:https://doi.org/10.1016/0375-9474(92)90635-W.
URL https://www.sciencedirect.com/science/article/pii/037594749290635W

[35] H. Yukawa, On the interaction of elementary particles. i, Nippon Sugaku-Buturigakkwai Kizi Dai 3 Ki 17 (1935) 48–57. doi:10.11429/ppmsj1919.17.0_48.

[36] M. Naghdi, Nucleon-nucleon interaction: A typical/concise review, Physics of Particles and Nuclei 45 (5) (2014) 924–971. doi:10.1134/S1063779614050050.
URL https://doi.org/10.1134/S1063779614050050

[37] M. Taketani, S. Nakamura, M. Sasaki, On the Method of the Theory of Nuclear Forces, Progress of Theoretical Physics 6 (4) (1951) 581–586. arXiv:https://

academic.oup.com/ptp/article-pdf/6/4/581/5419152/6-4-581.pdf, doi:10.1143/ptp/6.4.581.
URL https://doi.org/10.1143/ptp/6.4.581

[38] T. Hamada, I. Johnston, A potential model representation of two-nucleon data below 315 mev, Nuclear Physics 34 (2) (1962) 382–403. doi:https://doi.org/10.1016/0029-5582(62)90228-6.
URL https://www.sciencedirect.com/science/article/pii/0029558262902286

[39] I. Lagaris, V. Pandharipande, Phenomenological two-nucleon interaction operator, Nuclear Physics A 359 (2) (1981) 331–348. doi:https://doi.org/10.1016/0375-9474(81)90240-2.
URL https://www.sciencedirect.com/science/article/pii/0375947481902402

[40] R. B. Wiringa, R. A. Smith, T. L. Ainsworth, Nucleon-nucleon potentials with and without $\Delta(1232)$ degrees of freedom, Phys. Rev. C 29 (1984) 1207–1221. doi:10.1103/PhysRevC.29.1207.
URL https://link.aps.org/doi/10.1103/PhysRevC.29.1207

[41] R. B. Wiringa, V. G. J. Stoks, R. Schiavilla, Accurate nucleon-nucleon potential with charge-independence breaking, Phys. Rev. C 51 (1995) 38–51. doi:10.1103/PhysRevC.51.38.
URL https://link.aps.org/doi/10.1103/PhysRevC.51.38

[42] W. N. Cottingham, M. Lacombe, B. Loiseau, J. M. Richard, R. V. Mau, Nucleon-nucleon interaction from pion-nucleon phase-shift analysis, Phys. Rev. D 8 (1973) 800–819. doi:10.1103/PhysRevD.8.800.
URL https://link.aps.org/doi/10.1103/PhysRevD.8.800

[43] R. Machleidt, K. Holinde, C. Elster, The bonn meson-exchange model for the nucleon—nucleon interaction, Physics Reports 149 (1) (1987) 1–89. doi:https://doi.org/10.1016/S0370-1573(87)80002-9.
URL https://www.sciencedirect.com/science/article/pii/S0370157387800029

[44] V. G. J. Stoks, R. A. M. Klomp, C. P. F. Terheggen, J. J. de Swart, Construction of high-quality nn potential models, Phys. Rev. C 49 (1994) 2950–2962. doi:10.1103/PhysRevC.49.2950.
URL https://link.aps.org/doi/10.1103/PhysRevC.49.2950

[45] S. Weinberg, Phenomenological lagrangians, Physica A: Statistical Mechanics and its Applications 96 (1) (1979) 327–340. doi:https://doi.org/10.1016/0378-4371(79)90223-1.
URL https://www.sciencedirect.com/science/article/pii/0378437179902231

[46] S. Weinberg, Nuclear forces from chiral lagrangians, Physics Letters B 251 (2) (1990) 288–292. doi:https://doi.org/10.1016/0370-2693(90)90938-3.
URL https://www.sciencedirect.com/science/article/pii/0370269390909383

[47] S. Weinberg, Effective chiral lagrangians for nucleon-pion interactions and nuclear forces, Nuclear Physics B 363 (1) (1991) 3–18. doi:https://doi.org/10.1016/0550-3213(91)90231-L.
URL https://www.sciencedirect.com/science/article/pii/055032139190231L

[48] D. R. Entem, R. Machleidt, Accurate charge-dependent nucleon-nucleon potential at fourth order of chiral perturbation theory, Phys. Rev. C 68 (2003) 041001. doi:10.1103/PhysRevC.68.041001.
URL https://link.aps.org/doi/10.1103/PhysRevC.68.041001

[49] H. Primakoff, T. Holstein, Many-body interactions in atomic and nuclear systems, Phys. Rev. 55 (1939) 1218–1234. doi:10.1103/PhysRev.55.1218.
URL https://link.aps.org/doi/10.1103/PhysRev.55.1218

[50] J.-i. Fujita, H. Miyazawa, Pion Theory of Three-Body Forces, Progress of Theoretical Physics 17 (3) (1957) 360–365. arXiv:https://academic.oup.com/ptp/article-pdf/17/3/360/5252121/17-3-360.pdf, doi:10.1143/PTP.17.360.
URL https://doi.org/10.1143/PTP.17.360

[51] S. C. Pieper, Quantum monte carlo calculations of light nuclei, Nuclear Physics A 751 (2005) 516–532, proceedings of the 22nd International Nuclear Physics Conference (Part 1). doi:https://doi.org/10.1016/j.nuclphysa.2005.02.018.
URL https://www.sciencedirect.com/science/article/pii/S0375947405001247

[52] A. Akmal, V. R. Pandharipande, D. G. Ravenhall, Equation of state of nucleon matter and neutron star structure, Phys. Rev. C 58 (1998) 1804–1828. doi:10.1103/PhysRevC.58.1804.
URL https://link.aps.org/doi/10.1103/PhysRevC.58.1804

[53] S. Coon, M. Scadron, P. McNamee, B. Barrett, D. Blatt, B. McKellar, The two-pion-exchange three-nucleon potential and nuclear matter, Nuclear Physics A 317 (1) (1979) 242–278. doi:https://doi.org/10.1016/0375-9474(79)90462-7.
URL https://www.sciencedirect.com/science/article/pii/0375947479904627

[54] M. Robilotta, H. Coelho, Taming the two-pion exchange three-nucleon potential, Nuclear Physics A 460 (4) (1986) 645–674. doi:https://doi.org/10.1016/0375-9474(86)90530-0.
URL https://www.sciencedirect.com/science/article/pii/0375947486905300

[55] B. S. Pudliner, V. R. Pandharipande, J. Carlson, S. C. Pieper, R. B. Wiringa, Quantum monte carlo calculations of nuclei with $\sim$ 7, Phys. Rev. C 56 (1997) 1720–1750. doi:10.1103/PhysRevC.56.1720.
URL https://link.aps.org/doi/10.1103/PhysRevC.56.1720

[56] U. van Kolck, Few-nucleon forces from chiral lagrangians, Phys. Rev. C 49 (1994) 2932–2941. doi:10.1103/PhysRevC.49.2932.
URL https://link.aps.org/doi/10.1103/PhysRevC.49.2932

[57] E. Epelbaum, A. Nogga, W. Glöckle, H. Kamada, U.-G. Meißner, H. Witała, Three-nucleon forces from chiral effective field theory, Phys. Rev. C 66 (2002) 064001. doi:10.1103/PhysRevC.66.064001.
URL https://link.aps.org/doi/10.1103/PhysRevC.66.064001

[58] K. A. Brueckner, Two-body forces and nuclear saturation. iii. details of the structure of the nucleus, Phys. Rev. 97 (1955) 1353–1366. doi:10.1103/PhysRev.97.1353.
URL https://link.aps.org/doi/10.1103/PhysRev.97.1353

[59] J. Goldstone, Derivation of the brueckner many-body theory, Proceedings of the Royal Society of London. Series A, Mathematical and Physical Sciences 239 (1217) (1957) 267–279.
URL http://www.jstor.org/stable/100119

[60] H. A. Bethe, B. H. Brandow, A. G. Petschek, Reference spectrum method for nuclear matter, Phys. Rev. 129 (1963) 225–264. doi:10.1103/PhysRev.129.225.
URL https://link.aps.org/doi/10.1103/PhysRev.129.225

[61] D. Dean, T. Engeland, M. Hjorth-Jensen, M. Kartamyshev, E. Osnes, Effective interactions and the nuclear shell-model, Progress in Particle and Nuclear Physics 53 (2) (2004) 419–500. doi:https://doi.org/10.1016/j.ppnp.2004.05.001.
URL https://www.sciencedirect.com/science/article/pii/S0146641004000912

[62] M. Hjorth-Jensen, T. T. Kuo, E. Osnes, Realistic effective interactions for nuclear systems, Physics Reports 261 (3) (1995) 125–270. doi:https://doi.org/10.1016/0370-1573(95)00012-6.
URL https://www.sciencedirect.com/science/article/pii/0370157395000126

[63] A. Covello, F. Andreozzi, L. Coraggio, A. Gargano, T. Kuo, A. Porrino, Nuclear structure calculations with realistic effective interactions, Progress in Particle and Nuclear Physics 38 (1997) 165–172, 4 pi High Resolution Gamma Ray Spectroscopy and Nuclear Structure. doi:https://doi.org/10.1016/S0146-6410(97)00023-9.
URL https://www.sciencedirect.com/science/article/pii/S0146641097000239

[64] B. Wildenthal, Empirical strengths of spin operators in nuclei, Progress in Particle and Nuclear Physics 11 (1984) 5–51. doi:https://doi.org/10.1016/0146-6410(84)90011-5.
URL https://www.sciencedirect.com/science/article/pii/0146641084900115

[65] R. Roth, The 16 th CNS International Summer School, Lecture Notes: Ab Initio Nuclear Structure Theory, Lecture 3: Light Nuclei, uRL: https://indico2.cns.s.u-tokyo.ac.jp/event/8/attachments/42/114/cnsss_lecture03.pdf. Last visited on 2023/09/26 (2017).

[66] P. Navratil, S. Quaglioni, Ab initio nuclear reaction theory with applications to astrophysics (2022). arXiv:2204.01187.

[67] A. Ekström, C. Forssén, G. Hagen, G. R. Jansen, W. Jiang, T. Papenbrock, What is ab initio in nuclear theory?, Frontiers in Physics 11 (2023). doi:10.3389/fphy.2023.1129094.
URL https://www.frontiersin.org/articles/10.3389/fphy.2023.1129094

[68] W. Leidemann, G. Orlandini, Modern ab initio approaches and applications in few-nucleon physics with ageq4, Progress in Particle and Nuclear Physics 68 (2013) 158–214. doi:https://doi.org/10.1016/j.ppnp.2012.09.001.
URL https://www.sciencedirect.com/science/article/pii/S014664101200110X

[69] J. Carbonell, A. Deltuva, A. Fonseca, R. Lazauskas, Bound state techniques to solve the multiparticle scattering problem, Progress in Particle and Nuclear Physics 74 (2014) 55–80. doi:https://doi.org/10.1016/j.ppnp.2013.10.003.
URL https://www.sciencedirect.com/science/article/pii/S0146641013000938

[70] V. D. Efros, W. Leidemann, G. Orlandini, Response functions from integral transforms with a lorentz kernel, Physics Letters B 338 (2) (1994) 130–133. doi:https://doi.org/10.1016/0370-2693(94)91355-2.
URL https://www.sciencedirect.com/science/article/pii/0370269394913552

[71] N. Barnea, V. D. Efros, W. Leidemann, G. Orlandini, The lorentz integral transform and its inversion, Few-Body Systems 47 (4) (2010) 201–206. doi:10.1007/s00601-009-0081-0.
URL https://doi.org/10.1007/s00601-009-0081-0

[72] J. Nuttall, H. L. Cohen, Method of complex coordinates for three-body calculations above the breakup threshold, Phys. Rev. 188 (1969) 1542–1544. doi:10.1103/PhysRev.188.1542.
URL https://link.aps.org/doi/10.1103/PhysRev.188.1542

[73] N. Moiseyev, Quantum theory of resonances: calculating energies, widths and cross-sections by complex scaling, Physics Reports 302 (5) (1998) 212–293. doi:https://doi.org/10.1016/S0370-1573(98)00002-7.
URL https://www.sciencedirect.com/science/article/pii/S0370157398000027

[74] F. Hoyle, On Nuclear Reactions Occuring in Very Hot STARS.I. the Synthesis of Elements from Carbon to Nickel., The Astrophysical journal Supplemant Series 1 (1954) 121. doi:10.1086/190005.

[75] M. Freer, H. Fynbo, The hoyle state in 12c, Progress in Particle and Nuclear Physics 78 (2014) 1–23. doi:https://doi.org/10.1016/j.ppnp.2014.06.001.
URL https://www.sciencedirect.com/science/article/pii/S0146641014000453

[76] A. Tohsaki, H. Horiuchi, P. Schuck, G. Röpke, Alpha cluster condensation in ^{12}c and ^{16}o, Phys. Rev. Lett. 87 (2001) 192501. doi:10.1103/PhysRevLett.87.192501.
URL https://link.aps.org/doi/10.1103/PhysRevLett.87.192501

[77] S. E. Woosley, D. H. Hartmann, R. D. Hoffman, W. C. Haxton, The ν-Process, The Astrophysical Journal 356 (1990) 272. doi:10.1086/168839.

[78] H.-T. Janka, K. Langanke, A. Marek, G. Martínez-Pinedo, B. Müller, Theory of core-collapse supernovae, Physics Reports 442 (1) (2007) 38–74, the Hans Bethe Centennial Volume 1906-2006. doi:https://doi.org/10.1016/j.physrep.2007.02.002.
URL https://www.sciencedirect.com/science/article/pii/S0370157307000439

[79] T. Suzuki, T. Kajino, Element synthesis in the supernova environment and neutrino oscillations, Journal of Physics G: Nuclear and Particle Physics 40 (8) (2013) 083101. doi:10.1088/0954-3899/40/8/083101.
URL https://dx.doi.org/10.1088/0954-3899/40/8/083101

[80] T. Yoshida, T. Suzuki, S. Chiba, T. Kajino, H. Yokomakura, K. Kimura, A. Takamura, D. H. Hartmann, Neutrino-nucleus reaction cross sections for light element synthesis in supernova explosions, The Astrophysical Journal 686 (1) (2008) 448. doi:10.1086/591266.
URL https://dx.doi.org/10.1086/591266

[81] S. X. Nakamura, H. Kamano, Y. Hayato, M. Hirai, W. Horiuchi, S. Kumano, T. Murata, K. Saito, M. Sakuda, T. Sato, Y. Suzuki, Towards a unified model of neutrino-nucleus reactions for neutrino oscillation experiments, Reports on Progress in Physics 80 (5) (2017) 056301. doi:10.1088/1361-6633/aa5e6c.
URL https://dx.doi.org/10.1088/1361-6633/aa5e6c

[82] S. Nakamura, T. Sato, V. Gudkov, K. Kubodera, Neutrino reactions on the deuteron, Phys. Rev. C 63 (2001) 034617. doi:10.1103/PhysRevC.63.034617.
URL https://link.aps.org/doi/10.1103/PhysRevC.63.034617

[83] H. Ejiri, Nuclear spin isospin responses for low-energy neutrinos, Physics Reports 338 (3) (2000) 265–351. doi:https://doi.org/10.1016/S0370-1573(00)00044-2.
URL https://www.sciencedirect.com/science/article/pii/S0370157300000442

[84] H. Ejiri, A. I. Titov, M. Boswell, A. Young, Neutrino-nuclear response and photonuclear reactions, Phys. Rev. C 88 (2013) 054610. doi:10.1103/PhysRevC.88.054610.
URL https://link.aps.org/doi/10.1103/PhysRevC.88.054610

[85] M. Kusakabe, T. Kajino, T. Yoshida, T. Shima, Y. Nagai, T. Kii, New constraints on radiative decay of long-lived particles in big bang nucleosynthesis with new ^{4}He photodisintegration data, Phys. Rev. D 79 (2009) 123513. doi:10.1103/PhysRevD.79.123513.
URL https://link.aps.org/doi/10.1103/PhysRevD.79.123513

[86] E. Vangioni-Flam, M. Cassé, J. Audouze, Lithium–beryllium–boron: origin and evolution, Physics Reports 333–334 (2000) 365–387. doi:10.1016/s0370-1573(00)00030-2.
URL http://dx.doi.org/10.1016/S0370-1573(00)00030-2

[87] S. G. Ryan, T. C. Beers, K. A. Olive, B. D. Fields, J. E. Norris, Primordial lithium and big bang nucleosynthesis, The Astrophysical Journal 530 (2) (2000) L57. doi:10.1086/312492.
URL https://dx.doi.org/10.1086/312492

[88] J. Meléndez, I. Ramírez, Reappraising the spite lithium plateau: Extremely thin and marginally consistent with WMAP data, The Astrophysical Journal 615 (1) (2004) L33. doi:10.1086/425962.
URL https://dx.doi.org/10.1086/425962

[89] M. Asplund, D. L. Lambert, P. E. Nissen, F. Primas, V. V. Smith, Lithium isotopic abundances in metal-poor halo stars, The Astrophysical Journal 644 (1) (2006) 229. doi:10.1086/503538.
URL https://dx.doi.org/10.1086/503538

[90] B. D. Fields, K. A. Olive, T.-H. Yeh, C. Young, Big-bang nucleosynthesis after planck, Journal of Cosmology and Astroparticle Physics 2020 (03) (2020) 010. doi:10.1088/1475-7516/2020/03/010.
URL https://dx.doi.org/10.1088/1475-7516/2020/03/010

[91] A. Tamii, L. Pellegri, P. A. Söderström, D. Allard, S. Goriely, T. Inakura, E. Khan, E. Kido, M. Kimura, E. Litvinova, S. Nagataki, P. v. Neumann-Cosel, N. Pietralla,

N. Shimizu, N. Tsoneva, Y. Utsuno, S. Adachi, P. Adsley, A. Bahini, D. Balabanski, B. Baret, J. A. C. Bekker, S. D. Binda, E. Boicu, A. Bracco, I. Brandherm, M. Brezeanu, J. W. Brummer, F. Camera, F. C. L. Crespi, R. Dalal, L. M. Donaldson, Y. Fujikawa, T. Furuno, H. Haoning, R. Higuchi, Y. Honda, A. Gavrilescu, A. Inoue, J. Isaak, H. Jivan, P. Jones, S. Jongile, O. Just, T. Kawabata, T. Khumalo, J. Kiener, J. Kleemann, N. Kobayashi, Y. Koshio, A. Kuşoğlu, K. C. W. Li, K. L. Malatji, R. E. Molaeng, H. Motoki, M. Murata, A. A. Netshiya, R. Neveling, R. Niina, S. Okamoto, S. Ota, O. Papst, E. Parizot, T. Petruse, M. S. Reen, P. Ring, K. Sakanashi, E. Sideras-Haddad, S. Siem, M. Spall, T. Suda, T. Sudo, Y. Taniguchi, V. Tatischeff, H. Utsunomiya, H. Wang, V. Werner, H. Wibowo, M. Wiedeking, O. Wieland, Y. Xu, Z. H. Yang, P. Collaboration, Pandora project for the study of photonuclear reactions below $$a=60$$, The European Physical Journal A 59 (9) (2023) 208. doi:10.1140/epja/s10050-023-01081-w.
URL https://doi.org/10.1140/epja/s10050-023-01081-w

[92] K. Greisen, End to the cosmic-ray spectrum?, Phys. Rev. Lett. 16 (1966) 748–750. doi:10.1103/PhysRevLett.16.748.
URL https://link.aps.org/doi/10.1103/PhysRevLett.16.748

[93] G. T. Zatsepin, V. A. Kuz'min, Upper Limit of the Spectrum of Cosmic Rays, Soviet Journal of Experimental and Theoretical Physics Letters 4 (1966) 78.

[94] A. Aab, P. Abreu, M. Aglietta, E. J. Ahn, I. Al Samarai, I. F. M. Albuquerque, I. Allekotte, J. Allen, P. Allison, A. Almela, J. Alvarez Castillo, J. Alvarez-Muñiz, R. Alves Batista, M. Ambrosio, A. Aminaei, L. Anchordoqui, S. Andringa, C. Aramo, V. M. Aranda, F. Arqueros, H. Asorey, P. Assis, J. Aublin, M. Ave, M. Avenier, G. Avila, N. Awal, A. M. Badescu, K. B. Barber, J. Bäuml, C. Baus, J. J. Beatty, K. H. Becker, J. A. Bellido, C. Berat, M. E. Bertaina, X. Bertou, P. L. Biermann, P. Billoir, S. Blaess, M. Blanco, C. Bleve, H. Blümer, M. Boháčová, D. Boncioli, C. Bonifazi, R. Bonino, N. Borodai, J. Brack, I. Brancus, A. Bridgeman, P. Brogueira, W. C. Brown, P. Buchholz, A. Bueno, S. Buitink, M. Buscemi, K. S. Caballero-Mora, B. Caccianiga, L. Caccianiga, M. Candusso, L. Caramete, R. Caruso, A. Castellina, G. Cataldi, L. Cazon, R. Cester, A. G. Chavez, A. Chiavassa, J. A. Chinellato, J. Chudoba, M. Cilmo, R. W. Clay, G. Cocciolo, R. Colalillo, A. Coleman, L. Collica, M. R. Coluccia, R. Concei ç ao, F. Contreras, M. J. Cooper, A. Cordier, S. Coutu, C. E. Covault, J. Cronin, A. Curutiu, R. Dallier, B. Daniel, S. Dasso, K. Daumiller, B. R. Dawson, R. M. de Almeida, M. De Domenico, S. J. de Jong, J. R. T. de Mello Neto, I. De Mitri, J. de Oliveira, V. de Souza, L. del Peral, O. Deligny, H. Dembinski, N. Dhital, C. Di Giulio, A. Di Matteo, J. C. Diaz, M. L. Díaz Castro, F. Diogo, C. Dobrigkeit, W. Docters, J. C. D'Olivo, A. Dorofeev, Q. Dorosti Hasankiadeh, M. T. Dova, J. Ebr, R. Engel, M. Erdmann, M. Erfani, C. O. Escobar, J. Espadanal, A. Etchegoyen, P. Facal San Luis, H. Falcke, K. Fang, G. Farrar, A. C. Fauth, N. Fazzini, A. P. Ferguson, M. Fernandes, B. Fick, J. M. Figueira, A. Filevich, A. Filipčič, B. D. Fox, O. Fratu, U. Fröhlich, B. Fuchs, T. Fujii, R. Gaior, B. García, S. T. Garcia Roca,

D. Garcia-Gamez, D. Garcia-Pinto, G. Garilli, A. Gascon Bravo, F. Gate, H. Gemmeke, P. L. Ghia, U. Giaccari, M. Giammarchi, M. Giller, C. Glaser, H. Glass, M. Gómez Berisso, P. F. Gómez Vitale, P. Gonçalves, J. G. Gonzalez, N. González, B. Gookin, J. Gordon, A. Gorgi, P. Gorham, P. Gouffon, S. Grebe, N. Griffith, A. F. Grillo, T. D. Grubb, F. Guarino, G. P. Guedes, M. R. Hampel, P. Hansen, D. Harari, T. A. Harrison, S. Hartmann, J. L. Harton, A. Haungs, T. Hebbeker, D. Heck, P. Heimann, A. E. Herve, G. C. Hill, C. Hojvat, N. Hollon, E. Holt, P. Homola, J. R. Hörandel, P. Horvath, M. Hrabovský, D. Huber, T. Huege, A. Insolia, P. G. Isar, I. Jandt, S. Jansen, C. Jarne, M. Josebachuili, A. Kääpä, O. Kambeitz, K. H. Kampert, P. Kasper, I. Katkov, B. Kégl, B. Keilhauer, A. Keivani, E. Kemp, R. M. Kieckhafer, H. O. Klages, M. Kleifges, J. Kleinfeller, R. Krause, N. Krohm, O. Krömer, D. Kruppke-Hansen, D. Kuempel, N. Kunka, D. LaHurd, L. Latronico, R. Lauer, M. Lauscher, P. Lautridou, S. Le Coz, M. S. A. B. Leão, D. Lebrun, P. Lebrun, M. A. Leigui de Oliveira, A. Letessier-Selvon, I. Lhenry-Yvon, K. Link, R. López, A. Lopez Agüera, K. Louedec, J. Lozano Bahilo, L. Lu, A. Lucero, M. Ludwig, M. Malacari, S. Maldera, M. Mallamaci, J. Maller, D. Mandat, P. Mantsch, A. G. Mariazzi, V. Marin, I. C. Mariş, G. Marsella, D. Martello, L. Martin, H. Martinez, O. Martínez Bravo, D. Martraire, J. J. Masías Meza, H. J. Mathes, S. Mathys, J. Matthews, J. A. J. Matthews, G. Matthiae, D. Maurel, D. Maurizio, E. Mayotte, P. O. Mazur, C. Medina, G. Medina-Tanco, R. Meissner, M. Melissas, D. Melo, A. Menshikov, S. Messina, R. Meyhandan, S. Mićanović, M. I. Micheletti, L. Middendorf, I. A. Minaya, L. Miramonti, B. Mitrica, L. Molina-Bueno, S. Mollerach, M. Monasor, D. Monnier Ragaigne, F. Montanet, C. Morello, M. Mostafá, C. A. Moura, M. A. Muller, G. Müller, S. Müller, M. Münchmeyer, R. Mussa, G. Navarra, S. Navas, P. Necesal, L. Nellen, A. Nelles, J. Neuser, P. Nguyen, M. Niechciol, L. Niemietz, T. Niggemann, D. Nitz, D. Nosek, V. Novotny, L. Nožka, L. Ochilo, A. Olinto, M. Oliveira, N. Pacheco, D. Pakk Selmi-Dei, M. Palatka, J. Pallotta, N. Palmieri, P. Papenbreer, G. Parente, A. Parra, T. Paul, M. Pech, J. Pękala, R. Pelayo, I. M. Pepe, L. Perrone, E. Petermann, C. Peters, S. Petrera, Y. Petrov, J. Phuntsok, R. Piegaia, T. Pierog, P. Pieroni, M. Pimenta, V. Pirronello, M. Platino, M. Plum, A. Porcelli, C. Porowski, R. R. Prado, P. Privitera, M. Prouza, V. Purrello, E. J. Quel, S. Querchfeld, S. Quinn, J. Rautenberg, O. Ravel, D. Ravignani, B. Revenu, J. Ridky, S. Riggi, M. Risse, P. Ristori, V. Rizi, W. Rodrigues de Carvalho, I. Rodriguez Cabo, G. Rodriguez Fernandez, J. Rodriguez Rojo, M. D. Rodríguez-Frías, D. Rogozin, G. Ros, J. Rosado, T. Rossler, M. Roth, E. Roulet, A. C. Rovero, S. J. Saffi, A. Saftoiu, F. Salamida, H. Salazar, A. Saleh, F. Salesa Greus, G. Salina, F. Sánchez, P. Sanchez-Lucas, C. E. Santo, E. Santos, E. M. Santos, F. Sarazin, B. Sarkar, R. Sarmento, R. Sato, N. Scharf, V. Scherini, H. Schieler, P. Schiffer, D. Schmidt, O. Scholten, H. Schoorlemmer, P. Schovánek, A. Schulz, J. Schulz, J. Schumacher, S. J. Sciutto, A. Segreto, M. Settimo, A. Shadkam, R. C. Shellard, I. Sidelnik, G. Sigl, O. Sima, A. Śmiałkowski, R. Šmída, G. R. Snow, P. Sommers, J. Sorokin, R. Squartini, Y. N. Srivastava, S. Stanič, J. Stapleton, J. Stasielak, M. Stephan, A. Stutz, F. Suarez, T. Suomijärvi, A. D. Supanitsky, M. S. Sutherland, J. Swain, Z. Szadkowski, M. Szuba, O. A. Taborda, A. Tapia, M. Tartare, A. Tepe, V. M. Theodoro,

C. Timmermans, C. J. Todero Peixoto, G. Toma, L. Tomankova, B. Tomé, A. Tonachini, G. Torralba Elipe, D. Torres Machado, P. Travnicek, E. Trovato, M. Tueros, R. Ulrich, M. Unger, M. Urban, J. F. Valdés Galicia, I. Valiño, L. Valore, G. van Aar, P. van Bodegom, A. M. van den Berg, S. van Velzen, A. van Vliet, E. Varela, B. Vargas Cárdenas, G. Varner, J. R. Vázquez, R. A. Vázquez, D. Veberič, V. Verzi, J. Vicha, M. Videla, L. Villaseñor, B. Vlcek, S. Vorobiov, H. Wahlberg, O. Wainberg, D. Walz, A. A. Watson, M. Weber, K. Weidenhaupt, A. Weindl, F. Werner, A. Widom, L. Wiencke, B. Wilczyńska, H. Wilczyński, M. Will, C. Williams, T. Winchen, D. Wittkowski, B. Wundheiler, S. Wykes, T. Yamamoto, T. Yapici, G. Yuan, A. Yushkov, B. Zamorano, E. Zas, D. Zavrtanik, M. Zavrtanik, I. Zaw, A. Zepeda, J. Zhou, Y. Zhu, M. Zimbres Silva, M. Ziolkowski, F. Zuccarello, Depth of maximum of air-shower profiles at the pierre auger observatory. i. measurements at energies above $10^{17.8}$ eV, Phys. Rev. D 90 (2014) 122005. doi:10.1103/PhysRevD.90.122005.
URL https://link.aps.org/doi/10.1103/PhysRevD.90.122005

[95] A. Aab, P. Abreu, M. Aglietta, J. M. Albury, I. Allekotte, A. Almela, J. Alvarez Castillo, J. Alvarez-Muñiz, R. Alves Batista, G. A. Anastasi, L. Anchordoqui, B. Andrada, S. Andringa, C. Aramo, P. R. Araújo Ferreira, H. Asorey, P. Assis, G. Avila, A. M. Badescu, A. Bakalova, A. Balaceanu, F. Barbato, R. J. Barreira Luz, K. H. Becker, J. A. Bellido, C. Berat, M. E. Bertaina, X. Bertou, P. L. Biermann, T. Bister, J. Biteau, A. Blanco, J. Blazek, C. Bleve, M. Boháčová, D. Boncioli, C. Bonifazi, L. Bonneau Arbeletche, N. Borodai, A. M. Botti, J. Brack, T. Bretz, F. L. Briechle, P. Buchholz, A. Bueno, S. Buitink, M. Buscemi, K. S. Caballero-Mora, L. Caccianiga, L. Calcagni, A. Cancio, F. Canfora, I. Caracas, J. M. Carceller, R. Caruso, A. Castellina, F. Catalani, G. Cataldi, L. Cazon, M. Cerda, J. A. Chinellato, K. Choi, J. Chudoba, L. Chytka, R. W. Clay, A. C. Cobos Cerutti, R. Colalillo, A. Coleman, M. R. Coluccia, R. Concei ç ao, A. Condorelli, G. Consolati, F. Contreras, F. Convenga, C. E. Covault, S. Dasso, K. Daumiller, B. R. Dawson, J. A. Day, R. M. de Almeida, J. de Jesús, S. J. de Jong, G. De Mauro, J. R. T. de Mello Neto, I. De Mitri, J. de Oliveira, D. de Oliveira Franco, V. de Souza, E. De Vito, J. Debatin, M. del Río, O. Deligny, H. Dembinski, N. Dhital, C. Di Giulio, A. Di Matteo, M. L. Díaz Castro, C. Dobrigkeit, J. C. D'Olivo, Q. Dorosti, R. C. dos Anjos, M. T. Dova, J. Ebr, R. Engel, I. Epicoco, M. Erdmann, C. O. Escobar, A. Etchegoyen, H. Falcke, J. Farmer, G. Farrar, A. C. Fauth, N. Fazzini, F. Feldbusch, F. Fenu, B. Fick, J. M. Figueira, A. Filipčič, T. Fodran, M. M. Freire, T. Fujii, A. Fuster, C. Galea, C. Galelli, B. García, A. L. Garcia Vegas, H. Gemmeke, F. Gesualdi, A. Gherghel-Lascu, P. L. Ghia, U. Giaccari, M. Giammarchi, M. Giller, J. Glombitza, F. Gobbi, F. Gollan, G. Golup, M. Gómez Berisso, P. F. Gómez Vitale, J. P. Gongora, N. González, I. Goos, D. Góra, A. Gorgi, M. Gottowik, T. D. Grubb, F. Guarino, G. P. Guedes, E. Guido, S. Hahn, R. Halliday, M. R. Hampel, P. Hansen, D. Harari, V. M. Harvey, A. Haungs, T. Hebbeker, D. Heck, G. C. Hill, C. Hojvat, J. R. Hörandel, P. Horvath, M. Hrabovský, T. Huege, J. Hulsman, A. Insolia, P. G. Isar, J. A. Johnsen, J. Jurysek, A. Kääpä, K. H. Kampert, B. Keilhauer,

J. Kemp, H. O. Klages, M. Kleifges, J. Kleinfeller, M. Köpke, G. Kukec Mezek, B. L. Lago, D. LaHurd, R. G. Lang, M. A. Leigui de Oliveira, V. Lenok, A. Letessier-Selvon, I. Lhenry-Yvon, D. Lo Presti, L. Lopes, R. López, R. Lorek, Q. Luce, A. Lucero, A. Machado Payeras, M. Malacari, G. Mancarella, D. Mandat, B. C. Manning, J. Manshanden, P. Mantsch, S. Marafico, A. G. Mariazzi, I. C. Mariş, G. Marsella, D. Martello, H. Martinez, O. Martínez Bravo, M. Mastrodicasa, H. J. Mathes, J. Matthews, G. Matthiae, E. Mayotte, P. O. Mazur, G. Medina-Tanco, D. Melo, A. Menshikov, K.-D. Merenda, S. Michal, M. I. Micheletti, L. Miramonti, D. Mockler, S. Mollerach, F. Montanet, C. Morello, M. Mostafá, A. L. Müller, M. A. Muller, K. Mulrey, R. Mussa, M. Muzio, W. M. Namasaka, L. Nellen, P. H. Nguyen, M. Niculescu-Oglinzanu, M. Niechciol, D. Nitz, D. Nosek, V. Novotny, L. Nožka, A. Nucita, L. A. Núñez, M. Palatka, J. Pallotta, M. P. Panetta, P. Papenbreer, G. Parente, A. Parra, M. Pech, F. Pedreira, J. Pękala, R. Pelayo, J. Peña Rodriguez, J. Perez Armand, M. Perlin, L. Perrone, C. Peters, S. Petrera, T. Pierog, M. Pimenta, V. Pirronello, M. Platino, B. Pont, M. Pothast, P. Privitera, M. Prouza, A. Puyleart, S. Querchfeld, J. Rautenberg, D. Ravignani, M. Reininghaus, J. Ridky, F. Riehn, M. Risse, P. Ristori, V. Rizi, W. Rodrigues de Carvalho, G. Rodriguez Fernandez, J. Rodriguez Rojo, M. J. Roncoroni, M. Roth, E. Roulet, A. C. Rovero, P. Ruehl, S. J. Saffi, A. Saftoiu, F. Salamida, H. Salazar, G. Salina, J. D. Sanabria Gomez, F. Sánchez, E. M. Santos, E. Santos, F. Sarazin, R. Sarmento, C. Sarmiento-Cano, R. Sato, P. Savina, C. Schäfer, V. Scherini, H. Schieler, M. Schimassek, M. Schimp, F. Schlüter, D. Schmidt, O. Scholten, P. Schovánek, F. G. Schröder, S. Schröder, A. Schulz, S. J. Sciutto, M. Scornavacche, R. C. Shellard, G. Sigl, G. Silli, O. Sima, R. Šmída, P. Sommers, J. F. Soriano, J. Souchard, R. Squartini, M. Stadelmaier, D. Stanca, S. Stanič, J. Stasielak, P. Stassi, A. Streich, M. Suárez-Durán, T. Sudholz, T. Suomijärvi, A. D. Supanitsky, J. Šupík, Z. Szadkowski, A. Taboada, A. Tapia, C. Timmermans, O. Tkachenko, P. Tobiska, C. J. Todero Peixoto, B. Tomé, G. Torralba Elipe, A. Travaini, P. Travnicek, C. Trimarelli, M. Trini, M. Tueros, R. Ulrich, M. Unger, M. Urban, L. Vaclavek, M. Vacula, J. F. Valdés Galicia, I. Valiño, L. Valore, A. van Vliet, E. Varela, B. Vargas Cárdenas, A. Vásquez-Ramírez, D. Veberič, C. Ventura, I. D. Vergara Quispe, V. Verzi, J. Vicha, L. Villaseñor, J. Vink, S. Vorobiov, H. Wahlberg, A. A. Watson, M. Weber, A. Weindl, L. Wiencke, H. Wilczyński, T. Winchen, M. Wirtz, D. Wittkowski, B. Wundheiler, A. Yushkov, O. Zapparrata, E. Zas, D. Zavrtanik, M. Zavrtanik, L. Zehrer, A. Zepeda, M. Ziolkowski, F. Zuccarello, Features of the energy spectrum of cosmic rays above 2.5×10^{18} eV using the pierre auger observatory, Phys. Rev. Lett. 125 (2020) 121106. doi:10.1103/PhysRevLett.125.121106.
URL https://link.aps.org/doi/10.1103/PhysRevLett.125.121106

[96] J. F. Soriano, L. A. Anchordoqui, D. F. Torres, Photo-disintegration of ^{4}He on the cosmic microwave background is less severe than earlier thought, Phys. Rev. D 98 (2018) 043001. doi:10.1103/PhysRevD.98.043001.
URL https://link.aps.org/doi/10.1103/PhysRevD.98.043001

[97] J. R. Calarco, B. L. Berman, T. W. Donnelly, Implications of the experimental

results on the photodisintegration of ^{4}He, Phys. Rev. C 27 (1983) 1866–1875. doi:10.1103/PhysRevC.27.1866.
URL https://link.aps.org/doi/10.1103/PhysRevC.27.1866

[98] R. Malfliet, J. Tjon, Solution of the faddeev equations for the triton problem using local two-particle interactions, Nuclear Physics A 127 (1) (1969) 161–168. doi:https://doi.org/10.1016/0375-9474(69)90775-1.
URL https://www.sciencedirect.com/science/article/pii/0375947469907751

[99] B. Wachter, T. Mertelmeier, H. M. Hofmann, Differences in the mirror reactions ^{3}H(p,γ)^{4}he and ^{3}He(n,γ)^{4}he from an isospin conserving nuclear force, Phys. Rev. C 38 (1988) 1139–1144. doi:10.1103/PhysRevC.38.1139.
URL https://link.aps.org/doi/10.1103/PhysRevC.38.1139

[100] T. Mertelmeier, H. Hofmann, Consistent cluster model description of the electromagnetic properties of lithium and beryllium nuclei, Nuclear Physics A 459 (2) (1986) 387–416. doi:https://doi.org/10.1016/0375-9474(86)90141-7.
URL https://www.sciencedirect.com/science/article/pii/0375947486901417

[101] S. A. Sofianos, H. Fiedeldey, W. Sandhas, Photodisintegration of ^{4}He in the integrodifferential equation approach, Phys. Rev. C 48 (1993) 2285–2289. doi:10.1103/PhysRevC.48.2285.
URL https://link.aps.org/doi/10.1103/PhysRevC.48.2285

[102] G. Ellerkmann, W. Sandhas, S. A. Sofianos, H. Fiedeldey, Integral equation calculations for the photodisintegration process $^4\mathrm{He}(\gamma, n)^3\mathrm{He}$, Phys. Rev. C 53 (1996) 2638–2644. doi:10.1103/PhysRevC.53.2638.
URL https://link.aps.org/doi/10.1103/PhysRevC.53.2638

[103] Y. Yamaguchi, Two-nucleon problem when the potential is nonlocal but separable. i, Phys. Rev. 95 (1954) 1628–1634. doi:10.1103/PhysRev.95.1628.
URL https://link.aps.org/doi/10.1103/PhysRev.95.1628

[104] V. D. Efros, W. Leidemann, G. Orlandini, Is there a pronounced giant dipole resonance in ^4he?, Phys. Rev. Lett. 78 (1997) 4015–4018. doi:10.1103/PhysRevLett.78.4015.
URL https://link.aps.org/doi/10.1103/PhysRevLett.78.4015

[105] R. De Tourreil, B. Rouben, D. Sprung, Super-soft-core nucleon-nucleon interaction with π-, ρ- and gw-exchange contributions, Nuclear Physics A 242 (3) (1975) 445–460. doi:https://doi.org/10.1016/0375-9474(75)90107-4.
URL https://www.sciencedirect.com/science/article/pii/0375947475901074

[106] V. D. Efros, W. Leidemann, G. Orlandini, Accurate four-body response function with full final state interaction: Application to electron scattering off ^{4}He, Phys.

Rev. Lett. 78 (1997) 432–435. doi:10.1103/PhysRevLett.78.432.
URL https://link.aps.org/doi/10.1103/PhysRevLett.78.432

[107] J. Golak, R. Skibiński, W. Glöckle, H. Kamada, A. Nogga, H. Witała, V. Efros, W. Leidemann, G. Orlandini, E. Tomusiak, Benchmark calculation of the three-nucleon photodisintegration, Nuclear Physics A 707 (3) (2002) 365–378. doi:https://doi.org/10.1016/S0375-9474(02)00989-2.
URL https://www.sciencedirect.com/science/article/pii/S0375947402009892

[108] S. Quaglioni, W. Leidemann, G. Orlandini, N. Barnea, V. D. Efros, Two-body photodisintegration of ^{4}He with full final state interaction, Phys. Rev. C 69 (2004) 044002. doi:10.1103/PhysRevC.69.044002.
URL https://link.aps.org/doi/10.1103/PhysRevC.69.044002

[109] D. Gazit, S. Bacca, N. Barnea, W. Leidemann, G. Orlandini, Photoabsorption on ^{4}He with a realistic nuclear force, Phys. Rev. Lett. 96 (2006) 112301. doi:10.1103/PhysRevLett.96.112301.
URL https://link.aps.org/doi/10.1103/PhysRevLett.96.112301

[110] S. Bacca, Photodisintegration of light nuclei for testing a correlated realistic interaction in the continuum, Phys. Rev. C 75 (2007) 044001. doi:10.1103/PhysRevC.75.044001.
URL https://link.aps.org/doi/10.1103/PhysRevC.75.044001

[111] S. Quaglioni, P. Navrátil, The 4he total photo-absorption cross section with two- plus three-nucleon interactions from chiral effective field theory, Physics Letters B 652 (5) (2007) 370–375. doi:https://doi.org/10.1016/j.physletb.2007.06.082.
URL https://www.sciencedirect.com/science/article/pii/S0370269307007642

[112] W. Horiuchi, Y. Suzuki, K. Arai, Ab initio study of the photoabsorption of ^{4}He, Phys. Rev. C 85 (2012) 054002. doi:10.1103/PhysRevC.85.054002.
URL https://link.aps.org/doi/10.1103/PhysRevC.85.054002

[113] R. Tamagaki, Potential Models of Nuclear Forces at Small Distances, Progress of Theoretical Physics 39 (1) (1968) 91–107. arXiv:https://academic.oup.com/ptp/article-pdf/39/1/91/5204931/39-1-91.pdf, doi:10.1143/PTP.39.91.
URL https://doi.org/10.1143/PTP.39.91

[114] E. Hiyama, B. F. Gibson, M. Kamimura, Four-body calculation of the first excited state of ^{4}He using a realistic nn interaction: $^4\mathrm{He}(e,e')^4\mathrm{He}(0_2^+)$ and the monopole sum rule, Phys. Rev. C 70 (2004) 031001. doi:10.1103/PhysRevC.70.031001.
URL https://link.aps.org/doi/10.1103/PhysRevC.70.031001

[115] T. Shima, S. Naito, Y. Nagai, T. Baba, K. Tamura, T. Takahashi, T. Kii, H. Ohgaki, H. Toyokawa, Simultaneous measurement of the photodisintegration of ^{4}He in the

giant dipole resonance region, Phys. Rev. C 72 (2005) 044004. doi:10.1103/PhysRevC.72.044004.
URL https://link.aps.org/doi/10.1103/PhysRevC.72.044004

[116] R. Raut, W. Tornow, M. W. Ahmed, A. S. Crowell, J. H. Kelley, G. Rusev, S. C. Stave, A. P. Tonchev, Photodisintegration cross section of the reaction ^{4}He(γ,p)^{3}H between 22 and 30 MeV, Phys. Rev. Lett. 108 (2012) 042502. doi:10.1103/PhysRevLett.108.042502.
URL https://link.aps.org/doi/10.1103/PhysRevLett.108.042502

[117] T. Shima, Y. Nagai, S. Miyamoto, S. Amano, K. Horikawa, T. Mochizuki, New results on photodisintegration of ^{4}He, PoS CD09 (2010) 107. doi:10.22323/1.086.0107.

[118] W. Tornow, J. H. Kelley, R. Raut, G. Rusev, A. P. Tonchev, M. W. Ahmed, A. S. Crowell, S. C. Stave, Photodisintegration cross section of the reaction ^{4}He(γ,n)^{3}He at the giant dipole resonance peak, Phys. Rev. C 85 (2012) 061001(R). doi:10.1103/PhysRevC.85.061001.
URL https://link.aps.org/doi/10.1103/PhysRevC.85.061001

[119] B. Nilsson, J.-O. Adler, B.-E. Andersson, J. R. M. Annand, I. Akkurt, M. J. Boland, G. I. Crawford, K. G. Fissum, K. Hansen, P. D. Harty, D. G. Ireland, L. Isaksson, M. Karlsson, M. Lundin, J. C. McGeorge, G. J. Miller, H. Ruijter, A. Sandell, B. Schröder, D. A. Sims, D. Watts, Measurement of the ^{4}He(γ, n) reaction from $23 < E_\gamma < 70$ MeV, Phys. Rev. C 75 (2007) 014007. doi:10.1103/PhysRevC.75.014007.
URL https://link.aps.org/doi/10.1103/PhysRevC.75.014007

[120] H. Beil, R. Bergere, Monochromatic and identifiable photons used in photonuclear research, Tech. rep., CEA Centre d'Etudes Nucleaires de Saclay (1980).

[121] W. H. Barkas, R. W. Deutsch, F. C. Gilbert, C. E. Violet, High energy electron-electron scattering, Phys. Rev. 86 (1952) 59–63. doi:10.1103/PhysRev.86.59.
URL https://link.aps.org/doi/10.1103/PhysRev.86.59

[122] C. Tzara, Compt. Rend. Acad. Sci. 245 (1957).

[123] J. W. Weil, B. D. McDaniel, The production of protons from carbon by monoenergetic gamma rays, Phys. Rev. 92 (1953) 391–400. doi:10.1103/PhysRev.92.391.
URL https://link.aps.org/doi/10.1103/PhysRev.92.391

[124] R. H. Milburn, Electron scattering by an intense polarized photon field, Phys. Rev. Lett. 10 (1963) 75–77. doi:10.1103/PhysRevLett.10.75.
URL https://link.aps.org/doi/10.1103/PhysRevLett.10.75

[125] F. Arutyunian, V. Tumanian, The compton effect on relativistic electrons and the possibility of obtaining high energy beams, Physics Letters 4 (3) (1963) 176–178. doi:https://doi.org/10.1016/0031-9163(63)90351-2.

URL https://www.sciencedirect.com/science/article/pii/0031916363903512

[126] G. Breit, E. Wigner, Capture of slow neutrons, Phys. Rev. 49 (1936) 519–531. doi:10.1103/PhysRev.49.519.
URL https://link.aps.org/doi/10.1103/PhysRev.49.519

[127] N. Otuka, E. Dupont, V. Semkova, B. Pritychenko, A. Blokhin, M. Aikawa, S. Babykina, M. Bossant, G. Chen, S. Dunaeva, R. Forrest, T. Fukahori, N. Furutachi, S. Ganesan, Z. Ge, O. Gritzay, M. Herman, S. Hlavač, K. Katō, B. Lalremruata, Y. Lee, A. Makinaga, K. Matsumoto, M. Mikhaylyukova, G. Pikulina, V. Pronyaev, A. Saxena, O. Schwerer, S. Simakov, N. Soppera, R. Suzuki, S. Takács, X. Tao, S. Taova, F. Tárkányi, V. Varlamov, J. Wang, S. Yang, V. Zerkin, Y. Zhuang, Towards a more complete and accurate experimental nuclear reaction data library (exfor): International collaboration between nuclear reaction data centres (nrdc), Nuclear Data Sheets 120 (2014) 272–276. doi:https://doi.org/10.1016/j.nds.2014.07.065.
URL https://www.sciencedirect.com/science/article/pii/S0090375214005171

[128] A. Gorbunov, V. Spiridonov, Photodisintegration of helium, i., Zh. Eksp. Teor. Fiz. 33 (1957) 21–32, [Sov. Phys. JETP **6**, 16 (1958)].

[129] A. Gorbunov, V. Spiridonov, Photodisintegration of helium. ii, Zh. Eksp. Teor. Fiz. 34 (1958) 862–865, [Sov. Phys. JETP **34**, 596 (1958)].

[130] A. Gorbunov, Study of the ^{4}He $(\gamma, p)^3$H and ^{4}He$(\gamma, n)^3$He reactions, Physics Letters B 27 (7) (1968) 436–438. doi:https://doi.org/10.1016/0370-2693(68)90230-X.
URL https://www.sciencedirect.com/science/article/pii/037026936890230X

[131] H. Clerc, R. Stewart, R. Morrison, Photodisintegration of ^{4}He, Physics Letters 18 (3) (1965) 316–318. doi:https://doi.org/10.1016/0031-9163(65)90353-7.
URL https://www.sciencedirect.com/science/article/pii/0031916365903537

[132] J. Sanada, M. Yamanouchi, N. Sakai, S. Seki, Study of the excited states in ^{4}He through the ^{4}He$(\gamma, p)^3$H reaction, Journal of the Physical Society of Japan 28 (3) (1970) 537–541. arXiv:https://doi.org/10.1143/JPSJ.28.537, doi:10.1143/JPSJ.28.537.
URL https://doi.org/10.1143/JPSJ.28.537

[133] B. Berman, F. Firk, C.-P. Wu, The 90° differential cross section for the reaction ^{4}He $(\gamma, n_0)^3$He and evidence for isospin mixing in the dipole states of ^{4}He, Nuclear Physics A 179 (3) (1972) 791–795. doi:https://doi.org/10.1016/0375-9474(72)90620-3.

URL https://www.sciencedirect.com/science/article/pii/0375947472906203

[134] J. D. Irish, R. G. Johnson, B. L. Berman, B. J. Thomas, K. G. McNeill, J. W. Jury, 90° differential cross section for the reaction ^{4}He$(\gamma, n)^3$He, Phys. Rev. C 8 (1973) 1211–1214. doi:10.1103/PhysRevC.8.1211.
URL https://link.aps.org/doi/10.1103/PhysRevC.8.1211

[135] C. Malcom, D. Webb, Y. Shin, D. Skopik, Evidence of a 2^+ state from the ^{4}He$(\gamma, n)^3$He reaction, Physics Letters B 47 (5) (1973) 433–435. doi:https://doi.org/10.1016/0370-2693(73)90106-8.
URL https://www.sciencedirect.com/science/article/pii/0370269373901068

[136] Y. M. Arkatov, P. Vatset, V. Voloshchuk, V. Zolenko, I. Prokhorets, A. Khodyachikh, V. Chmil', Cross section ratio of the reactions he 4 (γ, p) h 3 and he 4 (γ, n) he 3 in the region of giant resonance, and charge symmetry, ZhETF Pis ma Redaktsiiu 17 (1973) 356, [JETP Lett. **17**, 253 (1973)].

[137] Y. M. Arkatov, P. Vatset, V. Voloshchuk, V. Zolenko, I. Prokhorets, V. Chmil', Energy moments of the total γ-quanta absorption cross section for ^{4}He nucleus, Yadernaya Fizika 19 (6) (1974) 1172–1176, [Sov. J. Nucl. Phys. **19**, 598 (1974)].

[138] F. Balestra, E. Bollini, L. Busso, R. Garfagnini, C. Guaraldo, G. Piragino, R. Scrimaglio, A. Zanini, Photodisintegration of ^{4}He in the giant-resonance region, Il Nuovo Cimento A (1965-1970) 38 (2) (1977) 145–166. doi:10.1007/BF02724538.
URL https://doi.org/10.1007/BF02724538

[139] B. L. Berman, D. D. Faul, P. Meyer, D. L. Olson, Photoneutron cross section for ^{4}He, Phys. Rev. C 22 (1980) 2273–2281. doi:10.1103/PhysRevC.22.2273.
URL https://link.aps.org/doi/10.1103/PhysRevC.22.2273

[140] H. B. Willard, J. K. Bair, J. D. Kington, The reactions T(p, n)he^3 and T(p, γ)he^4, Phys. Rev. 90 (1953) 865–867. doi:10.1103/PhysRev.90.865.
URL https://link.aps.org/doi/10.1103/PhysRev.90.865

[141] J. E. Perry, S. J. Bame, T(p, γ)he^4 reaction, Phys. Rev. 99 (1955) 1368–1375. doi:10.1103/PhysRev.99.1368.
URL https://link.aps.org/doi/10.1103/PhysRev.99.1368

[142] C. C. Gardner, J. D. Anderson, Gamma yield from the proton bombardment of tritium, Phys. Rev. 125 (1962) 626–628. doi:10.1103/PhysRev.125.626.
URL https://link.aps.org/doi/10.1103/PhysRev.125.626

[143] D. Gemmell, G. Jones, The T(p, γ)He^4 reaction, Nuclear Physics 33 (1962) 102–109. doi:https://doi.org/10.1016/0029-5582(62)90508-4.
URL https://www.sciencedirect.com/science/article/pii/0029558262905084

[144] W. E. Meyerhof, M. Suffert, W. Feldman, ^{3}H(p,γ)^{4}He reaction from 3 to 18 MeV, Nuclear Physics A 148 (1) (1970) 211–224. doi:https://doi.org/10.1016/0375-9474(70)90619-6.
URL https://www.sciencedirect.com/science/article/pii/0375947470906196

[145] R. C. McBroom, H. R. Weller, N. R. Roberson, D. R. Tilley, ^{3}H(p,γ)^{4}He reaction below $E_p = 30$ MeV, Phys. Rev. C 25 (1982) 1644–1648. doi:10.1103/PhysRevC.25.1644.
URL https://link.aps.org/doi/10.1103/PhysRevC.25.1644

[146] R. W. Zurmühle, W. E. Stephens, H. H. Staub, Gamma rays from neutron capture in helium-3 and deuteron capture in deuterium, Phys. Rev. 132 (1963) 751–754. doi:10.1103/PhysRev.132.751.
URL https://link.aps.org/doi/10.1103/PhysRev.132.751

[147] L. Ward, D. R. Tilley, D. M. Skopik, N. R. Roberson, H. R. Weller, Confirmation of the photoneutron cross section for ^{4}He below 33 MeV, Phys. Rev. C 24 (1981) 317–320. doi:10.1103/PhysRevC.24.317.
URL https://link.aps.org/doi/10.1103/PhysRevC.24.317

[148] J. R. Calarco, S. S. Hanna, C. C. Chang, E. M. Diener, E. Kuhlmann, G. A. Fisher, Absolute cross section for the reaction ^{3}H(p, γ_0)^{4}He and a review of ^{4}He(γ, p$_0$)^{3}H measurements, Phys. Rev. C 28 (1983) 483–488. doi:10.1103/PhysRevC.28.483.
URL https://link.aps.org/doi/10.1103/PhysRevC.28.483

[149] R. Bernabei, A. Chisholm, S. d'Angelo, M. P. De Pascale, P. Picozza, C. Schaerf, P. Belli, L. Casano, A. Incicchitti, D. Prosperi, B. Girolami, Measurement of the ^{4}He(γ,p)^{3}H total cross section and charge symmetry, Phys. Rev. C 38 (1988) 1990–1995. doi:10.1103/PhysRevC.38.1990.
URL https://link.aps.org/doi/10.1103/PhysRevC.38.1990

[150] G. Feldman, M. J. Balbes, L. H. Kramer, J. Z. Williams, H. R. Weller, D. R. Tilley, ^{3}H(p,γ)^{4}He reaction and the (γ,p)/(γ,n) ratio in ^{4}He, Phys. Rev. C 42 (1990) R1167–R1170. doi:10.1103/PhysRevC.42.R1167.
URL https://link.aps.org/doi/10.1103/PhysRevC.42.R1167

[151] D. P. Wells, D. S. Dale, R. A. Eisenstein, F. J. Federspiel, M. A. Lucas, K. E. Mellendorf, A. M. Nathan, A. E. O'Neill, Elastic photon scattering from ^{4}He: Charge symmetry problem, Phys. Rev. C 46 (1992) 449–454. doi:10.1103/PhysRevC.46.449.
URL https://link.aps.org/doi/10.1103/PhysRevC.46.449

[152] L. Van Hoorebeke, R. Van de Vyver, V. Fiermans, D. Ryckbosch, C. Van den Abeele, J. Dias, Direct measurement of the ^{4}He(γ,p_0) absolute cross section, Phys. Rev. C 48 (1993) 2510–2513. doi:10.1103/PhysRevC.48.2510.
URL https://link.aps.org/doi/10.1103/PhysRevC.48.2510

[153] R. J. Komar, H.-B. Mak, J. R. Leslie, H. C. Evans, E. Bonvin, E. D. Earle, T. K. Alexander, ^{3}He(n,γ)^{4}He cross section and the photodisintegration of ^{4}He, Phys. Rev. C 48 (1993) 2375–2384. doi:10.1103/PhysRevC.48.2375.
URL https://link.aps.org/doi/10.1103/PhysRevC.48.2375

[154] K. I. Hahn, C. R. Brune, R. W. Kavanagh, ^{3}H(p,γ)^{4}He cross section, Phys. Rev. C 51 (1995) 1624–1632. doi:10.1103/PhysRevC.51.1624.
URL https://link.aps.org/doi/10.1103/PhysRevC.51.1624

[155] T. Kii, T. Shima, T. Baba, Y. Nagai, A time projection chamber for the study of nuclear photodisintegration, Nuclear Instruments and Methods in Physics Research Section A: Accelerators, Spectrometers, Detectors and Associated Equipment 552 (3) (2005) 329–343. doi:https://doi.org/10.1016/j.nima.2005.07.003.
URL https://www.sciencedirect.com/science/article/pii/S0168900205013951

[156] H. Ohgaki, H. Toyokawa, K. Kudo, N. Takeda, T. Yamazaki, Generation and application of laser-compton gamma-ray at etl, Nuclear Instruments and Methods in Physics Research Section A: Accelerators, Spectrometers, Detectors and Associated Equipment 455 (1) (2000) 54–59, proceedings of the Int. Symp. on New Visions in Laser-Beam. doi:https://doi.org/10.1016/S0168-9002(00)00693-8.
URL https://www.sciencedirect.com/science/article/pii/S0168900200006938

[157] A. Gorbunov, V. Spiridonov, Photodisintegration of helium. ii, Zh. Eksp. Teor. Fiz. 34 (1958) 866–873, [Sov. Phys. JETP **34**, 600 (1958)].

[158] B. Nilsson, J.-O. Adler, B.-E. Andersson, J. Annand, I. Akkurt, M. Boland, G. Crawford, K. Fissum, K. Hansen, P. Harty, D. Ireland, L. Isaksson, M. Karlsson, M. Lundin, J. McGeorge, G. Miller, H. Ruijter, A. Sandell, B. Schröder, D. Sims, D. Watts, Near-threshold measurement of the 4he(γ ,n) reaction, Physics Letters B 626 (1) (2005) 65–71. doi:https://doi.org/10.1016/j.physletb.2005.08.081.
URL https://www.sciencedirect.com/science/article/pii/S0370269305012050

[159] J.-O. Adler, B.-E. Andersson, K. Blomqvist, K. Fissum, K. Hansen, L. Isaksson, B. Nilsson, D. Nilsson, H. Ruijter, A. Sandell, B. Schröder, D. Sims, A broad range tagging spectrometer for the max-laboratory, Nuclear Instruments and Methods in Physics Research Section A: Accelerators, Spectrometers, Detectors and Associated Equipment 388 (1) (1997) 17–26. doi:https://doi.org/10.1016/S0168-9002(97)00347-1.
URL https://www.sciencedirect.com/science/article/pii/S0168900297003471

[160] T. Shima, Y. Nagai, T. Baba, T. Takahashi, T. Kii, H. Ohgaki, H. Toyokawa, Gdr problem in photodisintegration of 4he, Nuclear Physics A 687 (1) (2001) 127–131, giant Resonances 2000. doi:https://doi.org/10.1016/S0375-9474(01)

00611-X.
URL https://www.sciencedirect.com/science/article/pii/S037594740100611X

[161] D. Halderson, $\sigma(\gamma,p)\sigma(\gamma,n)$ ratio, current conservation, and nucleon scattering in ^{4}He, Phys. Rev. C 70 (2004) 034607. doi:10.1103/PhysRevC.70.034607.
URL https://link.aps.org/doi/10.1103/PhysRevC.70.034607

[162] S. Nakayama, E. Matsumoto, R. Hayami, K. Fushimi, H. Kawasuso, K. Yasuda, T. Yamagata, H. Akimune, H. Ikemizu, M. Fujiwara, M. Yosoi, K. Nakanishi, K. Kawase, H. Hashimoto, T. Oota, K. Sagara, T. Kudoh, S. Asaji, T. Ishida, M. Tanaka, M. B. Greenfield, Analog of the giant dipole resonance in ^{4}He, Phys. Rev. C 76 (2007) 021305(R). doi:10.1103/PhysRevC.76.021305.
URL https://link.aps.org/doi/10.1103/PhysRevC.76.021305

[163] M. Fujiwara, H. Akimune, I. Daito, H. Fujimura, Y. Fujita, K. Hatanaka, H. Ikegami, I. Katayama, K. Nagayama, N. Matsuoka, S. Morinobu, T. Noro, M. Yoshimura, H. Sakaguchi, Y. Sakemi, A. Tamii, M. Yosoi, Magnetic spectrometer grand raiden, Nuclear Instruments and Methods in Physics Research Section A: Accelerators, Spectrometers, Detectors and Associated Equipment 422 (1) (1999) 484–488. doi:https://doi.org/10.1016/S0168-9002(98)01009-2.
URL https://www.sciencedirect.com/science/article/pii/S0168900298010092

[164] W. Tornow, J. Esterline, C. Leckey, G. Weisel, High-pressure 3he–xe gas scintillators for simultaneous detection of neutrons and gamma rays over a large energy range, Nuclear Instruments and Methods in Physics Research Section A: Accelerators, Spectrometers, Detectors and Associated Equipment 647 (1) (2011) 86–93. doi:https://doi.org/10.1016/j.nima.2011.05.022.
URL https://www.sciencedirect.com/science/article/pii/S0168900211008965

[165] Y. Wu, et al., Performance and Capabilities of Upgraded High Intensity Gamma-Ray Source at Duke University, in: Particle Accelerator Conference (PAC 09), 2010, p. TH4PBC06.

[166] A. Ando, S. Amano, S. Hashimoto, H. Kinosita, S. Miyamoto, T. Mochizuki, M. Niibe, Y. Shoji, M. Terasawa, T. Watanabe, N. Kumagai, Isochronous storage ring of the New SUBARU project, Journal of Synchrotron Radiation 5 (3) (1998) 342–344. doi:10.1107/S0909049597013150.
URL https://doi.org/10.1107/S0909049597013150

[167] Web site of SPring-8, http://www.spring8.or.jp/.

[168] Web site of NewSUBARU, https://www.lasti.u-hyogo.ac.jp/NS-en/.

[169] H. Utsunomiya, T. Shima, K. Takahisa, D. M. Filipescu, O. Tesileanu, I. Gheorghe, H.-T. Nyhus, T. Renstrøm, Y.-W. Lui, Y. Kitagawa, S. Amano, S. Miyamoto, Energy calibration of the newsubaru storage ring for laser compton-scattering gamma rays and applications, IEEE Transactions on Nuclear Science 61 (3) (2014) 1252–1258. doi:10.1109/TNS.2014.2312323.

[170] S. Miyamoto, Y. Asano, S. Amano, D. Li, K. Imasaki, H. Kinugasa, Y. Shoji, T. Takagi, T. Mochizuki, Laser compton back-scattering gamma-ray beamline on newsubaru, Radiation Measurements 41 (2006) S179–S185, the 3rd International Workshop on Radiation Safety at Synchrotron Radiation Sources. doi:https://doi.org/10.1016/j.radmeas.2007.01.013.
URL https://www.sciencedirect.com/science/article/pii/S1350448707000194

[171] A. D'angelo, O. Bartalini, V. Bellini, P. L. Sandri, D. Moricciani, L. Nicoletti, A. Zucchiatti, Generation of compton backscattering-ray beams (2000).

[172] T. Furuno, T. Kawabata, H. Ong, S. Adachi, Y. Ayyad, T. Baba, Y. Fujikawa, T. Hashimoto, K. Inaba, Y. Ishii, S. Kabuki, H. Kubo, Y. Matsuda, Y. Matsuoka, T. Mizumoto, T. Morimoto, M. Murata, T. Sawano, T. Suzuki, A. Takada, J. Tanaka, I. Tanihata, T. Tanimori, D. Tran, M. Tsumura, H. Watanabe, Performance test of the maiko active target, Nuclear Instruments and Methods in Physics Research Section A: Accelerators, Spectrometers, Detectors and Associated Equipment 908 (2018) 215–224. doi:https://doi.org/10.1016/j.nima.2018.08.042.
URL https://www.sciencedirect.com/science/article/pii/S0168900218309951

[173] M. Murata, Master's thesis, Kyoto University (2015). [link].
URL https://www-nh.scphys.kyoto-u.ac.jp/articles/thesis/mron/murata_master.pdf

[174] K. Inaba, Master's thesis, Kyoto University (2017). [link].
URL https://www-nh.scphys.kyoto-u.ac.jp/articles/thesis/mron/inaba_master.pdf

[175] T. Furuno, T. Kawabata, S. Adachi, Y. Ayyad, Y. Kanada-En'yo, Y. Fujikawa, K. Inaba, M. Murata, H. J. Ong, M. Sferrazza, Y. Takahashi, T. Takeda, I. Tanihata, D. T. Tran, M. Tsumura, Neutron quadrupole transition strength in ^{10}C deduced from the ^{10}C(α, α') measurement with the maiko active target, Phys. Rev. C 100 (2019) 054322. doi:10.1103/PhysRevC.100.054322.
URL https://link.aps.org/doi/10.1103/PhysRevC.100.054322

[176] Furuno, Tatsuya, Doi, Takanobu, Himi, Kanako, Kawabata, Takahiro, Adachi, Satoshi, Akimune, Hidetoshi, Enyo, Shiyo, Fujikawa, Yuki, Hijikata, Yuto, Inaba, Kento, Itoh, Masatoshi, Kubono, Shigeru, Matsuda, Yohei, Murata, Isao, Murata, Motoki, Okamoto, Shintaro, Sakanashi, Kosuke, Tamaki, Shingo, Measurement of

12c(n,n´) reaction cross section to determine triple-alpha reaction rate in high-density environments, EPJ Web Conf. 260 (2022) 11010. doi:10.1051/epjconf/202226011010.
URL https://doi.org/10.1051/epjconf/202226011010

[177] F. Sauli, Gem: A new concept for electron amplification in gas detectors, Nuclear Instruments and Methods in Physics Research Section A: Accelerators, Spectrometers, Detectors and Associated Equipment 386 (2) (1997) 531–534. doi:https://doi.org/10.1016/S0168-9002(96)01172-2.
URL https://www.sciencedirect.com/science/article/pii/S0168900296011722

[178] A. Ochi, T. Nagayoshi, S. Koishi, T. Tanimori, T. Nagae, M. Nakamura, Development of micro pixel chamber, Nuclear Instruments and Methods in Physics Research Section A: Accelerators, Spectrometers, Detectors and Associated Equipment 478 (1) (2002) 196–199, proceedings of the ninth Int.Conf. on Instrumentation. doi:https://doi.org/10.1016/S0168-9002(01)01756-9.
URL https://www.sciencedirect.com/science/article/pii/S0168900201017569

[179] T. Mizumoto, Y. Matsuoka, Y. Mizumura, T. Tanimori, H. Kubo, A. Takada, S. Iwaki, T. Sawano, K. Nakamura, S. Komura, S. Nakamura, T. Kishimoto, M. Oda, S. Miyamoto, T. Takemura, J. D. Parker, D. Tomono, S. Sonoda, K. Miuchi, S. Kurosawa, New readout and data-acquisition system in an electron-tracking compton camera for MeV gamma-ray astronomy (SMILE-II), Nuclear Instruments and Methods in Physics Research, Section A: Accelerators, Spectrometers, Detectors and Associated Equipment 800 (2015) 40–50. doi:10.1016/j.nima.2015.08.004.

[180] T. Furuno, Ph.D. thesis, Kyoto University (2020). [link].
URL https://www-nh.scphys.kyoto-u.ac.jp/articles/thesis/dron/d-furuno.pdf

[181] C. Altunbas, M. Capéans, K. Dehmelt, J. Ehlers, J. Friedrich, I. Konorov, A. Gandi, S. Kappler, B. Ketzer, R. De Oliveira, S. Paul, A. Placci, L. Ropelewski, F. Sauli, F. Simon, M. van Stenis, Construction, test and commissioning of the triple-gem tracking detector for compass, Nuclear Instruments and Methods in Physics Research Section A: Accelerators, Spectrometers, Detectors and Associated Equipment 490 (1) (2002) 177–203. doi:https://doi.org/10.1016/S0168-9002(02)00910-5.
URL https://www.sciencedirect.com/science/article/pii/S0168900202009105

[182] S. Biagi, Monte carlo simulation of electron drift and diffusion in counting gases under the influence of electric and magnetic fields, Nuclear Instruments and Methods in Physics Research Section A: Accelerators, Spectrometers, Detectors and Associated Equipment 421 (1) (1999) 234–240.

doi:https://doi.org/10.1016/S0168-9002(98)01233-9.
URL https://www.sciencedirect.com/science/article/pii/S0168900298012339

[183] Web site of RIBFDAQ, https://ribf.riken.jp/RIBFDAQ/.

[184] T. Kondo, H. Utsunomiya, H. Akimune, T. Yamagata, A. Okamoto, H. Harada, F. Kitatani, T. Shima, K. Horikawa, S. Miyamoto, Determination of the number of pulsed laser-compton scattering photons, Nuclear Instruments and Methods in Physics Research Section A: Accelerators, Spectrometers, Detectors and Associated Equipment 659 (1) (2011) 462–466. doi:https://doi.org/10.1016/j.nima.2011.08.035.
URL https://www.sciencedirect.com/science/article/pii/S0168900211016561

[185] H. Utsunomiya, T. Watanabe, T. Ari-izumi, D. Takenaka, T. Araki, K. Tsuji, I. Gheorghe, D. M. Filipescu, S. Belyshev, K. Stopani, D. Symochko, H. Wang, G. Fan, T. Renstrøm, G. M. Tveten, Y.-W. Lui, K. Sugita, S. Miyamoto, Photon-flux determination by the poisson-fitting technique with quenching corrections, Nuclear Instruments and Methods in Physics Research Section A: Accelerators, Spectrometers, Detectors and Associated Equipment 896 (2018) 103–107. doi:https://doi.org/10.1016/j.nima.2018.04.021.
URL https://www.sciencedirect.com/science/article/pii/S0168900218305151

[186] F. James, M. Roos, Minuit - a system for function minimization and analysis of the parameter errors and correlations, Computer Physics Communications 10 (6) (1975) 343–367. doi:https://doi.org/10.1016/0010-4655(75)90039-9.
URL https://www.sciencedirect.com/science/article/pii/0010465575900399

[187] R. Brun, F. Rademakers, Root — an object oriented data analysis framework, Nuclear Instruments and Methods in Physics Research Section A: Accelerators, Spectrometers, Detectors and Associated Equipment 389 (1) (1997) 81–86, new Computing Techniques in Physics Research V. doi:https://doi.org/10.1016/S0168-9002(97)00048-X.
URL https://www.sciencedirect.com/science/article/pii/S016890029700048X

[188] S. Agostinelli, J. Allison, K. Amako, J. Apostolakis, H. Araujo, P. Arce, M. Asai, D. Axen, S. Banerjee, G. Barrand, F. Behner, L. Bellagamba, J. Boudreau, L. Broglia, A. Brunengo, H. Burkhardt, S. Chauvie, J. Chuma, R. Chytracek, G. Cooperman, G. Cosmo, P. Degtyarenko, A. Dell'Acqua, G. Depaola, D. Dietrich, R. Enami, A. Feliciello, C. Ferguson, H. Fesefeldt, G. Folger, F. Foppiano, A. Forti, S. Garelli, S. Giani, R. Giannitrapani, D. Gibin, J. Gómez Cadenas, I. González, G. Gracia Abril, G. Greeniaus, W. Greiner, V. Grichine, A. Grossheim, S. Guatelli, P. Gumplinger, R. Hamatsu, K. Hashimoto, H. Hasui,

A. Heikkinen, A. Howard, V. Ivanchenko, A. Johnson, F. Jones, J. Kallenbach, N. Kanaya, M. Kawabata, Y. Kawabata, M. Kawaguti, S. Kelner, P. Kent, A. Kimura, T. Kodama, R. Kokoulin, M. Kossov, H. Kurashige, E. Lamanna, T. Lampén, V. Lara, V. Lefebure, F. Lei, M. Liendl, W. Lockman, F. Longo, S. Magni, M. Maire, E. Medernach, K. Minamimoto, P. Mora de Freitas, Y. Morita, K. Murakami, M. Nagamatu, R. Nartallo, P. Nieminen, T. Nishimura, K. Ohtsubo, M. Okamura, S. O'Neale, Y. Oohata, K. Paech, J. Perl, A. Pfeiffer, M. Pia, F. Ranjard, A. Rybin, S. Sadilov, E. Di Salvo, G. Santin, T. Sasaki, N. Savvas, Y. Sawada, S. Scherer, S. Sei, V. Sirotenko, D. Smith, N. Starkov, H. Stoecker, J. Sulkimo, M. Takahata, S. Tanaka, E. Tcherniaev, E. Safai Tehrani, M. Tropeano, P. Truscott, H. Uno, L. Urban, P. Urban, M. Verderi, A. Walkden, W. Wander, H. Weber, J. Wellisch, T. Wenaus, D. Williams, D. Wright, T. Yamada, H. Yoshida, D. Zschiesche, Geant4—a simulation toolkit, Nuclear Instruments and Methods in Physics Research Section A: Accelerators, Spectrometers, Detectors and Associated Equipment 506 (3) (2003) 250–303. doi:https://doi.org/10.1016/S0168-9002(03)01368-8.
URL https://www.sciencedirect.com/science/article/pii/S0168900203013688

[189] J. F. Ziegler, M. Ziegler, J. Biersack, Srim – the stopping and range of ions in matter (2010), Nuclear Instruments and Methods in Physics Research Section B: Beam Interactions with Materials and Atoms 268 (11) (2010) 1818–1823, 19th International Conference on Ion Beam Analysis. doi:https://doi.org/10.1016/j.nimb.2010.02.091.
URL https://www.sciencedirect.com/science/article/pii/S0168583X10001862

[190] Web site of Garfield++, http://garfieldpp.web.cern.ch/garfieldpp/.

[191] A. Takada, T. Tanimori, H. Kubo, J. D. Parker, T. Mizumoto, Y. Mizumura, S. Iwaki, T. Sawano, K. Nakamura, K. Taniue, N. Higashi, Y. Matsuoka, S. Komura, Y. Sato, S. Namamura, M. Oda, S. Sonoda, D. Tomono, K. Miuchi, S. Kabuki, Y. Kishimoto, S. Kurosawa, Simulation of gas avalanche in a micro pixel chamber using Garfield++, Journal of Instrumentation 8 (10) (2013) C10023. doi:10.1088/1748-0221/8/10/C10023.
URL https://dx.doi.org/10.1088/1748-0221/8/10/C10023

[192] E. A. Vinokurov, V. I. Voloshchuk, V. B. Ganenko, E. S. Gorbenko, V. N. Gu'rev, V. A. Gushchin, V. P. Ermak, V. A. Zolenko, Y. V. Zhebroskii, L. Y. Kolesnikov, Y. P. Lyakhno, V. A. Nikitin, A. L. Rubashkin, P. V. Sorokin, Study of (γ, n) and (γ, p) ractions in disintegration of ^{4}He by linearly polarized γ rays with energy 40 MeV, Yad. Fiz. 49 (1989) 1233, [Sov. J. Nucl. Phys. **49**, 767 (1989)].

[193] A. R. Edmonds, Angular Momentum in Quantum Mechanics, Princeton University Press, Princeton, 1957 [cited 2023-09-19]. doi:doi:10.1515/9781400884186.
URL https://doi.org/10.1515/9781400884186

[194] A. J. F. Siegert, Note on the interaction between nuclei and electromagnetic radiation, Phys. Rev. 52 (1937) 787–789. doi:10.1103/PhysRev.52.787.
URL https://link.aps.org/doi/10.1103/PhysRev.52.787

[195] M. Unkelbach, H. Hofmann, Meson-exchange currents in electromagnetic transitions of the 4he system, Nuclear Physics A 549 (4) (1992) 550–576. doi:https://doi.org/10.1016/0375-9474(92)90665-7.
URL https://www.sciencedirect.com/science/article/pii/0375947492906657

[196] V. F. Weisskopf, Radiative transition probabilities in nuclei, Phys. Rev. 83 (1951) 1073–1073. doi:10.1103/PhysRev.83.1073.
URL https://link.aps.org/doi/10.1103/PhysRev.83.1073

Appendix A

Derivation of Low-Energy Photoabsorption Cross Sections

Definitions

The cross section for a photoabsorption process induced by a photon of energy E_γ is given as [11],

$$\sigma_\gamma(E_\gamma) = (2\pi)^3 \frac{\hbar c}{E_\gamma} \frac{1}{2J_i+1} \sum_{J=1}^{\infty} \left\{ \left| \left\langle J_\mathrm{f} \left\| \hat{T}^E_J(E_\gamma) \right\| J_\mathrm{i} \right\rangle \right|^2 + \left| \left\langle J_\mathrm{f} \left\| \hat{T}^M_J(E_\gamma) \right\| J_\mathrm{i} \right\rangle \right|^2 \right\} \times \delta(E_\mathrm{f} - E_\mathrm{i} - E_\gamma). \tag{A.1}$$

Here, the initial and final state of the nucleus are characterized with the energy E_i, E_f and the spin J_i, J_f. The reduced matrix element for the M-th component of the spherical tensor operator of rank J, or $\hat{O}_{JM}$, is defined from the Wigner-Eckart theorem [193],

$$\left\langle J_\mathrm{f} M_\mathrm{f} \left| \hat{O}_{JM} \right| J_\mathrm{i} M_\mathrm{i} \right\rangle = \sqrt{2J_f+1} \left\langle J_\mathrm{i} M_\mathrm{i} JM | J_\mathrm{f} M_\mathrm{f} \right\rangle \left\langle J_\mathrm{f} \left\| \hat{O}_J \right\| J_\mathrm{i} \right\rangle, \tag{A.2}$$

where $\langle J_\mathrm{i} M_\mathrm{i} JM | J_\mathrm{f} M_\mathrm{f} \rangle$ is the Clebsch-Gordan coefficient for the coupling between $|J_\mathrm{i} M_\mathrm{i}>$ and $|JM>$ resulting in $|J_\mathrm{f} M_\mathrm{f}>$. The operators for the transition induced by a photon with a wave-number q are defined as,

$$\hat{T}^E_{JM}(q) = \frac{1}{c} \int \boldsymbol{A}_{lm}(\boldsymbol{r}; E) \cdot \hat{\boldsymbol{J}}(\boldsymbol{x}) d^3x = \frac{1}{cq} \int \{ \nabla \times [j_J(qr) \boldsymbol{Y}_{JM,J}(\theta, \phi)] \} \cdot \hat{\boldsymbol{J}}(\boldsymbol{r}) dr d\Omega, \tag{A.3}$$

$$\hat{T}^M_{JM}(q) = \frac{1}{c} \int \boldsymbol{A}_{lm}(\boldsymbol{r}; M) \cdot \hat{\boldsymbol{J}}(\boldsymbol{x}) d^3x = \frac{1}{c} \int j_J(qr) \boldsymbol{Y}_{JM,J}(\theta, \phi) \cdot \hat{\boldsymbol{J}}(\boldsymbol{r}) dr d\Omega. \tag{A.4}$$

$\hat{T}^E_{JM}(q)$ and $\hat{T}^M_{JM}(q)$ are associated with the electric and magnetic transition, respectively. The only transitions allowed under the transverse-wave property of real photon are these two transitions. The definitions are based on the coordinate system whose origin is fixed

at the center of mass of the nucleus. They are derived from the multipole expansion of the photon field, which obeys the Helmholtz equation. $\boldsymbol{A}_{l,m}$ is the dimensionless spherical wave, whereas $\hat{J}(\boldsymbol{r})$ is the electric current density operator. $j_J(x)$ is the spherical Bessel function.

In addition, there exist two extra multipole transition operators

$$\hat{T}^C_{JM}(q) = \int A_{lm}(\boldsymbol{r}; C)\hat{\rho}(\boldsymbol{x})d^3x = \int j_J(qr)Y_{JM}(\theta,\phi)\hat{\rho}(\boldsymbol{r})drd\Omega, \tag{A.5}$$

$$\hat{T}^L_{JM}(q) = \frac{1}{c}\int \boldsymbol{A}_{lm}(\boldsymbol{r}; L)\cdot\hat{\boldsymbol{J}}(\boldsymbol{x})d^3x = \frac{1}{cq}\int \nabla\left[j_J(qr)Y_{JM}(\theta,\phi)\right]\cdot\hat{\boldsymbol{J}}(\boldsymbol{r})drd\Omega. \tag{A.6}$$

They are Coulomb [Eq. (A.5)] and longitudinal [Eq. (A.6)] multipole operators, respectively. Here, $\hat{\rho}(\boldsymbol{r})$ is the charge density operator. These two classes of operators are not directly involved in the photonuclear cross sections. However, they are concerned with the electron and neutrino scattering cross sections.

$\boldsymbol{Y}_{JM,J}(\theta,\phi)$ is a vector spherical harmonics,

$$\boldsymbol{Y}_{lm,\lambda}(\theta,\phi) = \sum_{\mu,\mu'}\left\langle \lambda\mu 1\mu' | lm\right\rangle Y_{\lambda,\mu}(\theta,\phi)\boldsymbol{e}_{\mu'}. \tag{A.7}$$

$\boldsymbol{e}_\mu$ ($\mu = -1, 0, 1$) is the spherical unit vector defined as

$$\boldsymbol{e}_0 \;\coloneqq\; \boldsymbol{e}_z, \tag{A.8}$$

$$\boldsymbol{e}_{\pm1} \;\coloneqq\; \mp\frac{1}{\sqrt{2}}\left(\boldsymbol{e}_x \pm \boldsymbol{e}_y\right). \tag{A.9}$$

For simplicity, an incident photon parallel to the z-axis is assumed. Then, $\boldsymbol{e}_\mu$ is associated with a photon of its z-component of the spin is μ.

Long-wavelength Limit

When the long-wavelength limit,

$$qR \ll 1, \tag{A.10}$$

holds, two approximations below can be applied to Eq. (A.1).

Siegert's theorem

First one is the Siegert's theorem [194], which replaces the current density operator $\hat{J}(\boldsymbol{r})$ to the charge-density operator. The spherical Bessel function behaves like

$$j_J(qr) \sim \frac{(qr)^J}{(2l+1)!!}, \tag{A.11}$$

in the long wavelength limit. From Eq. (A.11) and the continuous equation of the electric current $\partial\rho/\partial t - \nabla\cdot\boldsymbol{j} = 0$, the transition matrix element of the electric transition is transformed to

$$\left\langle f \left| \hat{T}^{E,\mathrm{LWA}}_{JM}(q) \right| i \right\rangle = \left(\frac{J+1}{J}\right)^{1/2} \frac{E_i - E_f}{\hbar c q} \left\langle f \left| \hat{T}^{C,\mathrm{LWA}}_{JM}(q) \right| i \right\rangle . \tag{A.12}$$

Here, the operator in the right hand side is the Coulomb transition operator [Eq. (A.5)]. In the long-wavelength limit, the Coulomb transition operator is approximated as

$$\hat{T}^{C,\mathrm{LWA}}_{JM}(q) = \frac{q^J}{(2J+1)!!} \int r^J Y_{JM}(\theta,\phi)\hat{\rho}(\boldsymbol{r}) d^3 r. \tag{A.13}$$

Thus, the current-density operator in the electric transition operator Eq. (A.3) is replaced by the charge density operator. The charge operator is more tractable than the current operator which includes the non-negligible contributions from the magnetization current, and the meson exchange current (MEC) in addition to the proton convection current [195].

Dominance of $E1$ Transition

The second approximation is the dominance of the $E1$ transition. This is based on the rough estimation performed by Weiskopf [196]. The electric and magnetic transition rates are proportional to the reduced transition probability defined as,

$$B(EJ, J_i \to J_f) = \frac{2J_f+1}{2J_i+1} \left| \left\langle J_f \left\| \hat{T}^E_J(q) \right\| J_i \right\rangle \right|^2 , \tag{A.14}$$

$$B(MJ, J_i \to J_f) = \frac{2J_f+1}{2J_i+1} \left| \left\langle J_f \left\| \hat{T}^M_J(q) \right\| J_i \right\rangle \right|^2 . \tag{A.15}$$

These quantities are estimated under the assumption that the transition is caused by only one nucleon of $J_i = 1/2$ to the final state of $J_f = 1/2 + J$, and the nucleon uniformly exists within the nuclear radius.

$$B(EJ) \sim \frac{e^2}{4\pi}\left(\frac{3}{J+3}\right)^2 R^{2J} = \frac{(1.2)^{2J}}{4\pi}\left(\frac{3}{J+3}\right)^2 A^{2J/3} \left[e^2(\mathrm{fm})^{2\mathrm{J}}\right], \tag{A.16}$$

$$B(MJ) \sim \frac{10}{\pi}\left(\frac{3}{J+3}\right)^2 R^{2J-2}\mu_N^2 = \frac{10}{\pi}(1.2)^{2J-2}\left(\frac{3}{J+3}\right)^2 A^{(2J-2)/3} \left[\mu_N^2(\mathrm{fm})^{2\mathrm{J}-2}\right]. \tag{A.17}$$

That result is called as the Weiskopf unit, which gives a measure of strengths of single-particle transitions. In the long-wavelength limit, low-J transitions dominate high-J transitions due to the $(qr)^J$-scaling given from Eq. (A.11). In addition, the electric transition is one-order stronger than the magnetic one between the equal-J transitions [13]. These facts support the lowest order approximation that neglects all the competing transitions except the $E1$ transition.

Result

From the Siegert's theorem and the dominance of the $E1$ transition, the photo absorption cross section in Eq. (A.1) is simplified as,

$$\sigma_\gamma^{\mathrm{LWA}}(E_\gamma) \sim (2\pi)^3 \frac{\hbar c}{E_\gamma} \frac{1}{2J_i+1} \left| \left\langle J_f \left\| \hat{T}_1^{E,\mathrm{LWA}}(E_\gamma) \right\| J_i \right\rangle \right|^2 \delta(E_f - E_i - E_\gamma) \quad \text{(A.18)}$$

$$= \frac{4\pi^2}{\hbar c} E_\gamma \left| \left\langle J_f \left| \hat{D}_z \right| J_i \right\rangle \right|^2 \delta(E_f - E_i - E_\gamma), \quad \text{(A.19)}$$

where $\hat{D}_z$ is the dipole transition operator. When we assume the point-like charge distribution of nucleons, the dipole operator is defined as

$$\hat{D}_z = \sum_{k=1}^{A} \chi_i e(\boldsymbol{r}_i - \boldsymbol{R})_z. \quad \text{(A.20)}$$

Here, χ_i is the effective charge of the i-th nucleons: that value is N/A for protons and Z/A for neutrons in the cerner-of-mass frame. $(\boldsymbol{r}_i - \boldsymbol{R})_z$ indicates the z-component of the displacement of the i-th nucleon with respect to the center of mass the $\boldsymbol{R}$.

Appendix B

Data Tables of Cross Sections

The numerical data on the differential cross sections of the $^4\mathrm{He}(\gamma, n)^3\mathrm{He}$ and $^4\mathrm{He}(\gamma, p)^3\mathrm{H}$ are listed in the Tables. B.1 – B.24. These values are the same to the ones depicted in Figs. 4.1 – 4.4, and the cross section averaged over the beam energy and in the angular bins spanning 20 degrees. See text for details.

Table B.1: θ dependence of ϕ-averaged differential cross sections $\left\langle \frac{d\sigma_\theta}{d\Omega} \right\rangle$ (Eq. 4.1) of the $^4\mathrm{He}(\gamma, n)^3\mathrm{He}$ reaction at $\langle E_\gamma \rangle = 22.5$ MeV.

θ (degree)	$\left\langle \frac{d\sigma}{d\Omega} \right\rangle$ (mb/sr)	$\Delta \left\langle \frac{d\sigma}{d\Omega} \right\rangle_{\mathrm{stat}}$ (mb/sr)
30	0.10	0.10
50	0.07	0.02
70	0.11	0.01
90	0.14	0.02
110	0.07	0.02
130	0.12	0.02
150	0.10	0.04

Table B.2: θ dependence of ϕ-averaged differential cross sections $\left\langle \frac{d\sigma_\theta}{d\Omega} \right\rangle$ (Eq. 4.1) of the ^{4}He$(\gamma, n)^3$He reaction at $\langle E_\gamma \rangle = 23.5$ MeV.

θ (degree)	$\left\langle \frac{d\sigma}{d\Omega} \right\rangle$ (mb/sr)	$\Delta \left\langle \frac{d\sigma}{d\Omega} \right\rangle_{\text{stat}}$ (mb/sr)
30	0.16	0.07
50	0.13	0.03
70	0.13	0.02
90	0.11	0.02
110	0.09	0.02
130	0.13	0.02
150	0.10	0.04

Table B.3: θ dependence of ϕ-averaged differential cross sections $\left\langle \frac{d\sigma_\theta}{d\Omega} \right\rangle$ (Eq. 4.1) of the ^{4}He$(\gamma, n)^3$He reaction at $\langle E_\gamma \rangle = 24.5$ MeV.

θ (degree)	$\left\langle \frac{d\sigma}{d\Omega} \right\rangle$ (mb/sr)	$\Delta \left\langle \frac{d\sigma}{d\Omega} \right\rangle_{\text{stat}}$ (mb/sr)
30	0.19	0.09
50	0.09	0.02
70	0.17	0.02
90	0.22	0.03
110	0.11	0.03
130	0.16	0.03

Table B.4: θ dependence of ϕ-averaged differential cross sections $\left\langle \frac{d\sigma_\theta}{d\Omega} \right\rangle$ (Eq. 4.1) of the ^{4}He$(\gamma, n)^3$He reaction at $\langle E_\gamma \rangle = 26.5$ MeV.

θ (degree)	$\left\langle \frac{d\sigma}{d\Omega} \right\rangle$ (mb/sr)	$\Delta \left\langle \frac{d\sigma}{d\Omega} \right\rangle_{\text{stat}}$ (mb/sr)
50	0.15	0.07
70	0.26	0.05
90	0.27	0.05
110	0.18	0.06
130	0.15	0.05
150	0.13	0.13

Table B.5: θ dependence of ϕ-averaged differential cross sections $\left\langle \frac{d\sigma_\theta}{d\Omega} \right\rangle$ (Eq. 4.1) of the ^{4}He$(\gamma, n)^3$He reaction at $\langle E_\gamma \rangle = 27.5$ MeV.

θ (degree)	$\left\langle \frac{d\sigma}{d\Omega} \right\rangle$ (mb/sr)	$\Delta \left\langle \frac{d\sigma}{d\Omega} \right\rangle_{\text{stat}}$ (mb/sr)
50	0.19	0.06
70	0.17	0.04
90	0.20	0.03
110	0.25	0.06
130	0.15	0.04
150	0.13	0.09

Table B.6: θ dependence of ϕ-averaged differential cross sections $\left\langle \frac{d\sigma_\theta}{d\Omega} \right\rangle$ (Eq. 4.1) of the ^{4}He$(\gamma, n)^3$He reaction at $\langle E_\gamma \rangle = 29.4$ MeV.

θ (degree)	$\left\langle \frac{d\sigma}{d\Omega} \right\rangle$ (mb/sr)	$\Delta \left\langle \frac{d\sigma}{d\Omega} \right\rangle_{\text{stat}}$ (mb/sr)
50	0.13	0.03
70	0.15	0.02
90	0.14	0.02
110	0.02	0.02
130	0.10	0.03

Table B.7: ϕ dependence of θ-averaged differential cross sections $\left\langle \frac{d\sigma_\phi}{d\Omega} \right\rangle$ (Eq. 4.2) of the ^{4}He$(\gamma, n)^3$He reaction at $\langle E_\gamma \rangle = 22.5$ MeV.

θ (degree)	$\left\langle \frac{d\sigma}{d\Omega} \right\rangle$ (mb/sr)	$\Delta \left\langle \frac{d\sigma}{d\Omega} \right\rangle_{\text{stat}}$ (mb/sr)
10	0.15	0.03
30	0.14	0.03
50	0.11	0.02
70	0.07	0.03
130	0.11	0.03
150	0.09	0.02
170	0.15	0.03
190	0.07	0.03
210	0.13	0.03
230	0.08	0.02
250	0.05	0.02
290	0.04	0.03
310	0.06	0.02
330	0.11	0.03
350	0.09	0.03

Table B.8: ϕ dependence of θ-averaged differential cross sections $\left\langle \frac{d\sigma_\phi}{d\Omega} \right\rangle$ (Eq. 4.2) of the ^{4}He$(\gamma, n)^3$He reaction at $\langle E_\gamma \rangle = 23.5$ MeV.

θ (degree)	$\left\langle \frac{d\sigma}{d\Omega} \right\rangle$ (mb/sr)	$\Delta \left\langle \frac{d\sigma}{d\Omega} \right\rangle_{\text{stat}}$ (mb/sr)
10	0.19	0.04
30	0.15	0.03
50	0.05	0.03
130	0.17	0.05
150	0.11	0.03
170	0.16	0.03
190	0.13	0.04
210	0.14	0.03
230	0.08	0.03
250	0.03	0.03
290	0.05	0.03
310	0.05	0.02
330	0.11	0.06
350	0.13	0.04

Table B.9: ϕ dependence of θ-averaged differential cross sections $\left\langle \frac{d\sigma_\phi}{d\Omega} \right\rangle$ (Eq. 4.2) of the ^{4}He$(\gamma, n)^3$He reaction at $\langle E_\gamma \rangle = 24.5$ MeV.

θ (degree)	$\left\langle \frac{d\sigma}{d\Omega} \right\rangle$ (mb/sr)	$\Delta \left\langle \frac{d\sigma}{d\Omega} \right\rangle_{\text{stat}}$ (mb/sr)
10	0.27	0.05
30	0.21	0.04
50	0.05	0.02
150	0.28	0.05
170	0.25	0.04
190	0.22	0.05
210	0.23	0.05
230	0.12	0.04
250	0.05	0.05
310	0.07	0.03
330	0.20	0.05
350	0.22	0.07

Table B.10: ϕ dependence of θ-averaged differential cross sections $\left\langle \frac{d\sigma_\phi}{d\Omega} \right\rangle$ (Eq. 4.2) of the ^{4}He$(\gamma, n)^3$He reaction at $\langle E_\gamma \rangle = 26.5$ MeV.

θ (degree)	$\left\langle \frac{d\sigma}{d\Omega} \right\rangle$ (mb/sr)	$\Delta \left\langle \frac{d\sigma}{d\Omega} \right\rangle_{\text{stat}}$ (mb/sr)
10	0.42	0.09
30	0.19	0.07
50	0.18	0.08
150	0.29	0.10
170	0.33	0.08
190	0.23	0.08
210	0.22	0.11
230	0.18	0.09
250	0.13	0.13
310	0.17	0.07
330	0.22	0.09

Table B.11: ϕ dependence of θ-averaged differential cross sections $\left\langle \frac{d\sigma_\phi}{d\Omega} \right\rangle$ (Eq. 4.2) of the ^{4}He$(\gamma, n)^3$He reaction at $\langle E_\gamma \rangle = 27.5$ MeV.

θ (degree)	$\left\langle \frac{d\sigma}{d\Omega} \right\rangle$ (mb/sr)	$\Delta \left\langle \frac{d\sigma}{d\Omega} \right\rangle_{\text{stat}}$ (mb/sr)
10	0.13	0.09
30	0.14	0.04
50	0.14	0.04
130	0.24	0.07
150	0.17	0.04
170	0.22	0.05
190	0.19	0.08
210	0.17	0.05
230	0.13	0.05
250	0.06	0.04
290	0.15	0.11
310	0.14	0.05
330	0.08	0.05

Table B.12: ϕ dependence of θ-averaged differential cross sections $\left\langle \frac{d\sigma_\phi}{d\Omega} \right\rangle$ (Eq. 4.2) of the ^{4}He$(\gamma, n)^3$He reaction at $\langle E_\gamma \rangle = 29.4$ MeV.

θ (degree)	$\left\langle \frac{d\sigma}{d\Omega} \right\rangle$ (mb/sr)	$\Delta \left\langle \frac{d\sigma}{d\Omega} \right\rangle_{\text{stat}}$ (mb/sr)
30	0.18	0.06
50	0.07	0.02
130	0.07	0.05
150	0.15	0.03
170	0.20	0.03
190	0.12	0.03
210	0.23	0.04
230	0.08	0.03
250	0.03	0.03
310	0.06	0.03

Table B.13: θ dependence of ϕ-averaged differential cross sections $\left\langle \frac{d\sigma_\theta}{d\Omega} \right\rangle$ (Eq. 4.1) of the ^{4}He$(\gamma, p)^3$H reaction at $\langle E_\gamma \rangle = 22.5$ MeV.

θ (degree)	$\left\langle \frac{d\sigma}{d\Omega} \right\rangle$ (mb/sr)	$\Delta \left\langle \frac{d\sigma}{d\Omega} \right\rangle_{\text{stat}}$ (mb/sr)
50	0.14	0.03
70	0.16	0.02
90	0.14	0.02
110	0.11	0.01
130	0.07	0.01
150	0.05	0.01

Table B.14: θ dependence of ϕ-averaged differential cross sections $\left\langle \frac{d\sigma_\theta}{d\Omega} \right\rangle$ (Eq. 4.1) of the ^{4}He$(\gamma, p)^3$H reaction at $\langle E_\gamma \rangle = 23.3$ MeV.

θ (degree)	$\left\langle \frac{d\sigma}{d\Omega} \right\rangle$ (mb/sr)	$\Delta \left\langle \frac{d\sigma}{d\Omega} \right\rangle_{\text{stat}}$ (mb/sr)
30	0.08	0.03
50	0.11	0.02
70	0.19	0.02
90	0.12	0.01
110	0.13	0.01
130	0.09	0.01
150	0.07	0.02

Table B.15: θ dependence of ϕ-averaged differential cross sections $\left\langle \frac{d\sigma_\theta}{d\Omega} \right\rangle$ (Eq. 4.1) of the ^{4}He$(\gamma, p)^3$H reaction at $\langle E_\gamma \rangle = 24.3$ MeV.

θ (degree)	$\left\langle \frac{d\sigma}{d\Omega} \right\rangle$ (mb/sr)	$\Delta \left\langle \frac{d\sigma}{d\Omega} \right\rangle_{\text{stat}}$ (mb/sr)
50	0.14	0.03
70	0.21	0.02
90	0.18	0.02
110	0.16	0.02
130	0.09	0.01
150	0.06	0.01

Table B.16: θ dependence of ϕ-averaged differential cross sections $\left\langle \frac{d\sigma_\theta}{d\Omega} \right\rangle$ (Eq. 4.1) of the ^{4}He$(\gamma, p)^3$H reaction at $\langle E_\gamma \rangle = 25.7$ MeV.

θ (degree)	$\left\langle \frac{d\sigma}{d\Omega} \right\rangle$ (mb/sr)	$\Delta \left\langle \frac{d\sigma}{d\Omega} \right\rangle_{\text{stat}}$ (mb/sr)
30	0.17	0.10
50	0.19	0.03
70	0.28	0.03
90	0.12	0.02
110	0.17	0.02
130	0.11	0.02
150	0.07	0.03

Table B.17: θ dependence of ϕ-averaged differential cross sections $\left\langle \frac{d\sigma_\theta}{d\Omega} \right\rangle$ (Eq. 4.1) of the ^{4}He$(\gamma, p)^3$H reaction at $\langle E_\gamma \rangle = 26.5$ MeV.

θ (degree)	$\left\langle \frac{d\sigma}{d\Omega} \right\rangle$ (mb/sr)	$\Delta \left\langle \frac{d\sigma}{d\Omega} \right\rangle_{\text{stat}}$ (mb/sr)
50	0.14	0.02
70	0.19	0.02
90	0.15	0.04
110	0.16	0.02
130	0.09	0.01
150	0.04	0.01

Table B.18: θ dependence of ϕ-averaged differential cross sections $\left\langle \frac{d\sigma_\theta}{d\Omega} \right\rangle$ (Eq. 4.1) of the ^{4}He$(\gamma, p)^3$H reaction at $\langle E_\gamma \rangle = 28.7$ MeV.

θ (degree)	$\left\langle \frac{d\sigma}{d\Omega} \right\rangle$ (mb/sr)	$\Delta \left\langle \frac{d\sigma}{d\Omega} \right\rangle_{\text{stat}}$ (mb/sr)
30	0.09	0.02
50	0.15	0.01
70	0.20	0.01
90	0.19	0.01
110	0.14	0.01
130	0.09	0.01
150	0.05	0.01

Table B.19: ϕ dependence of θ-averaged differential cross sections $\left\langle \frac{d\sigma_\phi}{d\Omega} \right\rangle$ (Eq. 4.2) of the ^{4}He$(\gamma, p)^3$H reaction at $\langle E_\gamma \rangle = 22.5$ MeV.

θ (degree)	$\left\langle \frac{d\sigma}{d\Omega} \right\rangle$ (mb/sr)	$\Delta \left\langle \frac{d\sigma}{d\Omega} \right\rangle_{\text{stat}}$ (mb/sr)
10	0.12	0.02
30	0.10	0.02
50	0.12	0.03
130	0.11	0.03
150	0.10	0.02
170	0.13	0.02
190	0.12	0.02
210	0.15	0.03
230	0.11	0.03
290	0.06	0.04
310	0.08	0.03
330	0.10	0.02
350	0.09	0.02

Table B.20: ϕ dependence of θ-averaged differential cross sections $\left\langle \frac{d\sigma_\phi}{d\Omega} \right\rangle$ (Eq. 4.2) of the ^{4}He$(\gamma, p)^3$H reaction at $\langle E_\gamma \rangle = 23.5$ MeV.

θ (degree)	$\left\langle \frac{d\sigma}{d\Omega} \right\rangle$ (mb/sr)	$\Delta \left\langle \frac{d\sigma}{d\Omega} \right\rangle_{\text{stat}}$ (mb/sr)
10	0.16	0.02
30	0.10	0.02
50	0.12	0.03
130	0.11	0.02
150	0.11	0.02
170	0.16	0.02
190	0.14	0.02
210	0.15	0.02
230	0.11	0.03
290	0.06	0.04
310	0.09	0.03
330	0.12	0.02
350	0.15	0.02

Table B.21: ϕ dependence of θ-averaged differential cross sections $\left\langle \frac{d\sigma_\phi}{d\Omega} \right\rangle$ (Eq. 4.2) of the ^{4}He$(\gamma, p)^3$H reaction at $\langle E_\gamma \rangle = 24.3$ MeV.

θ (degree)	$\left\langle \frac{d\sigma}{d\Omega} \right\rangle$ (mb/sr)	$\Delta \left\langle \frac{d\sigma}{d\Omega} \right\rangle_{\text{stat}}$ (mb/sr)
10	0.21	0.03
30	0.18	0.03
50	0.13	0.03
130	0.08	0.02
150	0.14	0.02
170	0.20	0.03
190	0.20	0.03
210	0.15	0.02
230	0.08	0.04
310	0.08	0.03
330	0.15	0.03
350	0.19	0.03

Table B.22: ϕ dependence of θ-averaged differential cross sections $\left\langle \frac{d\sigma_\phi}{d\Omega} \right\rangle$ (Eq. 4.2) of the ^{4}He$(\gamma, p)^3$H reaction at $\langle E_\gamma \rangle = 25.7$ MeV.

θ (degree)	$\left\langle \frac{d\sigma}{d\Omega} \right\rangle$ (mb/sr)	$\Delta \left\langle \frac{d\sigma}{d\Omega} \right\rangle_{\text{stat}}$ (mb/sr)
10	0.15	0.03
30	0.18	0.03
50	0.15	0.05
130	0.21	0.07
150	0.18	0.04
170	0.21	0.04
190	0.25	0.05
210	0.18	0.04
230	0.29	0.15
310	0.22	0.09
330	0.17	0.03
350	0.22	0.04

Table B.23: ϕ dependence of θ-averaged differential cross sections $\left\langle \frac{d\sigma_\phi}{d\Omega} \right\rangle$ (Eq. 4.2) of the ^{4}He$(\gamma, p)^3$H reaction at $\langle E_\gamma \rangle = 26.5$ MeV.

θ (degree)	$\left\langle \frac{d\sigma}{d\Omega} \right\rangle$ (mb/sr)	$\Delta \left\langle \frac{d\sigma}{d\Omega} \right\rangle_{\text{stat}}$ (mb/sr)
10	0.29	0.04
30	0.16	0.02
50	0.10	0.04
130	0.07	0.04
150	0.16	0.03
170	0.17	0.03
190	0.27	0.05
210	0.20	0.05
310	0.08	0.05
330	0.16	0.03
350	0.23	0.03

Table B.24: ϕ dependence of θ-averaged differential cross sections $\left\langle \frac{d\sigma_\phi}{d\Omega} \right\rangle$ (Eq. 4.2) of the ^{4}He$(\gamma, p)^3$H reaction at $\langle E_\gamma \rangle = 28.7$ MeV.

θ (degree)	$\left\langle \frac{d\sigma}{d\Omega} \right\rangle$ (mb/sr)	$\Delta \left\langle \frac{d\sigma}{d\Omega} \right\rangle_{\text{stat}}$ (mb/sr)
10	0.20	0.02
30	0.16	0.02
50	0.14	0.02
70	0.05	0.05
110	0.09	0.09
130	0.10	0.02
150	0.16	0.02
170	0.21	0.02
190	0.19	0.02
210	0.20	0.02
230	0.13	0.02
290	0.07	0.04
310	0.10	0.02
330	0.14	0.02
350	0.20	0.02